Università degli Studi di Ferrara

Department of Physics and Earth Science

Ph.D. Thesis

A perspective on the high-energy transient sky: from gamma-ray bursts to the search for fast radio burst counterparts

Advisor:

Cristiano Guidorzi

Co-Advisor:

Lorenzo Amati

Candidate:

Renato Martone

ID:

131695

Academic Year 2019/2020

Abstract

My work of thesis focuses on two protagonists of the transient sky, gamma-ray bursts (GRBs) and fast radio bursts (FRBs), tackling both the open issues behind their emission and the technological challenges connected with their observation.

In the context of an in-depth understanding of GRBs and their possible use in cosmology, some important correlations between the parameters that describe their emission have been discovered, among which the "$E_{\rm p,i} - E_{\rm iso}$" correlation is the most studied. $E_{\rm p,i}$ and $E_{\rm iso}$ are the peak frequency of the νf_ν spectrum, in the rest frame of the source and the total energy emitted in γ after assuming isotropic emission. Because of this, it is fundamental to shed light on the peculiar behaviour of a few events, namely GRB 980425 and GRB 031203, that appear to be important outliers of the $E_{\rm p,i} - E_{\rm iso}$ correlation.

In the first part of thesis, I investigate if the locations in the $E_{\rm p,i}/E_{\rm iso}$ plane of these two bursts may be due to the fact that a substantial fraction of their energy was released in the soft X-ray band, and consequently missed by the instruments that detected them (BATSE and *INTEGRAL*/IBIS). I analysed the observed emission of other similar sub-energetic bursts (GRBs 060218, 100316D and 161219B) observed by *Swift* and whose integrated emissions match the $E_{\rm p,i} - E_{\rm iso}$ relation. Then, I simulated their integrated and time-resolved emissions as would have been observed by the same detectors that observed GRB 980425 and GRB 031203, aimed at reconstructing the lightcurve and spectra of these bursts. I estimated the $E_{\rm p,i}$ and the $E_{\rm iso}$ parameters from the time-resolved and total integrated simulated spectra of GRBs 060218, 100316D and 161219B as observed by *BeppoSAX*, BATSE, *INTEGRAL* and the WFM proposed for the *LOFT*, and *eXTP* missions. My results show that, if observed by old generation instruments, GRB 060218, 100316D and 161219B would appear as outliers of the $E_{\rm p,i}$–$E_{\rm iso}$ relation, while if observed with Swift or WFM GRB 060218 would perfectly match the correlation. We also noticed that the instrument BAT alone (15-150 keV) actually measured 060218 as an outlier. My result suggests that if GRB 980425 and GRB 031203 would have been observed by *Swift* and by *eXTP* they may have matched the $E_{\rm p,i}$–$E_{\rm iso}$ relation. This provides strong support to the idea that instrumental biases can make some events in the lower-left corner of the $E_{\rm p,i} - E_{\rm iso}$ plane appearing as outliers.

GRB prompt emission mechanism is still an open issue, despite the tremendous progress made in the last decades in the comprehension of the GRB phenomenon. It has been realised that only a very broadband analysis (from soft X–rays to MeV) provides a stringent test to the proposed models in the literature. I tackled the problem performing a systematic, broadband, temporally-resolved spectral analysis of a number of GRBs to test three out of the most popular models: the empirical Band function, and more physically grounded models like the synchrotron (in the form of a double broken power–law), and the Comptonisation model "grbcomp". I also considered possible additional components, such as black body or further absorption. I selected 17 GRBs detected by both *Swift* and *Fermi* and that lasted long enough (typically $\gtrsim$ 70–100 s) to allow the former to re-point the X–ray telescope before the prompt emission was over. The spectral analysis was carried out in time intervals that had been determined with a Bayesian-block algorithm. I ended up with 93 time-resolved spectra in the energy range 0.3 keV–30 MeV. I successfully modelled about 3/4 of the entire sample using the Band function, a sizeable fraction of which requires an extra component, though. Both synchrotron and `grbcomp` are somewhat less successful (both slightly more than 50%). Interestingly, roughly 20% spectra are truly problematic for any model and are characterised by a markedly different X–ray light curve with respect to the γ–ray one. Adding X–ray data turned out essential (i) to assess the frequent presence of extra components, like in the case of the Band function; (ii) to validate physical models like synchrotron and `grbcomp`, at the same time

emphasising their limits.

In the era of multi-messenger astronomy, the exploration of the early emission from transients is a key task for understanding the encoded physics, while current generation networks of fully-robotic telescopes provide new opportunities in terms of fast followup and sky coverage. In this context, I designed a robotic pipeline for robotic optical followup of gamma-ray bursts with the Las Cumbrés Observatory network aimed at automatically submitting a request for observations within 3 minutes from the discovery alert. Via Telegram the pipeline keeps the users informed, allowing them to take control upon request. Using this code, our group was able to track the early phases of the optical evolution of GRBs with a fully-robotic procedure. I report the case of GRB 180720B as an example. The pipeline represents a key ingredient for any reliable and rapid (minutes timescale) robotic telescope system, that can also be adapted to any other robotic facilities.

The last part of my thesis focuses on FRBs, millisecond-long bursts uniquely detected at radio frequencies, with the only possible exception of FRB 131104, for which a γ–ray transient positionally and temporally consistent was claimed. This high-energy transient had a duration of $\sim$ 400 s and a 15–150 keV fluence $S_\gamma \sim 4 \times 10^{-6}$ erg cm^{-2}. However, the association with the FRB is still debated. The aim of my work was testing the systematic presence of an associated transient high-energy counterpart throughout a sample of the FRB population. I used an approach like that used in machine learning methodologies to accurately model the highly-variable *Fermi*/GBM instrumental background on a time interval comparable to the duration of the proposed γ–ray counterpart of FRB 131104. Then, I constrained the possible γ–ray signal considering sample average lightcurves. My result constrains the fluence of the possible γ–ray signal in the 8–1000 keV band down to 6.4×10^{-7} (7.1×10^{-8}) erg cm^{-2} for a 200-s (1-s) integration time. Furthermore, I found the radio-to-gamma fluence ratio to be $\eta > 10^8$ Jy ms erg^{-1} cm^2. These fluence limits exclude $\sim$ 94% of *Fermi*/GBM detected long gamma–ray bursts and $\sim$ 96% of *Fermi*/GBM detected short gamma–ray bursts. In addition, the limits point to a different emission mechanism from that of magnetar giant flares. My result excludes a γ–ray counterpart as fluent as the one possibly associated with FRB 131104 to be a common feature of FRBs.

Abstract

Il mio lavoro di tesi è incentrato su due tra i protagonisti del cielo transiente, i lampi di raggi gamma (in inglese *gamma-ray bursts*-GRBs) e i lampi veloci radio (in inglese *fast radio bursts*-FRBs), affrontando le questioni aperte circa il loro meccanismo di emissione e le sfide tecnologiche legate alla loro osservazione.

Nell'ottica di una più profonda comprensione dei GRB e del loro possibile uso in ambito cosmologico, sono state scoperte alcune importanti relazioni tra le grandezze caratterizzanti. Tra queste, la relazione "$E_{\rm p,i} - E_{\rm iso}$", popolarmente nota come "relazione di Amati" è la più studiata. $E_{\rm p,i}$ e $E_{\rm iso}$ sono rispettivamente la frequenza di picco dello spettro nella rappresentazione νf_ν nel rest frame della sorgente e l'energia totale emessa nel γ, assumendo che l'emissione sia isotropa. L'esistenza di pochi eventi (980425 e 031202 in primis) che sembrano non rispettare tale relazione rende ancora più urgente approfondirne l'origine e i limiti di applicabilità.

Nella prima parte della tesi ho investigato la possibilità che per questi GRB problematici una parte sostanziale della radiazione potrebbe essere avvenuta nella banda soft X, ovvero fuori dalla banda passante degli strumenti coinvolti nell'osservazione (nella fattispecie BATSE e *INTEGRAL*/IBIS). Ho analizzato quindi l'emissione di altri GRB sub-energetici (060218, 100316D e 161219B), simili a 980425 e 031203 per diversi aspetti ma osservati con il satellite *Swift* e che invece sono in accordo con la relazione di Amati. Ho poi simulato le curve di luce e gli spettri temporalmente risolti che si sarebbero misurati per questi eventi qualora fossero stati osservati dagli stessi detector che osservarono 980425 e 031203. Ho infine stimato le quantità $E_{\rm p,i}$ ed $E_{\rm iso}$ (sia per gli spettri simulati integrati che risolti temporalmente) di 060218, 100316D e 161219B, così come osservati da *BeppoSAX*, BATSE, *INTEGRAL* e lo strumento WFM proposto per le missioni *LOFT* e *eXTP*. I miei risultati mostrano che, se osservati con la passata generazione di strumenti, anche eventi in accordo con la Amati sarebbero invece apparsi in disaccordo con la stessa. Questa evidenza supporta fortemente la presenza di un bias strumentale che fa apparire come eccezioni alla relazione GRB che invece la rispettano.

La natura del meccanismo di emissione attivo durante la fase istantanea "prompt" dei GRB è ancora un problema aperto, nonostante il progresso degli ultimi anni sia in termini di caratterizzazione delle proprietà mostrate che nell'interpretazione. Un test stringente sui modelli proposti in letteratura può essere fornito solo tramite un'analisi a banda larga (dai raggi X soffici al gamma). Ho affrontato questo problema realizzando un'analisi sistematica, a banda larga e temporalmente risolta su diversi GRB, con lo scopo di testare tre dei modelli più diffusi: la funzione empirica di Band e due modelli con basi fisiche più definite, cioè un modello basato sull'emissione di sincrotrone (qui nella forma di una legge di potenza con cambi di pendenza-"break") e un modello basato sulla Comptonizzazione, battezzato "grbcomp". Sono stati inoltre considerati possibili componenti aggiuntive, come spettri di corpo nero e assorbimenti addizionali. Ho selezionato 17 GRB rivelati sia da *Swift* che da *Fermi* e che sono durati abbastanza (tipicamente $\gtrsim$ 70 − 100 s) da consentire al primo di ripuntare l' X-ray telescope prima del termine dell'emissione prompt. L'analisi spettrale è stata condotta su intervalli temporali preliminarmente determinati con l'algoritmo dei blocchi Bayesiani, che ha portato a 93 spettri risolti temporalmente con una copertura nell'intero range 0.3 keV-30 MeV. Circa tre quarti di questi sono stati modellati con successo usando la funzione di Band, nonostante si sia reso necessario l'uso di componenti aggiuntive per una frazione significativa. Sia il modello basato sul sincrotrone che `grbcomp` hanno avuto in qualche misura meno successo, riuscendo a fittare gli spettri in poco più del 50 % dei casi. E' interessante notare che circa il 20 % degli spettri sono problematici per tutti i modelli e sono inoltre caratterizzati da una differenza marcata tra la curva di luce in banda X e quella nei raggi γ. L'aggiunta di dati X si è mostrata essenziale per (i) affermare la presenza frequente di componenti aggiuntive, come nel caso della funzione

di Band; (ii) validare modelli fisici come quello basato sul sincrotrone o `grbcomp`, enfatizzando al contempo i loro limiti di applicabilità.

Nell'era dell'astronomia multi messaggero, l'esplorazione delle prime fasi dell'emissione dai transienti è la chiave per capirne la fisica. Al contempo, reti di telescopi robotici forniscono opportunità nuove in termini di puntamento rapido e copertura del cielo. In questo contesto, ho progettato e realizzato una pipeline robotica per l'osservazione automatica di GRB con la rete Las Cumbrés Observatory, con lo scopo precipuo di sottomettere richieste di osservazione entro 3 minuti dalla ricezione della notifica distribuita via socket. La pipeline comunica con gli utenti via Telegram, consentendo loro di prendere il controllo delle operazioni su richiesta. L'utilizzo di questo codice ha consentito al nostro gruppo di monitorare le prime fasi dell'evoluzione dell'emissione ottica dei GRB con una procedura totalmente autonoma. A titolo di esempio, nella tesi riporto il caso di GRB 170820B. La pipeline ha il vantaggio di potersi adattare anche ad altre infrastrutture e rappresenta l'ingrediente chiave per qualunque sistema robotico che abbia come obiettivi la velocità e l'affidabilità.

L'ultima parte della mia tesi si focalizza sugli FRB, lampi di durata dell'ordine del millisecondo rilevati solo nel radio. L'unica possibile e controversa eccezione in tal senso è rappresentata da FRB 131104, per cui alcuni autori hanno sostenuto la presenza di un transiente γ temporalmente e spazialmente coincidente. Il transiente presenta una durata di $\sim$ 400 s e una fluence $S_\gamma \sim 4 \times 10^{-6}$ erg cm^{-2} nella banda 15-150 keV. Lo scopo del mio lavoro è stato quello di testare la presenza sistematica di una controparte transiente alle alte energie per un campione di FRB. Ho fatto uso di un approccio analogo a quello usato abitualmente nei problemi di machine learning al fine di modellare il fondo strumentale altamente variabile di *Fermi*/GBM in un intervallo comparabile con la durata della ipotetica controparte γ proposta nel caso di FRB 131104. Dopodiché, ho vincolato la possibile presenza di segnale γ considerando curve di luce medie. Il mio risultato vincola la fluence di questo possibile segnale nel range 8-1000 keV ad essere al di sotto di 6.4×10^{-7} (7.1×10^{-8} erg cm^{-2}) per un tempo di integrazione di 200 s (1 s). Inoltre, ho trovato che il rapporto radio-gamma è $\eta > 10^8$ Jy ms erg^{-1} cm^2. Questo limite esclude $\sim$ 94% dei GRB lunghi e il $\sim$ 96% dei GRB corti rivelati da *Fermi*/GBM. Questi limiti puntano inoltre a un meccanismo di emissione diverso da quello osservato nei flare giganti da magnetar. Infine, il risultato esclude che una controparte γ fluente come quella proposta per FRB 131104 sia una caratteristica comune a tutti gli FRB.

Contents

Chapter 1

GRB generalities

This first chapter provides a brief description of the basic properties of GRBs. A complete and exhaustive treatment of the arguments treated in this chapter is beyond the aim of the thesis.

1.1 A brief history of GRBs

The discovery of GRBs was a fortuitous consequence of the Cold War. In October 1962, as a direct effect of the Cuban Missile Crisis, USA, URSS and UK agreed on the necessity to improve the control on the nuclear weapons testing. Soon after the agreement, the US Army started to project and launch a series of satellites called Vela (from the spanish *Velador*, meaning *Watchman*), specifically designed to detect secondary products of nuclear detonation different from optical photons, like Neutrons, X-rays and particularly γ-rays. The facilities used to work in pairs, in order to reduce the effects of the background that was completely unknown at that time. The first couple was launched in 1963. Interestingly, no events from Earth were detected, but the data analysis started in 1969 recognized events from unknown sources that triggered multiple satellites: an event happened on July 2, 1967 particularly stood out in reason of the sharp rising in the number of counts with respect to the gamma-ray background and immediately became the object of further investigation. The crude triangulation capability of the Vela network led to the conclusion that the event was not of Solar System origin and so the discovery of a completely new class of phenomena was established. This discovery was made public only in 1973 at the annual Meeting of the *American Astronomical Society* (Klebesadel et al. 1973; Strong 1975).

The following years were dedicated to the identification of the source: theoretical works tested the hypothesis of a connection between these GRBs and SNe. Unfortunately, the final experimental proof was almost impossible to obtain, since the difficulties in focusing γ-rays made an accurate localization impossible.

In this context, a debate set on between the supporters of a Galactic and extragalactic origin of the phenomenon, both groups having good arguments in the framework of the observations available at that time. The discovery of the isotropic distribution of GRBs did not settle the question because both groups stated it was a strong confirmation of their hypothesis: while the "extragalactic origin supporters" asserted this was an effect of the Cosmological Principle, their opponents used the example of the 790305 event (unambiguously connected to a SN remnant and so, to a *neutron star* (NS)) to infer that spacial isotropy was due to neutron stars populating the galactic halo. Events like 790305 are now considered the prototype of a class of objects called *Soft Gamma Ray Repeaters* (SGRs). In this situation, the only way to get a verdict was a direct distance measure.

This revolution happened in 1996, with the launch of the Italian (with Dutch participation)

satellite *BeppoSAX* (Boella et al. 1997), that used to allow a localization of the sources into an error box radius of ∼ 5-10 arcminute in a matter of few hours (Costa et al. 1997; Costa & Frontera 2003). The first goal reached by the new satellite was the detection of the first *afterglows*, the X-ray emission that usually follows the prompt γ-ray emission from a GRB. The quickness and accuracy on the burst position determination allowed rapid optical followup and so a number GRB optical counterparts were identified. Examples in this sense is the very first detected afterglow, identified for GRB 970228 (van Paradijs et al. 1997), and GRB 970508, for which optical observations allowed a precise redshift determination, namely $z = 0.835$ (Metzger et al. 1997). However, in all the cases in which this kind of followup were possible, the sources were placed at cosmological distance, plenty outside from the halo of the Milky Way, so the new Great Debate was closed and the extragalactic origin of GRBs was finally settled.

In the last decades, the detection of neutrino emission associated with SN 1987A (Hirata et al. 1987; Bionta et al. 1987; Alexeyev et al. 1987; Aglietta et al. 1987) and, more recently, GW (Abbott et al. 2016a,b) observations opened brand-new observational windows, giving birth to Multi-Messenger astronomy. On 17 August 2017, GRB science officially entered this new era, with the detection in GW of a neutron star-neutron star merger event (Abbott et al. 2017b) associated with a Short GRB (GRB 170817A, Abbott et al. 2017a). GRB 170817A was the object of an extended, multi-wavelength follow-up campaign that resulted in detections also in optical, radio, and X-rays, and in the identification of its elliptical host galaxy at a distance ∼ 40 Mpc (Smartt et al. 2017; Pian et al. 2017). After that moment, the study and the rapid follow-up of every new GW transient have become a global effort that teases the interest of the whole astronomical community.

1.2 GRB emission

GRB emission happens in two very different stages: the explosion itself, during which the erratic γ-ray emission is detected, called *prompt emission*, and its aftermath, constituted by a shallower signal at lower frequencies, called *afterglow*. The exact moment between the end of the first and the onset of second is often difficult to recognize beyond any doubt.

1.2.1 The prompt emission

The prompt phase is the first emission detected with high-energy instruments. The bulk of the energy is emitted during this phase, that can last from fraction of seconds up to minutes without any sign of periodicity. This emission is believed to originate from the energy dissipation that happens in the jet, that loses energy via shocks or magnetic dissipation. Because of this, synchrotron emission is believed to contribute for the major part of the flux, producing a highly non-thermal spectrum, with a powerlaw decrease of the flux at high energies. However, a thermal contribution has been observed in many cases (e.g. Campana et al. 2006; Guiriec et al. 2011; Axelsson et al. 2012; Guiriec et al. 2013) and many authors identify three main spectral components (see e.g. Zhang (2011)):

- I. A non-thermal component (see 1.2.2 for details) extending in the range ∼ a few keV up to hundreds of keV that is believed to originate from a non-thermal synchrotron radiation from an optically-thin region.

- II. Thermal or quasi thermal component, usually extending in the range ∼ a few keV up to ∼ a few tens of keV and that is believed to originate from the photosphere surrounding the center of the explosion.

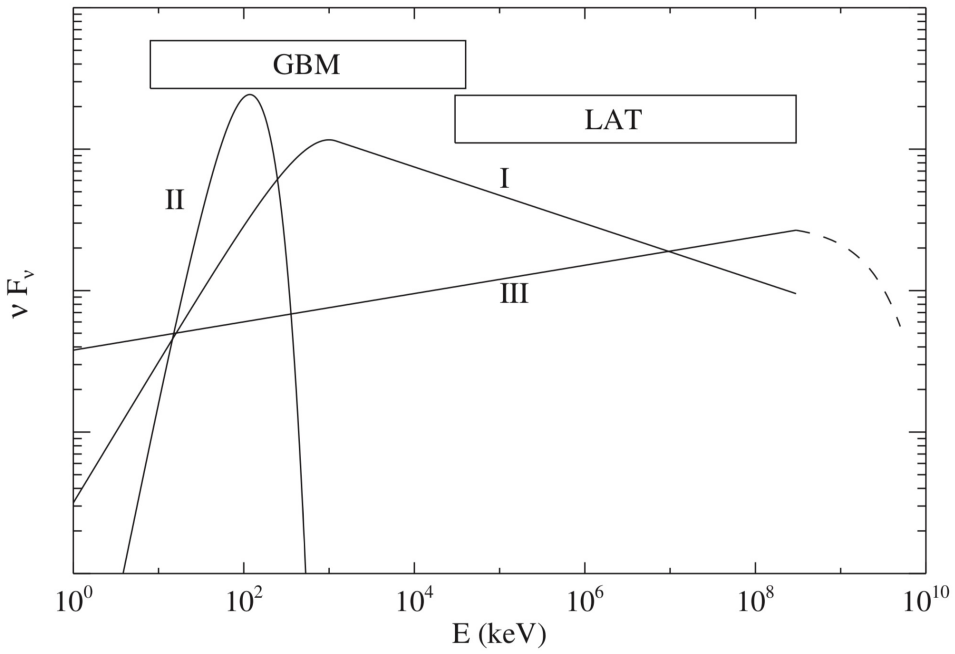

Figure 1.1: The three possible spectral components that shape the observed time-resolved spectra of GRBs. There are many variations on this general picture. Figure from Zhang (2011).

- III. A long non-thermal tail extending up to $\sim$ GeV energies (e.g. in Ackermann et al. 2010). This component is the most largely uncertain, even if it could be naturally explained considering inverse Compton scatterings, while Other authors suggest it could be part afterglow emission (Ghisellini et al. 2010).

A sketch of this basic scheme is reported in Figure 1.1. In the vast majority of cases, the non-thermal component (I) is the main contributor in terms of flux. However, its interpretation in terms of pure synchrotron radiation (observed in other astrophysical objects like blazars, supernova remnant, etc.), is challenged by the tension between theoretical predictions and observations. In GRBs, given the strong magnetic fields present in the prompt emission region, electrons are expected to lose energy on a time-scale much shorter than the dynamical one. This is called fast-cooling regime and predicts a spectral index under the peak of the νF_ν spectrum ~ -1.5, in contrast with the observed typical value ~ -1. A number of different mechanisms has been proposed to solve this tension, invoking both a modification of the pure fast-cooling synchrotron scenario and completely different paradigms. We present further details in the introduction of chapter 3.

The prompt estimated isotropic luminosity is in the range $10^{47}-10^{54}$ erg/s, implying isotropic energies of about $10^{48} - 10^{54}$ erg. Even if this kind of high energy emission is the most characterizing feature of the prompt phase, lower-energies photons can be detected, also in the optical domain: interestingly, the lightcurves associated with these low-energy emissions sometimes follow the evolution of γ-ray ones simultaneously (see e.g. Akerlof et al. 1999; Blake et al. 2005; Guidorzi et al. 2011), while in other cases a time lag with respect to the high-energy emission is observed (see e.g. Rykoff et al. 2004; Klotz et al. 2008).

To provide a general description of the prompt phase is a very difficult exercise, due to the plethora of different behaviours that we can observe in the GRB populations; indeed we do not detect even a couple of objects that are perfectly identical.

Lightcurves are sometimes very complex and structured, with a wide number of different pulses, but also single pulses are commonly observed. Figure 1.2 provides a feeling of the zoo

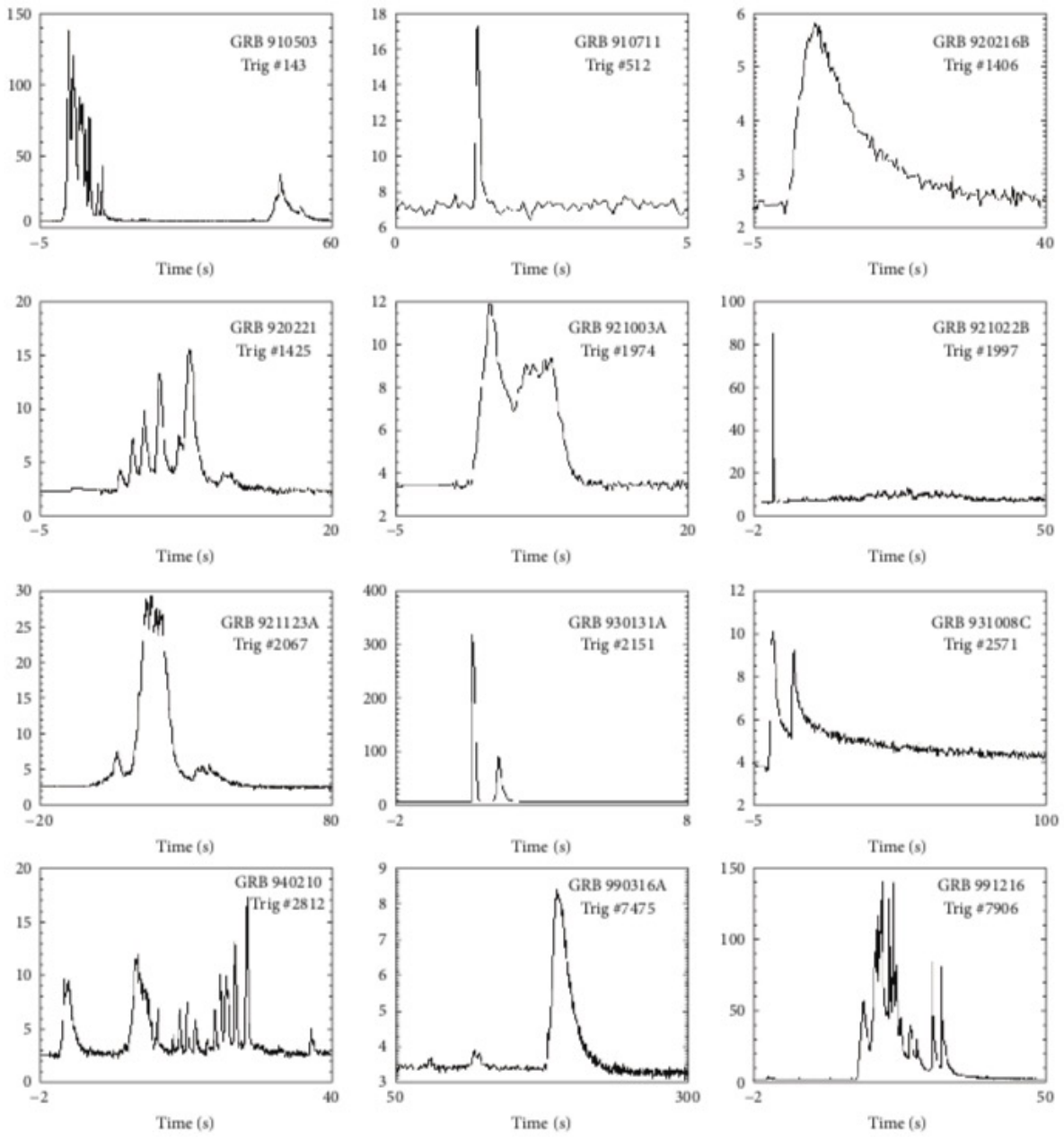

Figure 1.2: Lightcurves of 12 bright gamma-ray bursts detected by BATSE. Gamma-ray bursts lightcurves display a tremendous amount of diversity and few discernible patterns. Figure from Pe'er (2015).

of different observed lightcurves. Chromatic behaviours are also very common, and typically narrower profiles are observed at higher energies.

The duration of the burst can be estimated using a wide set of parameters, including T_{90}, the most broadly used in literature. This quantity is defined as the total time between when 5 % and 95 % of the total energy above the background level is accumulated. Unfortunately, this is a detector−dependent parameter, depending on the trigger mechanism and, above all, on the efficiency of the instrument in the energy bands involved in the detection. In addition to this, T_{90} becomes almost worthless when the event presents gaps during which no emission is detected, in these cases leading to an overestimation of the time during which the central engine is active. In spite of these caveats, T_{90} is useful in the sense of a general indication on the duration of the burst.

1.2.2 Prompt emission spectral modelling

The Band function

The continuum of the prompt spectral emission of a wide number of GRBs is described by the empirical (Band et al. 1993). This models the number of photons as a function of energy, using the shape of two smoothly-connected powerlaws and a total of 4 parameters that are:

1. the normalization constant K;
2. the low-energy photon spectra index α, with typical values in the range $-1.5 \leq \alpha \leq 0.5$;
3. the high-energy photon spectra index β, that usually is in the range $-2.5 \leq \beta \leq -2$;
4. the peak energy $E_{\rm p}$ of the νf_ν spectrum, that usually is in the range from several keV to a few MeV.

The fitting function can be written as:

$$N(E) = K \begin{cases} \left(\frac{E}{100}\right)^{\alpha} exp\left[\frac{-E(2+\alpha)}{E_p}\right] & E \leq \left(\frac{\alpha-\beta}{2+\alpha}\right) E_p \\ \left(\frac{E}{100}\right)^{\beta} exp[\beta-\alpha] \left[\frac{(\alpha-\beta)E_p}{2+\alpha}\right]^{\alpha-\beta} & E > \left(\frac{\alpha-\beta}{2+\alpha}\right) E_p \end{cases} \tag{1.1}$$

This function reduces to:

- a powerlaw for $\alpha \to \beta$ or $\beta \to \alpha$;
- a cut-off powerlaw for $\beta \to \infty$.

All these parameters can show a moderate to strong (more often) time evolution, sometimes tracking the evolution of the lightcurve.

GRBCOMP

In the work we present in chapter 3, we perform a broadband, time-resolved analysis on a number of very fluent GRBs, aimed at testing different models for the prompt spectra. GRBCOMP, first proposed in Titarchuk et al. (2012), is one the two physical models we test. It consists in a photospheric model in which a bath of soft seed photons at temperature kT_s is up-scattered through Compton scattering by a subrelativistically expanding Maxwellian electron plasma with temperature kT_e and with Thomson optical depth τ. In this picture, the spectrum up to the peak

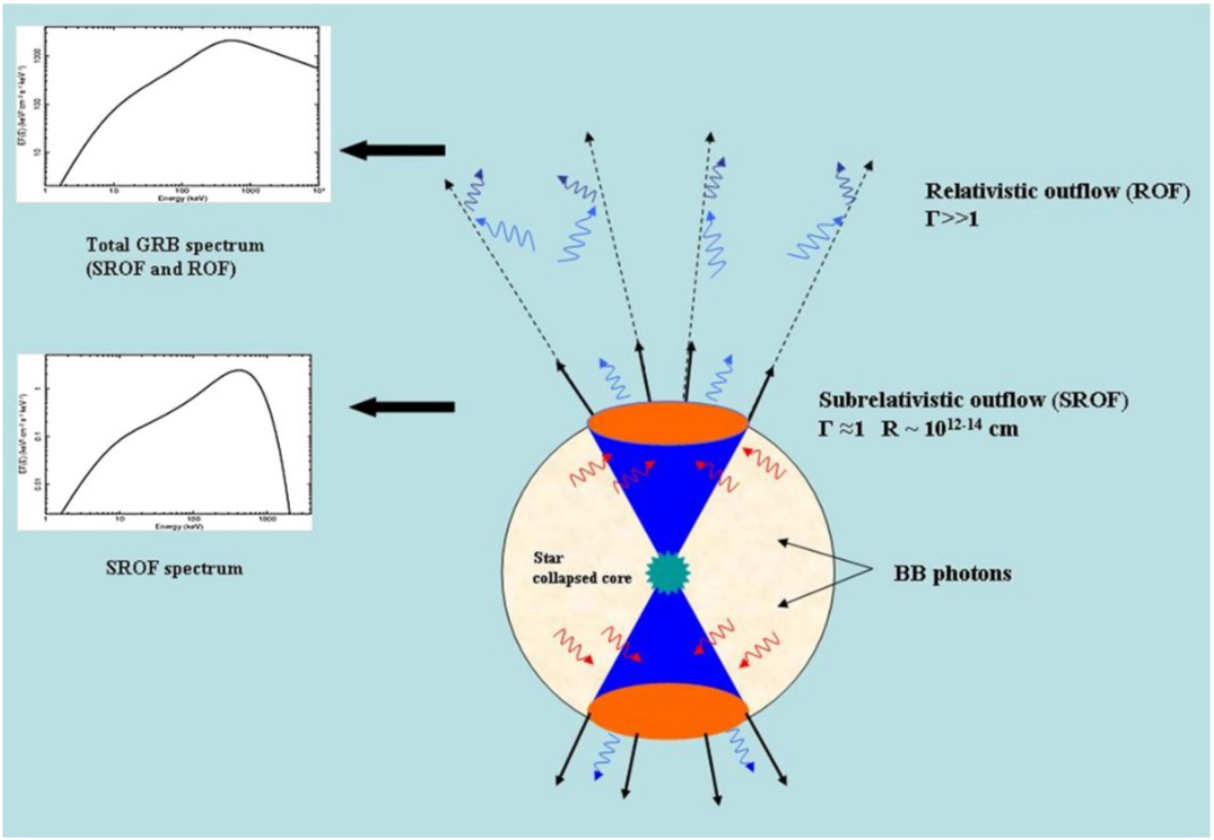

Figure 1.3: Schematic view of the explosion of a massive star and associated emergent spectral components. At the first stage, the spectrum is formed by Comptonisation of blackbody-like seed photons (red arrows) placed at the bottom of a hot subrelativistic outflow (SROF or Compton cloud) with Lorentz factor $\Gamma \approx 1$ on the top of the star photosphere (orange region). The Compton cloud can be accelerated by the underlying radiation pressure of the star photosphere leading to the relativistic outflow (ROF). Inverse Compton scattering of the Comptonized photons of the subrelativistic phase off non-thermal relativistic electrons of the ROF with $\Gamma \gg 1$ can be the origin of the extended power law observed above the peak in the EF(E) diagram (dark blue arrows). Figure from Titarchuk et al. (2012).

of the νF_ν spectrum (corresponding to the Band's $E_{\rm p}$) is the result of these multiple scatterings in a regime in which $\tau > 1$ and the position of the peak depends (in first-order approximation) only on kT_e. The high-energy part of the spectrum is instead generated in the region where the relativistic jet is launched: here the optical depth is < 1 and so only a small fraction of photons that were Comptonized during the previous phase are further upper-scattered, with the majority that passes freely though the jet region. According to this picture, the photons Comptonized in the subrelativistic phase are emitted isotropically, while the smaller further upper-scattered fraction is only emitted in a small angle along the jet direction, modifying only the high-energy tail of the emitted spectrum. A sketch of the described scenario is proposed in Figure 1.3.

We performed our analysis using the `xspec` implementation of GRBCOMP[1], that contains the following parameters:

- kT_s: the temperature of the seed blackbody spectrum (keV).
- gamma: this parameter rules the shape of the soft seed spectrum. When gamma=3, the seed photon spectrum is a blackbody.
- kT_e: the electron temperature of the subrelativistic outflow (keV).
- tau: the radial optical depth of the subrelativistic outflow.
- beta: the bulk outflow velocity of the thermal electrons.
- fbflag: this parameter rules the treatment of the Comptonisation process. If fbflag=0, only the first-order term is considered, while if fbflag=1 also the second-order term is computed.
- log(A): this factor determines the relative weights of the seed and Comptonized spectra to the total flux.
- z: the redshift of the source.
- α_{boost}: energy index of the Green's function with which the Componization spectrum is convoluted to model the high-energy powerlaw tail of the spectrum.
- norm: R_g^2/D_{Mpc}^2, being R_g the apparent blackbody radius in units of 10^9 cm, while D_{Mpc} is the source distance in Mpc.

1.2.3 Afterglow

After their discovery in 1997, afterglows have become fundamental in the field of research on GRBs, overcoming in this sense even the prompt emission. It has happened for a wide number of reasons, we can briefly describe as it follows:

- localization: X-rays, ultraviolet and optical photons can be focused, even if with different efficiencies, leading often to the precise localization that is the starting point for further analysis. So, the first, rapid localization with γ-rays (with an accuracy of $\sim$ a few arcminutes in the best cases) is refined using X-rays and ultraviolet, trying to shrink the field for the research of an optical counterpart;
- duration: afterglows can last for weeks, making possible to understand the long time evolution of the spectrum, as well as the complex interplay between the event and the circumburst medium;

[1] https://heasarc.gsfc.nasa.gov/xanadu/xspec/manual/node178.html

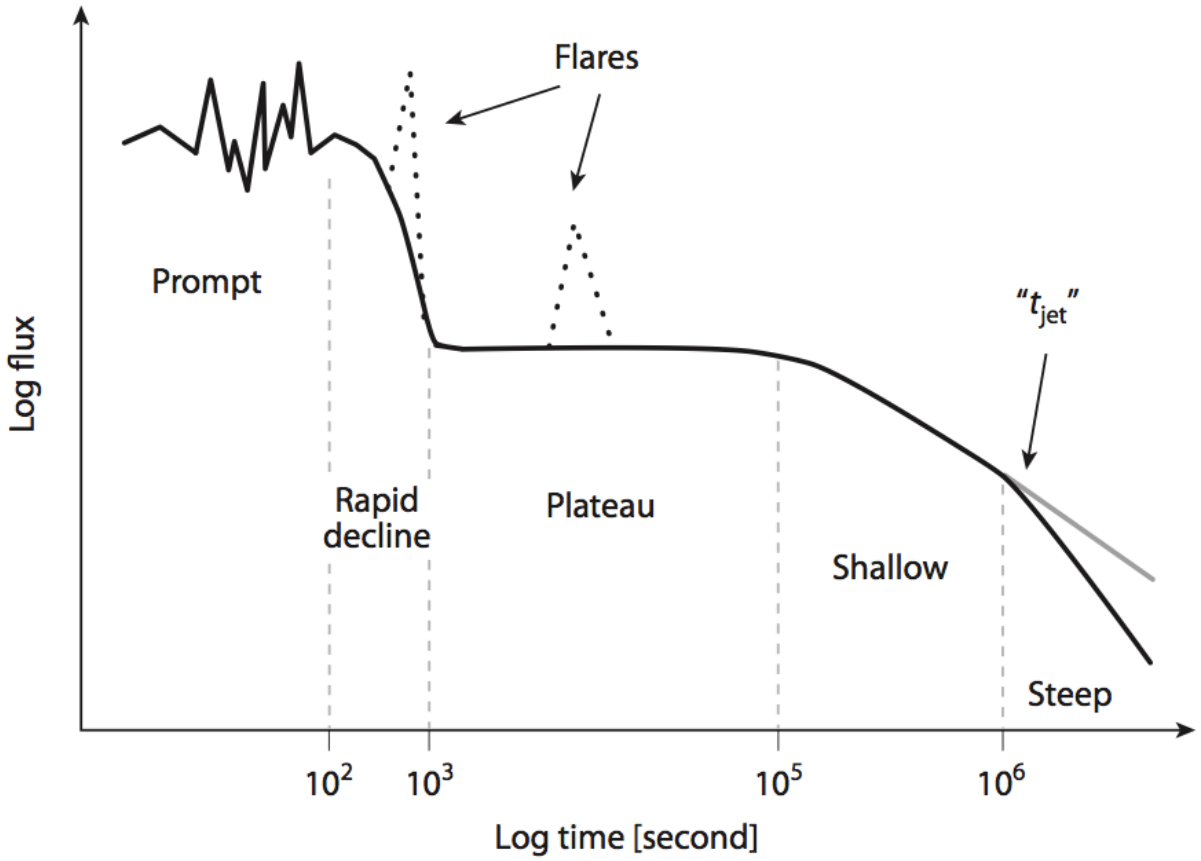

Figure 1.4: Canonical X-ray lightcurve following the evolution from the trigger time. After an initial, erratic phase, a rapid decline is then often seen. Then, a period of relatively steady flux follows, called the ”plateau” phase. The ”shallow” and the ”steep” phases are seen after several hours. The transition (”break”) from shallow to steep is often referred to as the *jet break time* (t_{jet}). Bright pulses seen after the prompt phase are called ”*flares*”. There are many variations on this general picture from Bloom (2011).

- long wavelength emission: afterglows emit even in the range of micro and radio waves, radiations that are able to get over the dust obscuration. Thanks to the reduced absorption at these frequencies, collection of data from the core of the emission becomes possible.

However, in a wide number of cases, no afterglows are observed and so a sub-arcminute localization is nearly impossible. This has been reduced in the last decade thanks to the beginning of the *Swift* era (Gehrels et al. 2006): the facility has been a real revolution in this field of research, because more than 83 % of Swift-detected GRBs is associated to an X-ray afterglow[2].

During the first years after the discovery of afterglows, the most widespread picture used to describe the prompt emission as a an erratic sequence of pulses in X and γ-rays and the afterglow as a powerlaw decay both in time and frequency. Now, thanks primarily to the advent of the *Swift* era, the old picture has been revised, and the powerlaw behaviour is now considered too simple: the current description involves the use of different powerlaws superimposed by an occasional flaring activity, that is detected for the vast majority of the afterglows. Even if a general trend is impossible to define, we can recognize qualitatively the following phases in an X-ray afterglow (see Figure 1.4):

1. lower energy extension of the prompt emission, showing usually an erratic activity;

2. steep decline phase, with a dimming of several magnitudes in hundreds of seconds and a decay index $\alpha \leq 3$;

3. shallow or plateau phase lasting for about tens of thousands of seconds, usually with $0 \leq \alpha \leq 0.5$;

4. mid-steep decline phase that can last hundreds of thousands of seconds, usually with $\alpha \leq 1.2$, even if steeper decays can be observed. The observation of a steeper behaviour is usually of the maximum importance, posing constraints on the geometry of the emission: an achromatic break could be connected with the presence of a jetted emission.

An overlook on the relation between the prompt γ-ray and the X-ray afterglow properties based on hundreds of Swift-detected GRBs can be found in Margutti et al. (2013), while Melandri et al. (2008) provide an extensively analysis the early afterglow behaviour in the optical and its relation with the X-ray afterglow emission. The flaring activity, when present, consists in a rapid rising and falling of the X-ray emission observed usually during the early steps of the afterglow. The energy release is usually of the order of a few percent of the total emission and the duration is about the 10% of the whole afterglow.

1.3 hard vs soft bursts

In the early 90s, BATSE find a bimodal distribution both in duration and spectral hardness, with long GRBs ($T_{90} > 2$ s), on average, softer than short bursts ($T_{90} < 2$ s). This initial picture was then strengthened during the *Swift* era, when redshift measurements became available for a wide number of bursts and so intrinsic quantities could be calculated[3].

The second important caveat is that T_{90} is detector-dependent, because different detectors are able to detect photons in different bands of energy, tracking different components of the

[2]Information extracted from the catalogue https://swift.gsfc.nasa.gov/results/batgrbcat/index_tables.html

[3]High-redshift events are both stretched by cosmological time dilation and shortened by the fact that only a fraction of their emission overcomes the background. This can reduce the effects of the cosmological redshift on T_{90} (Lü et al. 2014)

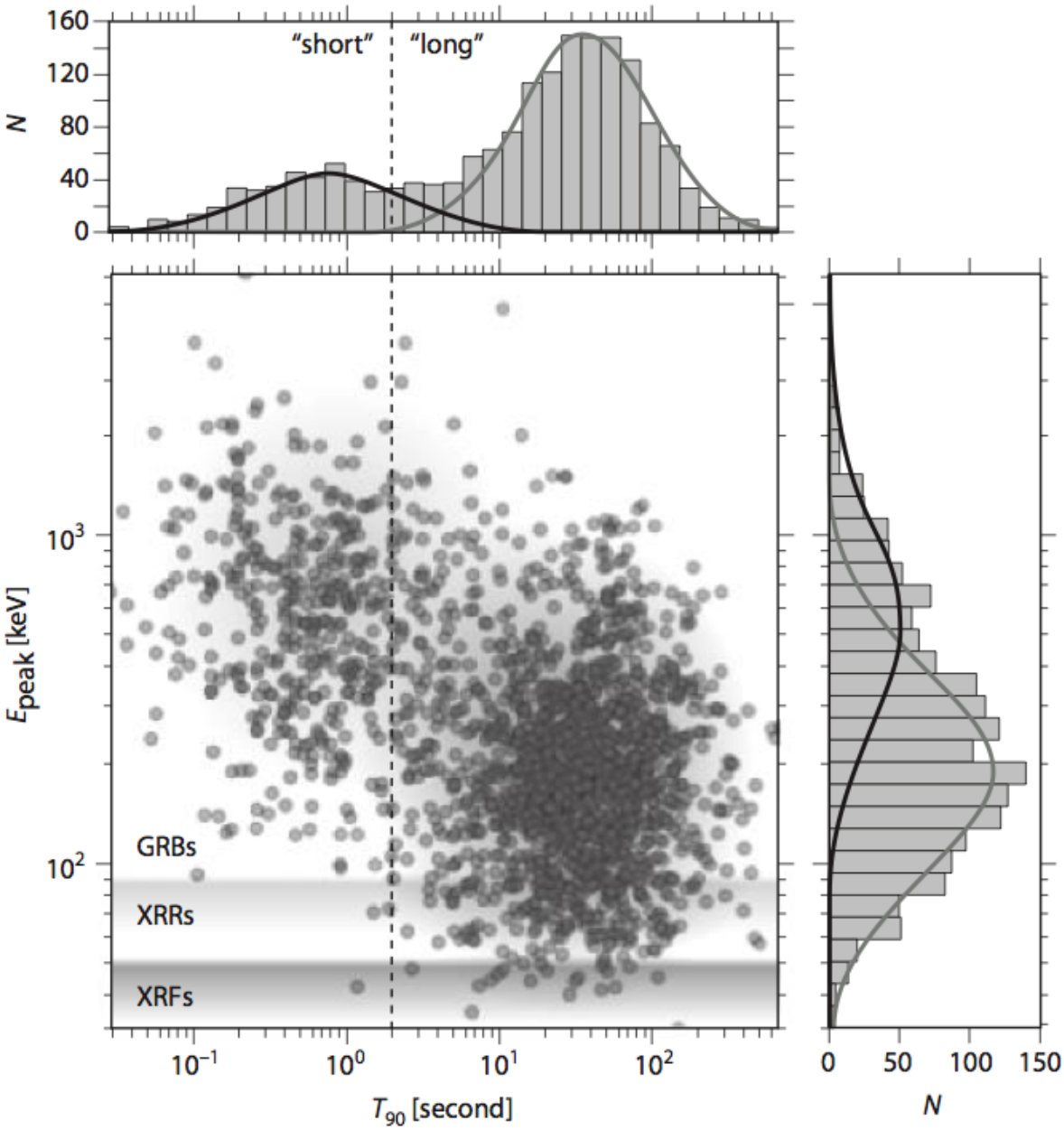

Figure 1.5: The spectral-duration distribution of GRBs as seen by BATSE. The scatter plot of E_p versus T_{90} shows two clear loci of events (shaded regions) with shorter events appearing preferentially harder (i.e., larger E_p). The approximate E_p distribution of XRFs, and X-ray Repeaters (XRRs), and GRBs is shown as horizontal gray regions. The outset histograms, showing the number of events in a certain parameter range (top: duration; right: peak energy) also show a separation (most prominently in duration). The smooth curves atop the histograms show representative log-Gaussian fits to the distributions. The traditional two-second dividing line between "short" and "long" GRBs is shown. While the bimodal distribution in duration persists across instruments, a plot of hardness versus duration for Swift-only GRBs would appear differently: since Swift is relatively insensitive to detecting very hard events of short duration and very soft events at long duration, there is no clear bimodality in hardness of Swift events. The uncertainties in the measured quantities for each event are not shown for clarity. Figure from Bloom (2011).

emission. So, since GRB spectra are the convolution of different spectra originating at different times and with a different duration, differences in energy sensitivities usually mean differences in the estimated duration of the burst. The proof is that different instruments detect different percentages for the number of short GRBs with respect to their long counterpart: for example, for BATSE (energy range 25-1900 keV) about 25% of GRBs were short, while they are about 10% for Swift (energy range 0.3-150 keV).

The existence of these two classes is supported also by other pieces of evidence:

- *isotropic energies*: short GRBs have isotropic energies in the range $10^{49} - 10^{52}$ erg, while Long GRBs can reach energies up to 10^{55} erg;
- *redshift*: short GRBs have usually median redshift of $z \sim 0.5$, while the long class $z \sim 2$, although they can be observed up to $z \sim 8 - 9$ (Salvaterra et al. 2009; Cucchiara et al. 2011);
- *spectral lags*: the time delay between the arrival of high and low energy photons is usually positive for long GRBs and null for their short counterpart (Norris et al. 2010);
- *progenitors*: follow up in ultraviolet, optical and infrared bands suggest that short GRBs are usually connected with old stellar populations, while long GRBs trace star formation regions. This picture is strongly supported by the two "smoking guns", the short-GRB/GW event 170817 and the number of SN-associated long GRBs.

However, this summary is probably too simple. There is evidence for the existence of intermediate ($T_{90} \gtrsim 2$ s) and ultralong ($T_{90} \gtrsim 1000$ s) durations event classes (Gendre et al. 2013) even if an appropriate statistical analyses is difficult to perform given their relatively small number (Ripa & Meszaros 2015).

In addition, we note the existence of events with long-short hybrid properties: an example is GRB 060614, a member of the short group when one looks at the hardness of the spectrum and time lag, but with a duration typical of a long event. This event has been unsuccessfully studied for searching an associated SN Della Valle et al. (2006a), Fynbo et al. (2006), and Gal-Yam et al. (2006). More recently, Yang et al. (2015) suggested the detection of a kilonova-like bump in the near-infrared spectrum of GRB 060614, then suggesting a compact-binary-merging origin.

Finally, some authors infer that the long group should be further divided into two groups on the basis of the luminosity: according to these authors, the "low luminosity long GRBs" form a different group from classical GRBs, showing smoother lightcurves and exploding at a higher rate (Guetta & Della Valle 2007; Virgili et al. 2009).

However, the debate on this controversial argument is far from its end, and the simple long/short picture is argument of active research still today.

1.4 Environment and possible progenitors

Nowadays, the identification of the location in the host galaxy has become possible for a number of events. Here we present a brief general description of the results of these researches, following Berger (2009):

- *type of host galaxy*: short bursts are found in both early and late type galaxy, even if there is a clear preference for the latter type ($\sim 80\%$ of cases), while long bursts are almost ever found in late type galaxies. Short-GRBs hosts have usually higher masses than galaxies that host their long bursts, with median values of the stellar population age respectively of 250 and 60 Myr (Leibler & Berger 2010);

- *star formation rate*: in the same redshift range, short GRB hosts present a star formation rate in the range $0.2 - 6\ M_\odot\ \mathrm{yr}^{-1}$, while in the long-GRB case this parameter is significantly higher, being in the range $0.2 - 50\ M_\odot\ \mathrm{yr}^{-1}$. However, even the star-forming hosts of short GRBs have different properties from the long GRB hosts (Fong et al. 2010);

- *metallicity*: long-bursts hosts present a metallicity $Z < Z_\odot$, while short-bursts hosts present $Z \approx Z_\odot$, at $z < 1$;

- *luminosity*: short-GRB hosts are usually more luminous than long-GRBs hosts, with an average difference in the optical blue band of $\Delta M_B = 1.1$ mag;

- *distance from the center of the galaxy*: short GRBs are found on average five times farther from the center of their host galaxy with respect to their long counterpart (Fong et al. 2010).

All these pieces of evidence suggest that short events are connected with the merging of old, compact objects like white dwarfs, neutron stars or black holes. In this picture, the last point is justified by the strong momentum a compact object receives after the explosion of a SN, given its great spatial asymmetry with respect to the center of the explosion. The presence of short events in both early and late type galaxies is not surprising, since old system can be present in young galaxies too, even if their presence in elliptical galaxies is obviously stronger.

On the other hand, long-GRB progenitors are believed to be massive short-living stars, living and dying next to their birthplace and tracing star-forming regions, that are mainly present in late-type galaxies.

1.5 The $E_{\mathrm{p,i}}/E_{\mathrm{iso}}$ relation and other correlations

One of the most quoted and studied of correlation between the parameters describing GRB emission is the $E_{\mathrm{p,i}}/E_{\mathrm{iso}}$ relation (also called *Amati relation*), that involves the rest-frame peak energy in the νf_ν, $E_{\mathrm{p,i}}$, and the isotropic rest-frame energy in the $1 - 10^4$ keV range $E_{\gamma,\mathrm{iso}}$ (Amati et al. 2002). Amati (2006) on the basis of 41 events, derive the correlation in the form:

$$\frac{E_{\mathrm{p}}}{1\ \mathrm{keV}} = (81 \pm 2)\left(\frac{E_{\gamma,\mathrm{iso}}}{10^{52}\ \mathrm{erg}}\right)^{0.57\pm0.02} \tag{1.2}$$

.

In spite of its importance, outliers do exist. One of the most outstanding is GRB 980425, because it is considered the prototype of the GRB-SN connection (GRB 980425/SN 1998bw). A possible explanation for their origin is discussed in Chapter 2.

This is not the only interesting correlation that has been found between the parameters of GRBs. An interesting example is the *Yonetoku correlation* (Yonetoku et al. 2004), that involves E_{p} and the isotropic peak luminosity L_{iso} and that, in its original form, was based on 16 events:

$$\frac{10^5 L_{\mathrm{iso}}}{10^{52}\ \mathrm{erg\ s^{-1}}} = \left(2.34^{+2.29}_{-1.76}\right)\left(\frac{E_{peak}}{1\ \mathrm{keV}}\right)^{2.0\pm0.2} \tag{1.3}$$

Another interesting example of correlation is similar to the Amati but involves the collimation-corrected energy E_γ instead of $E_{\gamma,\mathrm{iso}}$ (Ghirlanda et al. 2004). The correlation can be written in the form:

$$\frac{E_{peak}}{100\ \mathrm{keV}} \simeq 4.8\left(\frac{E_\gamma}{10^{51}\ \mathrm{erg}}\right)^{0.7} \tag{1.4}$$

Where E_γ is:

$$E_\gamma = \frac{E_{\rm iso}}{2\pi} \int 2\pi \ \sin\theta \, d\theta = \Big(1 - \cos\theta_j\Big) E_{\rm iso}. \tag{1.5}$$

where θ_j is the jet half opening angle.

1.6 Long-GRB/SN Connection

The idea of a possible connection between GRBs and SNe is an old one and has been one of the most active field of research since the very beginning. This is because, at the time, SN explosions were the only known events considered capable of producing such a wide amount of high energy photons. This consideration came from theoretical works preceding the GRB discovery, where the presence of a signature in γ-rays of the SN emission was suggested (Colgate 1974).

Furthermore, the most accepted models for the origin of GRB (like, for example, the *collapsar model*) connect this kind of phenomena with the death of massive stars, in regions where very high star formation rate is inferred (see Kovacevic et al. 2014). However, binary scenarios have been proposed too, involving the interaction between a compact object and a dying massive star. An example in this sense is the induced gravitational collapse (IGC) model (Ruffini et al. 2001, 2008), in which the proposed progenitor is a tight binary system composed of a carbon-oxygen (CO) core and a NS companion. The ejecta of the CO explosion into a SN leads to hypercritical accretion onto the NS companion, that eventually collapses into a BH. During this last stage, the GRB is emitted shortly after the SN, in $\approx 10^1 - 10^3$ s (Izzo et al. 2012; Fryer et al. 2014).

An important breakthrough came out in 1998, with the detection of GRB 980326 (Bloom et al. 1999; Reichart 1997) and mostly GRB 980425, with the identification of s SN in the *BeppoSAX* errorbox (Galama et al. 1998; Kulkarni et al. 1998). After that first detection, a red bump very similar in shape with what observed in SNe was detected in the optical lightcurve of several other GRBs (Bloom et al. 1999; Della Valle et al. 2006b). GRB 980425 showed also a number of peculiar characteristics: the GRB had a very low energy output, together with a very high value of $E_{\rm p}$, while the SN was very bright and classified as "peculiar". These circumstances enriched the simple long/short picture and led some authors to propose the existence of distinct progenitors for this kind of low luminous, long GRB and for the classical, long ones.

Currently, we have obtained dozens of photometric and spectroscopic identifications of SNe connected to GRBs. However, there are long events that did not show a connection with a concurrent SN, in spite of deep inspection and analysis: important examples in this sense are GRB 060505 and GRB 060614, for which no SN signals were observed down to $\rm M_i = -12.6$ (Ofek et al. 2007) and $\rm M_v = -13.7$ (Della Valle et al. 2006a) respectively. However, these two examples seem peculiar under many aspects, showing characteristics associated to both long and short GRBs (Gehrels et al. 2006). In any case, the failure in SN detection cannot be explained with a "by chance" superposition with foreground galaxies.

1.7 Instruments

In this section we provide a brief overview on the two high-energy instruments that were most widely used for the works contained in this thesis, namely the *Swift* observatory and the *Fermi* telescope. The other instruments are briefly described in the attached papers, when needed.

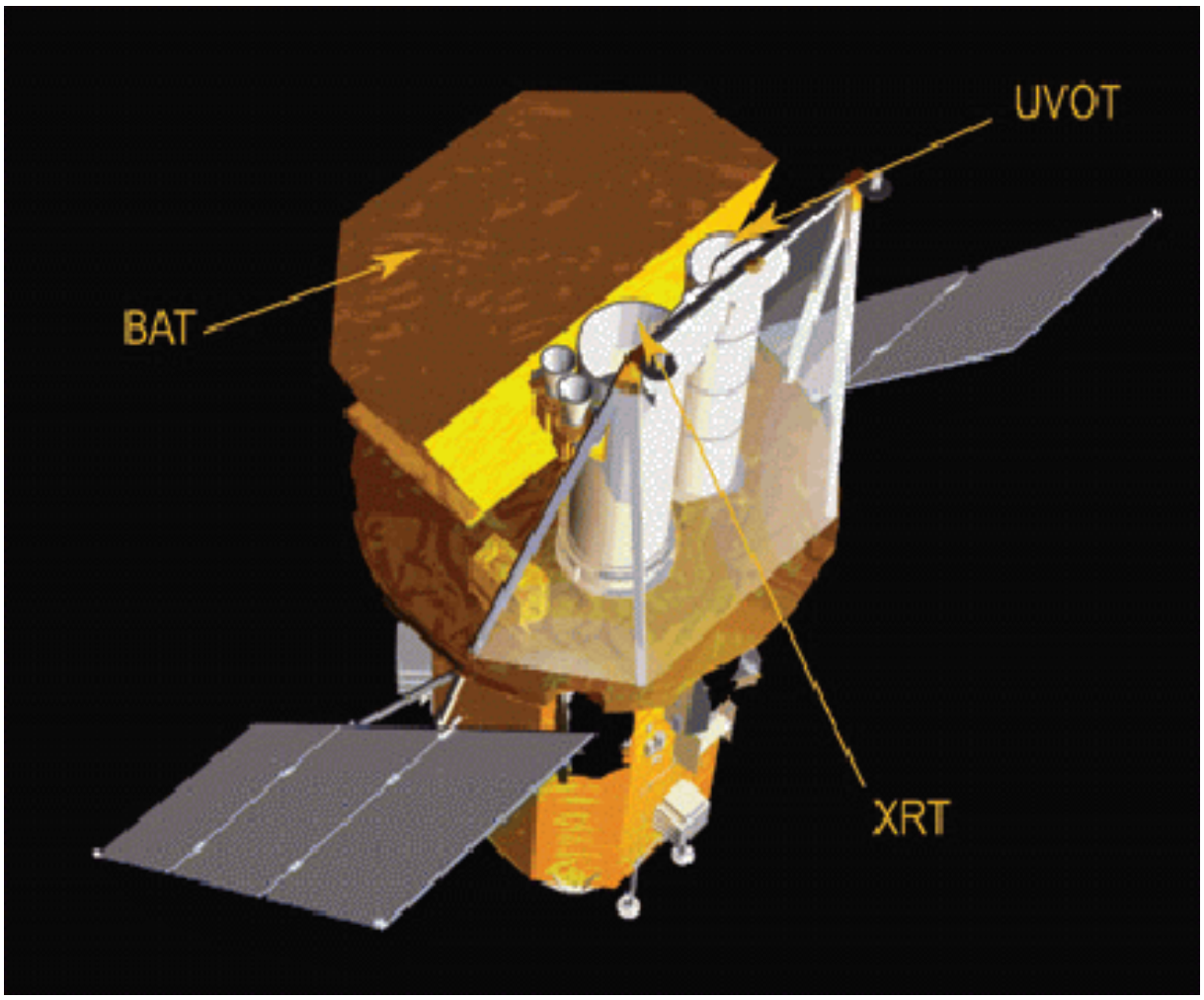

Figure 1.6: A sketch of the Swift observatory.

1.7.1 The Swift observatory

The *Neil Gehrels Swift* observatory (Gehrels et al. 2004) is a multi-wavelength space observatory dedicated to the study of GRBs and their afterglows in the gamma-ray, X-ray, and ultraviolet. It was launched on November 20, 2004, as part of the NASA's Medium Explorer program (MIDEX) and in a joint partnership between Goddard and an international consortium from the United States, United Kingdom, and Italy. At its launch, the main objectives for the mission were planned to be:

- determine the origin of GRBs;
- classify GRBs and search for new types;
- determine how the burst evolves and interacts with its surroundings;
- use GRBs to study the early universe;
- perform the first sensitive hard X-ray survey of the sky.

The observatory consists of three instruments:

- **Bursts Alert Telescope (BAT, Barthelmy et al. 2005)**: the instrument works in the energy range 15 - 150 keV and with its large field-of-view (FOV) (2 steradians) and high

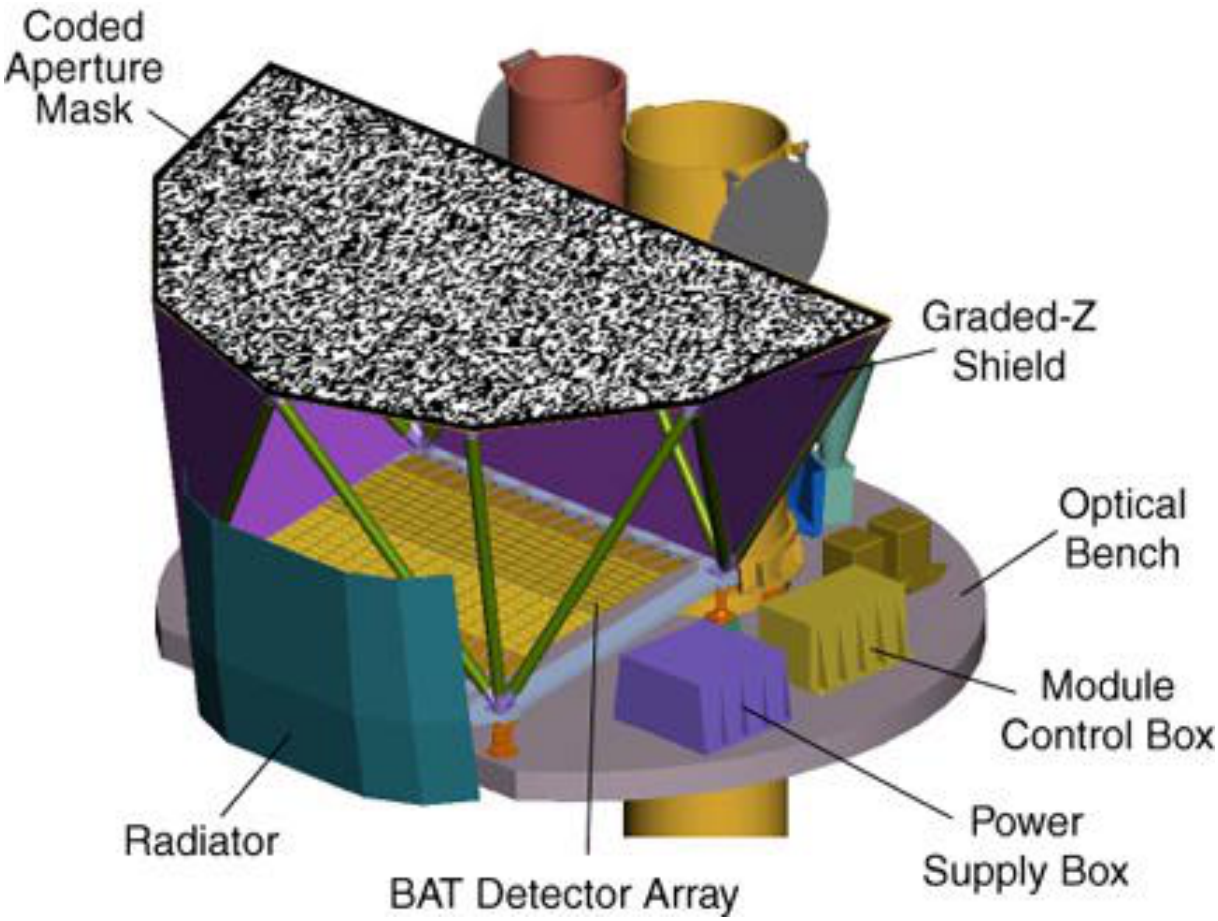

Figure 1.7: A sketch of the BAT layout.

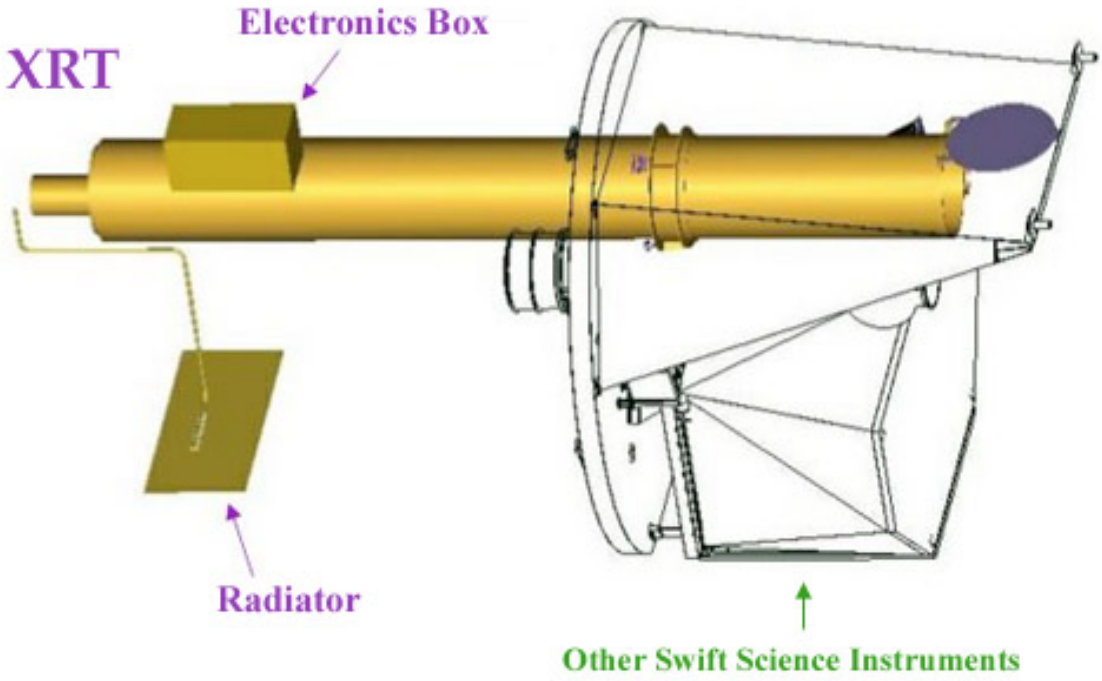

Figure 1.8: A sketch of the XRT layout.

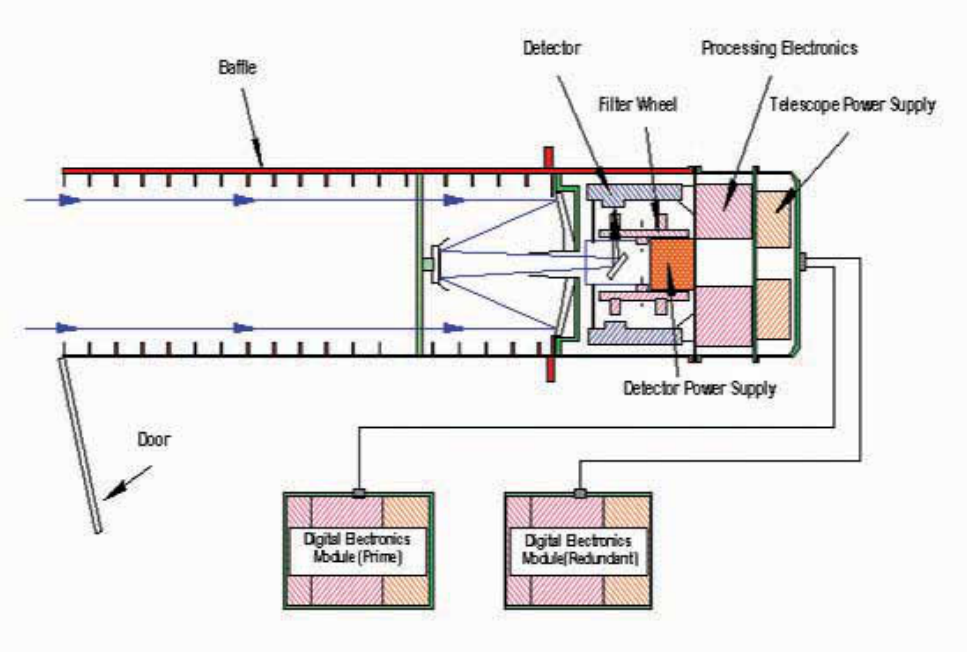

Figure 1.9: A sketch of the UVOT layout. The path of light through the telescope is denoted by arrows. First the light travels through an open door down the baffle until it is redirected into the detector.

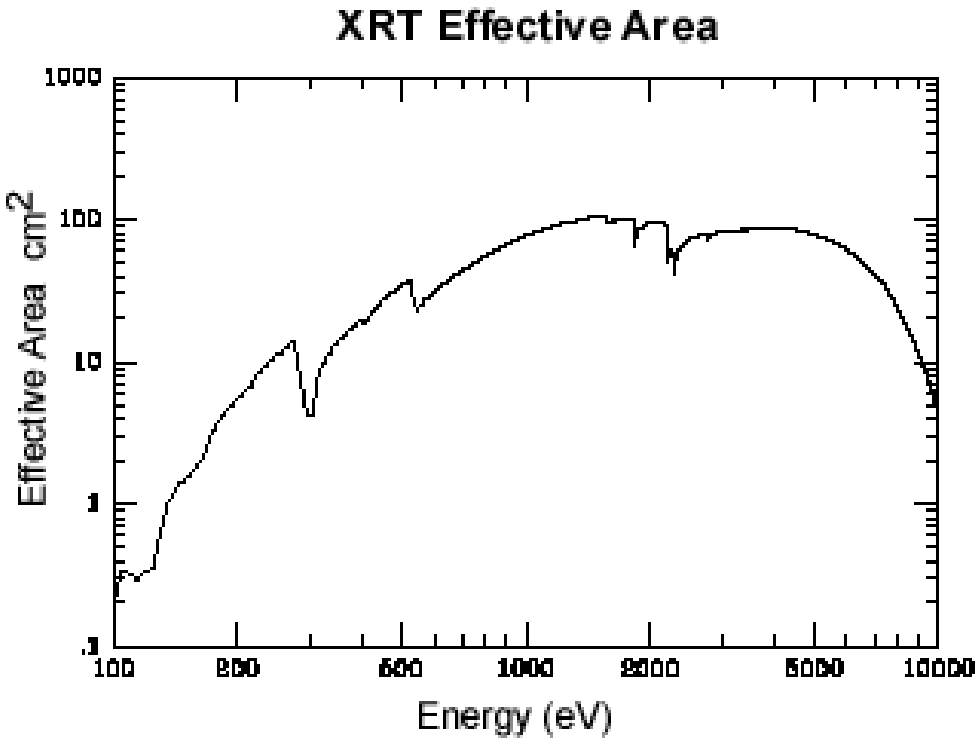

Figure 1.10: XRT Effective Area as a function of energy.

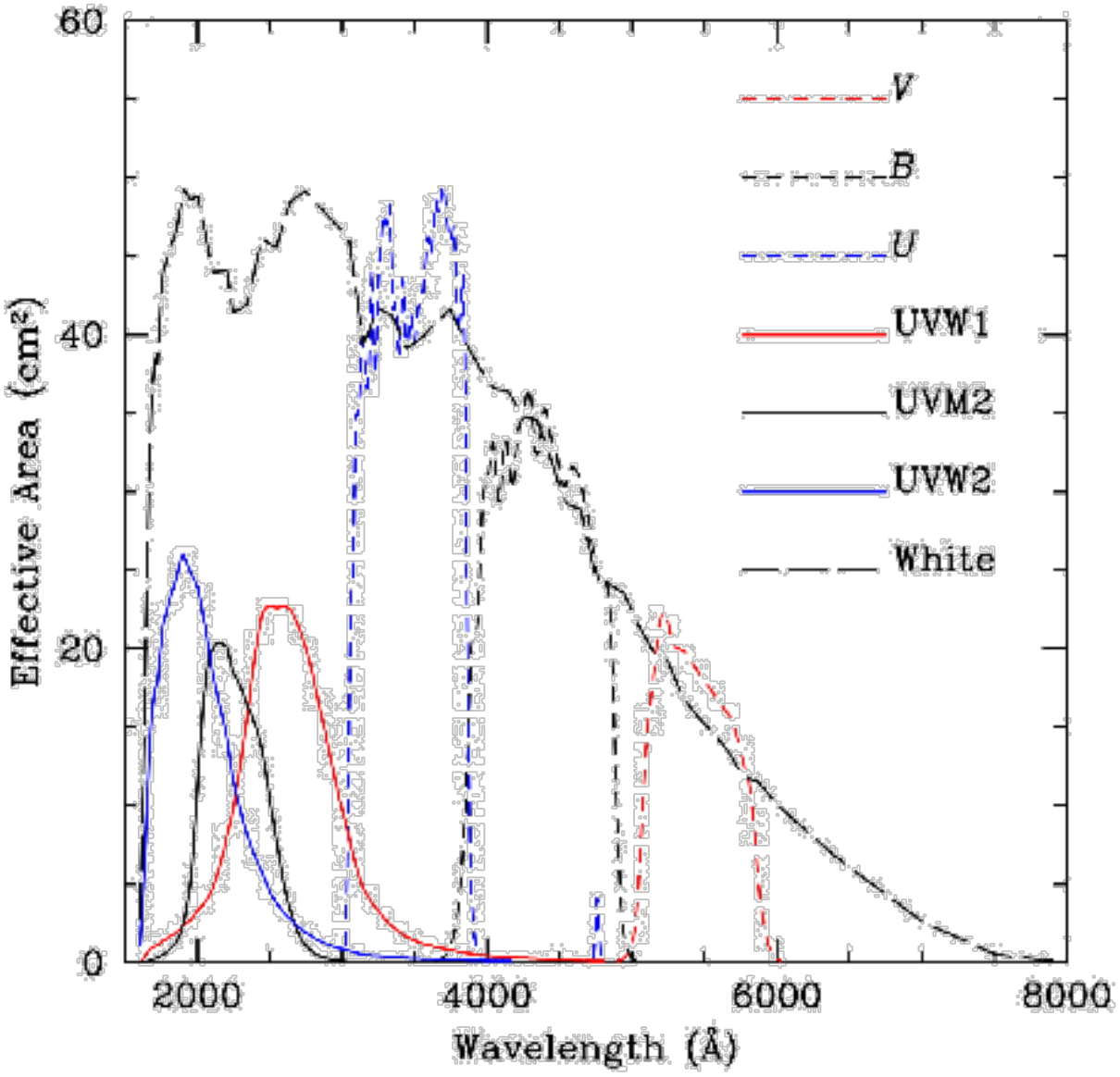

Figure 1.11: Effective area curves for the seven broadband UVOT filters shown as square centimeters versus wavelength in Angstroms. The white filter is shown in long dashed black. Dashed red - v, dashed black - b, dashed blue - u, solid red - uvw1, solid black - uvm2, solid blue - uvw2.

Property	Description
Aperture	Coded mask
Detecting Area	5200 cm^2
Detector	CdZnTe
Detector Operation	Photon counting
Field of View	1.4 sr (partially-coded)
Detection Elements	256 modules of 128 elements
Detector Size	4 mm x 4 mm x 2 mm
Telescope PSF	17 arcmin
Energy Range	15-150 keV

Table 1.1: Technical characteristic of the BAT instrument

Property	Description
Telescope	JET-X Wolter I
Focal Length	3.5 m
Effective Area	110 cm^2 at 1.5 keV
Telescope PSF	18 arcsec HPD at 1.5 keV
Detector	EEV CCD-22, 600 x 600 pixels
Detector Operation	Imaging, Timing, and Photon-counting
Detection Element	40 x 40 micron pixels
Pixel Scale	2.36 arcsec/pixel
Energy Range	0.2-10 keV
Sensitivity	2 x 10-14 erg cm^{-2} s^{-1} in 104 seconds

Table 1.2: Technical characteristic of the XRT instrument

Instrumentation	Description
Telescope	Modified Ritchey-Chretien
Focal Ratio	12.7
Detector Intensified	CCD
Detector Operation	Photon Counting
Field of View	17 x 17 arcmin
Detection Element	2048 x 2048 pixels
Telescope PSF	2.5 arcsec at 350 nm
Wavelength Range	170-650 nm
Number of Filters	7
Sensitivity	B = 22.3 in white light in 1000 s
Pixel Scale	0.502 arcsec
Brightness Limit	v = 7.4 mag
Camera Speed	11 ms

Table 1.3: Technical characteristic of the UVOT instrument

sensitivity, the BAT detects about 100 GRBs per year, and computes burst positions onboard the satellite with arc-minute positional accuracy. The detective area of the instrument is composed by 32,768 pieces of 4 x 4 x 2 mm CdZnTe (CZT) form a 1.2 x 0.6 m sensitive area in the detector plane. The localization of the bursts is due to a D-shaped coded aperture mask, made of $\sim 54,000$ lead tiles and with an area of 2.7 m^2, yielding a half-coded FOV of 100 degrees x 60 degrees, or 1.4 steradians. (See Figure 1.7). The main features of the instrument are sketched in Table 1.1.

- **X-ray Telescope (XRT, Burrows et al. 2005)**: the instrument operates in the energy range 0.2 - 10 keV and it takes images and is able to obtain spectra of GRB afterglows during pointed follow-up observations. It is a focusing X-ray telescope with a $110 cm^2$ effective area, 23.6×23.6 arcmin FOV, 18 arcsec resolution (half-power diameter). XRT uses a grazing incidence Wolter 1 telescope to focus X-rays onto a CCD (See Figure 1.8). The mirror point spread function has a 15 arcsec half-energy width, and, given sufficient photons, the centroid of a point source image can be determined to sub-arcsec accuracy in detector coordinates. A resume of the main features of the detector is provided in Table 1.2 and the effective area of the detector as a function of the energy is reported in Figure 1.10. This instrument is designed to work in four different modes: *photon counting mode* and *window timing mode*, *photodiode modes*, *image mode*. For our work of thesis, we are interested only in *photon counting mode* and *window timing mode*. Once on-target, it begins observing in Imaging Mode in order to determine the location of the GRB with a precision of better than 2.5 arcsec within 5 sec. In the other modes, the instrument measures the lightcurve and spectrum while the burst afterglow flux is rapidly fading. The XRT is designed to switch between these two different readout modes according to the instantaneous count rate in a completely autonomous operation.

- **UV/Optical Telescope (UVOT, Roming et al. 2005)**: The instrument works in the wavelength range 170-600 nm, taking images and obtaining spectra of GRB afterglows during pointed follow-up observations. The UVOT is a 30 cm diameter modified Ritchein-Cretien telescope with an $f/2.0$ primary that is re-imaged to $f/13$ by the secondary. The FOV is of about 17 arcmin square and the detectors are copies of two micro-channel plate intensified CCD (MIC). See Figure 1.9 and Table 1.3. The effective area in function of the energy for every band if provided in Figure 1.11.

These three instruments work together so the first rapid (within 20 seconds) 3 arc-minute burst localization performed at higher energies by BAT can be subsequently refined (down to arcseconds) at longer wavelength by XRT and UVOT, thanks to the high slewing capabilities of Swift (rotation in less than 90 seconds). The combined work of these three instruments gives the observatory state-of-the-art capabilities for rapid soft X and ultraviolet follow-up and position determination:

- $\sim$ 100 GRBs discovered per year;
- 0.5-5 arcsec positions for almost every GRB;
- multiwavelength observatory (gamma-ray, X-ray, UV, and optical);
- $<\sim$ 90 s reaction time for X-ray and UV/optical telescopes;
- spectroscopy from 180-600 nm and 0.3-150 keV;
- six colors covering 180-600 nm;
- results publicly distributed within seconds.

Parameter	Value or Range
Energy range	20 MeV-300 GeV
Max effective area at normal incidence	9500 cm^2
Energy resolution (equivalent Gaussian 1σ)	$\sim 10 - 15\%$
Field of View (FOV)	2.4 sr
Timing accuracy	$< 10\ \mu$s
GRB location accuracy on-board	< 10'
Point source sensitivity	3×10^{-9} ph cm^{-2} s^{-1}

Table 1.4: Summary of some technical characteristic of the Large Area Telescope on board the Fermi Telescope.

Instrumentation	Description
Energy range	8-40000 keV
Max effective area at normal incidence	$\sim 120 + 120$ cm^2
Field of View (FOV)	All-sky
GRB location accuracy on-board	< 15 degrees
Energy resolution (FWHM)	$\sim 15\%$ at 100 keV and $\sim 10\%$ at MeV
Timing accuracy	$2\ \mu$s
On-board Trigger Threshold	0.74 ph cm^{-2} s^{-1}

Table 1.5: Summary of some technical characteristic of the Gamma-ray burst Monitor on board the Fermi Telescope.

Name	Purpose	Temporal Resolution	Energy Resolution	Released
CTIME	Continous high time resolution	0.064 s	8 channels	daily
CSPEC	Continous high spectral resolution	1.024 s	128 channels	daily
TTE	Time-tagged events during bursts	$2\ \mu$s	128 channels	after a burst

Table 1.6: Summary of scientific files produced by the Fermi/GBM team.

1.7.2 The Fermi observatory

The *Fermi Gamma-ray Space Telescope* (previously known as *GLAST*) is a space observatory designed by the *National Aeronautics and Space Administration* (NASA) and launched on June 11 2008. It explores the broad energy range from the $\sim$ 8 keV up to $\sim$ 300 GeV thanks to the two on-board instruments: the *Large Area Telescope* (LAT, Atwood et al. 2009) and the *Gamma-ray Burst Monitor* (GBM, Meegan et al. 2009).

The main scientific goals of the mission are:

- study the mechanism powering very-high-energy particles from active galactic nuclei (AGNs), pulsars and supernova remnants;

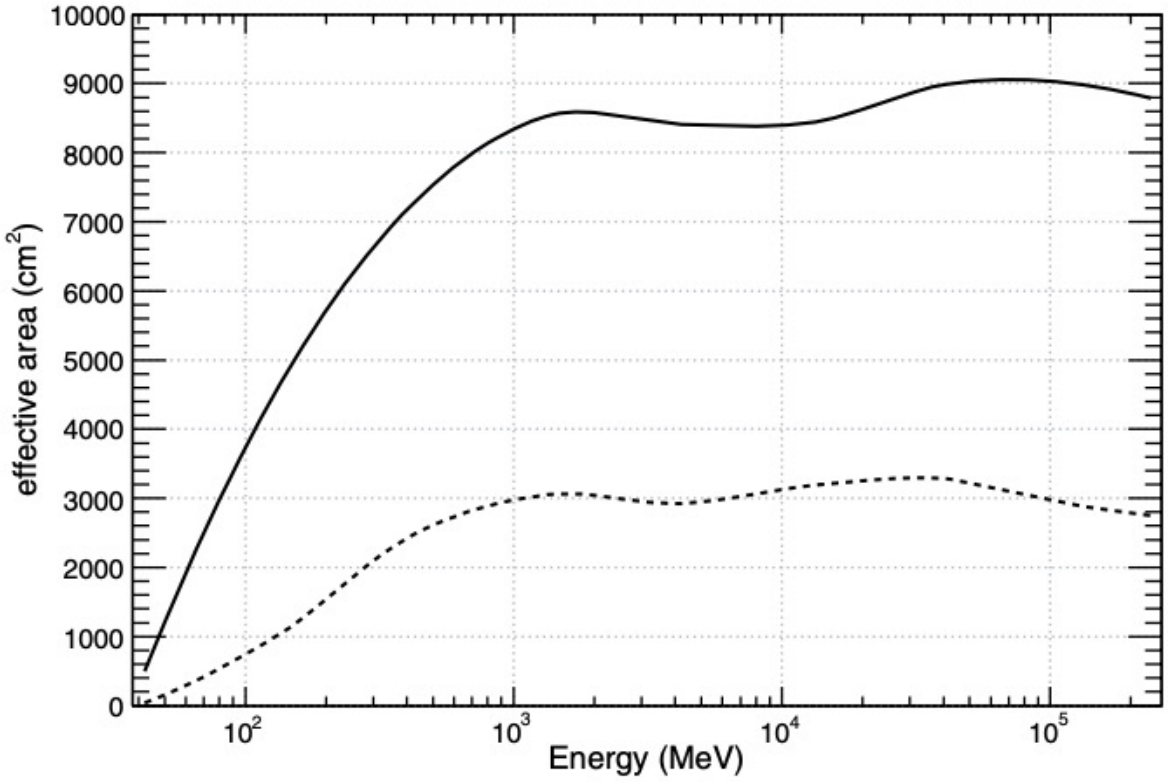

Figure 1.12: LAT effective area at normal incidence (solid curve) and 60° off-axis as a function of the energy. Figure from Atwood et al. (2009).

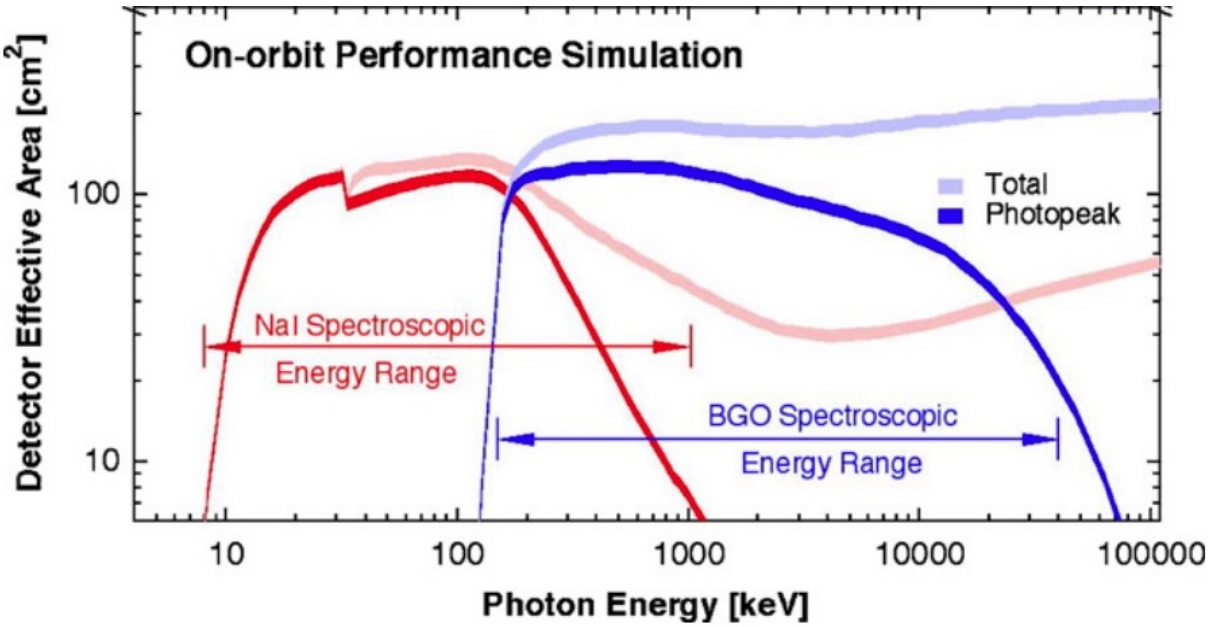

Figure 1.13: GBM effective area at normal incidence as a function of the energy for both NaI (red) and BGO (blue). Figure adapted from Meegan et al. (2009).

- resolve the diffuse high-energy emission to identify its source;
- study the sky-distribution and the emission of GRBs;
- probe dark-matter, studying the fingerprint of its decaying;
- study the high-energy emission from within the Solar system (for example, from the Sun);
- study of fundamental physics (e.g the presence quantum gravity effects reveled by a wavelength-dependent value of the speed of light).

The LAT instrument explores the 30 MeV-10 GeV energy using pair-conversion, that happens in its high-Z calorimeters (composed by CsI(TI) crystals) that are paired with a tracker module. This system makes the instrument capable to localize point sources with an accuracy of a few arcmins and determine the energy of incoming photons with an accuracy $\sim 10\%$. The FOV is of 2.4 sr, with a maximum effective area of 9500 cm^2. Further details are reported in Table 1.4.

The GBM instrument explores the range $8 - 40000$ keV trought the combined usage of two kinds of scintillators:

- 10 NaI(TI) (SOdium Iodide) crystals exploring the $8 - 1000$ keV range and looking at different directions with respect to the payload. The different flux observed in everyone is used to obtain a rough estimation of burst positions.
- 2 BGO (bismuth germanate) detectors for the $200 - 40000$ keV range. They cannot be used to localize the signal but the overlapping of their energy range with both GBM/NaI and LAT detectors is used for cross calibration and cross-checking.

  GBM can localize burst with an accuracy typically ~ 10 degrees, providing an energy resolution $\sim 10 - 15\%$. Further details are reported in Table 1.5, while in Table 1.6 we report a brief overview on the scientific files produced by the GBM team.

Chapter 2

Outliers of the $E_{\rm p,i}$ – $E_{\rm iso}$ correlation?

Authors: R. Martone[1 2] , L. Izzo[3] , M. Della Valle[4 5] , L. Amati[6] , G. Longo[2] , D. Götz[7]

Article by Martone et al., A&A 608, A52 (2017)

DOI: https://doi.org/10.1051/0004-6361/201730704

Summary

In the context of an in-depth understanding of GRBs and their possible use in cosmology, some important correlations between the parameters that describe their emission have been discovered, among which the "$E_{\rm p,i}$ – $E_{\rm iso}$" correlation is the most studied. Because of this, it is fundamental to understand the role of a few events, namely GRB 980425 and GRB 031203, that appear as to be outliers of the $E_{\rm p,i}$ – $E_{\rm iso}$ correlation.

We investigate the possibility that the locations in the $E_{\rm p,i}/E_{\rm iso}$ plane of these two bursts are caused by the fact that a substantial fraction of their energy was released in the soft X-ray band, and consequently missed by the instruments that detected them (BATSE and *INTEGRAL*/IBIS).

We analyse the emission of other similar sub-energetic bursts (GRBs 060218, 100316D, and 161219B) observed by Swift and whose integrated emissions match the $E_{\rm p,i}$ – $E_{\rm iso}$ relation. We simulate their integrated and time-resolved emissions as they would have been observed by the same detectors that observed GRB 980425 and GRB 031203, with the aim of reconstructing lightcurve and spectra.

We estimate the $E_{\rm p,i}$ and the $E_{\rm iso}$ parameters from the time-resolved and total integrated simulated spectra of 060218, 100316D, and 161219B as observed by BeppoSAX, BATSE, INTEGRAL and the WFM originally proposed for the LOFT (Feroci et al. 2012) and then eXTP missions (Zhang et al. 2016).

We conclude that, if observed by old generation instruments, GRB 060218, 100316D, and 161219B would appear as outliers of the $E_{\rm p,i}$–$E_{\rm iso}$ relation, while, if observed with Swift or

[1]Department of Physics and Earth Science, University of Ferrara, via Saragat 1, I–44122, Ferrara, Italy
[2]Università di Napoli "Federico II", Dipartimento di Fisica "Ettore Pancini", C. U. Monte S. Angelo, 80126 Napoli, Italy
[3]Instituto de Astrofisica de Andalucia (IAA-CSIC), Glorieta de la Astronomia s/n, 18008 Granada, Spain
[4]INAF-Osservatorio Astronomico di Napoli, Salita Moiariello, 16, I-80131 Napoli, Italy
[5]ICRANet, Piazzale della Repubblica 10, I–65122, Pescara, Italy
[6]INAF-IASF Bologna, via P. Gobetti, 101. I-40129 Bologna, Italy
[7]AIM–CEA/DRF/Irfu/Service d'Astrophysique, Orme des Merisiers, F-91191 Gif-sur-Yvette, France

WFM GRB 060218, they would be well consistent with it. We also note that the instrument BAT alone (15-150 keV) actually measured 060218 as an outlier.

We suggest the possibility that, if GRB 980425 and GRB 031203 would have been observed by Swift and by eXTP, they could have matched the $E_{\rm p,i}$–$E_{\rm iso}$ relation. This provides strong support to the idea that instrumental biases can make some events in the lower-left corner of the $E_{\rm p,i}$ – $E_{\rm iso}$ plane appear as outliers of the "Amati relation".

A copy of the full text (editorial version) of this paper is reported in Appendix of the thesis.

Chapter 3

Testing Synchrotron and Comptonisation models for GRB prompt emission through broadband (0.3 keV - 30 MeV) spectra

3.1 Introduction

In spite of deep investigation throughout the last 50 years, the prompt emission of GRBs is still not completely understood. In particular, the radiation mechanism(s) powering the X/γ–ray emission and what drives the jet, the structure of the emitting and dissipating regions, and the role of the magnetic field are still open issues. The answers are not necessarily expected to be unique, given the rich and complex GRB taxonomy.

From the very beginning of GRB astronomy, given the basic proposed picture of shock-accelerated electrons immersed in magnetic fields, the dominant part of the prompt emission was suggested to come from synchrotron radiation (e.g., Meszaros et al. 1994; Daigne & Mochkovitch 1998; Lloyd & Petrosian 2000; Daigne et al. 2011). However, this simple picture cannot account for the occasional need of additional components, like black body, multicolour black body, and Comptonisation signatures, that emerged in different cases (see Kumar & Zhang 2015 for a review). A smoothly broken power–law called Band function (hereafter `band`) was found to provide a good description of most GRB spectra (Band et al. 1993), even if a solid, physically rooted interpretation is still missing. This function works well in a relatively broad-band energy range, from 15-20 up to 1000 keV, both with time-integrated and time-resolved spectra. Typical values for the low-energy (α) and the high-energy photon index (β) are -1 and -2.3, respectively (Kaneko et al. 2006). However, the evidence for multiple components that were mostly observed since the advent of *Fermi*, along with the empirical nature of this function, urged the community to develop more physically grounded models (see Dai et al. 2017 for a recent review).

A pure synchrotron model presents some difficulty too, given the tension between the observed values of the low-energy photon index and the value of $-3/2$, which is expected in the fast cooling scenario (Granot et al. 2000; Granot & Sari 2002), and the value $-2/3$ expected in slow cooling scenario (Sari et al. 1998). This is the "line of death" problem with the low-energy index (e.g., Preece et al. 1998). A number of different effects have been proposed to modify the low-energy shape and alleviate this tension, like complex behaviours of the jet, Compton scattering in the Klein-Nishina regime or the marginally fast cooling regime (Oganesyan et al. 2017, 2018, hereafter O17 and O18). Completely different paradigms that do not invoke synchrotron are possible, too: photospheric (see Beloborodov & Mészáros 2017 and references therein) and Comptonisation components (Titarchuk et al. 2012) have been put forward.

The first systematic observations of GRB prompt emission down to 2 keV were obtained by *BeppoSAX* (Frontera et al. 2000; Amati et al. 2002; Frontera et al. 2013) and provided the first compelling evidence of the problems faced by extending a simple band down to X–rays. Now, that effort can be pushed further thanks to the contribution of instruments exploring the soft X–ray range like the XRT on board the *Swift* (Gehrels et al. 2004), that allows for the investigation down to 0.3 keV.

In order to study the broadband spectrum of GRBs exploiting the potential of this instrument, we tested in parallel band, a double peaked broken power–law representing a pure synchrotron scenario, and the photospheric model with a Comptonisation component proposed by Titarchuk et al. (2012). We collected a data set of 17 GRB that were detected by both *Swift* and *Fermi* and that were long enough to have XRT cover a significant fraction of the prompt emission. We performed a time-resolved analysis to track the temporal evolution of the spectral parameters, while we defined the time intervals using a Bayesian-block algorithm, which is considered one the most un-biased algorithms for this purpose (Burgess 2014).

In section 3.2 we describe the data set selection, together with the algorithm for the time slicing, section 3.3 describes the spectral models, whereas section 3.4 reports the results. These are discussed in section 3.5, followed by our conclusions in section 3.6.

The content of this Chapter will be the subject of a dedicated paper to be submitted to a peer-review journal.

3.2 Data set

We first selected events that were detected by both *Fermi* and *Swift* in the time interval August 2008 through April 2017, ending up with 289 GRBs. The sample was then further narrowed down through the following requirements:

- threshold on the 10-1000 keV fluence (as measured by GBM and reported in Bhat et al. 2016): $\Phi_{10-1000} > 10^{-7}$ erg/cm^2.

- XRT began observing within the T_{90} time interval as measured by BAT (T_{90} values were taken either from Lien et al. (2016) or from the corresponding *Swift* team BAT refined GCN circular when the GRB was not reported in the former).

The aim of the first was to have a large enough number of photons to perform a time-resolved spectral analysis. The second criterion selected bursts for which XRT observation started during the prompt phase. The goal was to identify those GRBs for which a broadband coverage (0.3 keV - 30 MeV) of a portion at least of the prompt emission is available. This implied the selection of GRBs with a prolonged ($\gtrsim$ 80 s) prompt emission, given the dozens of seconds typically required by *Swift* to pinpoint the source after the BAT trigger.

These criteria were fulfilled by 55 GRBs. We further discarded the cases for which GBM data are affected by critical background subtraction: 121123A, 140206A, 140817A, 150727A. Other events were discarded because of a poor temporal coverage: 101030A, 120909A, 140709A, 141031A. Lightcurves of the same GRBs measured with different spacecraft were synchronised by converting the corresponding mission elapsed times (METs) to UT using a specific web tool[1]. Next, GRBs for which GBM data collected in the time window covered by both BAT and XRT did not make up a spectrum with sufficient (see below) statistical quality, were also rejected. Eventually 17 GRBs survived, that hereafter will be referred to as the common sample. In the

[1] https://heasarc.gsfc.nasa.gov/cgi-bin/Tools/xTime/xTime.pl

GRB	$t_0^{(BAT)}$ UT	$t_0^{(GBM)}$ UT	$t_0^{(BAT)} - t_0^{(GBM)}$ (s)	$t_0^{(XRT)} - t_0^{(BAT)}$ (s)	$T_{90}^{(BAT)(a)}$ (s)	$z^{(b)}$	$N_{int}^{(c)}$
080810	13:10:12.288	13:10:12.581	−0.293	76.0	107.7	3.35	1
090926B	21:55:48.416	21:55:28.525	19.892	88.8	99.3	1.24	1
100619A	00:21:07.247	00:21:07.026	0.221	76.4	97.7	–	3
100728A	02:18:24.246	02:17:30.611	53.635	76.7	193.4	1.567	15
100814A	03:50:11.265	03:50:08.809	2.456	87.3	177.3	1.44	3
100906A	13:49:27.417	13:49:27.630	−0.213	80.2	114.6	1.727	4
110102A	18:52:25.475	18:54:36.007	−130.532	148.6	265.9	–	17
130528A	16:41:23.920	16:41:24.409	−0.489	64.9	640.0	1.250	1
130609B	21:38:40.417	21:38:35.610	4.806	76.0	211.2	–	4
140108A	17:18:42.522	17:18:42.988	−0.467	68.7	95.2	–	9
140323A	10:23:11.917	10:22:53.120	18.797	97.5	106.5	–	2
140512A	19:31:49.214	19:31:42.502	6.712	98.4	154.1	0.725	15
150430A	00:21:15.254	00:21:05.647	9.608	80.0	106.9	–	2
151006A	09:55:01.886	09:54:57.825	4.062	48.6	211.1	–	4
151027A	03:58:24.159	03:58:24.033	0.126	87.0	129.6	0.81	8
161117A	01:35:36.685	01:35:31.357	5.328	60.8	125.7	1.549	13
170405A	18:39:48.432	18:39:22.886	25.546	120.6	164.7	3.510	3

Table 3.1: GRBs observed with both *Swift* and *Fermi* that were used in the present analysis. We report the trigger times of both BAT and GBM, relative delay, the start times of XRT data, the T_{90} duration as measured with BAT, and the number of time windows used for extracting as many broadband energy spectra.

[(a)] All values are taken from Lien et al. (2016), except for 161117A (Stamatikos et al. 2016) and 170405A (Palmer et al. 2017).

[(b)] Spectroscopic redshift.

[(c)] Number of intervals.

following, both *Fermi* and *Swift* data were processed through specific pipelines using `lheasoft (v21)`[2].

3.2.1 *Fermi*-GBM data

For each *Fermi*-GBM GRB we first identified the two NaI most illuminated detectors, hereafter respectively NaI1 and NaI2. We extracted the lightcurves for both NaI in the 8-900 keV range and that for the BGO in the 200-3000 keV range with 64 ms time resolution following. Using `rmfit` (v.4.3.2)[3], we reduced spectra through the following steps:

- we selected the energy channels in the range 8-900 keV for the NaI detectors and in range 200-30000 keV for BGO detectors;
- we interpolated the background with polynomials up to order 4.
- we finally extracted the background-subtracted spectra.

We eventually grouped the energy channels of the background-subtracted spectra ensuring a minimum significance of 2σ to adopt the χ^2 statistic for final spectral modelling. We obtained

[2] https://heasarc.gsfc.nasa.gov/docs/software/lheasoft/download.html
[3] https://fermi.gsfc.nasa.gov/ssc/data/analysis/scitools/rmfit_tutorial.html

64-ms uniformly spaced lightcurves from the corresponding event files. Background interpolation and subtraction were done using customised own python code.

3.2.2 *Swift* data

BAT

All GRBs here considered triggered BAT onboard, so that event data are available for them all. For each GRB of the common sample we extracted the 15–150 keV mask-weighted, background-subtracted time profile with 64 ms time resolution following the same procedure as in Guidorzi et al. (2016). Energy spectra in the same energy band were extracted following the standard pipeline as in Rizzuto et al. (2007), with the only difference that we finally grouped energy channels requiring a minimum significance per grouped channel of at least 2σ.

XRT

All of the time windows here considered happened to be covered by XRT entirely in Window Timing (WT) mode. For each GRB we built the 0.3–10 keV lightcurve with 1-s uniform bins from the Leicester *Swift*-XRT portal[4]. Energy source and background spectra in the same energy band were built in the same way, along with the corresponding ancillary files and response function. Eventually, the energy channels of each individual background-subtracted spectrum were grouped so as to ensure a minimum significance of 2σ as we did for BAT energy spectra.

3.2.3 Time slicing

For any GRB of the common sample, once the 64-ms background-subtracted, properly synchronised, multi-instrument (XRT, BAT, GBM-NaI1, GBM-NaI2, and GBM-BGO) lightcurves were made available, we first identified the time window covered by all instruments. We then split it into subintervals of variable durations adopting the following procedure. We first binned up the original 64-ms profile of NaI2 by a factor of 32 (except for three GRBs for which 16, 24, and 28 worked better), corresponding to a resolution of 2.048 s. The rebinned profile was then fed to the Bayesian block algorithm[5] (Scargle et al. 2013), that was shown to be preferable for reconstructing the intrinsic spectral evolution of GRBs (Burgess 2014). The S/N of the net fluence for the resulting intervals was finally checked against a minimum threshold of 2σ: the blocks with S/N below threshold were merged with the following ones until the S/N requirement was satisfied. The reason behind this choice is that, for any time interval, the S/N of the involved instruments ranks from best to worst as XRT, BAT, NaI1, NaI2, and BGO. Ensuring a minimum S/N on the spectra of the lowest S/N instrument (i.e., BGO) would be too demanding, to the point that considerable time-resolvable information would be washed out in excessively long time intervals. Thus, the choice for NaI2 (i.e., the second worst S/N instrument) is a trade off between dealing with statistically significant spectra over all (but one, in the worst case) instruments on one side, and preserving information on the spectral evolution on the other side. The need for preliminarily binning the NaI profile up was due to the poor results obtained by running the Bayesian blocks over the original 64-ms profile: the blocks looked way shorter than any apparent temporal structure as suggested by visual inspection mainly in the form of recognisable, well separated pulses. The optimal values reported above for the temporal binning of

[4] http://www.swift.ac.uk/user_objects/

[5] We used the python function `bayesian_blocks` under the `astroML.density_estimation` module (Vanderplas et al. 2012).

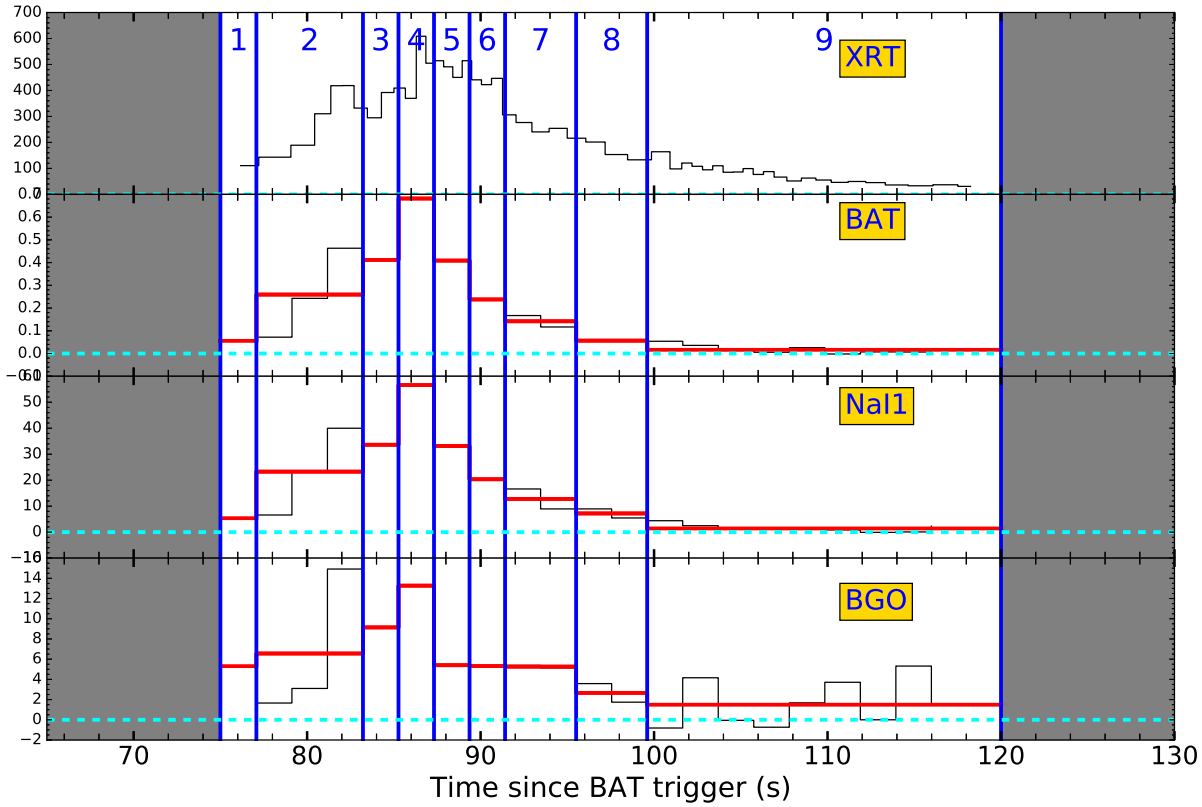

Figure 3.1: Simultaneous lightcurves of 140108A as measured with the four instruments with increasing mean passband energy from top to bottom (we do not show the NaI2 profile since it adds no further graphical information to that of NaI1). Dashed lines show the background level. Vertical blue lines mark the boundaries between adjacent time intervals, as they were determined with the slicing procedure of Sect. 3.2.3. Thick red lines show the average value for each interval/instrument. Y-axis values are background-subtracted rates (mask-weighted rates per detector for an on-axis source for BAT). Shaded windows either are not covered by all instruments or they do not include any detectable signal from the GRB.

the lightcurves for the Bayesian blocks were determined as a consequence. Figure 3.1 is an illustrative example of the resulting time slicing for GRB 140108A.

3.3 Data analysis

We accounted for the uncertainty on the cross-calibration of the different instruments following Page et al. (2011). In particular, we made the following choice:

- set to 1.0 the normalisation constants for both BAT and BGO;
- let the XRT normalisation vary within the range 0.7 – 1.3;
- let the normalisation for both NaI's vary together within the range 1.0 – 1.4.

For spectral modelling we adopted the χ^2 minimisation, rejecting p-values outside the range 0.05–0.95 to avoid both under- and over-fitting. Furthermore, we applied also the runs test[6] to exclude the presence of trends in the residuals between the model and the data. Also in this case

[6]The test can be performed using the Xspec command `statistic test runs` .

we adopted a threshold of 0.05 on the p-value for the null hypothesis of no trends. For the runs test, the p-value cannot be directly inferred from the value of the statistic and so Montecarlo simulations have to be performed[7].

We first tested the following models for GRB spectra:

1. band. Here the low-energy photon index α, the peak energy $E_{\rm p}$ and the normalization are left free to vary, while the high-energy photon index β is fixed to -2.3, following the results reported in Kaneko et al. (2006). To ease the comparison with the analogous low-energy index of other models (which are defined > 0), we considered $-\alpha$ for band;

2. synchrotron, as described by a double broken power-law (hereafter, sync) implemented under xspec as bkn2pow[8]; here the low-energy photon index α_1, the low-energy break E_{b1}, the high-energy break E_{b2} and the normalization are left free to vary, while the the second powerlaw index α_2 is fixed to -1.5 and the high-energy photon index β is fixed to -2.3, in parallel with our choice regarding the Band function.

3. the grbcomp model by Titarchuk et al. (2012) implemented under xspec as GRBCOMP[9]; here the seed photons temperature kT_s, the electron temperature kT_e, the optical depth τ and the normalization are left free to vary, while all the other parameters are fixed ($\gamma = 3.0$, $\beta = 0.2$, fbflag= 0, $\log A = 5.0$, $\alpha_{\rm boost} = 1.3$). In particular, the value of the parameter A reflects the degree of Comptonisation of the seed photons: a very high value means that all these photons are Comptonised (up-scattered) and no blackbody component is expected to emerge. Our choice $\log A = 5.0$ reflects the assumption of a dominant Comptonisation component with respect to the thermal one, in agreement with the assumption of Frontera et al. (2013) (hereafter F13).

These models are tested systematically and independently for all spectra. Upon initial failure, we try to modify it in the following ways (in the order we present them):

1. for band: addition of a further free absorption and, in parallel, addition of a blackbody component (hereafter, BB);

2. for sync: addition of a BB (in this case we fix $\alpha_1 = 0.67$ to avoid degeneracy);

3. for grbcomp: addition of a further free absorption; when the value of kT_s is very close to the limit of our passband (0.3 keV), it is fixed to 0.3 keV.

There are cases in which either the break(s) lie outside the overall energy band, or the overall S/N is too poor to detect any break and only an average power-law slope can be estimated. This usually happens at the very end of the lightcurve segment, when the S/N significantly decreases.

3.4 Results

In this section we report an overview on the results of our analysis, devoting a brief description of the overall behaviour of each GRB. The plots show, together with the XRT, BAT, GBM, and BGO lightcurves, the values of best-fit parameters as a function of the corresponding time interval. All the quantities referring to band and sync are reported in the observer frame, while quantities referring to grbcomp are reported in the rest frame. For the GRBs without redshift,

[7] This task can be handled in XSPEC with the command goodness. We decided to use the options nosim fit.

[8] https://heasarc.gsfc.nasa.gov/xanadu/xspec/manual/node141.html

[9] https://heasarc.nasa.gov/docs/xanadu/xspec/models//grbcomp.html

we consider $z = 0$, as done by F13. In the plots we report also the presence of additional components, namely BB or additional absorption (A). Finally, there are cases in which only the XRT data can be used and can be modelled by a power-law (P in the plots). The intervals for which all the considered models failed, are left blank.

3.4.1 080810

Only in the first interval the signal is bright enough to perform the analysis. All the three models fit the data, with sync that seems to just mimic band (Fig. 3.2).

3.4.2 090926B

In the only available interval only band and sync are not rejected, with the addition of a BB (with the same temperature ≈ 0.26 keV), while grbcomp fails. The Γ panel suggests a different behaviour between sync and band (Fig. 3.3).

3.4.3 100619A

In the first two intervals band provides a good fit, with the addition of a BB in the second interval, while grbcomp and sync are rejected in the second interval due to the runs test. The models were not tested in the last interval, since only the XRT signal is present. (Fig. 3.4).

3.4.4 100728A

band and grbcomp provide good fits, describing almost all the intervals, with the only exception of interval 1. In this case, the failure is due to the χ^2 test. sync cannot describe a number of spectra, mainly because of the lack of a low-energy cut. In the intervals where this model works, the behaviour of the low energy index seems to perfectly mimic the low energy index of band and $E_{\rm b1}$ is close to the lower end of the investigated energy range, suggesting that sync does not improve the band result. Across the whole lightcurve, both $E_{\rm p}$ and kT_e track the high-energy flux (Fig. 3.5).

Ni absorption line?

The XRT spectrum relative to the very first interval shows something similar to an absorption edge (Fig. 3.6), that disappears in the next intervals (Fig. 3.7). The redshift is 1.567 and the line energy is in the range 3.0–3.2 keV, corresponding to an intrinsic range of 7.7–8.1 keV. This is reminiscent of the emission line at 7.85 keV found in the early afterglow of GRB 060904B (Moretti et al. 2008) and possibly interpreted as a nickel recombination line in a reflection scenario (Margutti et al. 2008).

3.4.5 100814A

The first two intervals are well described by all the models. The last one, dominated by XRT data, can be modelled only by BB+band. In this interval, the presence of a peak in the νF_ν spectrum is not clear, as testified by the large uncertainty on $E_{\rm p}$. For the same reason a simple power-law plus bb works well. sync tracks band, as shown in the Γ panel (Fig. 3.8).

Figure 3.2: 080810

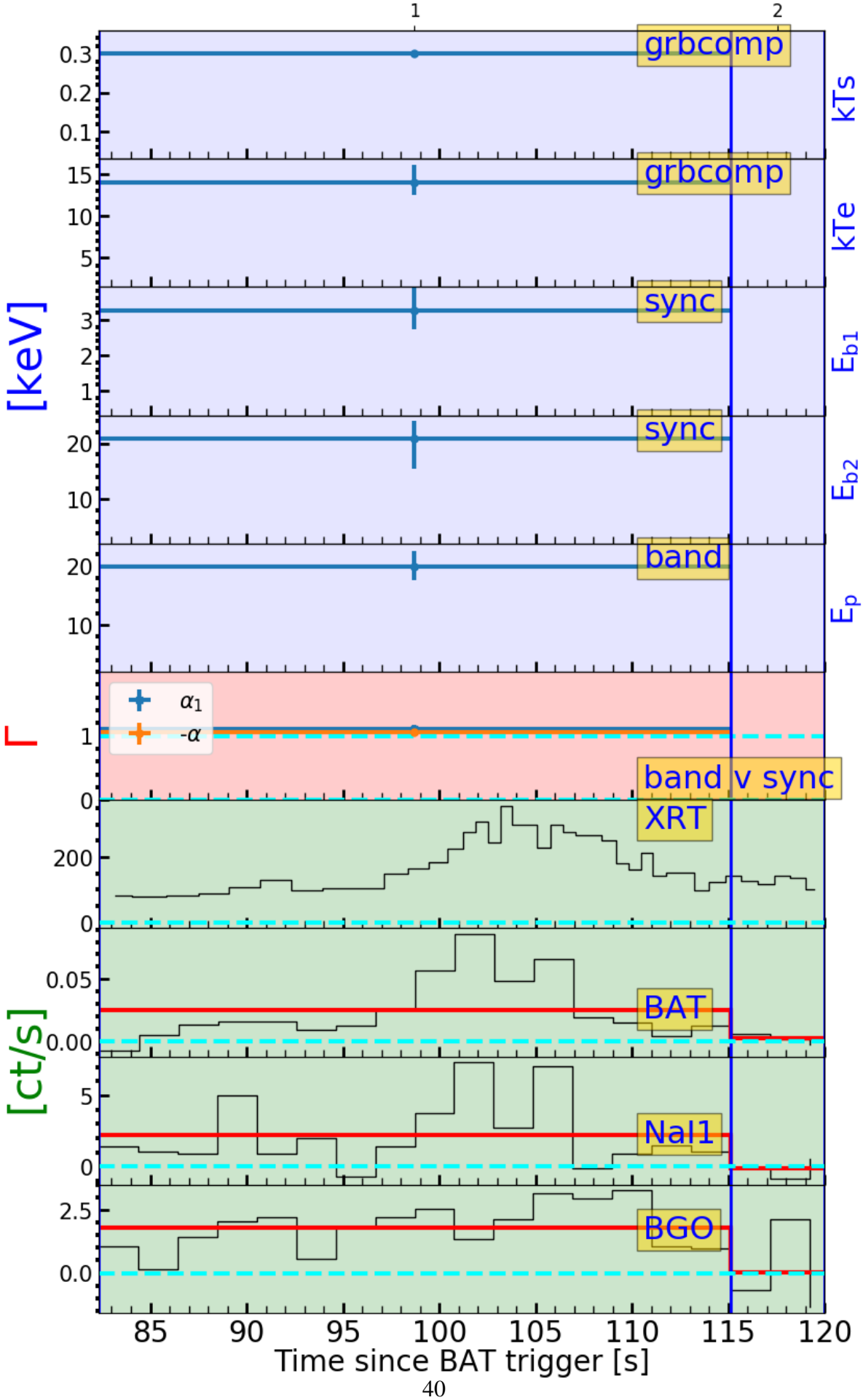

Figure 3.3: 090926B

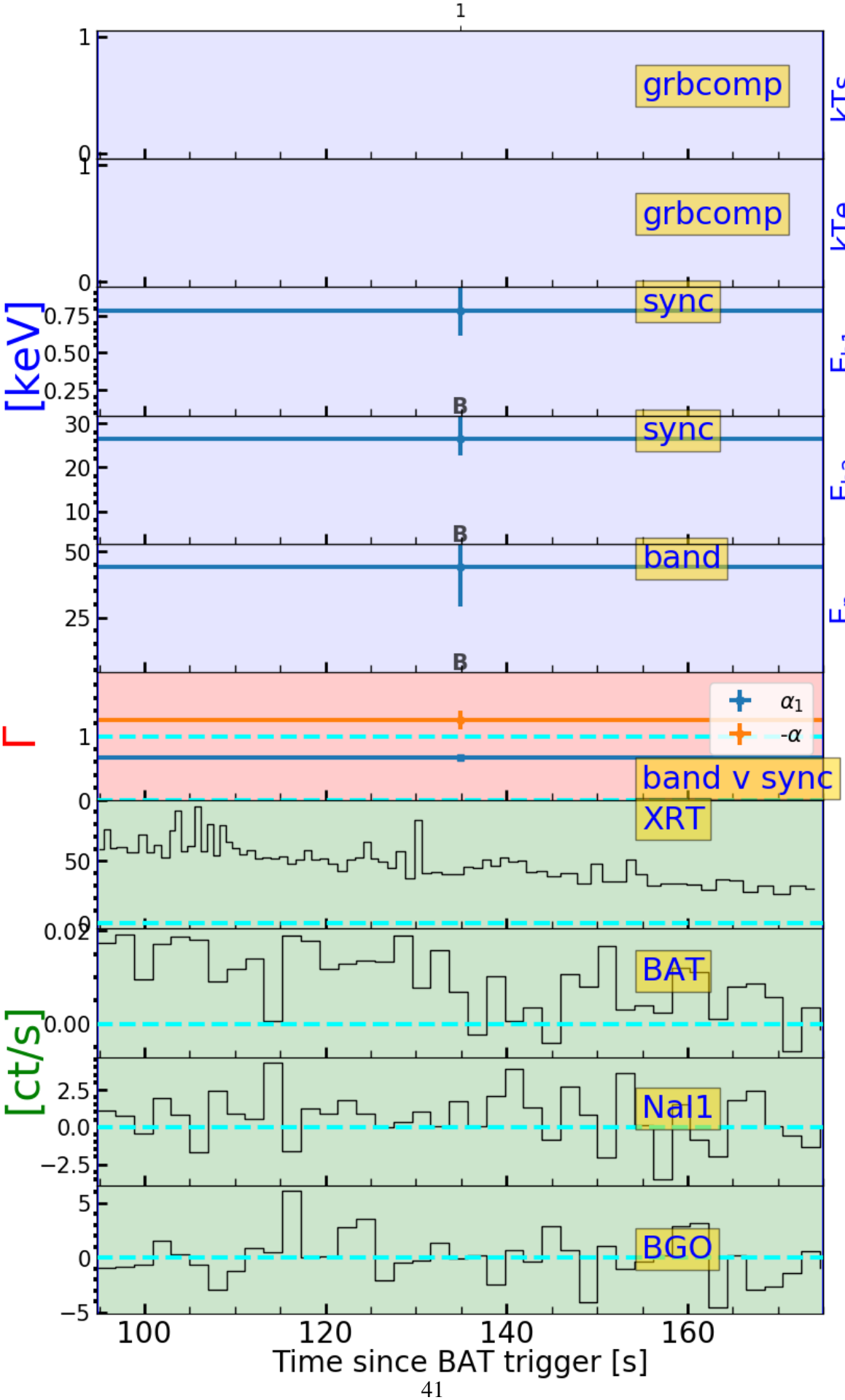

Figure 3.4: 100619A

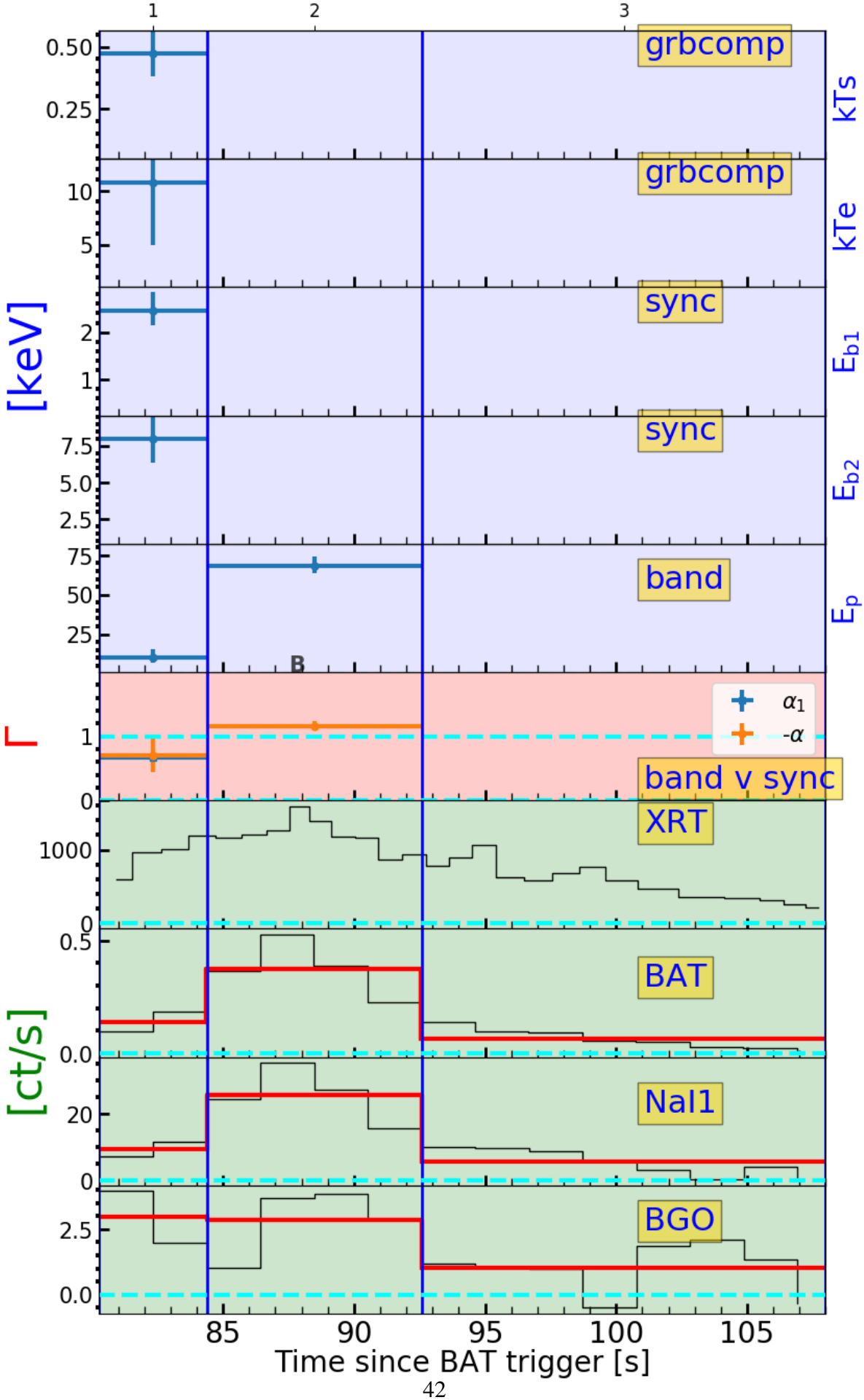

Figure 3.5: 100728A

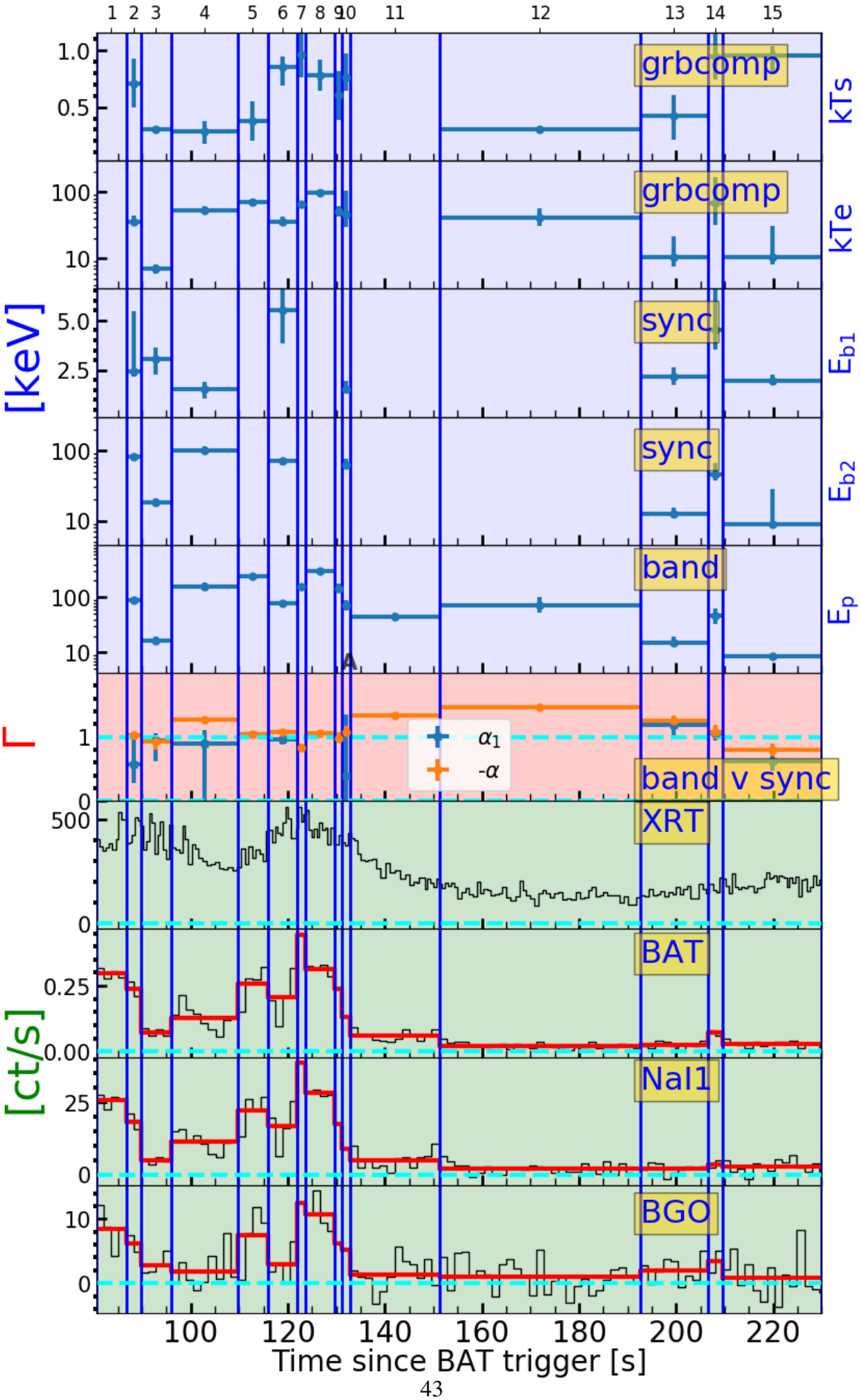

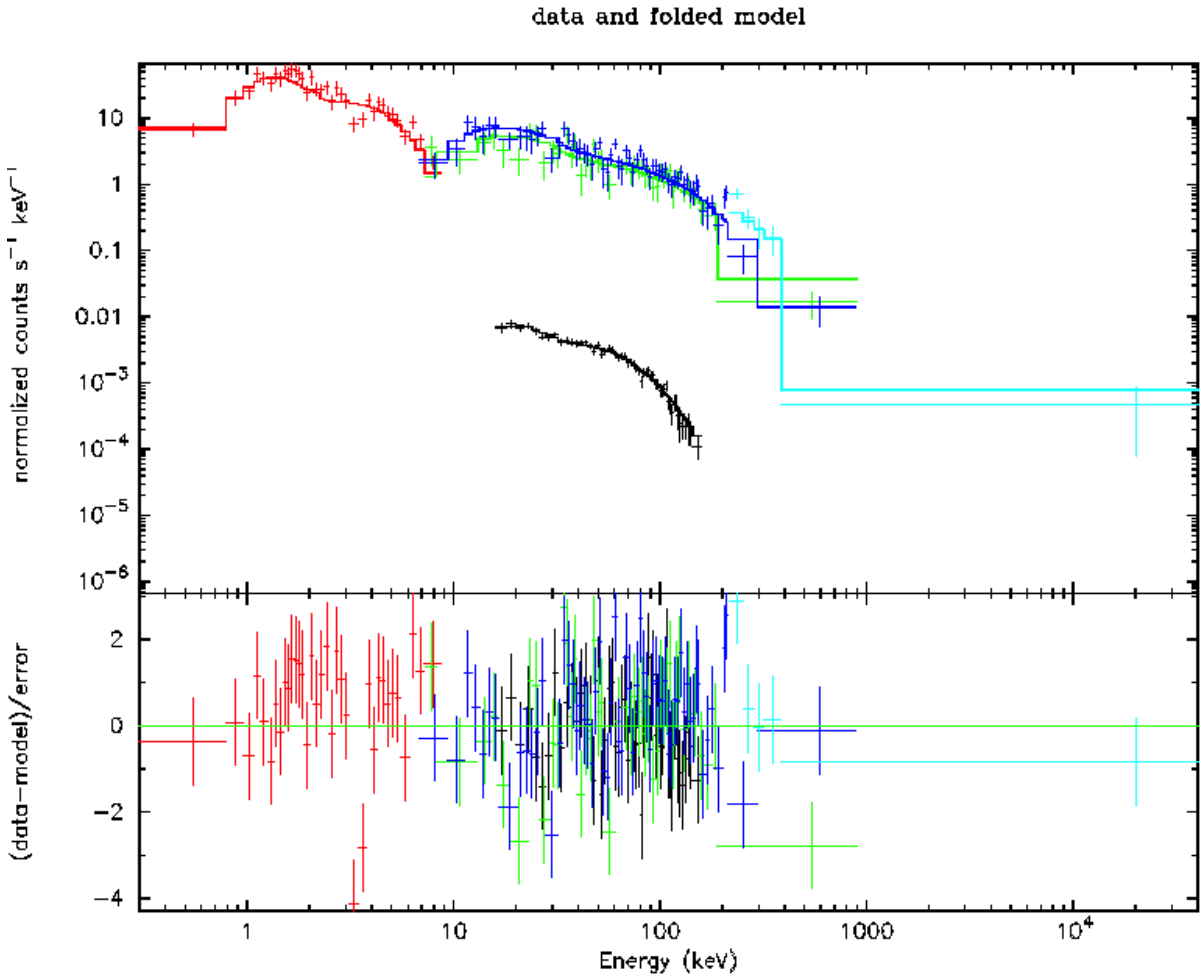

Figure 3.6: 100728A-interval 1: absorption edge?

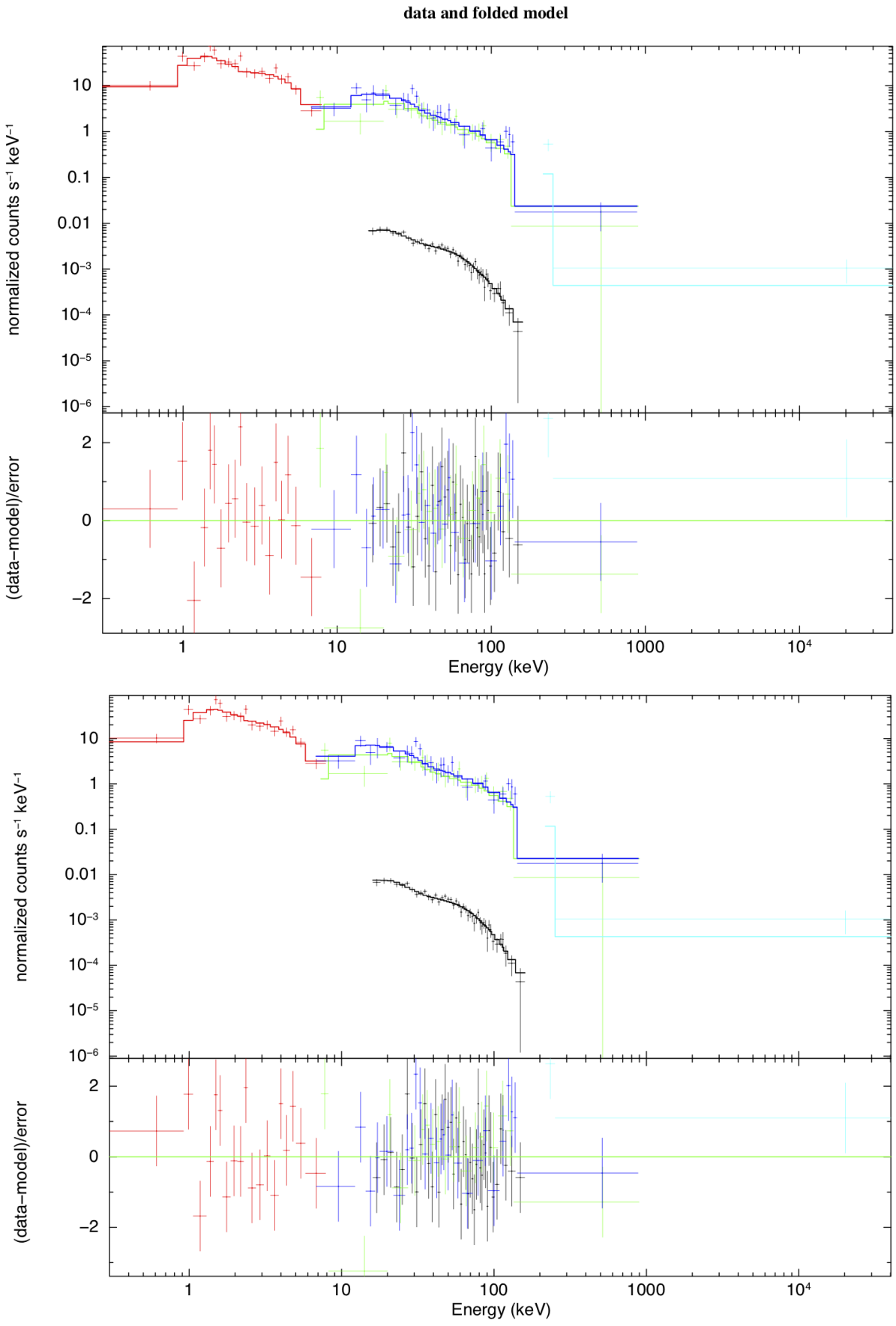
data and folded model
normalized counts s^{-1} keV^{-1}
(data−model)/error
Energy (keV)
10
1
0.1
0.01
10^{-3}
10^{-4}
10^{-5}
10^{-6}
2
0
−2
1
10
100
1000
10^4

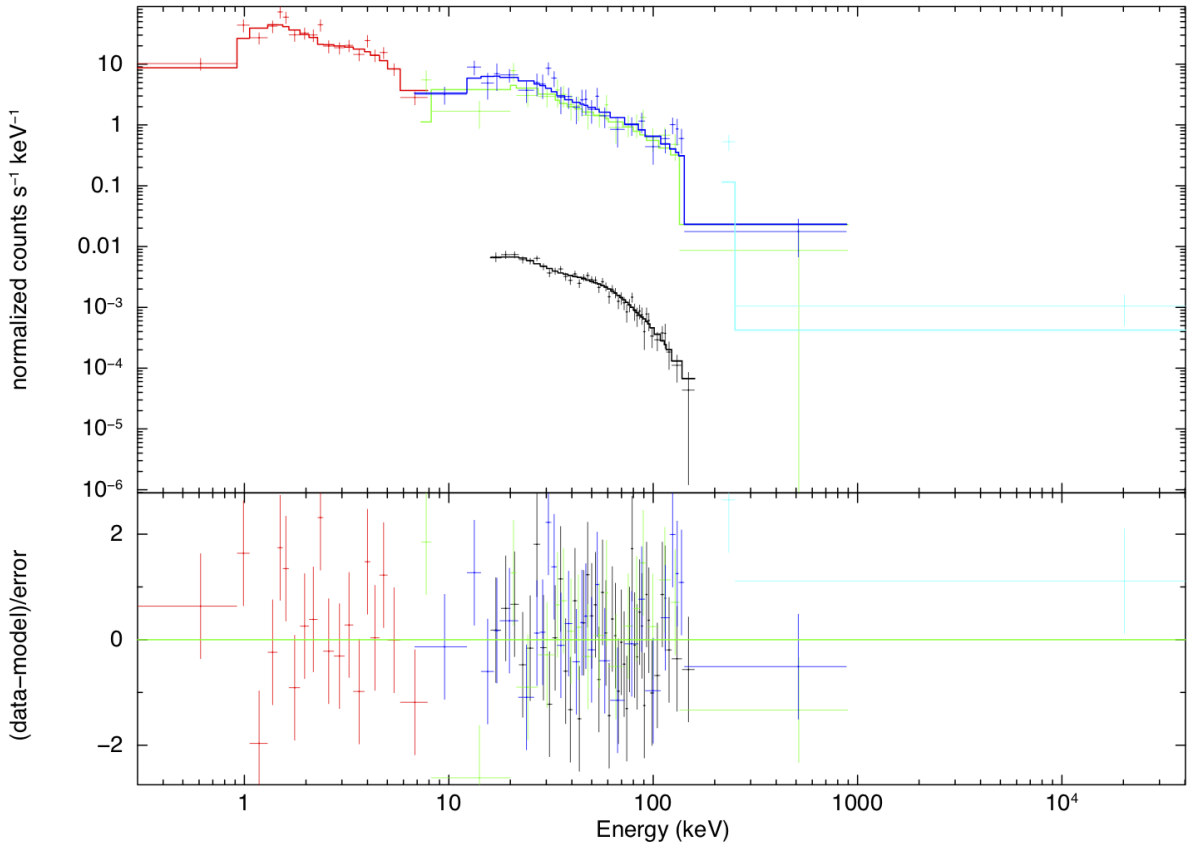

Figure 3.7: **100728A: interval 2.** *Top*: Band; *Middle*: Sync; *Bottom*: `grbcomp`.

3.4.6 100906A

Only the first three intervals can be analysed over the entire energy band, since in the last one only XRT data are detectable. `band` and `grbcomp` provide a good fit in the first interval, even if kT_s had to be fixed to 0.3 keV; `sync` has problems because the low energy break cannot be determined, possibly lying below 0.3 keV. The second interval presents problems for all the models, even if excluding XRT data provides good results with `band` (fixing $-\alpha = 1.$ and thawing β). Finally, the third interval can be fitted with `BB+band`, whereas `grbcomp` and `sync` do not pass both tests. It is not possible to try to fit ignoring XRT data, because of insufficient S/N (Fig. 3.9). The problems faced for this event are probably connected with the significantly different time profiles exhibited by X– and γ–rays.

3.4.7 110102A

The first two intervals are well described by a power-law, even if interval 1 requires an additional absorption and interval 2 requires the addition of `BB`. The last two intervals are problematic for every model, due to the low flux at high energies. All the models provide a good description of the data according to the χ^2 test across the central intervals, even if they sometimes do not pass the runs test. A noticeable case is represented by interval 8, where all the models fail the runs test. This suggests the possible presence of trends (Fig. 3.11), that are probably not due to XRT data, since the same problem is found even when XRT data are ignored (Fig. 3.12). For intervals 6, 9, 10, 12, 15 an additional `BB` to `band` is required. For intervals 4 to 15 `sync` provides a good description of data, showing a different behaviour of the low-energy index compared to `band`. The $-\alpha/\alpha_1$ spread increases as much as E_{b1} differs from the low energy boundary.

Figure 3.8: 100814A

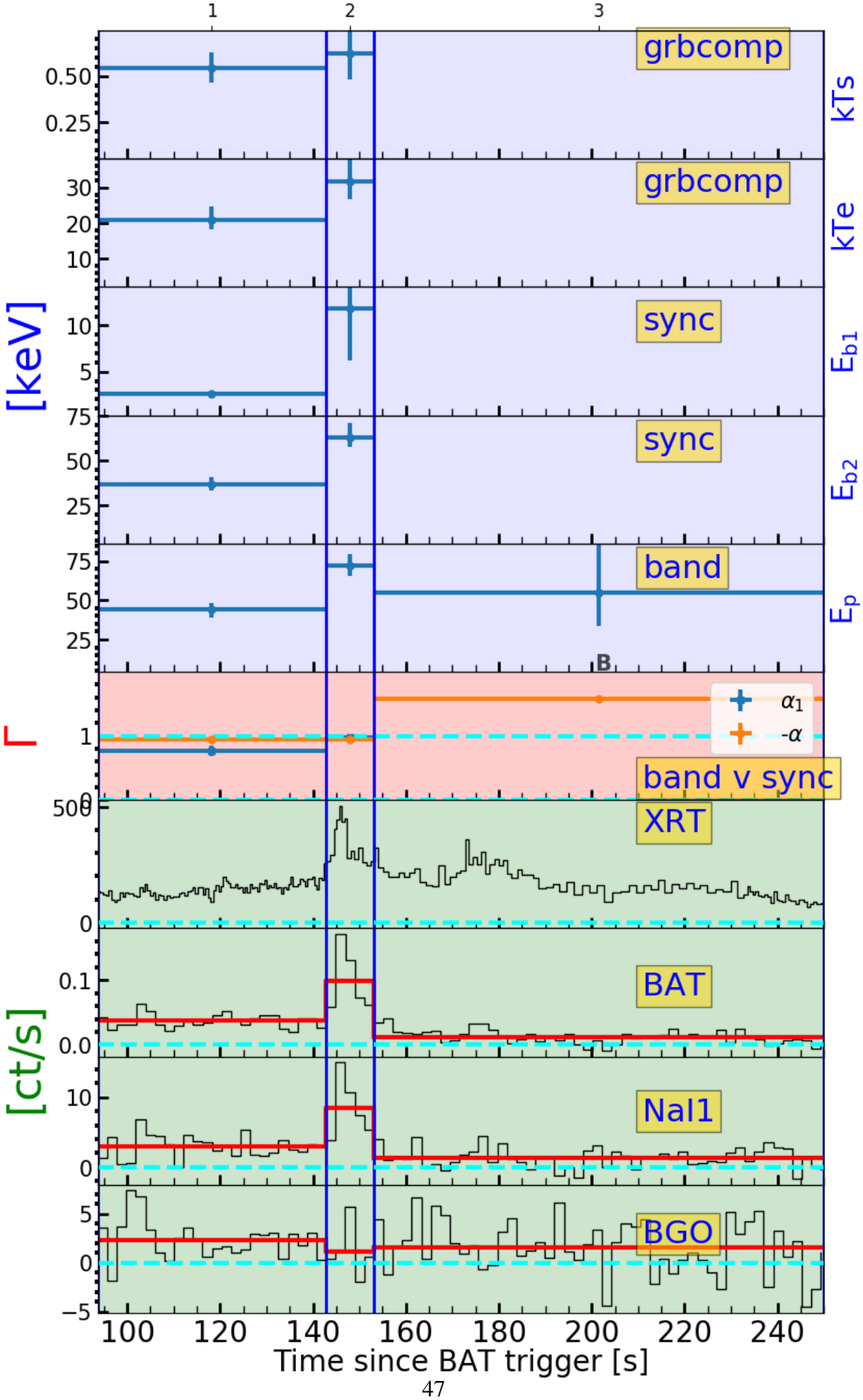

Figure 3.9: 100906A

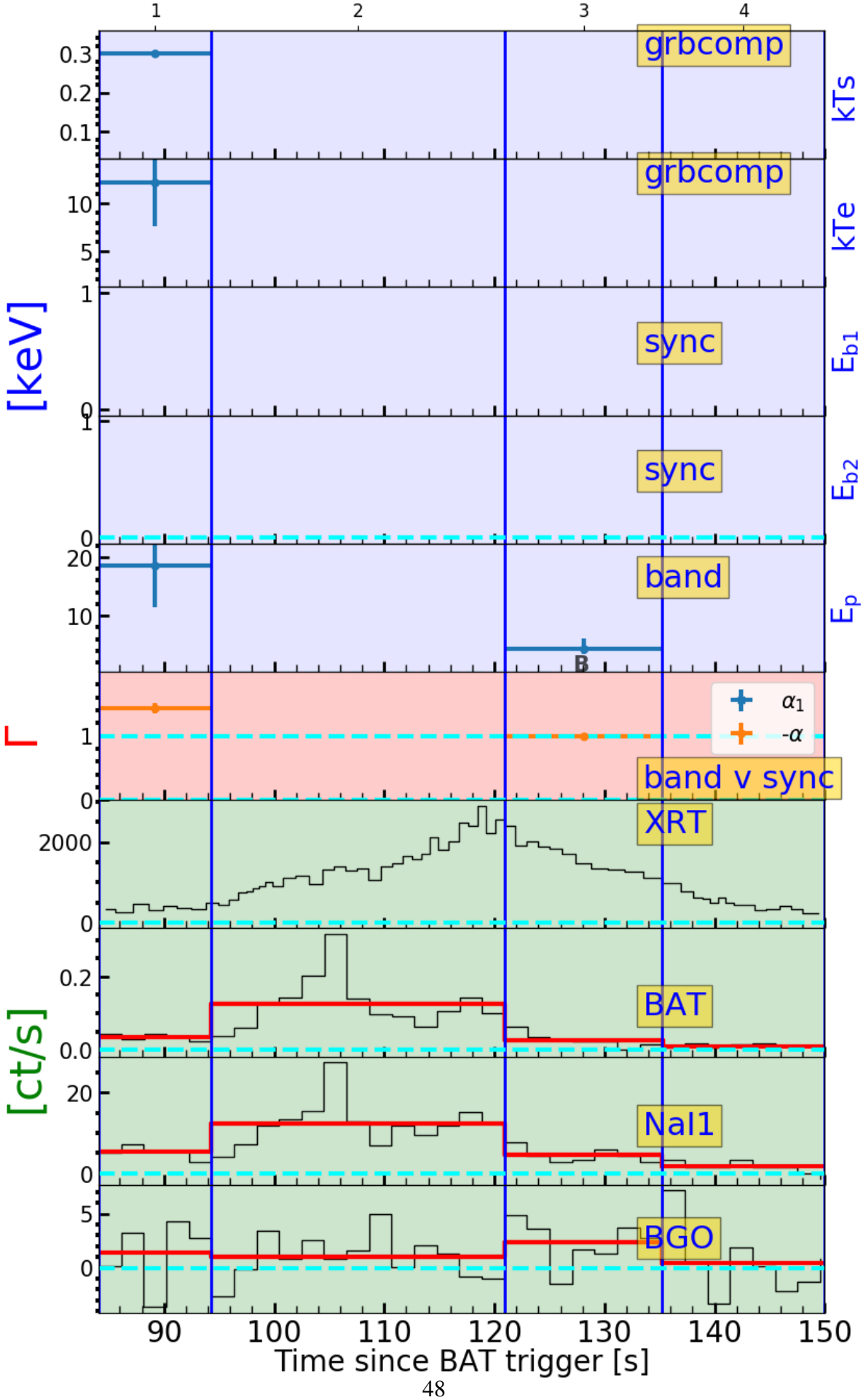

Figure 3.10: 110102A

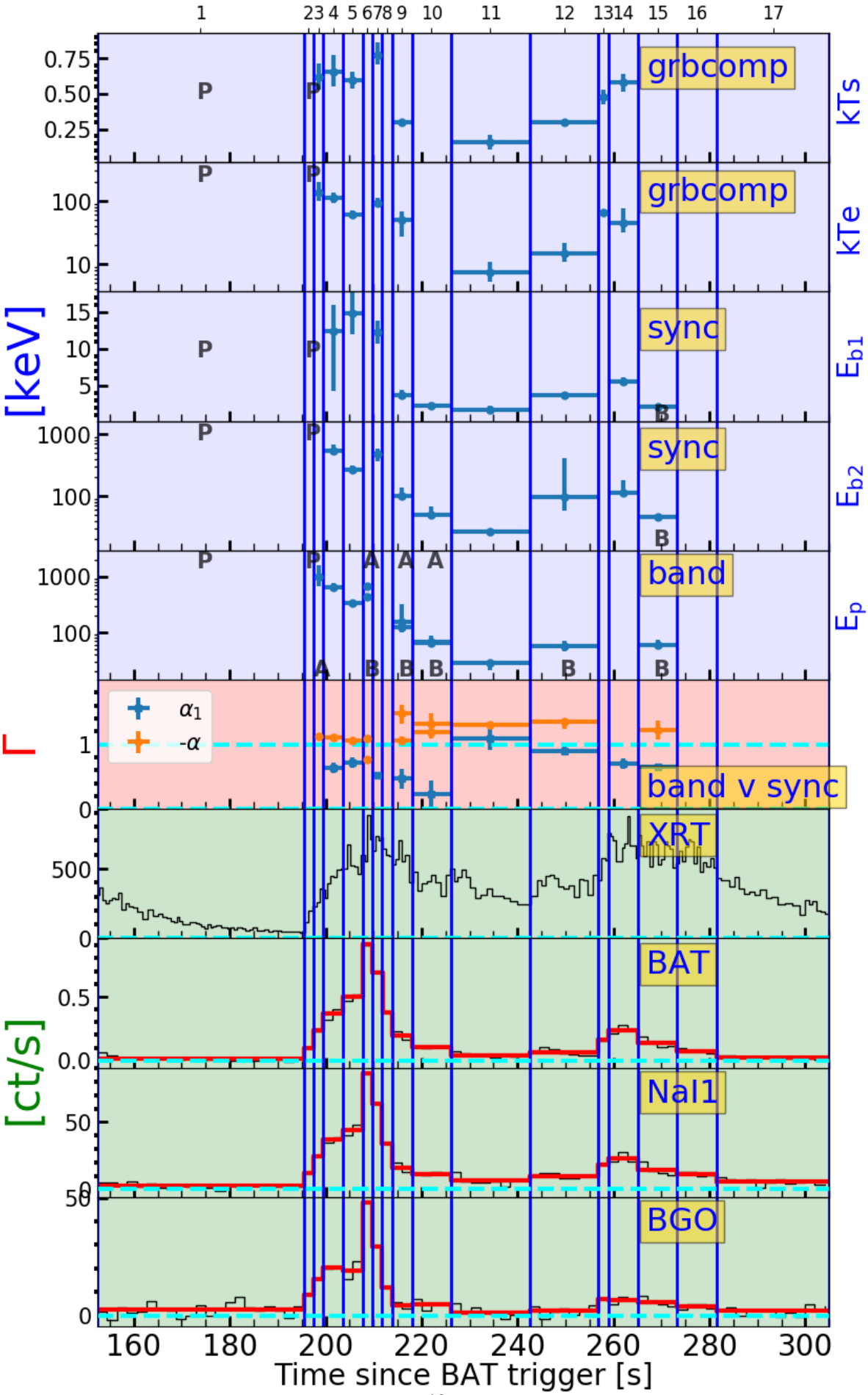

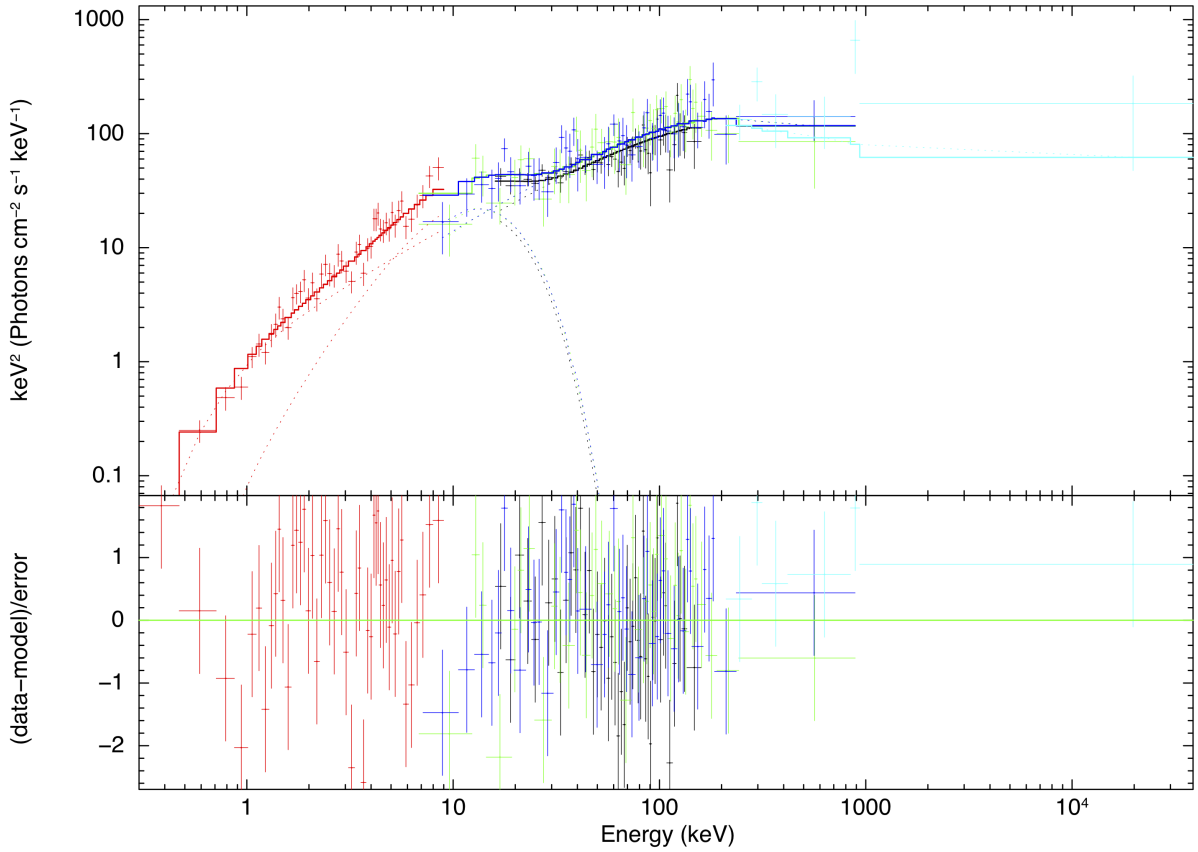
keV² (Photons cm⁻² s⁻¹ keV⁻¹)
1000
100
10
1
0.1
(data−model)/error
1
0
−1
−2
1
10
100
1000
10⁴
Energy (keV)

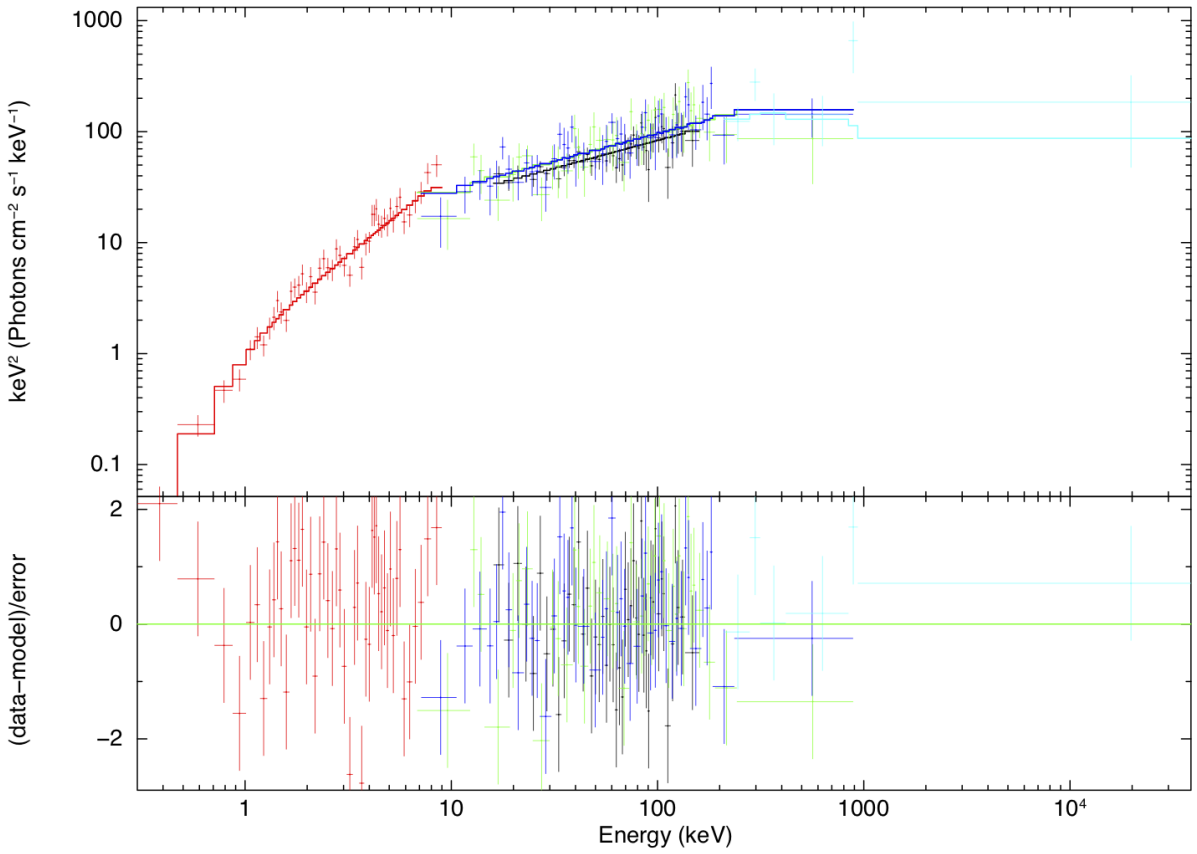
keV² (Photons cm⁻² s⁻¹ keV⁻¹)
1000
100
10
1
0.1
(data−model)/error
2
0
−2
1
10
100
1000
10⁴
Energy (keV)

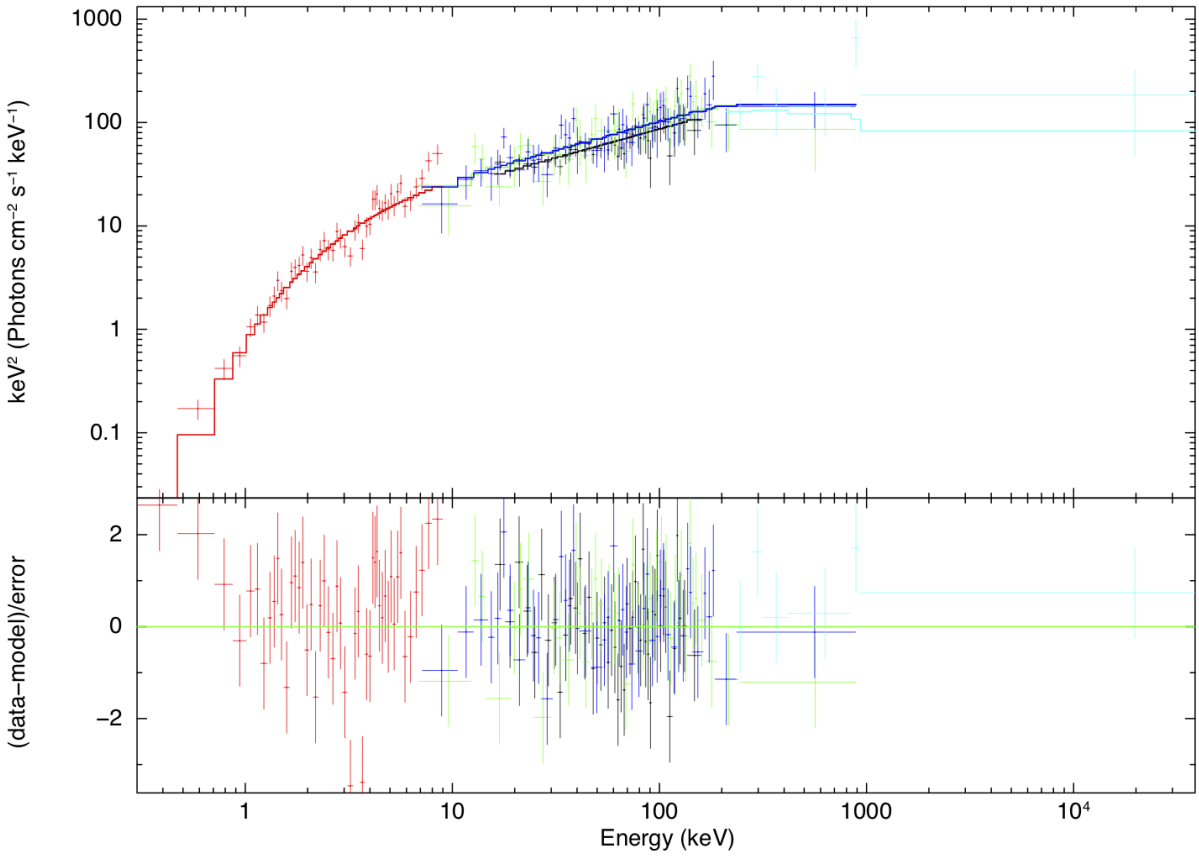

Figure 3.11: **110102A Interval 8.** *Top* BB+Band; *Middle* Sync; *Bottom* grbcomp.

3.4.8 130528A

Data in the only available interval are well fitted by every model. In this case the low-energy part of sync simply mimics band (Fig. 3.13).

3.4.9 130609B

band works well for all spectra, with intervals 2 and 3 requiring additional absorption. grbcomp is not rejected only for intervals 2 and by fixing $kT_s = 0.3$ keV, while in the other cases, like for sync, the fit does not converge. For interval 4 only the XRT signal is present and the broadband analysis cannot be done (Fig. 3.14).

3.4.10 140108A

band, sync and grbcomp fit the data in all the intervals, with the only exception of the first one and the last two, where data are well fitted by simple power-laws. grbcomp does not pass the runs test in interval 2 and is over the 95% threshold in interval 4, while band requires either further absorption or BB to fit interval 5, since a simple band does not pass the runs test. The sync low-energy index mimics the analogous one of band, with the only exception of interval 5, where the two low-energy indeces are different (Fig. 3.15).

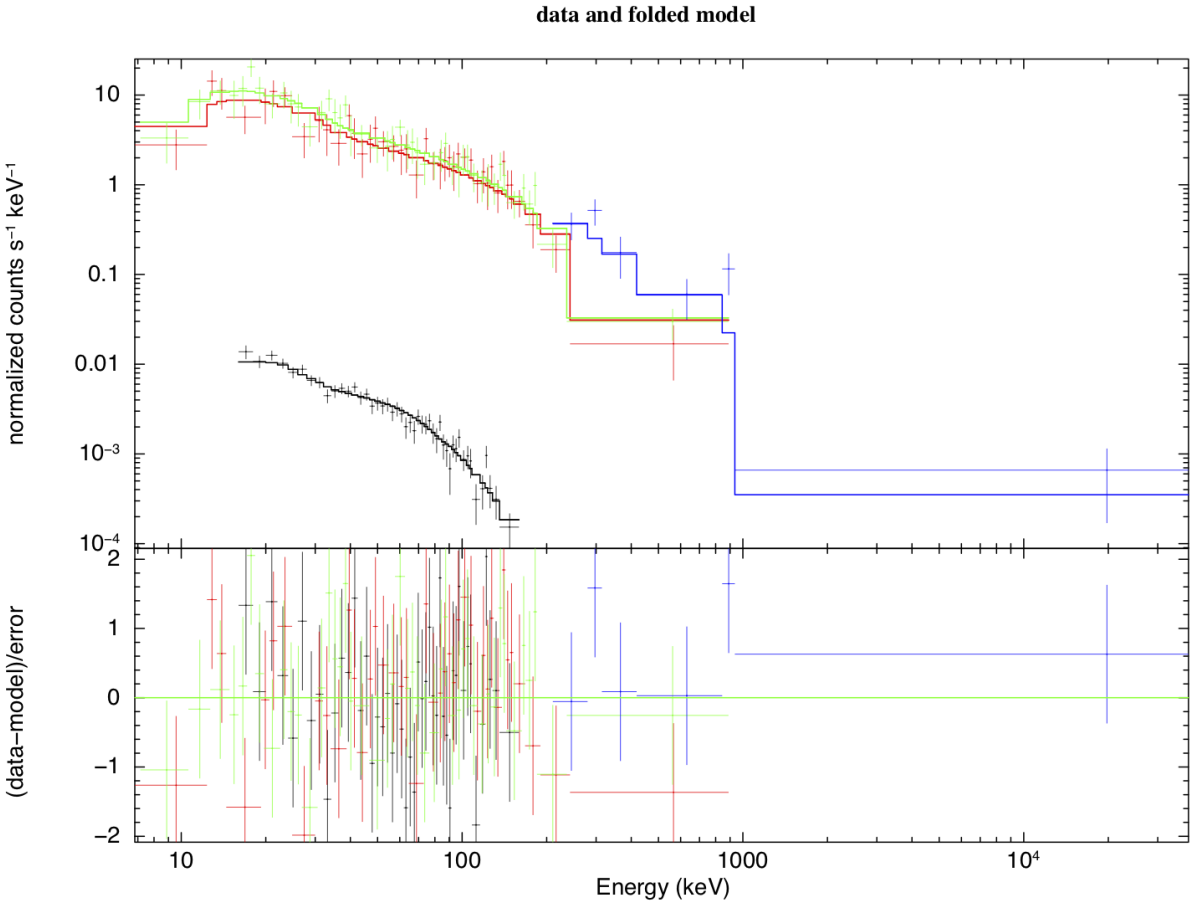
data and folded model
normalized counts s⁻¹ keV⁻¹
(data−model)/error
Energy (keV)

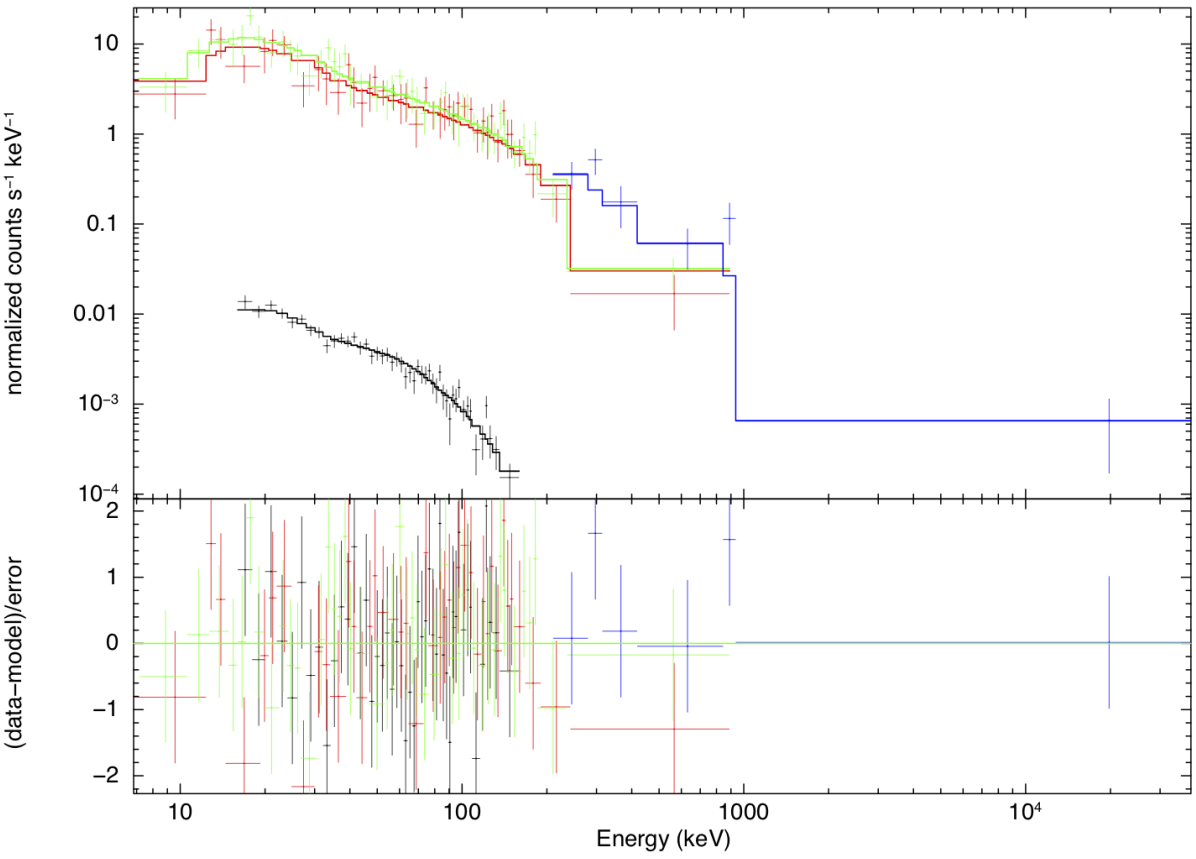
normalized counts s⁻¹ keV⁻¹
(data−model)/error
Energy (keV)

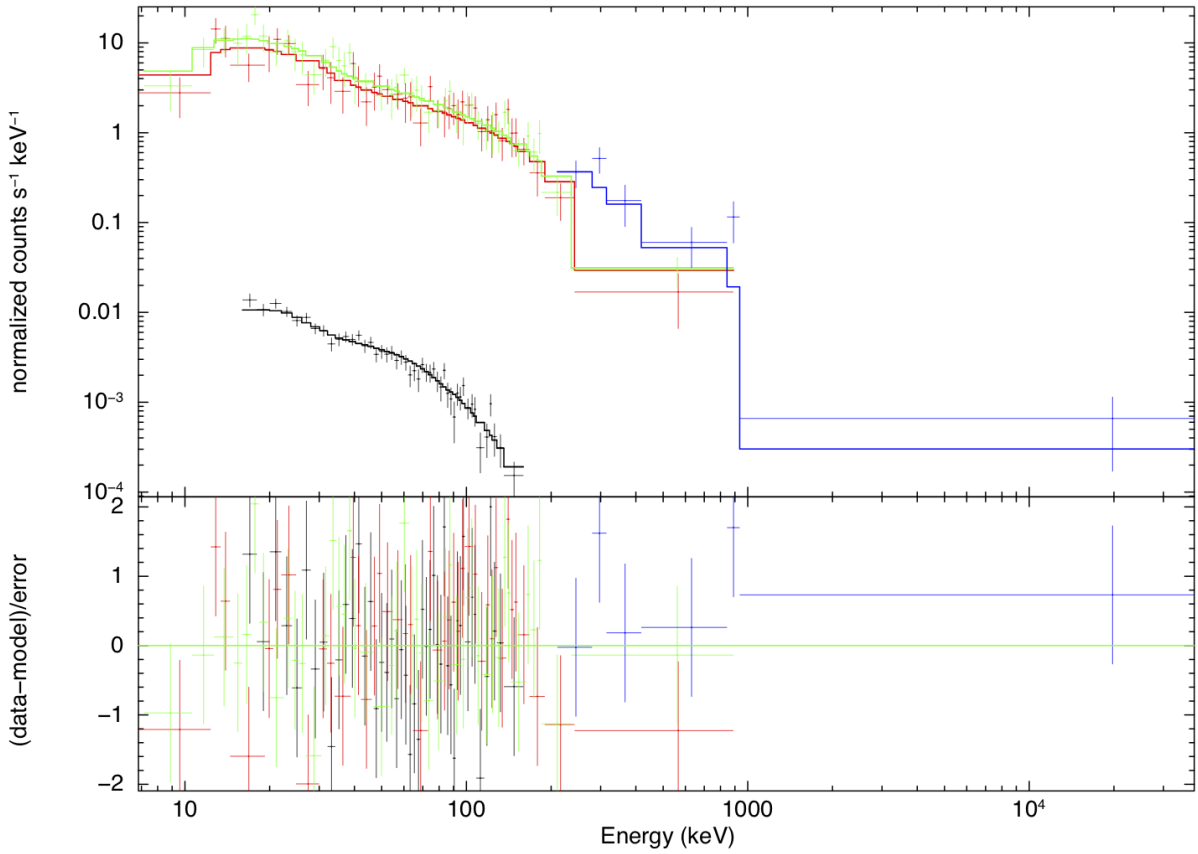

Figure 3.12: **110102A-no-XRT.** *Top*: Band; *Middle*: Sync; *Bottom*: `grbcomp`.

3.4.11 140323A

The analysis can be carried out only in the first two intervals. All models provide a good description of the spectra in both intervals, with the only exception of `grbcomp`, slightly over the χ^2 upper threshold in interval 2. In this case too `sync` mimics `band`, as shown by the comparison between the two low-energy photon indices (Fig. 3.16).

3.4.12 140512A

Almost all the intervals are well described by all models, with the exception of intervals 4, 8, and 9. Ignoring XRT data, a good fit is obtained for interval 8 with both `band` and the `grbcomp` model, while the runs test is not passed for intervals 4 and 9. For the remaining intervals, every model works well, even if `band` requires the addition of a further component (third absorption or `BB`) in intervals 1, 2, 3, 5, and 10. In this case the Γ panel suggests the `sync` does not simply mimic the `band` behaviour (Fig. 3.17).

3.4.13 150430A

Only the first interval has a S/N ratio high enough to perform the analysis. We obtain a good fit with both `band` and `sync`, even if the addition of a `BB` (with a temperature ≈ 0.38 keV) is required in both cases. The `sync` simply mimics the `band`, since the E_{b1} panel suggests that the break energy is not really seen, given the very large uncertainty and the simultaneous presence of the `BB`. On the other hand, `grbcomp` provides a bad fit for the χ^2 test (Fig. 3.18).

Figure 3.13: 130528A

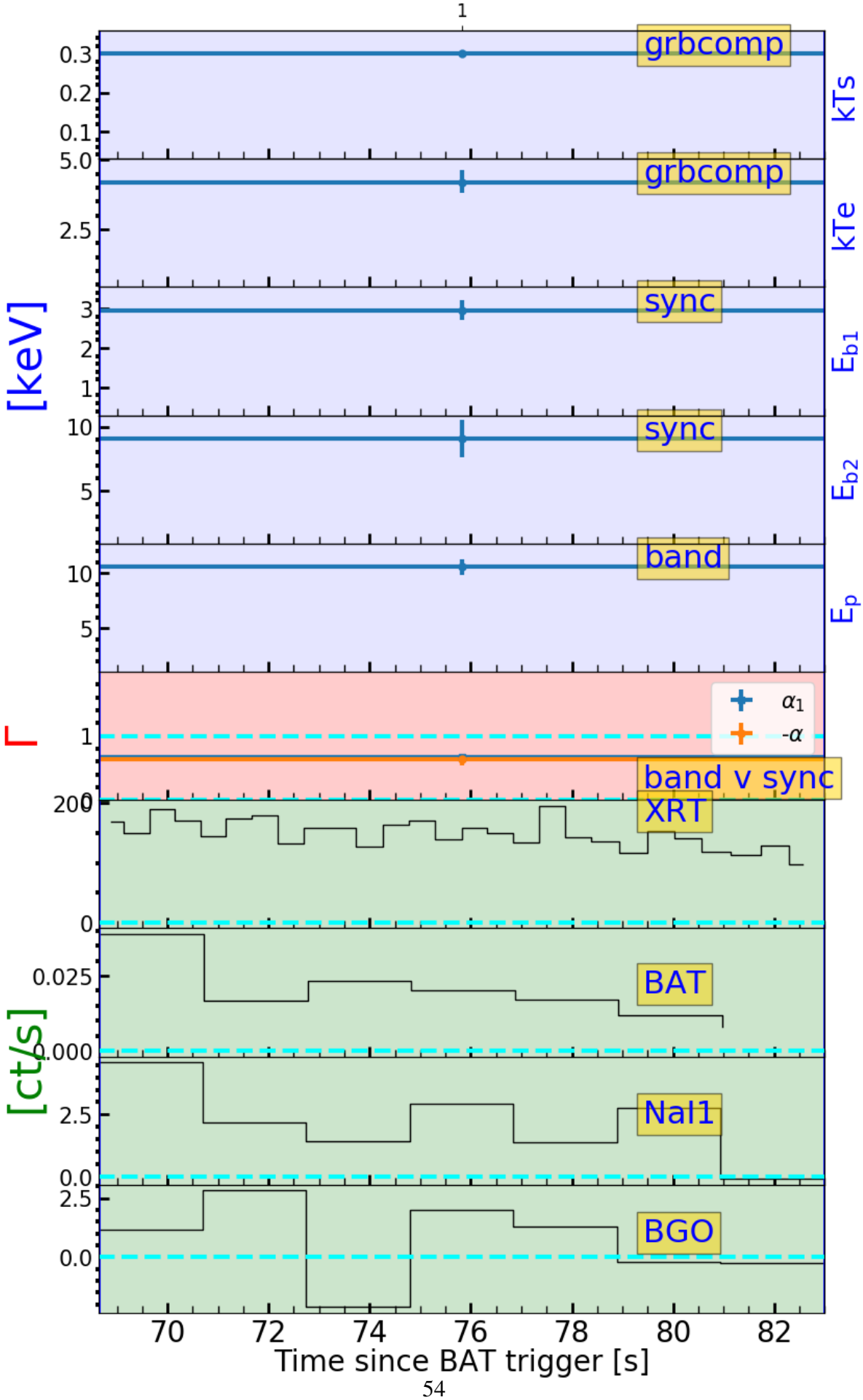

Figure 3.14: 130609B

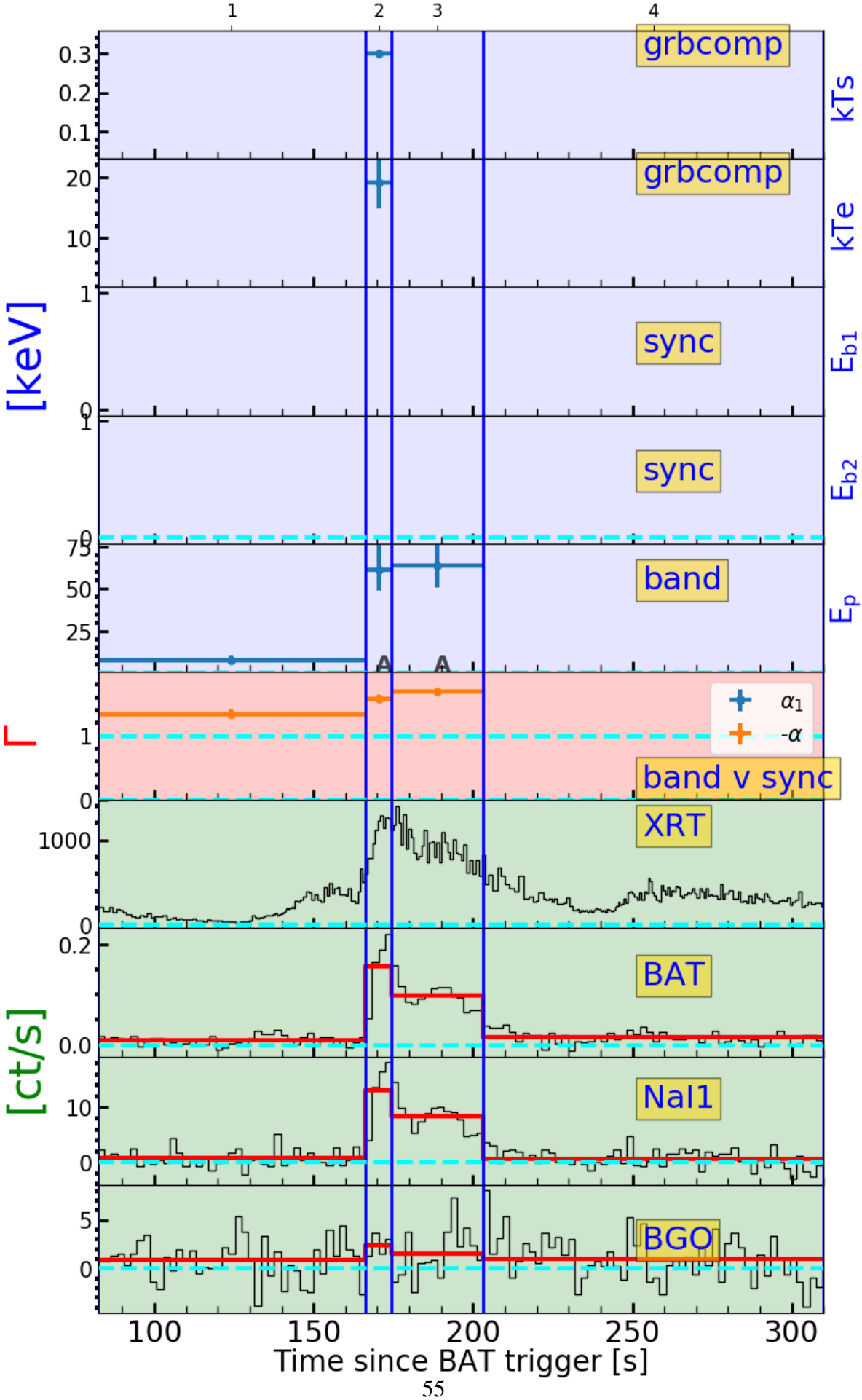

Figure 3.15: 140108A

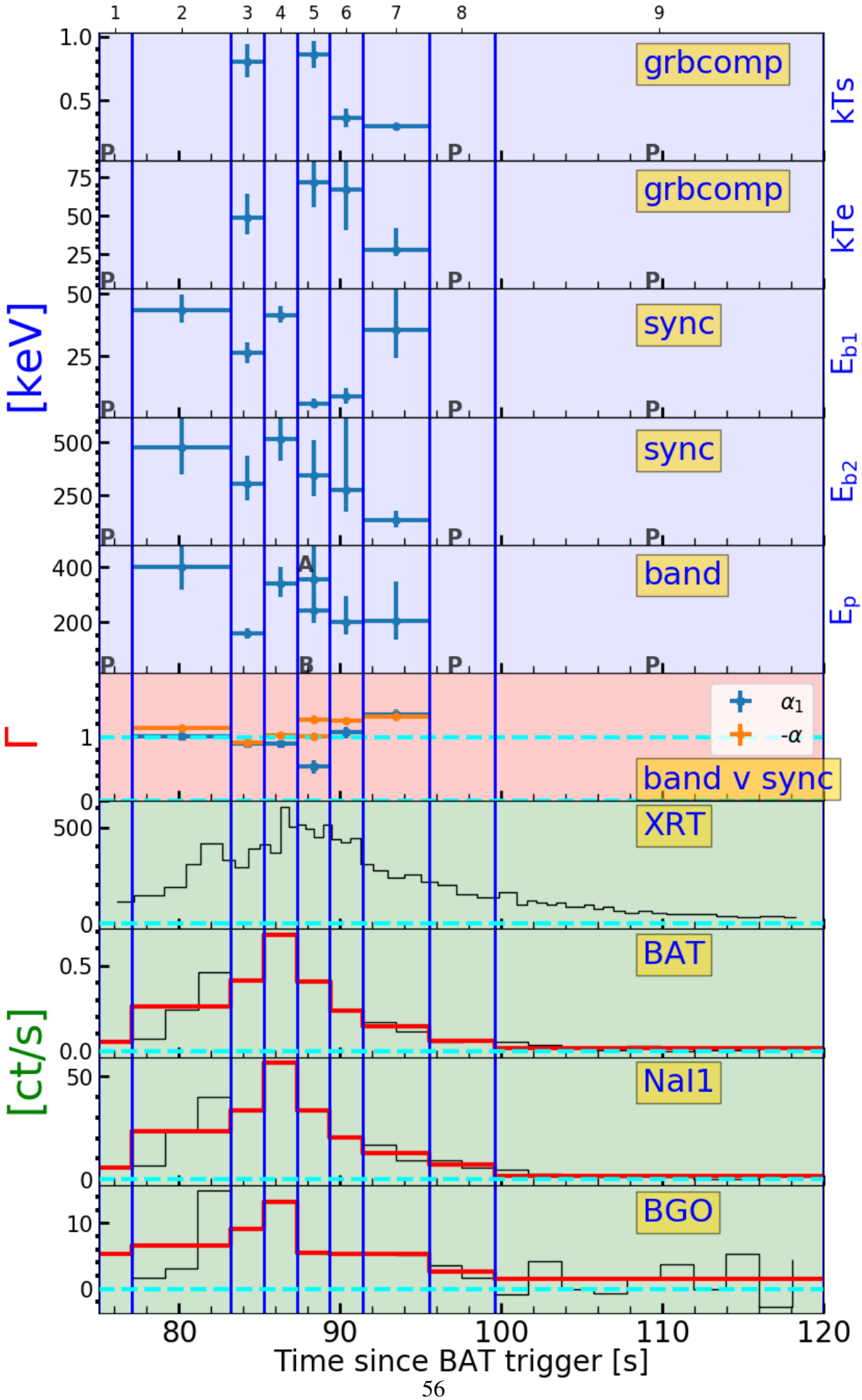

Figure 3.16: 140323A

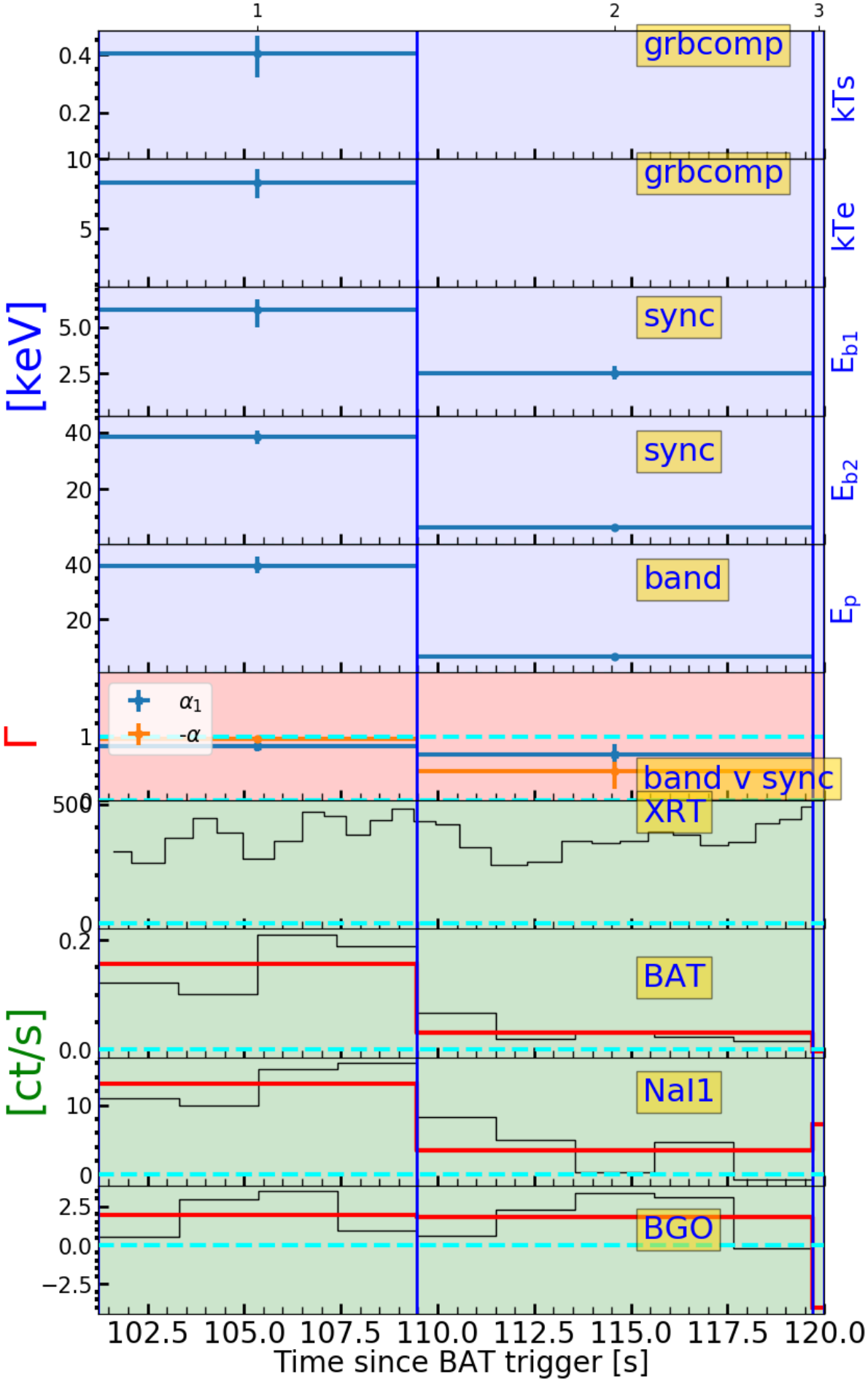

Figure 3.17: 140512A

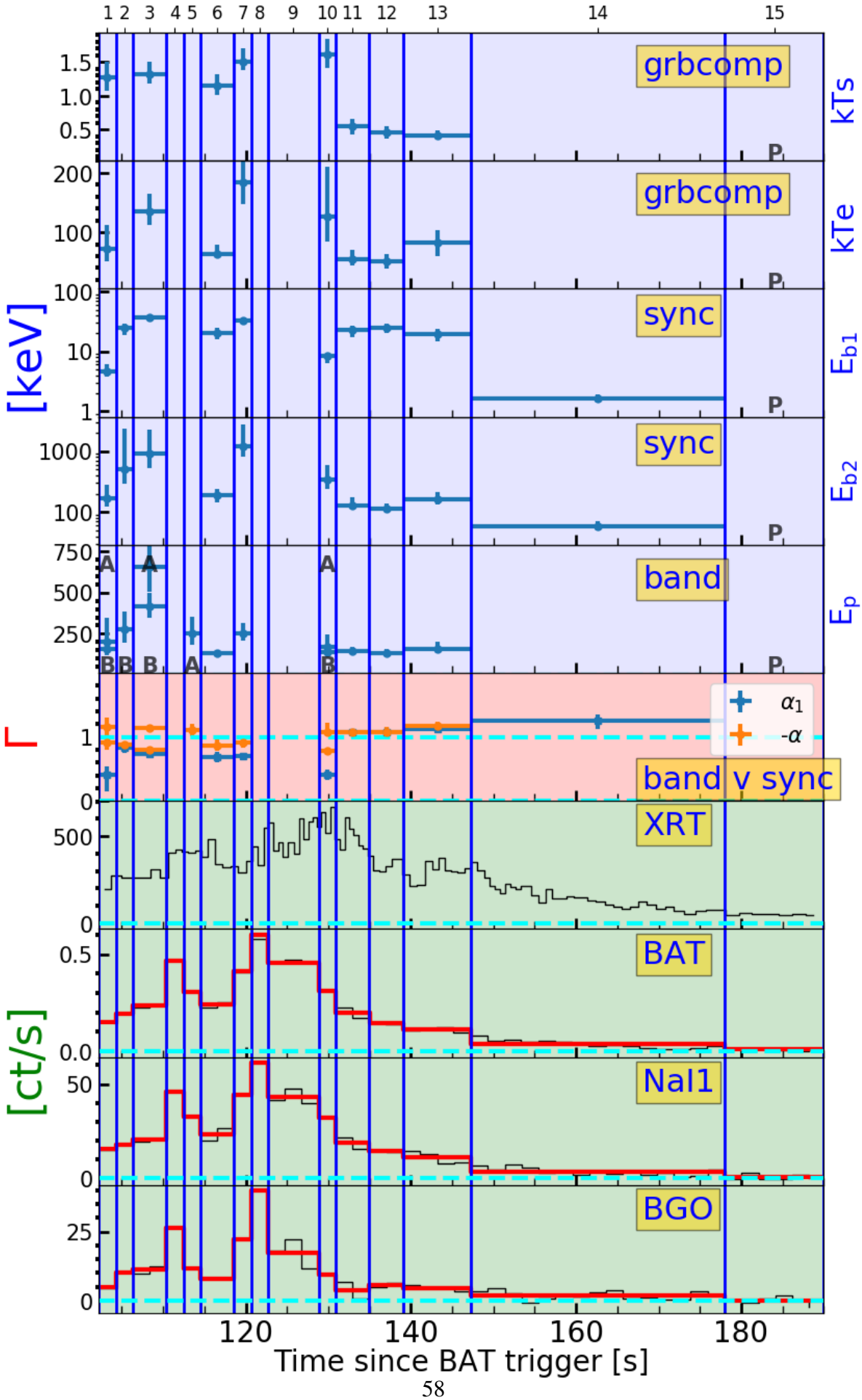

Figure 3.18: 150430A

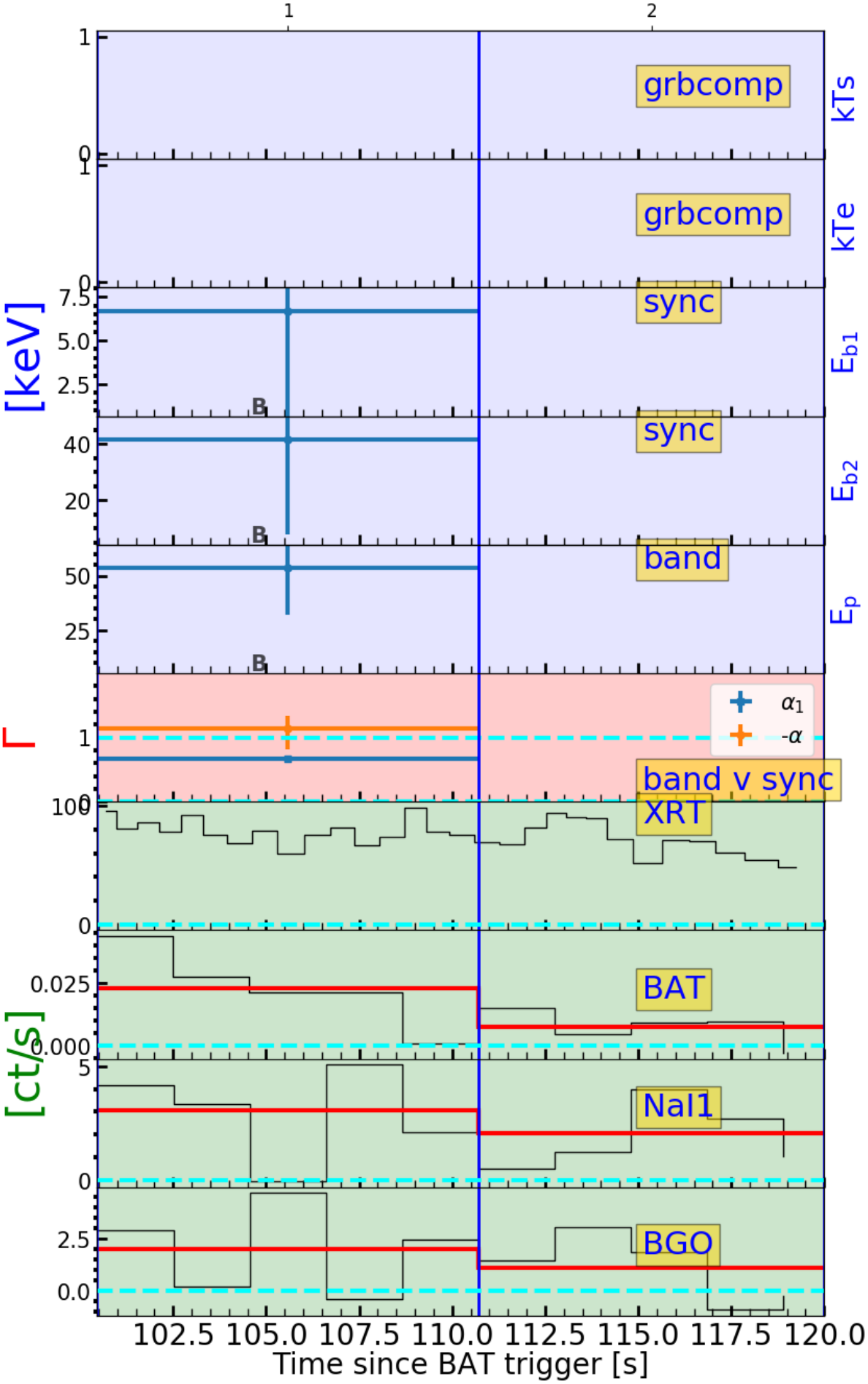

3.4.14 151006A

Only intervals 2, 3, and 4 can be studied over the entire energy range, since in intervals 1 and 5 the signal is very weak in all detectors. Interval 2 is well described by a band with the addition of a BB, while intervals 3 and 4 are well fitted with a simple powerlaw, as expected given the weak high-energy signal (Fig. 3.19).

3.4.15 151027A

We obtain a good fit with both band and sync model in the first interval. Starting from the second interval (when XRT data start to dominate the dataset), BB+band (or band plus a third absorption in the second interval) fits the data, while sync and grbcomp provide good results only for some intervals (1, 4 and 2, 4, respectively). Interval 5 is problematic for all models: the best result is obtained by a BB+band, which is only a little bit under threshold. This behaviour, with the strong presence of a BB, confirms the results by Nappo et al. (2017). In the last two intervals there is almost only XRT signal, so the broadband analysis cannot be performed (Fig. 3.20).

3.4.16 161117A

All the models fail to describe intervals 5, 7, 8, and 9. This could be due to the different peak times observed in the different energy bands. Ignoring XRT data, intervals 5 and 8 data can be well described by band. The combination of the γ–ray signal from interval 7 with the XRT signal from 8 or 9 leads to a bad fit too. In the first intervals sync provides a good description of the data, while band requires additional components: this suggests sync is not a simple mimic.

3.4.17 170405A

Both band and sync work well in all intervals. grbcomp offers a good description only for interval 3, while in the other two cases it does not pass the runs test. α_1 mimics the band $-\alpha$, suggesting the equivalence of the two models as far as the modelling on a pure statistical basis is concerned (Fig. 3.22).

3.4.18 Thermal (un-scattered) component in GRBCOMP

In most of the cases in which grbcomp gives a poor result while BB+band and/or BB+sync work well, a further attempt was made by relaxing the initial assumption of a dominant Componisation component over the thermal one. The ratio between the contribution of the two is ruled in the grbcomp model by the A parameter (as specified in Subsection 1.2.2), and the initial assumption of a dominant Comptonisation component was set fixing a large value (log(A) = 5). In the light of this, the emergence of an un-scattered thermal component comes out self-consistently inside the model for small values of the A parameter, with no need for further independent BB components like in the cases of sync and band. To test the existence of this further component, we thawed log(A), assigning it a small or negative value as a starting point. We did this on spectra 6 and 15 of GRB 110102A, 1 of GRB 150430A, 1 of GRB 151006A, and 1 of GRB 090926B, finding a major improvement for both the χ^2 and runs statistics in all cases. For all these trials grbcomp passed both thresholds, with the only exception of 151006A, for which we obtained a p-value=4.6 % for the runs test. It is worth noting that this attempt is doable only when the statistical quality of the spectra is good enough. Otherwise,

Figure 3.19: 151006A

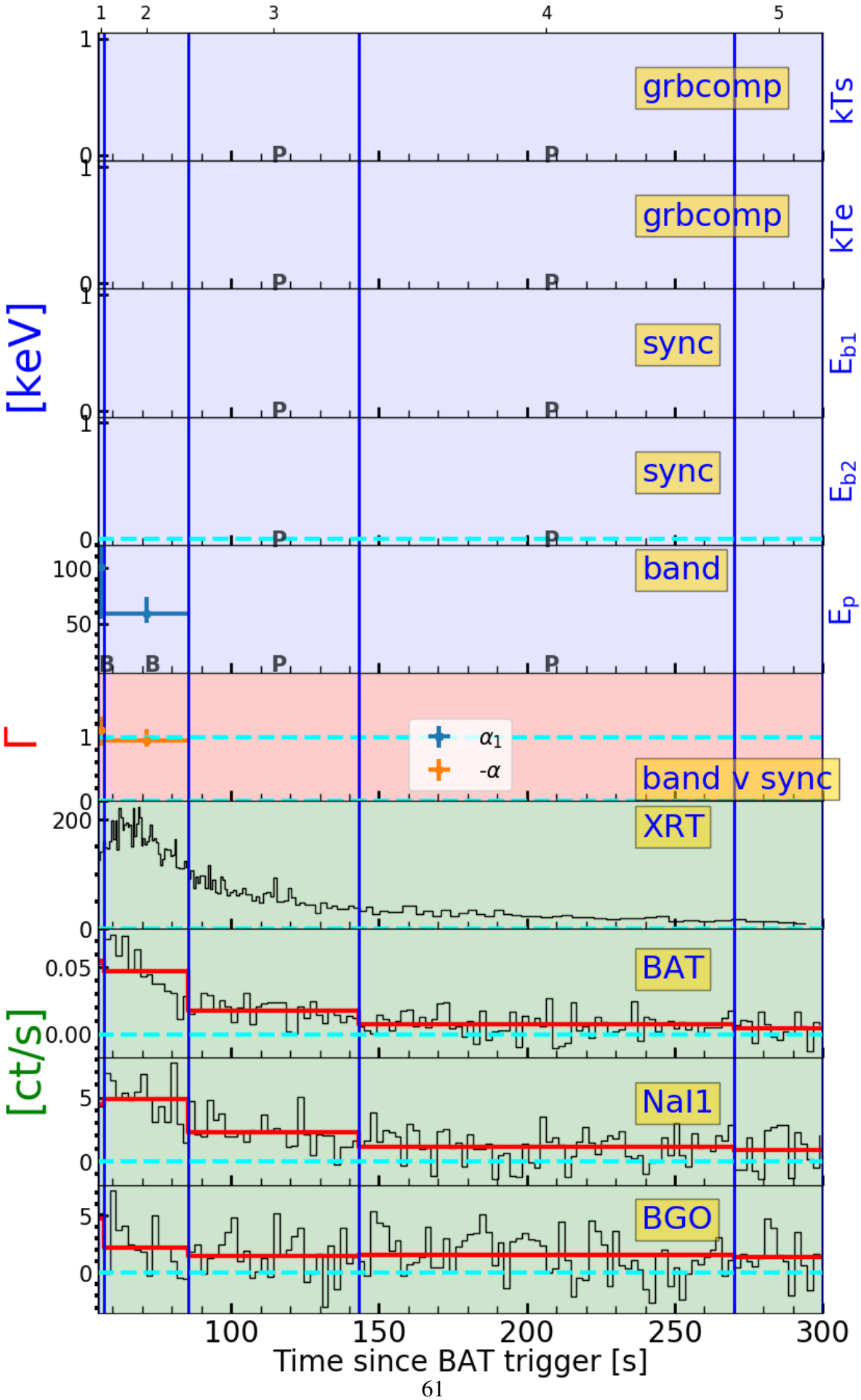

Figure 3.20: 151027A

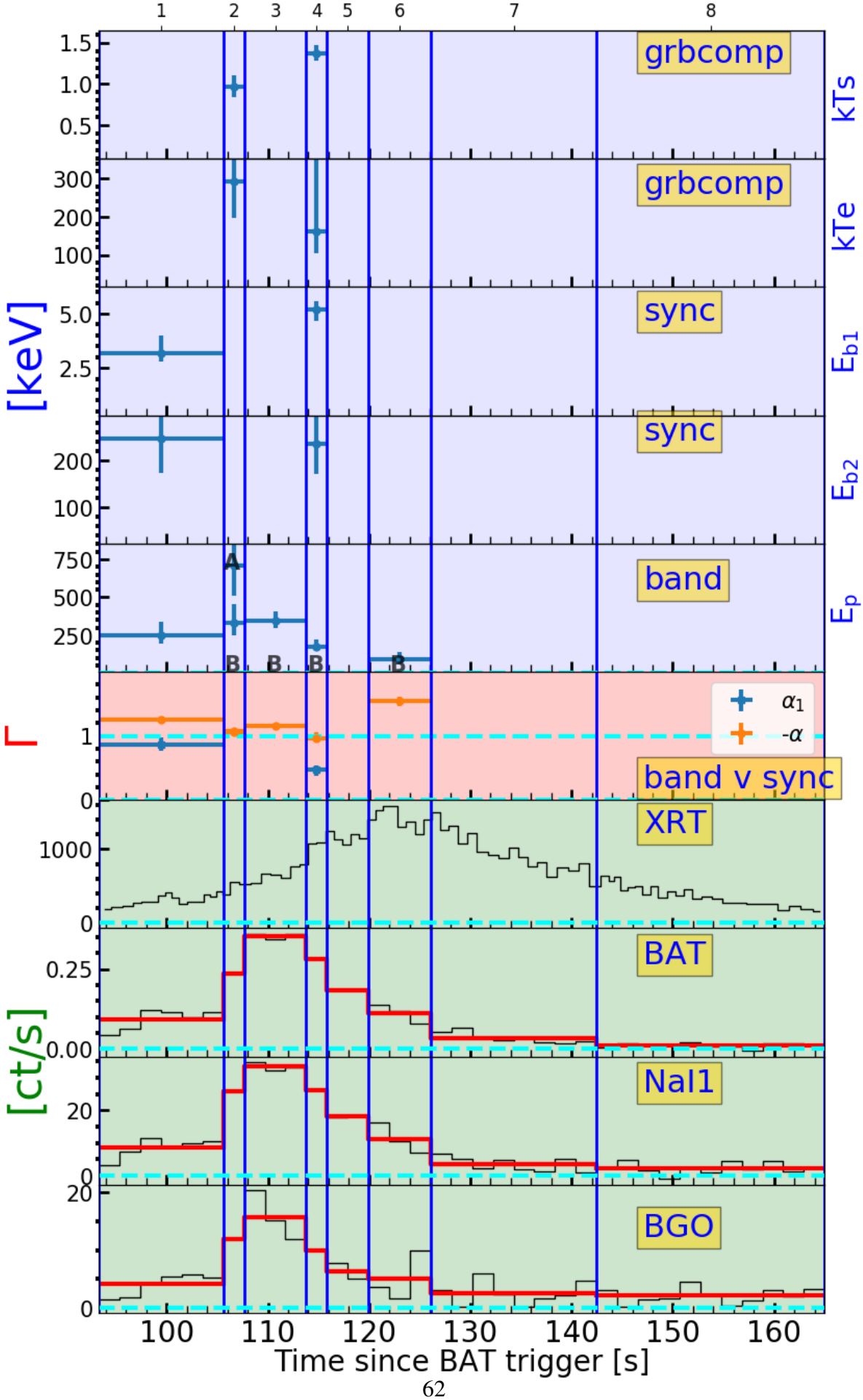

Figure 3.21: 161117A

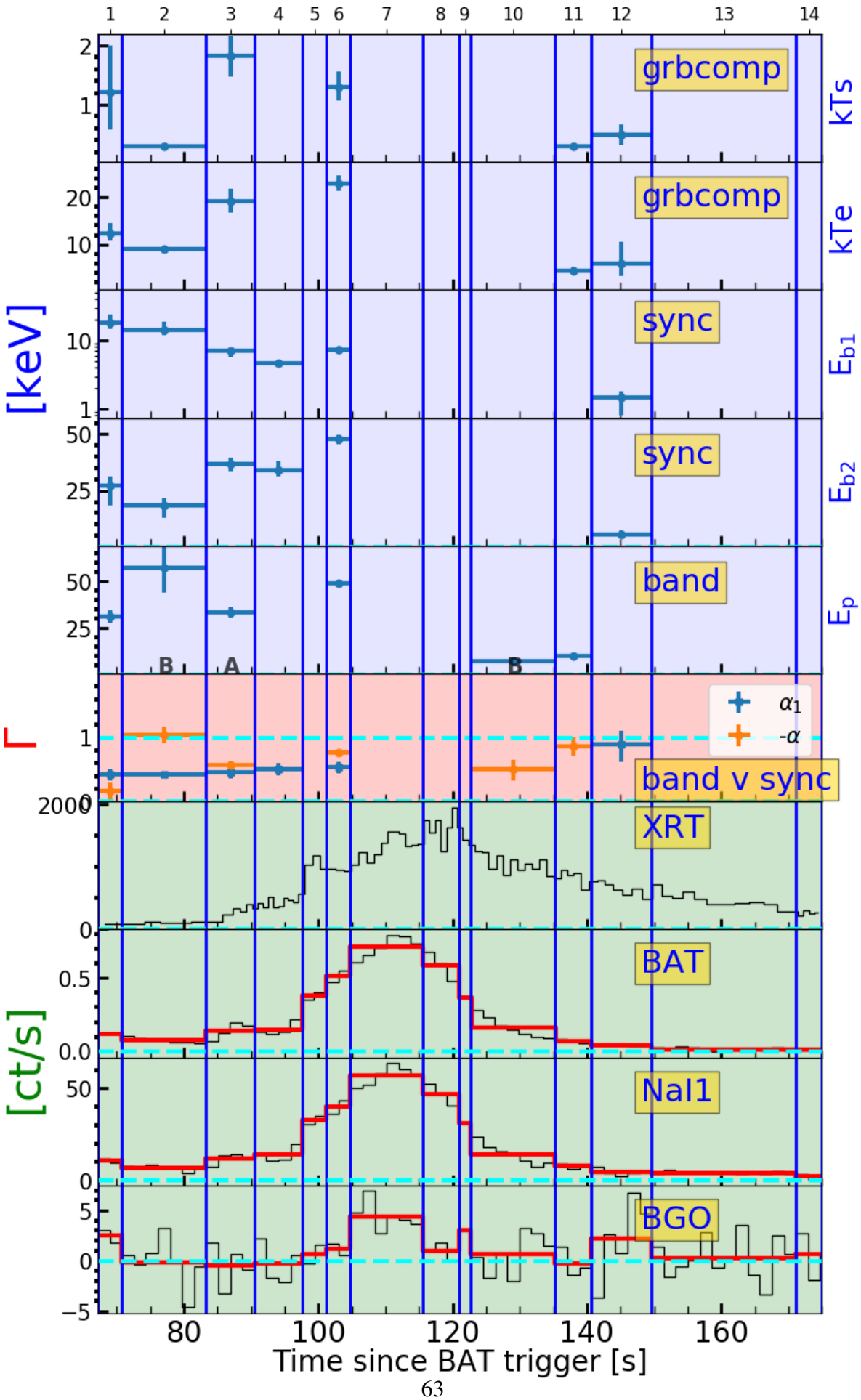

Figure 3.22: 170405A

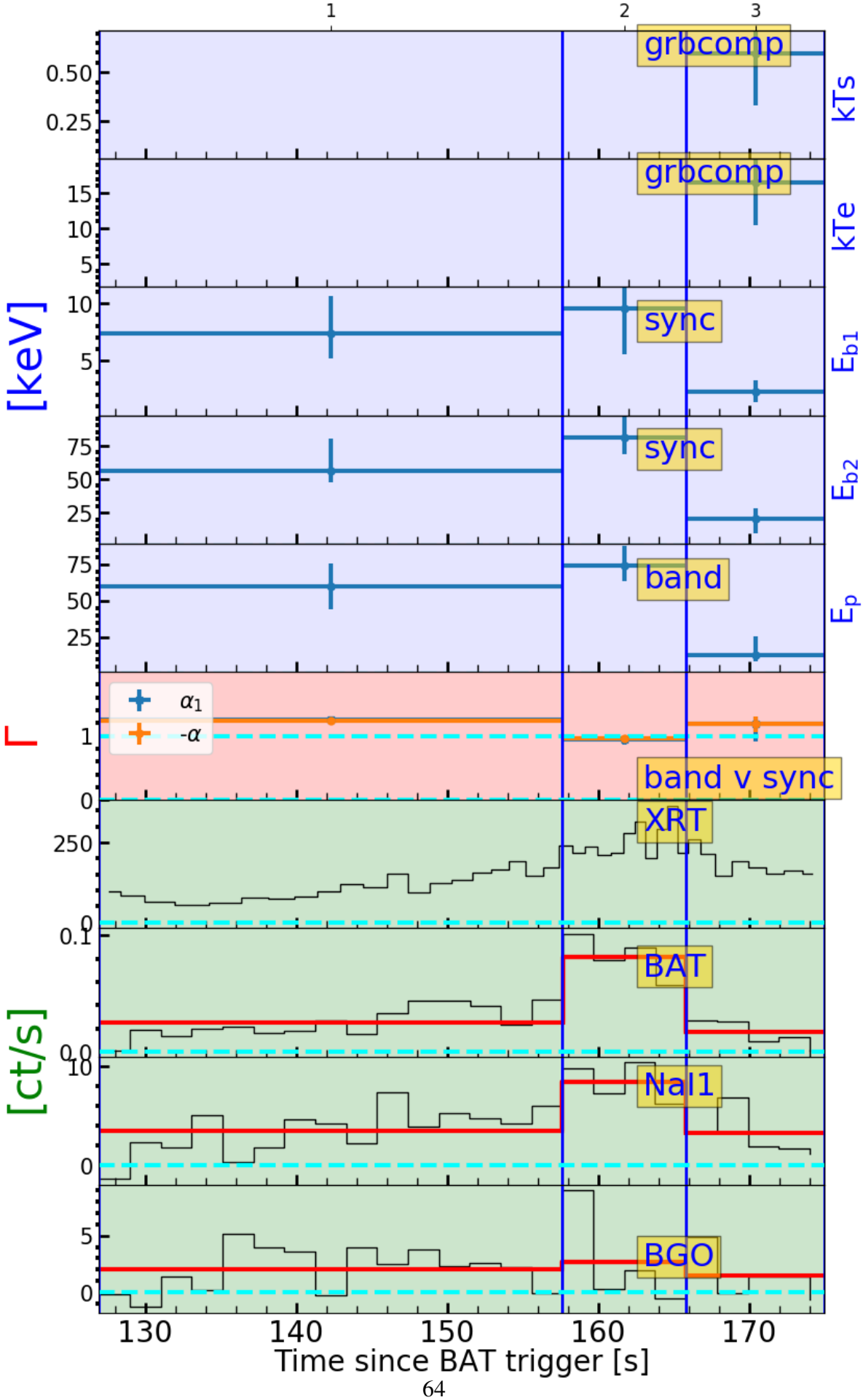

allowing a further model parameter to vary without the required statistical quality of the data would inevitably increase the degeneracy between the parameters.

3.5 Discussion

We were able to perform a time-resolved analysis in the broad 0.3 keV–30 MeV energy range of 17 long GRBs thanks to the combined use of *Swift* and *Fermi* data. Given the time required to pinpoint the UVOT, the study inevitably concerned events that present a prolonged ($\gtrsim 80s$) high-energy emission. In the majority of cases, the lightcurves were also structured, so a number of intervals were identified. Figure 3.28 summarises the outcome of this analysis, showing the fraction of spectra that can be described by the different models. In general, we found that pure `band` and `sync` have similar performance, providing a good fit in slightly less than 50% of cases. At the same time, `grbcomp` yields an plausible description in the majority of cases, outperforming pure `band` and `sync`. On the other hand, `band` performance shows a major improvement when the additional components (BB or a third absorption) are considered. The same is not true in the case of `sync`, since only a minor improvement is overall observed. However, the problematic cases for `grbcomp` should be considered with care: the results of the additional test performed thawing the log(A) parameter suggest that a not-fully-Comptonised scenario could provide a good description of the spectra in a at least some cases (see Section 3.4.18). Unfortunately, in the majority of cases the statistics of time resolved spectra is not good-enough to constrain an additional parameter, so the exact impact of this effect can hardly be quantified. For this reason, the result of Figure 3.28 should be received as a lower limit on the `grbcomp` performance.

Notably, all models fail in describing 16 out of 93 spectra ($\sim$ 17% of cases; lower right panel of Figure 3.28). An exact calculation of the significance of this result is not straightforward, but in Sect. 3.5.1 we provide a rough estimation of the probability to find this result by chance. However, the visual inspection of the figures relative to these cases (namely Figures 3.4, 3.9, 3.14, 3.17, 3.18, 3.20, 3.21) suggests a connection between the occurrence of such problematic intervals and the property that the soft X–ray time profile does not track the γ–ray one, but shows either a delayed peak or remarkably different temporal structures.

O17 and O18 support the almost ubiquitous presence of a low energy break in the soft X–ray range of GRB prompt spectra, leading to the identification of a further powerlaw at low energies. This component can be recognised only at $\lesssim$ 1 keV energy, in the XRT data. The combined O17 and O18 samples share 8 events with our work, and the different aim and methodology make these three works somehow complementary. In fact, O17 and O18 investigate the critical low-energy range using a decision tree, whose specific purpose is the identification of the low-energy break. In a complementary way, we fit in parallel a model having a low-energy break (`sync` and its derivations) and a model without it (`band` and its derivations), enabling a more direct comparison with what i known from the literature. On the other hand, we propose also a comparison with physical grounded models (`sync` and `grbcomp`) to shed some light on the GRB physics. In this context, the fundamental role played by the runs test is to ensure the absence of trends on a objective (i.e., not left to human eye) basis. Other technical differences concern the algorithm used to determine the time intervals: we made use of a fully Bayesian-Block driven algorithm (requiring a minimum S/N ratio) to prevent bias effects (Scargle et al. 2013), while O17 and O18 opted for visual inspection. Finally, our fitting functions (`band` and `sync`) present powerlaw high-energy component, smoothly connected with the lower-energy component, while O17 and O18 prefer a high-energy cutoff that present the advantage of a larger flexibility.

The `band`/`sync` comparison suggests that in the vast majority of cases the latter mimics the

former thanks to the additional degree of freedom. In spite of that, there are also cases in which a pure sync provides a good fit, while band needs further component(s) to obtain the same result. Examples are GRB 110102A (Fig. 3.10) and GRB 140108A (Fig. 3.15). Further insight can be obtained studying the distribution of the two low-energy indices α and α_1: Figure 3.23 shows that the band $-\alpha$ distribution peaks around $-\alpha = 1$ (red vertical line), with a long tail extending over $-\alpha = 1.5$, while α_1 presents a broader distribution, centred around $\alpha_1 \approx 0.8$. The large superposition between the two distributions is due to those cases in which sync mimics band. A Kolmogorov-Smirnov (KS) test performed on the two populations rejects the null hypothesis that the two samples are driven by a common distribution (p-value of 1.3×10^{-15}). On the other hand, the KS test performed between the band $E_{\rm p}$ and sync $E_{\rm b2}$ distribution cannot reject the same null hypothesis, as expected given the overall similar spectral shape at high-energy.

Moving to our test on grbcomp, Figure 3.26 shows the distribution of the seed photon and electron temperature kT_s and kT_e, reporting in red those cases in which kT_s had to be fixed to 0.3 keV. Our results are naturally compared with those obtained by F13 on a sample of four GRBs studied in the range 2 keV–2 MeV with *BeppoSAX* data. Figure 3.32 shows that kT_s and kT_e in our sample are systematically lower than those found by F13. We identified two possible reasons:

1. thanks to *Swift*/XRT, our analysis extends to 0.3 keV, i.e. softer than 2 keV of F13;
2. unlike F13, who carried out the analysis on the entire profile, with no constraints on the GRB duration, our sample includes the final part ($t \gtrsim 80$ s, which is the time it takes for *Swift* to slew its narrow field instruments) of the prompt emission of long lasting GRBs.

We find also a strong correlation between band $E_{\rm p}$ and grbcomp kT_e, testified by the Pearson correlation coefficient $\rho = 0.91$ reported in Fig. 3.33. This is in perfect agreement with Titarchuk et al. (2012), that predicts that the peak energy of the νF_ν spectrum strongly correlates with the temperature kT_e of the hot, sub-relativistically-moving shell of plasma that upper-scatters soft photons with temperature kT_s.

3.5.1 Problematic cases

Our sample consists of 93 intervals for which band, sync and grbcomp can be tested. This number excludes intervals for which XRT data are dominant and simple powerlaws provide a good fit. We can estimate the probability of type-I errors for $k = 16$ spectra out of $n = 93$ trials using a binomial distribution, under the null hypothesis that for each spectrum there is at least one model that works. Estimating the probability of a type-I error (i.e., that none of the models can fit a given spectrum, even accounting for the possibility of adding extra components) is complex, due to the fact that the models are not wildly different from each other and so a non-zero correlation is present. The only way to address it would a Monte Carlo simulation to generate a sample of 93 synthetic spectra and carry out the same analysis as for the real sample, which is beyond the aim of our work. However, a rough estimation can be obtained as follows. Given the $5\% - 95\%$ thresholds we use for two independent tests (χ^2 and runs), we expect a $p_{\rm single} = 1 - 0.9^2 = 0.19$ probability of a type-I error in at least one test for a given model. The problem is now to combine the three cases. We could proceed considering an intermediate situation between the case in which the three models are completely uncorrelated ($p = p_{\rm single}^3 = 6.86 \times 10^{-3}$) and that in which they are completely correlated ($p = p_{\rm single} = 0.19$): thus, a reasonable trade-off would be given by $p \simeq p_{\rm single}^2 = 0.0361$. Under this assumption for the single spectrum case, the combined probability of having ≥ 16 problematic cases out of 93 is 2.2×10^{-7}, which suggests that these spectra are truly problematic for the three considered models and are not the result of a fluctuation.

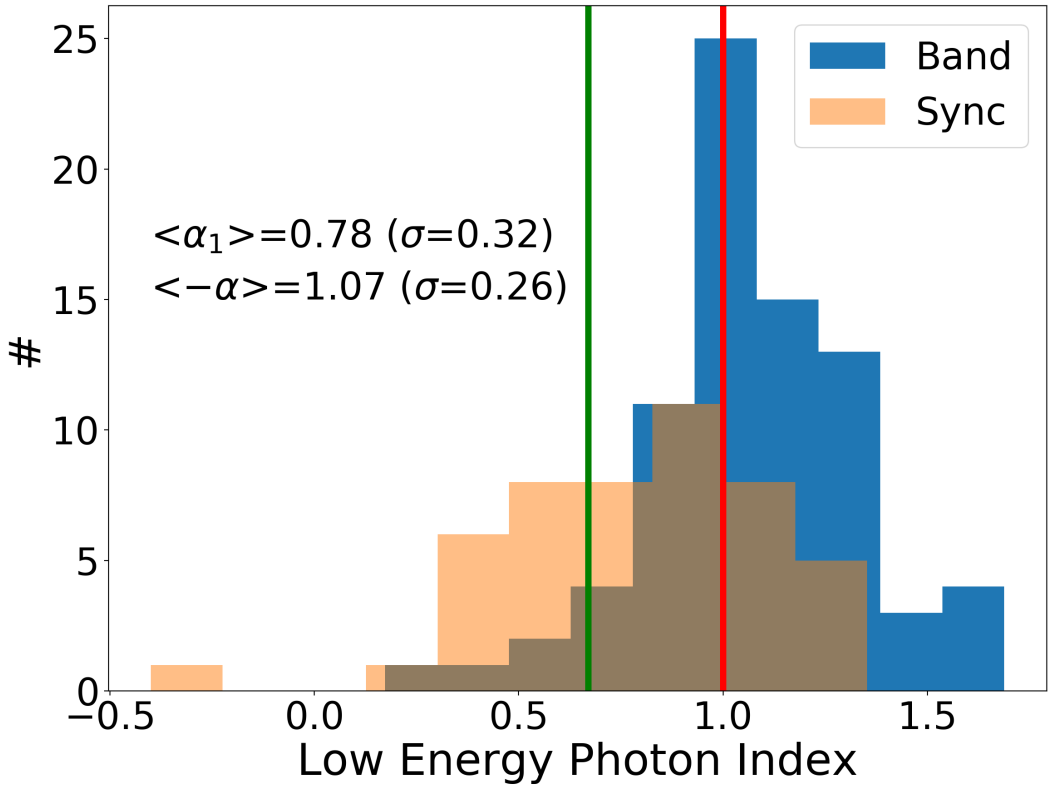

Figure 3.23: Distribution of Band $-\alpha$ indeces (blue), together with its typical value reported in literature $-\alpha = 1$ (in red), compared with the distribution of `sync` α_1 (orange), together with the value $\alpha_1 = 0.67$ expected from theory (in green).

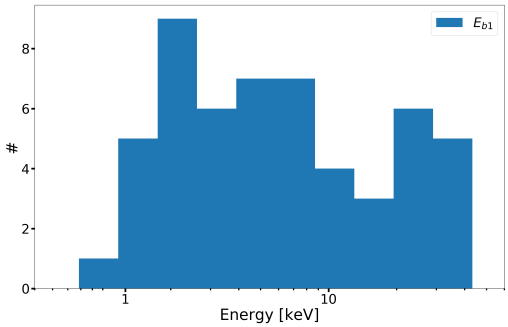

Figure 3.24: Distribution of $E_{\rm b1}$ from the `sync`.

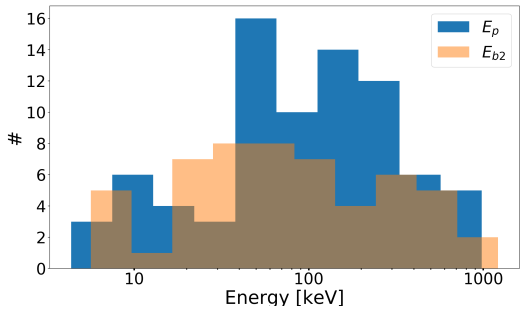

Figure 3.25: Distribution of $E_{\rm p}$ energies from the `band` (in blue) and of $E_{\rm b2}$ from the `sync` (in orange).

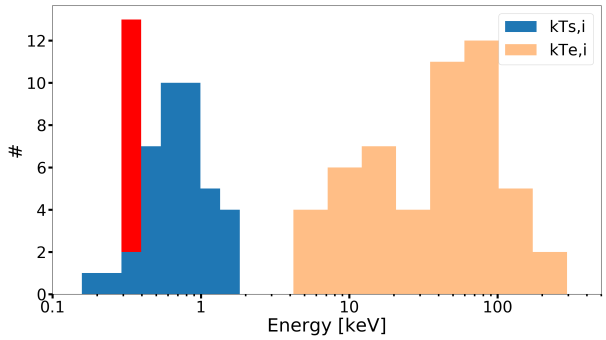

Figure 3.26: Distribution of kT_s and kT_e of the `grbcomp` model. The red bin includes the cases in which kTs was fixed to 0.3 keV.

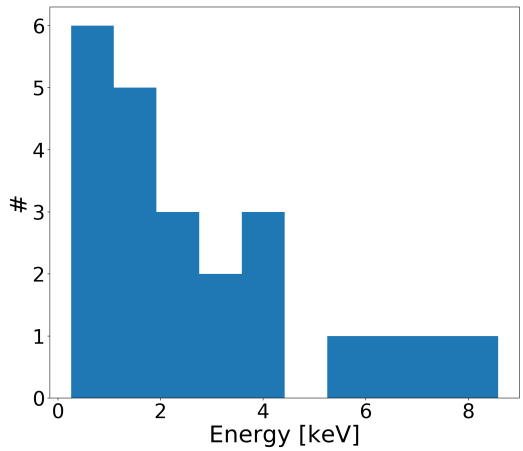

Figure 3.27: BB temperatures from BB+Band fits.

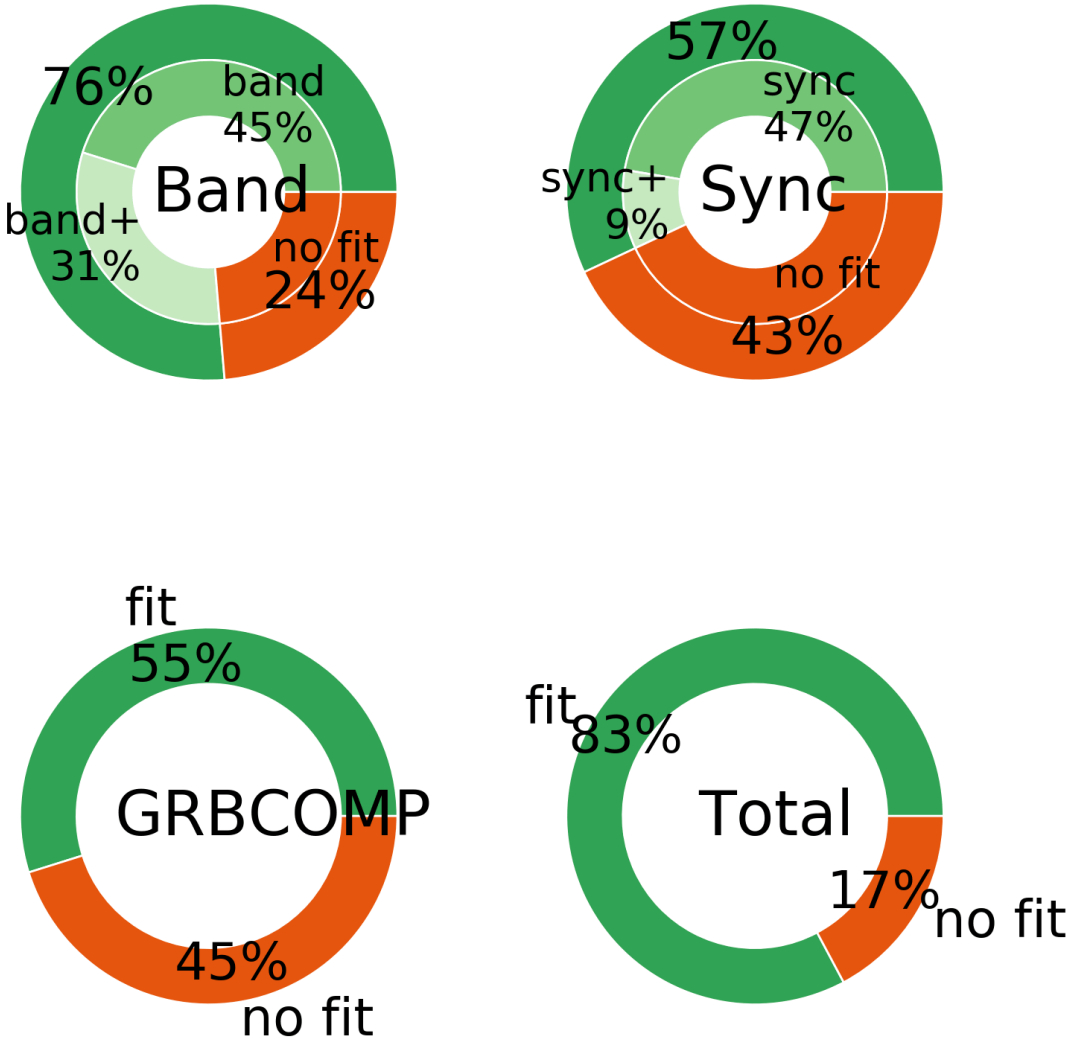

Figure 3.28: Pie charts representing the rate of success of `band` (upper left) and `sync` (upper right) and `grbcomp` (lower left) models. In the first two cases, we report also the percentages of good fits obtained with the model alone and with the addition of the components described in the text. The lower right panel shows the rate of successful cases, where for each given spectrum there was at least one successful model.

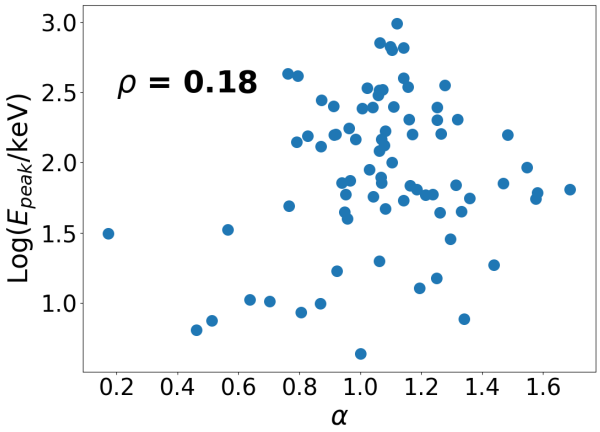

Figure 3.29: band α vs $E_{\rm p}$.

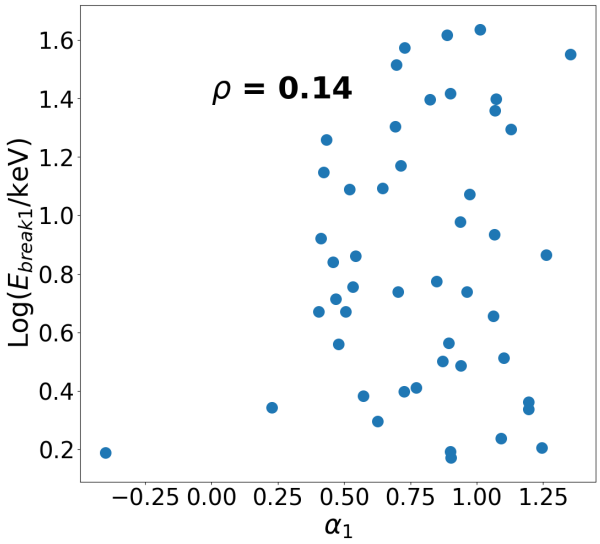

Figure 3.30: synch α_1 vs $E_{\rm b1}$.

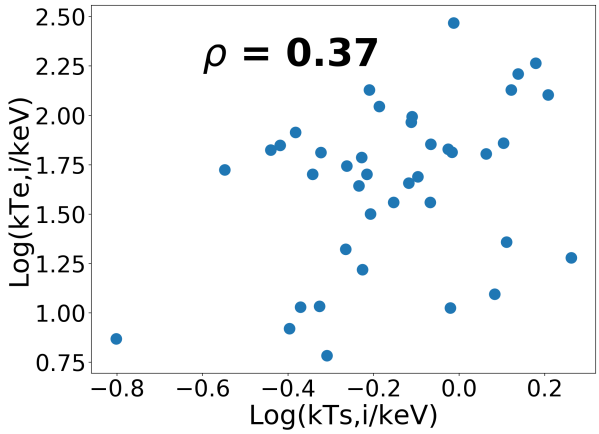

Figure 3.31: grbcomp kT_s vs kT_e.

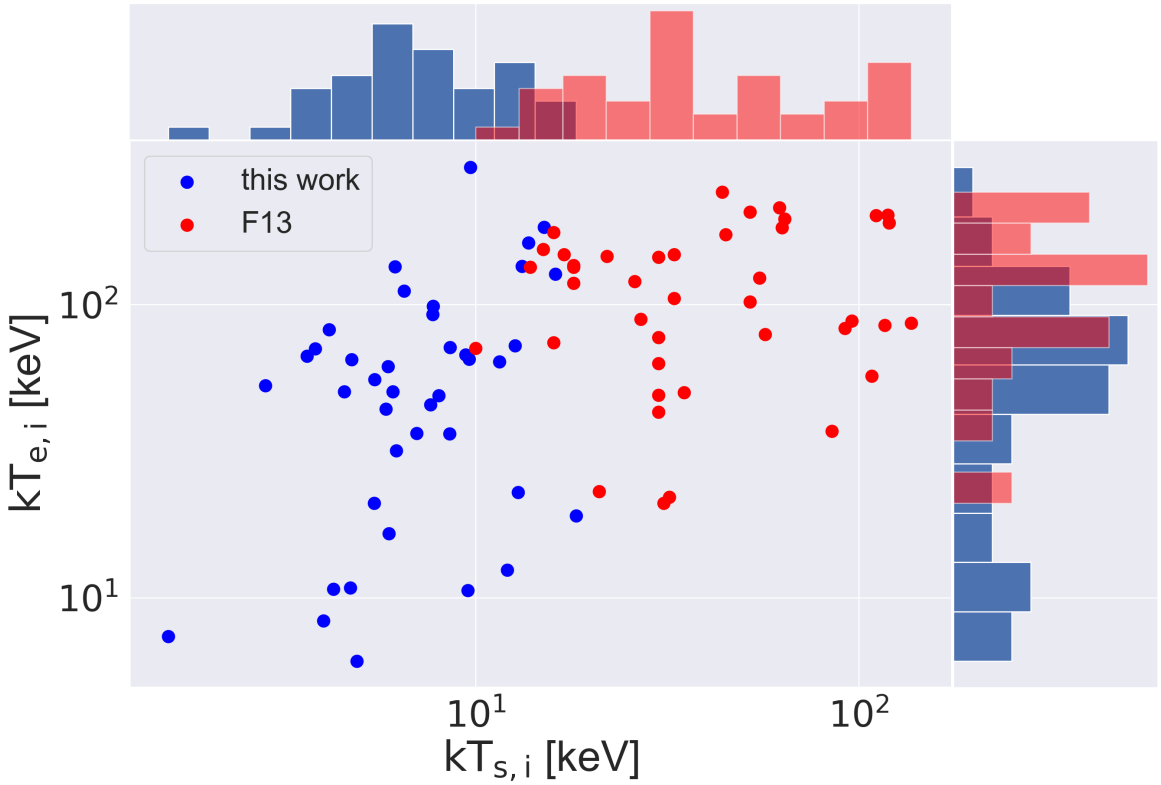

Figure 3.32: `grbcomp` $kT_{s,i}$ vs $kT_{e,i}$ as obtained in this work (blue) and in Frontera et al. (2013, red).

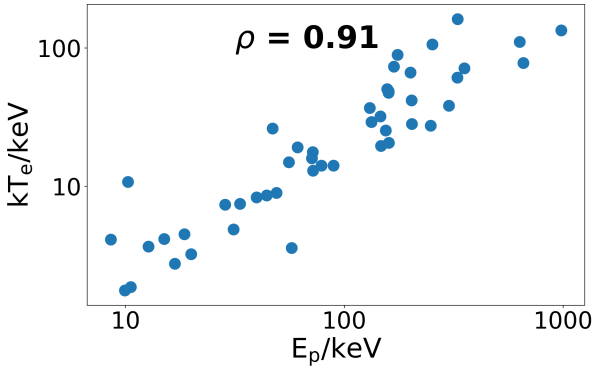

Figure 3.33: `band` $E_{\rm p}$ vs `grbcomp` kT_e.

3.6 Conclusions

We performed a broadband (0.3–3 $\times$ 10^4 keV) time-resolved spectra analysis of the prompt emission of 17 very fluent GRBs. We exploited the large bandpass provided by the combination of *Swift* (BAT+XRT) and *Fermi*/GBM data to test three models: the Band function (`band`), a double broken powerlaw representing a synchrotron model (`sync`), and the Comptonisation model proposed by Titarchuk et al. (2012, `grbcomp`). Given the time required to XRT to start data acquisition, our work focuses on bursts with a prolonged (an often structured) prompt emission, typically $\gtrsim$ 80 s. We made use of the Bayesian blocks algorithm to reduce the bias effect that can be introduced with the selection of the time bins. We applied the runs test to systematically check the presence of trends in the residuals, that cannot be identified using the χ^2 test alone. The models were tested in parallel in order to track and compare the time evolution of their parameters in every time slice.

The broadband analysis was feasible for 93 spectra. In almost half of cases the `sync` could not provide an acceptable description, even when we tried adding further components. At the same time, the Band function works well in the majority of cases, even if the addition of extra components is required as often as $\sim$ 40% of successful cases. Interestingly, we found evidence for a Comptonisation signature in more than $\sim$ 54% of cases. However, this fraction should be considered as a lower limit, since our analysis does not consider cases of partial Comptonisation, i.e. cases in which some seed photons would escape any up-scattering.

Furthermore, in comparison with the previous results obtained by F13 for a sample observed with *BeppoSAX*, our work explores an unprecedented soft energy range down to 0.3 keV at the cost of missing the earliest part of the prompt γ–ray emission (typically the first 70–100 s, that is the time it takes for *Swift* to repoint its narrow field instruments). This implies that our spectra were obtained when both seed photons and electrons temperatures are expected to be lower with respect to the earlier emission.

In 16 cases, no model gave a good description of the spectra, despite the further attempt of using additional components. Such number can hardly be explained in terms of type I errors, even if an exact estimate is not straightforward and lies beyond the aim of this paper. These problematic intervals are characterised by an X–ray lightcurve that looks significantly different from the simultaneous γ–ray one. In these cases we observe either a delayed peak or a much broader temporal structure of the softer profile with respect to the harder one. Furthermore, this is observed also when the X–ray data are ignored, suggesting that the γ–ray data themselves present some additional or unusual features that cannot be described with any of the considered models.

Fitting results

GRB	interval	BB_{temp} keV	$BB_{temp_{sx}}$ keV	$BB_{temp_{dx}}$ keV	BB_{norm}	$BB_{norm_{sx}}$	$BB_{norm_{dx}}$	γ	γ_{sx}	γ_{dx}	norm	$norm_{sx}$	$norm_{dx}$	χ^2	runs	dof
110102A	1	–	–	–	–	–	–	1.68	-0.04	0.05	0.51	-0.02	0.08	120.77	0.01	120
110102A	2	2.89	-0.29	0.32	1.77e-01	-4.72e-02	4.81e-02	1.30	-0.03	0.03	0.88	-0.12	0.10	63.19	-1.06	63
140108A	1	–	–	–	–	–	–	1.69	-0.11	0.06	2.33	-0.80	0.25	20.68	-0.85	20
140108A	8	–	–	–	–	–	–	1.76	-0.07	0.05	3.35	-0.80	0.57	55.31	-0.47	55
140108A	9	0.19	-0.04	0.04	6.83e-02	-2.45e-02	6.29e-02	1.86	-0.10	0.06	1.32	-0.39	0.16	65.93	-0.52	65
140512A	15	–	–	–	–	–	–	1.90	-0.11	0.11	0.44	-0.09	0.03	29.71	0.27	29
151006A	3	–	–	–	–	–	–	1.53	-0.04	0.04	0.41	-0.07	0.08	144.59	0.81	144
151006A	4	–	–	–	–	–	–	1.39	-0.04	0.05	0.06	-0.00	0.01	89.96	-1.45	89

Table 3.2: Powerlaw table: for typographic reasons, here we report only those intervals for which this model provided a good fit.

GRB	interval	wabs	$wabs_{sx}$	$wabs_{dx}$	BB_{temp}	$BB_{temp_{sx}}$	$BB_{temp_{dx}}$	BB_{norm}	$BB_{norm_{sx}}$	$BB_{norm_{dx}}$	α	α_{sx}	α_{dx}	E_p	$E_{p_{sx}}$	$E_{p_{dx}}$	norm	$norm_{sx}$	$norm_{dx}$	χ^2	runs	dof
		1×10^{-22} cm^{-2}	1×10^{-22} cm^{-2}	1×10^{-22} cm^{-2}	keV	keV	keV							keV	keV	keV	keV	keV	keV			
080810	1	–	–	–	–	–	–	–	–	–	-1.06	-0.06	0.06	19.91	-2.28	2.77	0.00	-0.00	0.00	93.97	-0.49	93
090926B	1	–	–	–	0.29	-0.01	0.01	7.06e-03	-8.12e-04	1.83e-03	-1.26	-0.14	0.15	44.02	-14.69	25.92	0.00	-0.00	0.00	146.17	1.65	145
100619A	1	–	–	–	–	–	–	–	–	–	-0.70	-0.29	0.27	10.25	-3.06	5.57	0.19	-0.19	0.63	70.11	0.46	67
100619A	2	–	–	–	1.94	-0.30	0.24	3.59e-01	-6.90e-02	1.20e-01	-1.16	-0.08	0.05	68.54	-4.96	5.45	0.02	-0.00	0.00	186.46	-1.46	194
100619A	3	–	–	–	–	–	–	–	–	–	–	–	–	–	–	–	–	–	–	–	–	–
100728A	1	–	–	–	–	–	–	–	–	–	–	–	–	–	–	–	–	–	–	–	–	–
100728A	2	–	–	–	–	–	–	–	–	–	-1.03	-0.07	0.04	89.31	-8.92	11.01	0.01	-0.00	0.00	108.16	0.80	107
100728A	3	–	–	–	–	–	–	–	–	–	-0.92	-0.11	0.12	16.81	-2.43	2.38	0.02	-0.01	0.02	72.35	-0.16	64
100728A	4	–	–	–	–	–	–	–	–	–	-1.26	-0.04	0.02	159.63	-21.67	30.28	0.00	-0.00	0.00	159.46	-0.07	168
100728A	5	–	–	–	–	–	–	–	–	–	-1.04	-0.02	0.02	247.72	-24.12	29.63	0.01	-0.00	0.00	180.63	0.00	191
100728A	6	–	–	–	–	–	–	–	–	–	-1.07	-0.03	0.03	78.57	-5.77	7.37	0.01	-0.00	0.00	164.51	0.49	152
100728A	7	–	–	–	–	–	–	–	–	–	-0.83	-0.07	0.06	154.60	-15.34	19.46	0.03	-0.00	0.00	131.64	-1.36	152
100728A	8	–	–	–	–	–	–	–	–	–	-1.06	-0.02	0.02	300.76	-28.53	33.19	0.01	-0.00	0.00	200.55	-0.34	224
100728A	9	–	–	–	–	–	–	–	–	–	-0.98	-0.09	0.08	147.03	-22.95	34.17	0.01	-0.00	0.00	72.84	0.61	84
100728A	10	0.19	-0.14	0.17	–	–	–	–	–	–	-1.07	-0.10	0.06	71.59	-13.00	19.40	0.01	-0.00	0.00	48.51	-1.23	55
100728A	11	–	–	–	–	–	–	–	–	–	-1.33	-0.05	0.04	44.90	-5.64	8.98	0.00	-0.00	0.00	96.74	0.98	128
100728A	12	–	–	–	–	–	–	–	–	–	-1.47	-0.03	0.03	71.04	-18.30	32.26	0.00	-0.00	0.00	159.60	0.05	163
100728A	13	–	–	–	–	–	–	–	–	–	-1.25	-0.08	0.09	15.02	-1.51	4.26	0.00	-0.00	0.00	91.30	-0.10	72
100728A	14	–	–	–	–	–	–	–	–	–	-1.08	-0.10	0.11	46.98	-14.02	17.34	0.00	-0.00	0.00	58.01	0.11	60
100728A	15	–	–	–	–	–	–	–	–	–	-0.81	-0.09	0.10	8.57	-0.93	1.08	0.03	-0.01	0.02	115.01	0.47	118
100814A	1	–	–	–	–	–	–	–	–	–	-0.95	-0.03	0.03	44.21	-5.52	4.13	0.00	-0.00	0.00	168.93	-1.29	146
100814A	2	–	–	–	–	–	–	–	–	–	-0.94	-0.05	0.03	71.83	-6.54	7.60	0.01	-0.00	0.00	127.11	0.95	115
100814A	3	–	–	–	0.34	-0.04	0.06	4.09e-03	-9.82e-04	1.12e-03	-1.58	-0.05	0.05	54.97	-21.10	44.26	0.00	-0.00	0.00	227.31	-0.17	200
100906A	1	–	–	–	–	–	–	–	–	–	-1.44	-0.08	0.09	18.59	-7.14	4.49	0.00	-0.00	0.00	88.62	-0.86	82
100906A	2	–	–	–	–	–	–	–	–	–	–	–	–	–	–	–	–	–	–	–	–	–
100906A	3	–	–	–	0.82	-0.07	0.09	2.88e-01	-3.02e-02	4.93e-02	-1.00	0.00	0.00	4.35	-0.90	1.72	0.05	-0.02	0.01	117.10	-1.38	99
110102A	1	–	–	–	–	–	–	–	–	–	–	–	–	–	–	–	–	–	–	–	–	–
110102A	2	–	–	–	–	–	–	–	–	–	–	–	–	–	–	–	–	–	–	–	–	–
110102A	3	0.42	-0.12	0.12	–	–	–	–	–	–	-1.12	-0.02	0.05	978.90	-305.35	631.40	0.01	-0.00	0.00	112.25	-1.33	122
110102A	4	–	–	–	–	–	–	–	–	–	-1.10	-0.02	0.03	632.76	-101.99	113.79	0.01	-0.00	0.00	235.23	-0.58	217
110102A	5	–	–	–	–	–	–	–	–	–	-1.06	-0.02	0.03	328.20	-33.66	35.19	0.02	-0.00	0.00	217.10	1.58	230
110102A	6	0.60	-0.10	0.10	–	–	–	–	–	–	-1.10	-0.02	0.03	666.12	-77.34	69.70	0.03	-0.00	0.00	318.71	-1.25	297
110102A	6	–	–	–	6.08	-0.48	0.53	8.18e-01	-7.72e-02	7.81e-02	-0.76	-0.02	0.02	430.76	-29.62	33.68	0.04	-0.00	0.00	310.99	-1.13	296
110102A	7	–	–	–	–	–	–	–	–	–	–	–	–	–	–	–	–	–	–	–	–	–
110102A	8	–	–	–	–	–	–	–	–	–	–	–	–	–	–	–	–	–	–	–	–	–
110102A	9	0.70	-0.18	0.19	–	–	–	–	–	–	-1.48	-0.13	0.16	156.92	-53.64	169.11	0.00	-0.00	0.00	109.75	-0.52	110
110102A	9	–	–	–	3.11	-0.47	0.20	2.99e-01	-5.54e-02	5.78e-02	-1.06	-0.07	0.05	121.33	-23.11	34.81	0.01	-0.00	0.00	107.89	0.38	109
110102A	10	–	–	–	1.26	-0.14	0.23	1.10e-01	-4.21e-02	2.53e-02	-1.19	-0.07	0.09	64.38	-10.28	13.14	0.01	-0.00	0.00	112.06	-0.37	99
110102A	10	0.34	-0.09	0.16	–	–	–	–	–	–	-1.31	-0.16	0.04	68.93	-12.54	20.58	0.00	-0.00	0.00	114.97	-0.26	100
110102A	11	–	–	–	–	–	–	–	–	–	-1.30	-0.05	0.05	28.52	-7.11	4.33	0.00	-0.00	0.00	109.97	0.17	106
110102A	12	–	–	–	1.22	-0.10	0.13	1.20e-01	-5.25e-02	1.42e-02	-1.36	-0.05	0.12	55.82	-10.08	15.05	0.00	-0.00	0.00	136.32	-1.01	136
110102A	13	–	–	–	–	–	–	–	–	–	–	–	–	–	–	–	–	–	–	–	–	–
110102A	14	–	–	–	–	–	–	–	–	–	–	–	–	–	–	–	–	–	–	–	–	–
110102A	15	–	–	–	1.14	-0.16	0.15	1.45e-01	-7.79e-02	1.40e-01	-1.21	-0.16	0.13	58.56	-9.12	14.72	0.01	-0.00	0.00	145.19	-0.21	124
110102A	16	–	–	–	–	–	–	–	–	–	–	–	–	–	–	–	–	–	–	–	–	–
110102A	17	–	–	–	–	–	–	–	–	–	–	–	–	–	–	–	–	–	–	–	–	–
130528A	1	–	–	–	–	–	–	–	–	–	-0.64	-0.09	0.09	10.57	-0.71	0.65	0.03	-0.01	0.02	99.69	-0.55	95
130609B	1	–	–	–	–	–	–	–	–	–	-1.34	-0.07	0.07	7.65	-1.39	2.72	0.00	-0.00	0.00	207.04	0.03	223
130609B	2	0.39	-0.08	0.10	–	–	–	–	–	–	-1.58	-0.05	0.05	61.08	-11.84	18.65	0.00	-0.00	0.00	157.49	-1.31	136
130609B	3	0.15	-0.02	0.03	–	–	–	–	–	–	-1.69	-0.03	0.03	64.11	-13.32	20.23	0.00	-0.00	0.00	222.64	-0.34	209
130609B	4	–	–	–	–	–	–	–	–	–	–	–	–	–	–	–	–	–	–	–	–	–
140108A	1	–	–	–	–	–	–	–	–	–	–	–	–	–	–	–	–	–	–	–	–	–
140108A	2	–	–	–	–	–	–	–	–	–	-1.14	-0.05	0.06	400.79	-82.27	120.28	0.01	-0.00	0.00	181.54	-1.34	204
140108A	3	–	–	–	–	–	–	–	–	–	-0.92	-0.04	0.03	159.09	-17.43	20.86	0.02	-0.00	0.00	179.50	-0.75	166
140108A	4	–	–	–	–	–	–	–	–	–	-1.02	-0.05	0.05	339.00	-47.73	60.33	0.03	-0.00	0.00	236.26	-1.03	248
140108A	5	–	–	–	3.74	-0.54	0.72	3.46e-01	-7.30e-02	7.49e-02	-1.01	-0.04	0.04	243.77	-45.54	68.03	0.02	-0.00	0.00	185.81	-0.28	179
140108A	5	1.20	-0.22	0.23	–	–	–	–	–	–	-1.28	-0.06	0.07	353.84	-92.76	154.00	0.01	-0.00	0.00	166.76	0.08	180
140108A	6	–	–	–	–	–	–	–	–	–	-1.25	-0.04	0.03	200.26	-45.34	95.77	0.01	-0.00	0.00	145.58	0.17	120
140108A	7	–	–	–	–	–	–	–	–	–	-1.32	-0.10	0.06	203.11	-67.39	143.59	0.00	-0.00	0.00	80.05	0.57	91
140108A	8	–	–	–	–	–	–	–	–	–	–	–	–	–	–	–	–	–	–	–	–	–
140108A	9	–	–	–	–	–	–	–	–	–	–	–	–	–	–	–	–	–	–	–	–	–
140323A	1	–	–	–	–	–	–	–	–	–	-0.96	-0.04	0.04	39.66	-2.90	3.17	0.02	-0.00	0.00	143.21	0.27	144
140323A	2	–	–	–	–	–	–	–	–	–	-0.46	-0.14	0.28	6.43	-1.05	0.68	0.21	-0.10	0.62	55.20	1.45	74
140512A	1	0.63	-0.20	0.22	–	–	–	–	–	–	-1.16	-0.15	0.14	202.78	-59.49	144.54	0.01	-0.00	0.00	64.63	0.84	81
140512A	1	–	–	–	1.97	-0.53	1.59	1.52e-01	-5.65e-02	6.72e-02	-0.91	-0.08	0.11	156.77	-36.62	56.18	0.01	-0.00	0.00	69.22	-0.57	80
140512A	2	–	–	–	3.72	-0.75	0.80	1.65e-01	-6.04e-02	5.11e-02	-0.87	-0.05	0.06	278.07	-82.60	109.73	0.01	-0.00	0.00	97.83	-0.96	103
140512A	3	0.69	-0.18	0.20	–	–	–	–	–	–	-1.14	-0.03	0.05	657.68	-152.75	207.05	0.01	-0.00	0.00	161.66	-0.74	167
140512A	3	–	–	–	6.96	-0.99	1.11	2.18e-01	-3.92e-02	4.03e-02	-0.80	-0.04	0.04	414.22	-66.06	83.28	0.01	-0.00	0.00	163.38	-0.48	166
140512A	4	–	–	–	–	–	–	–	–	–	–	–	–	–	–	–	–	–	–	–	–	–
140512A	5	0.85	-0.18	0.19	–	–	–	–	–	–	-1.11	-0.10	0.10	249.95	-64.88	105.92	0.01	-0.00	0.00	150.74	-1.41	162
140512A	6	–	–	–	–	–	–	–	–	–	-0.87	-0.09	0.09	130.71	-14.55	19.40	0.01	-0.00	0.00	144.25	-1.12	159
140512A	7	–	–	–	–	–	–	–	–	–	-0.91	-0.06	0.08	252.40	-45.73	61.83	0.02	-0.00	0.00	212.43	-1.28	195
140512A	8	–	–	–	–	–	–	–	–	–	–	–	–	–	–	–	–	–	–	–	–	–
140512A	9	–	–	–	–	–	–	–	–	–	–	–	–	–	–	–	–	–	–	–	–	–
140512A	10	–	–	–	3.08	-0.44	0.36	2.80e-01	-7.07e-02	6.51e-02	-0.79	-0.05	0.06	140.54	-22.83	28.92	0.02	-0.00	0.00	156.45	-0.96	149
140512A	10	0.64	-0.15	0.21	–	–	–	–	–	–	-1.08	-0.13	0.05	168.27	-28.33	80.65	0.01	-0.00	0.00	154.37	0.33	150
140512A	11	–	–	–	–	–	–	–	–	–	-1.07	-0.06	0.03	146.06	-18.48	26.18	0.01	-0.00	0.00	124.61	0.86	139
140512A	12	–	–	–	–	–	–	–	–	–	-1.08	-0.07	0.07	132.75	-19.38	27.25	0.01	-0.00	0.00	135.24	-1.29	111
140512A	13	–	–	–	–	–	–	–	–	–	-1.17	-0.06	0.06	159.27	-27.83	41.28	0.00	-0.00	0.00	151.14	-1.20	136
140512A	14	–	–	–	–	–	–	–	–	–	–	–	–	–	–	–	–	–	–	–	–	–
140512A	15	–	–	–	–	–	–	–	–	–	–	–	–	–	–	–	–	–	–	–	–	–
150430A	1	–	–	–	0.37	-0.02	0.03	2.52e-02	-5.02e-03	3.90e-03	-1.14	-0.20	0.33	53.49	-21.24	47.28	0.00	-0.00	0.00	48.39	-0.07	42
151006A	1	–	–	–	0.26	-0.16	0.19	4.40e-03	-4.40e-03	4.79e-03	-1.10	-0.21	0.23	100.50	-46.15	143.07	0.00	-0.00	0.00	19.56	-0.56	17
151006A	2	–	–	–	0.47	-0.02	0.02	1.48e-02	-2.22e-03	2.21e-03	-0.95	-0.17	0.10	59.41	-9.20	14.61	0.00	0.00	0.00	196.10	-1.45	181
151006A	3	–	–	–	–	–	–	–	–	–	–	–	–	–	–	–	–	–	–	–	–	–
151006A	4	–	–	–	–	–	–	–	–	–	–	–	–	–	–	–	–	–	–	–	–	–
151027A	1	–	–	–	–	–	–	–	–	–	-1.25	-0.02	0.02	246.58	-54.98	89.29	0.00	-0.00	0.00	149.58	-1.39	144
151027A	2	–	–	–	3.66	-0.36	0.31	2.95e-01	-4.61e-02	4.66e-02	-1.06	-0.03	0.03	711.84	-198.98	6197.63	0.01	-0.00	0.00	126.32	-0.25	142
151027A	2	0.35	-0.11	0.10	–	–	–	–	–	–	-1.07	-0.03	0.03	329.27	-82.27	128.99	0.01	-0.00	0.00	170.97	-0.91	144
151027A	3	–	–	–	1.77	-0.12	0.17	3.97e-01	-5.81e-02	5.29e-02	-1.16	-0.03	0.03	345.47	-45.91	63.65	0.01	-0.00	0.00	245.19	-1.49	237
151027A	4	–	–	–	2.73	-0.44	0.17	4.92e-01	-6.17e-02	1.22e-01	-0.96	-0.09	0.04	174.72	-30.71	45.72	0.01	-0.00	0.00	160.72	-1.43	163
151027A	5	–	–	–	–	–	–	–	–	–	–	–	–	–	–	–	–	–	–	–	–	–
151027A	6	–	–	–	1.10	-0.07	0.08	7.76e-01	-1.52e-01	7.01e-02	-1.55	-0.07	0.09	92.76	-22.25	45.10	0.00	-0.00	0.00	88.88	-0.68	105
161117A	1	–	–	–	–	–	–	–	–	–	-0.17	-0.13	0.13	31.12	-3.41	3.47	0.10	-0.03	0.05	56.74	-0.24	59
161117A	2	–	–	–	5.78	-0.30	0.37	2.36e-01	-3.30e-02	3.12e-02	-1.04	-0.13	0.13	57.36	-13.76	26.29	0.00	-0.00	0.00	107.53	0.92	85
161117A	3	–	–	–	–	–	–	–	–	–	-0.57	-0.06	0.07	33.36	-2.77	2.94	0.05	-0.01	0.01	111.73	-0.83	100
161117A	4	–	–	–	–	–	–	–	–	–	–	–	–	–	–	–	–	–	–	–	–	–
161117A	5	–	–	–	–	–	–	–	–	–	–	–	–	–	–	–	–	–	–	–	–	–
161117A	6	–	–	–	–	–	–	–	–	–	-0.77	-0.03	0.04	48.93	-2.28	1.22	0.07	-0.01	0.01	145.78	-1.19	148
161117A	7	–	–	–	–	–	–	–	–	–	–	–	–	–	–	–	–	–	–	–	–	–
161117A	8	–	–	–	–	–	–	–	–	–	–	–	–	–	–	–	–	–	–	–	–	–
161117A	9	–	–	–	–	–	–	–	–	–	–	–	–	–	–	–	–	–	–	–	–	–
161117A	10	–	–	–	8.58	-0.37	0.38	3.92e-01	-4.38e-02	2.17e-02	-0.51	-0.13	0.19	7.45	-1.30	1.05	0.38	-0.20	0.70	149.76	-0.75	140
161117A	11	–	–	–	–	–	–	–	–	–	-0.87	-0.14	0.15	9.94	-1.80	1.40	0.06	-0.03	0.06	68.39	0.56	52
161117A	12	–	–	–	–	–	–	–	–	–	–	–	–	–	–	–	–	–	–	–	–	–
161117A	13	–	–	–	–	–	–	–	–	–	–	–	–	–	–	–	–	–	–	–	–	–
170405A	1	–	–	–	–	–	–	–	–	–	-1.24	-0.03	0.03	59.55	-15.83	15.66	0.00	-0.00	0.00	148.92	-0.99	149
170405A	2	–	–	–	–	–	–	–	–	–	-0.97	-0.05	0.05	74.29	-10.72	13.55	0.01	-0.00	0.00	91.31	-0.27	89
170405A	3	–	–	–	–	–	–	–	–	–	-1.19	-0.11	0.14	12.72	-3.96	12.87	0.00	-0.00	0.00	24.92	-0.13	32

Table 3.3: Band function table

GRB	interval	BB_{temp} keV	$BB_{temp_{sx}}$ keV	$BB_{temp_{dx}}$ keV	BB_{norm} keV	$BB_{norm_{sx}}$ keV	$BB_{norm_{dx}}$ keV	α_1	$\alpha_{1_{sx}}$	$\alpha_{1_{dx}}$	E_{b1} keV	$E_{b1_{sx}}$ keV	$E_{b1_{dx}}$ keV	E_{b2} keV	$E_{b2_{sx}}$ keV	$E_{b2_{dx}}$ keV	norm	$norm_{sx}$	$norm_{dx}$	χ^2	runs	dof
080810	1	–	–	–	–	–	–	1.10	-0.07	0.07	3.26	-0.54	2.85	20.89	-5.44	3.22	0.53	-0.02	0.02	94.71	-0.56	92
090926B	1	0.28	-0.01	0.01	5.32e-03	-3.51e-04	5.47e-04	0.67	0.00	0.00	0.78	-0.17	0.16	26.47	-3.81	5.80	0.23	-0.03	0.05	171.15	0.40	145
100619A	1	–	–	–	–	–	–	0.67	0.00	0.00	2.46	-0.31	0.38	7.98	-1.62	4.72	4.93	-1.61	1.11	69.99	0.69	67
100728A	2	–	–	–	–	–	–	0.57	-0.29	0.51	2.41	-0.25	3.02	80.83	-7.53	9.21	2.44	-0.40	0.55	112.87	-0.02	106
100728A	3	–	–	–	–	–	–	0.94	-0.32	0.12	3.07	-0.78	0.55	18.46	-2.27	2.13	1.54	-0.19	0.15	72.73	0.14	63
100728A	4	–	–	–	–	–	–	0.90	-1.33	0.21	1.56	-0.49	0.37	101.75	-9.58	12.91	2.25	-0.18	0.37	163.38	-0.38	167
100728A	5	–	–	–	–	–	–	–	–	–	–	–	–	–	–	–	–	–	–	–	–	–
100728A	6	–	–	–	–	–	–	0.96	-0.08	0.09	5.49	-1.66	3.39	71.20	-5.59	5.56	1.92	-0.53	0.27	164.27	0.80	151
100728A	7	–	–	–	–	–	–	–	–	–	–	–	–	–	–	–	–	–	–	–	–	–
100728A	8	–	–	–	–	–	–	–	–	–	–	–	–	–	–	–	–	–	–	–	–	–
100728A	9	–	–	–	–	–	–	–	–	–	–	–	–	–	–	–	–	–	–	–	–	–
100728A	10	–	–	–	–	–	–	-0.40	-1.22	0.96	1.54	-0.14	0.42	63.25	-8.22	13.81	1.35	-0.40	0.42	44.31	-0.12	54
100728A	11	–	–	–	–	–	–	–	–	–	–	–	–	–	–	–	–	–	–	–	–	–
100728A	12	–	–	–	–	–	–	–	–	–	–	–	–	–	–	–	–	–	–	–	–	–
100728A	13	–	–	–	–	–	–	1.19	-0.19	0.12	2.17	-0.45	0.49	12.43	-1.41	2.98	0.99	-0.17	0.07	88.34	-0.10	71
100728A	14	–	–	–	–	–	–	1.06	-0.12	0.12	4.53	-1.01	7.68	45.73	-8.78	21.85	0.81	-0.23	0.16	57.47	-1.26	59
100728A	15	–	–	–	–	–	–	0.63	-0.14	0.18	1.97	-0.12	0.29	9.05	-0.93	19.07	1.03	-0.46	0.12	102.63	-0.63	117
100814A	1	–	–	–	–	–	–	0.77	-0.08	0.08	2.57	-0.25	0.38	36.58	-3.03	4.20	0.48	-0.04	0.04	155.91	0.29	145
100814A	2	–	–	–	–	–	–	0.97	-0.05	0.05	11.82	-5.66	6.34	62.88	-5.28	8.04	0.65	-0.14	0.28	125.23	0.83	114
110102A	4	–	–	–	–	–	–	0.64	-0.09	0.08	12.38	-8.12	3.53	541.25	-82.82	136.06	0.73	-0.07	0.54	199.63	0.28	215
110102A	5	–	–	–	–	–	–	0.71	-0.08	0.09	14.77	-2.85	4.60	268.30	-31.46	39.82	1.10	-0.19	0.29	195.78	1.75	228
110102A	7	–	–	–	–	–	–	0.52	-0.06	0.06	12.29	-1.67	1.53	484.48	-118.39	105.94	1.14	-0.08	0.14	251.07	-0.60	251
110102A	9	–	–	–	–	–	–	0.48	-0.17	0.14	3.63	-0.49	0.77	99.77	-12.61	34.60	1.11	-0.15	0.18	107.62	0.27	110
110102A	10	–	–	–	–	–	–	0.23	-0.26	0.21	2.20	-0.19	0.25	50.16	-5.99	18.23	0.94	-0.12	0.13	112.27	-0.50	100
110102A	11	–	–	–	–	–	–	1.09	-0.18	0.15	1.73	-0.27	0.57	26.59	-4.05	3.33	1.11	-0.05	0.10	105.26	-0.62	105
110102A	12	–	–	–	–	–	–	0.89	-0.07	0.06	3.67	-0.28	0.27	95.34	-37.14	310.13	1.71	-0.32	0.23	127.02	-1.03	136
110102A	13	–	–	–	–	–	–	–	–	–	–	–	–	–	–	–	–	–	–	–	–	–
110102A	14	–	–	–	–	–	–	0.70	-0.08	0.08	5.49	-0.55	0.56	114.22	-13.48	65.29	1.80	-0.18	0.32	164.91	-0.64	168
110102A	15	1.64	-0.45	0.64	6.09e-02	-2.38e-02	1.06e-01	0.66	0.00	0.00	2.08	-0.41	0.31	46.67	-3.97	4.96	1.76	-0.16	0.54	147.56	-0.53	123
130528A	1	–	–	–	–	–	–	0.67	0.00	0.00	2.95	-0.23	0.27	9.07	-1.44	1.46	0.49	-0.02	0.10	112.76	-1.21	95
140108A	2	–	–	–	–	–	–	1.01	-0.03	0.07	43.29	-4.74	6.39	478.05	-128.13	268.51	1.01	-0.07	0.27	175.01	-0.88	203
140108A	3	–	–	–	–	–	–	0.90	-0.05	0.04	26.16	-4.14	4.29	302.39	-79.57	135.47	1.35	-0.10	0.11	171.76	-1.05	165
140108A	4	–	–	–	–	–	–	0.89	-0.02	0.03	41.47	-3.19	3.38	518.77	-103.95	156.27	1.75	-0.10	0.20	234.61	-1.41	247
140108A	5	–	–	–	–	–	–	0.53	-0.11	0.11	5.71	-0.58	2.40	341.39	-96.26	169.14	1.70	-0.27	0.30	172.98	0.04	180
140108A	6	–	–	–	–	–	–	1.07	-0.08	0.09	8.62	-2.69	3.34	276.43	-106.75	345.54	2.03	-0.21	0.35	138.66	0.30	119
140108A	7	–	–	–	–	–	–	1.35	-0.05	0.09	35.61	-11.39	49.73	132.72	-35.67	42.06	1.91	-0.26	0.80	78.98	0.00	90
140323A	1	–	–	–	–	–	–	0.85	-0.08	0.09	5.96	-0.98	0.56	38.26	-2.48	2.45	1.28	-0.12	0.21	137.11	-0.46	143
140323A	2	–	–	–	–	–	–	0.73	-0.21	0.15	2.50	-0.33	0.43	6.44	-0.75	0.82	1.34	-0.13	0.15	54.54	0.46	73
140512A	1	–	–	–	–	–	–	0.40	-0.26	0.14	4.70	-0.93	1.50	168.06	-43.47	108.22	0.60	-0.11	0.08	68.09	0.36	81
140512A	2	–	–	–	–	–	–	0.82	-0.08	0.05	24.87	-5.84	4.82	499.90	-208.29	1790.65	0.52	-0.16	0.04	101.00	-0.91	104
140512A	3	–	–	–	–	–	–	0.73	-0.03	0.09	37.39	-2.97	3.38	897.78	-375.17	1301.58	0.36	-0.03	0.12	183.99	-0.35	167
140512A	6	–	–	–	–	–	–	0.69	-0.09	0.08	20.18	-3.87	4.61	185.67	-41.33	52.11	0.48	-0.05	0.09	131.83	0.47	158
140512A	7	–	–	–	–	–	–	0.70	-0.03	0.03	32.76	-2.87	2.76	1214.54	-418.38	1562.38	0.61	-0.04	0.06	172.51	-0.50	194
140512A	10	–	–	–	–	–	–	0.41	-0.08	0.08	8.34	-1.87	0.89	345.14	-104.79	246.34	0.67	-0.07	0.24	143.02	1.23	150
140512A	11	–	–	–	–	–	–	1.07	-0.05	0.04	22.88	-5.54	4.30	129.30	-15.55	48.70	1.14	-0.08	0.13	121.34	1.42	138
140512A	12	–	–	–	–	–	–	1.07	-0.05	0.08	24.97	-5.04	4.77	112.72	-13.86	26.40	0.85	-0.11	0.24	132.42	-0.79	110
140512A	13	–	–	–	–	–	–	1.13	-0.06	0.06	19.73	-4.80	3.89	159.60	-28.33	53.42	0.81	-0.12	0.17	144.35	0.65	135
140512A	14	–	–	–	–	–	–	1.25	-0.12	0.10	1.61	-0.23	0.31	58.07	-7.57	12.19	0.75	-0.05	0.05	162.42	-1.45	151
150430A	1	0.39	-0.03	0.02	3.06e-02	-1.10e-02	3.96e-02	0.67	0.00	0.00	6.68	-6.68	10.59	41.56	-33.94	26.38	0.12	-0.06	0.04	50.62	0.22	42
151027A	1	–	–	–	–	–	–	0.87	-0.11	0.11	3.18	-0.39	0.80	246.28	-73.09	285.84	0.99	-0.09	0.10	128.97	1.29	143
151027A	4	–	–	–	–	–	–	0.47	-0.09	0.07	5.19	-0.53	0.40	235.43	-65.46	130.81	1.15	-0.08	0.08	166.01	0.32	164
161117A	1	–	–	–	–	–	–	0.43	-0.11	0.08	18.16	-3.63	6.07	27.38	-8.93	4.05	0.17	-0.02	0.03	56.74	0.51	58
161117A	2	–	–	–	–	–	–	0.42	-0.06	0.06	14.07	-1.98	4.66	18.52	-5.55	3.22	0.17	-0.01	0.02	104.17	0.17	86
161117A	3	–	–	–	–	–	–	0.46	-0.09	0.09	6.94	-1.26	0.79	36.71	-3.32	2.74	0.51	-0.05	0.11	104.51	-0.98	99
161117A	4	–	–	–	–	–	–	0.51	-0.10	0.09	4.69	-0.40	0.49	34.01	-2.79	4.00	1.00	-0.09	0.09	108.22	-0.75	92
161117A	6	–	–	–	–	–	–	0.54	-0.10	0.08	7.26	-0.95	0.86	47.72	-2.19	2.14	1.96	-0.23	0.36	146.11	-1.50	147
161117A	12	–	–	–	–	–	–	0.90	-0.28	0.21	1.49	-0.67	0.32	5.65	-0.90	1.70	3.01	-0.54	0.60	72.13	-0.55	55
161117A	13	–	–	–	–	–	–	–	–	–	–	–	–	–	–	–	–	–	–	–	–	–
170405A	1	–	–	–	–	–	–	1.26	-0.03	0.03	7.33	-2.18	3.27	55.82	-8.13	24.55	0.38	-0.01	0.05	148.96	-1.01	148
170405A	2	–	–	–	–	–	–	0.94	-0.07	0.07	9.52	-3.93	3.41	81.39	-12.37	15.27	0.51	-0.08	0.20	84.62	0.68	88
170405A	3	–	–	–	–	–	–	1.19	-0.28	0.11	2.30	-0.92	1.01	20.17	-10.70	7.97	0.48	-0.09	0.32	23.53	-0.13	31

Table 3.4: Sync table: for typographic reasons, here we report only those intervals for which this model provided a good fit.

GRB	interval	kTs keV	kTs_{sx} keV	kTs_{dx} keV	kTe keV	kTe_{sx} keV	kTe_{dx} keV	τ	τ_{sx}	τ_{dx}	norm	$norm_{sx}$	$norm_{dx}$	χ^2	runs	dof
080810	1	[0.30]	–	–	14.07	-1.59	2.04	12.37	-1.48	1.67	17.73	-0.57	0.84	96.21	-0.91	96
100619A	1	0.47	-0.09	0.10	10.79	-5.78	26.95	7.87	-4.74	5.90	4.41	-2.08	5.39	65.66	0.09	65
100728A	2	0.70	-0.21	0.22	36.31	-2.33	7.95	7.11	-1.39	0.59	2.25	-1.29	4.51	106.14	0.74	106
100728A	3	[0.30]	–	–	7.07	-1.14	1.09	24.07	-4.94	6.14	27.19	-1.18	3.81	72.70	-0.16	72
100728A	4	0.28	-0.10	0.10	52.95	-5.59	9.33	5.38	-0.68	0.38	31.00	-19.17	111.62	154.36	0.98	154
100728A	5	0.38	-0.17	0.17	70.63	-6.18	7.16	5.52	-0.45	0.48	15.25	-15.25	98.01	168.20	0.84	168
100728A	6	0.86	-0.17	0.09	36.22	-3.33	6.46	6.55	-1.03	0.63	1.13	-0.49	0.96	163.83	0.66	163
100728A	7	0.96	-0.20	0.22	65.15	-7.11	8.55	5.51	-0.56	0.66	1.25	-0.62	1.47	131.25	-0.80	131
100728A	8	0.78	-0.13	0.14	98.54	-9.20	10.62	4.27	-0.29	0.32	2.04	-0.86	1.77	196.25	-0.90	196
100728A	9	0.61	-0.22	0.21	50.36	-8.05	11.02	6.50	-1.14	1.52	3.02	-1.84	9.24	68.43	1.13	68
100728A	10	0.76	-0.12	0.21	45.44	-15.98	59.78	4.95	-2.04	2.73	1.44	-0.77	2.44	47.01	-0.80	47
100728A	12	[0.30]	–	–	41.07	-9.65	16.94	4.78	-0.89	0.84	10.05	-1.25	1.44	164.10	-0.53	164
100728A	13	0.43	-0.22	0.18	10.69	-3.04	10.58	10.34	-4.70	5.42	4.63	-4.63	46.52	90.20	-0.64	90
100728A	14	0.94	-0.20	0.20	67.43	-35.73	102.02	3.26	-2.74	2.13	0.48	-0.22	0.54	56.25	-0.54	56
100728A	15	0.95	-0.16	0.09	10.58	-2.39	20.20	8.09	-4.43	4.54	0.41	-0.15	0.19	103.61	-0.32	103
100814A	1	0.54	-0.08	0.08	21.01	-2.66	3.68	9.29	-1.55	1.57	0.92	-0.28	0.47	150.70	0.49	150
100814A	2	0.62	-0.14	0.13	31.68	-5.07	7.25	7.46	-1.56	2.01	1.42	-0.57	1.33	129.20	0.39	129
100906A	1	[0.30]	–	–	12.28	-4.61	5.38	9.39	-2.25	2.21	27.76	-1.15	8.52	90.13	-0.78	90
110102A	3	0.62	-0.09	0.10	134.48	-35.16	60.78	3.65	-0.70	0.70	1.09	-0.42	0.71	104.88	-0.81	104
110102A	4	0.65	-0.10	0.12	111.18	-18.11	25.42	3.83	-0.43	0.42	1.45	-0.62	1.10	209.85	-0.54	209
110102A	5	0.59	-0.05	0.06	61.33	-6.74	7.96	5.10	-0.38	0.40	2.61	-0.69	0.95	201.17	1.44	201
110102A	7	0.77	-0.07	0.09	92.58	-15.01	20.85	3.86	-0.43	0.43	1.56	-0.48	0.54	276.84	-0.97	276
110102A	9	[0.30]	–	–	50.66	-23.84	17.71	4.33	-0.77	2.13	15.39	-1.87	0.59	124.96	-0.12	124
110102A	11	0.16	-0.05	0.05	7.38	-2.18	3.41	13.74	-4.29	6.17	50.43	-28.26	119.99	107.38	-0.76	107
110102A	12	[0.30]	–	–	14.93	-4.17	6.81	8.43	-2.04	2.26	6.39	-0.39	1.00	134.31	-0.66	134
110102A	13	0.47	-0.05	0.05	64.93	0.00	0.00	3.83	-0.22	0.18	2.45	-0.75	1.14	103.92	-0.94	103
110102A	14	0.58	-0.07	0.05	44.05	-12.22	32.22	4.42	-1.24	0.97	1.90	-0.47	1.07	177.70	-1.08	177
130528A	1	[0.30]	–	–	4.20	-0.41	0.43	46.18	-6.79	8.52	8.04	-0.28	0.33	99.92	-0.55	99
130609B	2	[0.30]	–	–	19.21	-4.30	10.40	6.69	-1.55	1.38	16.90	-0.53	0.57	150.85	0.01	150
140108A	3	0.80	-0.12	0.14	48.84	-10.61	15.80	5.34	-0.84	0.94	0.78	-0.33	0.58	162.39	0.39	162
140108A	5	0.86	-0.10	0.11	71.45	-15.72	23.67	4.12	-0.63	0.65	0.66	-0.22	0.37	162.77	1.32	162
140108A	6	0.36	-0.07	0.08	66.75	-25.65	70.46	4.20	-1.38	1.41	7.87	-3.84	9.02	141.13	0.37	141
140108A	7	[0.30]	–	–	28.24	-4.48	13.92	7.01	-1.68	0.92	8.41	-0.60	1.35	82.92	0.00	82
140323A	1	0.40	-0.08	0.06	8.33	-1.13	0.94	16.10	-2.10	4.32	3.75	-1.35	5.84	143.26	0.03	143
140512A	1	1.27	-0.20	0.24	72.42	-20.91	39.68	4.16	-0.99	1.10	0.13	-0.06	0.10	63.55	0.32	63
140512A	3	1.32	-0.14	0.19	134.83	-22.74	29.84	3.52	-0.38	0.29	0.17	-0.06	0.07	158.68	-0.46	158
140512A	6	1.16	-0.14	0.16	63.82	-5.30	15.90	4.57	-0.62	0.45	0.28	-0.10	0.14	130.42	0.51	130
140512A	7	1.51	-0.13	0.20	183.61	-36.33	75.45	2.82	-0.52	0.27	0.20	-0.07	0.06	180.15	-0.62	180
140512A	10	1.61	-0.20	0.23	127.12	-43.45	83.12	2.92	-0.71	0.80	0.12	-0.05	0.07	141.07	0.02	141
140512A	11	0.55	-0.11	0.12	55.41	-10.66	15.81	4.94	-0.77	0.87	3.06	-1.51	3.69	124.98	1.60	124
140512A	12	0.45	-0.09	0.09	50.39	-10.88	13.59	5.15	-0.72	1.07	4.51	-2.13	4.80	130.97	-0.62	130
140512A	13	0.41	-0.06	0.07	81.94	-22.76	21.53	3.73	-0.41	0.84	5.32	-2.24	2.47	144.87	0.36	144
151027A	2	0.97	-0.13	0.14	293.55	-97.07	295.05	2.13	-0.66	0.52	0.57	-0.21	0.34	131.68	-1.13	131
151027A	4	1.37	-0.09	0.09	162.16	-56.46	201.58	2.31	-0.82	0.62	0.25	-0.05	0.06	166.45	-0.06	166
161117A	1	1.21	-0.64	0.79	12.43	-1.54	2.02	32.71	-16.41	25.08	0.15	-0.15	1.21	143.26	-0.64	143
161117A	2	[0.30]	–	–	9.15	-0.91	0.27	69.79	-7.93	9.14	7.61	-0.28	1.19	104.64	0.38	104
161117A	3	1.83	-0.36	0.33	19.03	-2.35	2.76	9.34	-1.48	2.43	0.07	-0.03	0.07	103.82	-0.14	103
161117A	6	1.29	-0.23	0.27	22.83	-1.50	1.84	9.26	-1.00	1.02	0.68	-0.30	0.54	141.78	-1.16	141
161117A	11	[0.30]	–	–	4.50	-0.76	0.81	34.69	-8.88	11.74	40.65	-2.32	6.10	68.64	0.43	68
161117A	12	0.49	-0.18	0.17	6.07	-2.62	4.47	13.84	-3.96	15.82	7.42	-4.68	27.08	72.48	-0.73	72
170405A	3	0.59	-0.27	0.30	16.56	-6.13	23.10	8.28	-2.65	4.13	2.31	-2.31	6.41	24.31	-0.06	24

Table 3.5: GRBCOMP table: for typographic reasons, here we report only those intervals for which this model provided a good fit.

Chapter 4

A robotic pipeline for fast GRB followup with the Las Cumbrés Observatory Network

Authors: R. Martone[1] [2], C. Guidorzi[1], C. G. Mundell[3], S. Kobayashi[4], A. Cucchiara[5], A. Gomboc[6], N. Jordana[3], T. Laskar[3], M. Marongiu[1],[2], D. C. Morris[5], R. J. Smith[4], I. A. Steele[4]

Article by Martone, R., Guidorzi, C. et al. Exp Astron (2019) 48: 25
DOI:10.1007/s10686-019-09634-y

Summary

The study of GRB early emission of GRBs plays a role of great importance for the understanding of the physics of these relativistic explosions. This phase can provide insights on fundamental issues, like the energy of the reverse shock and the exact role of the magnetic field. Furthermore, when the afterglow onset is observed, the beginning of the interaction between the ejecta and the circumburst medium can be studied. The technological innovation in this field, both on the software and hardware side, has been driven by the necessity to track the complex, fast-evolving emission that characterises these early phases. In this context, the current generation of fully-robotic telescopes provides brand-new observation opportunities at early times for a large number of events.

The attached paper describes the pipeline I designed for robotic optical followup of GRBs with the Las Cumbrés Observatory network. My work exploits the vast experience in human-triggered, fast followup campaigns obtained by our group during the last 6 years of observations with this facility. The goal of my Python code is to promptly submit observation requests to the network within 3 minutes of the receipt of the socket notice. It also exploits instant messaging systems, using the Telegram platform to connect to the people involved in the observation campaign. The communication is bidirectional, since the pipeline both sends and receives messages, informing people on the state of the observation and allowing them to take control upon

[1]Department of Physics and Earth Science, University of Ferrara, via Saragat 1, I–44122, Ferrara, Italy
[2]ICRANet, Piazzale della Repubblica 10, I–65122, Pescara, Italy
[3]Department of Physics, University of Bath, Claverton Down, Bath, BA2 7AY, UK
[4]Astrophysics Research Institute, Liverpool John Moores University, Liverpool, L3 5RF, UK
[5]University of the Virgin Islands, #2 John Brewers Bay, 00802 St Thomas, VI, USA
[6]Centre for Astrophysics and Cosmology, University of Nova Gorica, Vipavska 11c, Ajdovščina 5270, Slovenia

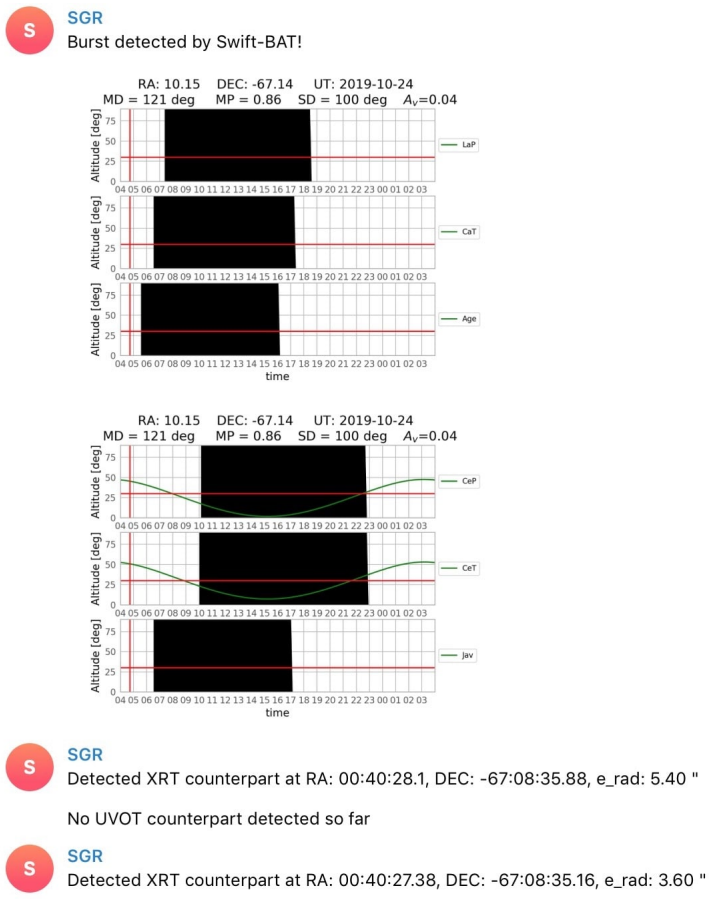

Figure 4.1: Example of our Telegram-distributed notification provided to the HETH group. Information about the position of the burst and the visibility of the target is promptly provided to the users, together with live updates about the discovery of XRT and UVOT counterparts.

request. Thanks to the code, we were able to track the early evolution of the optical afterglow from GRBs with a fully-robotic procedure for the first time on the LCO network. In the paper I report the case of GRB 180720B, whose optical afterglow was discovered by us and which happens to be one of the very few GRBs (to date) whose afterglow was detected up to TeV energies by the H.E.S.S. imaging air Cherenkov telescope array. The flexibility of our solution is guaranteed by the usage of open-source, cross platform libraries, that make the pipeline suitable to be easily adapted to any other robotic facility.

A copy of the full text (editorial version) of this paper is reported in Appendix of the thesis.

Other uses of our notification system

The notification system designed for our pipeline has been exported outside our group for the needs of other collaborations. It is currently used by the High-Energy Transients and their Hosts (HETH[7]) group in Granada and by the Stargate group for the follow-up activity of Swift bursts. An example of the provided notification is reported in figure 4.1: the provided information include visibility plots for the telescopes used by the groups and live updates about the discovery of XRT and UVOT counterparts.

[7] http://heth.iaa.es/

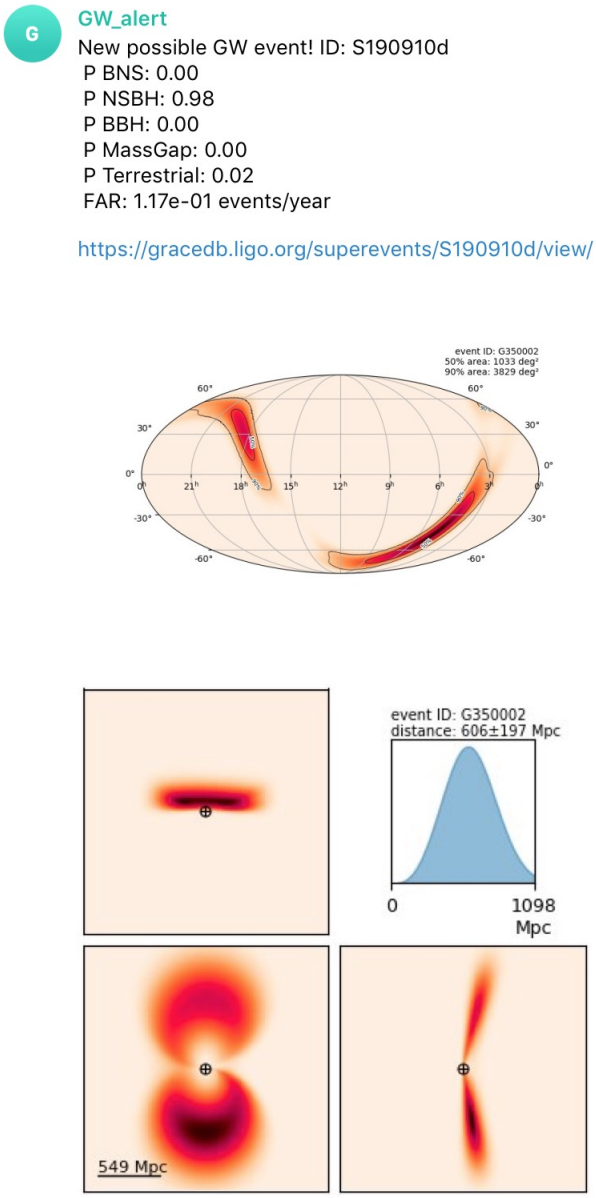

Figure 4.2: Example of our Telegram-distributed notification provided to the Grawita group. The probabilities of different scenarios, the link to the event webpage, the skymap, and the distance posterior distribution plot are promptly distributed to the users.

The Telegram notification system described in this chapter has been also adapted to provide quicklook information for rapid GW follow-up. Figure shows an example of the messages prompty provided to the GRAvitational Wave Inaf TeAm (GRAWITA[8]) upon the reception of a new-GW detection Notice. The code extracts from it the probabilities of the signal being the result of different events[9]:

- BNS: Binary Neutron Star merging;
- NSBH: Neutron Star-Black Hole merging;
- BBH: Binary Black Hole Merging;
- MassGap: MassGap Merging;
- Terrestrial: Terrestrial Noise

. Furthermore, the plots reporting the skymap and the distance estimation are provided (Figure 4.2).

In the following, we report a brief summary of the pieces of code designed to support my follow-up activity, both in the context our group and in external collaboration.

Follow-up activity

My work included an optical follow-up activity of *Swift*-detected bursts with the LCO network, that resulted in 23 issued notices submitted to the Gamma-ray Coordinates Network (GCN-these communications are usually referred to GCNs), with the discovery of three optical counterparts (for GRB 180703A, GRB 180715A, and GRB 180720B) and a number of afterglow confirmations and upper limits. In this context, my activity also consisted in the design of Python code for different scopes:

- **Photometry**: the code estimates from digital frames the magnitude of the source specified in input. In this process, the zero point is calibrated through the comparison with the catalogues, that are automatically downloaded for the sky region correspondent to the analysed frame. Both aperture and Point Spread Function (PSF) photometry can be performed, simply specifying the desired modality in input. A version of this code was also designed for parallel computing, while a third version features also a graphic interface for source selection.
- **Spectroscopy**: the code was the result of my collaboration with the HETH group in Granada. It consisted in the Python translation of an IRAF[10] pipeline previously developed by Luca Izzo for semi-automatic spectrum extraction from digital frames. My contribution consisted in a full automation of those part of Izzo's code that still required human intervention.
- **Uncatalogued source identification**: the code[11] searches for uncatalogued sources in digital frames, performing also an accurate photometry. It is designed for parallel computing to improve the performances on the large, crowded frames usually produced as result of optical follow-ups of GW triggers.

[8] https://www.grawita.inaf.it/

[9] See https://emfollow.docs.ligo.org/userguide/content.html for details

[10] http://ast.noao.edu/data/software

[11] named MAREC (MARtone Electromagnetic Counterpart) on Massimo Della Valle's proposal

- **GW follow-up**: the code takes in input the skymaps produced after every GW trigger and produces in output a list of the galaxies contained in the error region. Galaxies are ordered according to different criteria, including the visibility from the location specified in input, their type and luminosity, etc. This information is extracted from the *Galaxy List for the Advanced Detector Era* (GLADE[12]) catalogue.

[12] http://glade.elte.hu/Download.html

Chapter 5

Fast Radio Bursts

5.1 The serendipitous discovery of a new class of transients

FRBs are bright (0.5 – 200 Jy) radio pulses detected in the 400 MHz – 8 GHz energy band lasting from fraction up to dozens of milliseconds. They were serendipitously discovered in 2007 (Lorimer et al. 2007) in an off-line analysis of data collected in 2001 during a survey aimed at the studying radio pulsars. However, a real interest around this transient begun years later, since this first discovery remained a one-off feature until the discovery of a very similar pulse in 2011 (Keane et al. 2011), even if, given its low Galactic latitude, this event was early considered a Rotating Radio Transient (RRAT), a class of Galactic transients first discovered by McLaughlin et al. (2006). A strong suggestion supporting the extragalactic origin of the these pulses came two years later, when a number of pulses with a very high dispersion measure (DM) were discovered by Thornton et al. (2013) during an off-line search on archival data in the High Time Resolution Universe survey at the Parkes telescope (HTRU; Keith et al. 2010).

FRBs have been attracting great interest ever since the first rough distance and intrinsic energetic estimation. The inferred DM implied a luminosity distance up to $\approx$ 6 Gpc (z $\approx$ 0.96) that, considering a flux density $\approx$ 1 Jy, implied an isotropic energy release up to $E_{iso} \approx 10^{39}$erg; furthermore, the $\approx$ 1 ms duration meant a peak luminosity $L_{iso} \approx 10^{42}$ erg s^{-1}, making of FRBs one of brightest class of transients. This new interest triggered further searches and discoveries both at the Parkes telescope (Burke-Spolaor & Bannister 2014; Ravi et al. 2015; Champion et al. 2016) and at other radio facilities, namely the Arecibo Observatory (Spitler et al. 2014) and the Green Bank Telescope (Masui et al. 2015). Furthermore, the latest years saw the employment of the new generation of interferometric facilities, that started to become the main FRB-detection factories thanks to their large FOV: a number of detection came from the Upgrade Molonglo Synthesis Telescope (UTMOST, Caleb et al. 2016), the Australian Square Kilometer Array Pathfinder (ASKAP, Bannister et al. 2017; Shannon et al. 2018) and the Canadian Hydrogen Intensity Mapping Experiment (CHIME, CHIME/FRB Collaboration et al. 2019a). Thanks to these facilities, the number of known FRB, currently $\approx$ 90, is expected to rapidly grow. Interestingly, with the rising number of detected events, it is becoming clear that this class of transients suffered from the so-called *discovery bias* sources should be very easy to detect, since its first representative (also known as the "Lorimer burst") was actually very peculiar, showing the highest recorded peak flux density (> 30 Jy), that saturated the Parkes receivers (Lorimer et al. 2007). The idea behind this bias is that the first-discovered representative of a new class should be very easy to detect, showing peculiar characteristics with respect to the rest of the population, that otherwise would have been already detected. This existence of this effect has been suggested for the Lorimer burst by Macquart & Ekers (2018).

These huge efforts resulted in a number of breakthrough discoveries, among which we re-

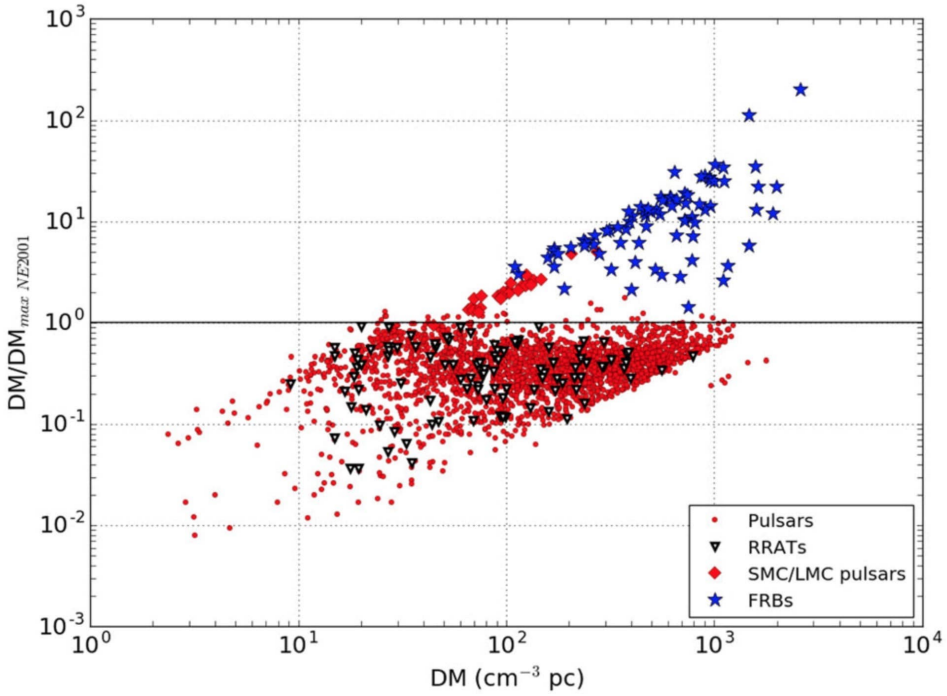

Figure 5.1: Dispersion measures (DMs) of FRBs, Small and Large Magellanic Cloud radio pulsars (SMC and LMC respectively), Galactic rotating radio transients (RRATs) and Galactic pulsars. On the y-axis is reported the ratio between the measured DM and the DM expected from the maximum Galactic contribution, estimated using the NE2001 model (Cordes & Lazio 2002). Figure from Petroff et al. (2019).

port the measure of the polarization profiles of a number of FRB (Petroff et al. 2015; Masui et al. 2015; Ravi et al. 2016; Petroff et al. 2017; Michilli et al. 2018; Caleb et al. 2018), the discovery of repeating sources FRB 121102 (Spitler et al. 2016; Scholz et al. 2016; Chatterjee et al. 2017), FRB 180814.J0422+73 (CHIME/FRB Collaboration et al. 2019a), and others (CHIME/FRB Collaboration et al. 2019c), and the detection of transients with interferometric techniques (Caleb et al. 2016; Bannister et al. 2017; Chatterjee et al. 2017; Marcote et al. 2017).

5.2 FRB observed properties

As pointed out by Petroff et al. (2019), a clear and standard definition is still missing, even if the attempts to formalise the classification are ongoing (Foster et al. 2018). Instead a radio transient is considered an FRB when it matches a series of blurred criteria like the millisecond or sub-millisecond duration, and a DM higher than expected from the Galactic contribution. However, the main discriminating quantity is the DM, that for FRBs should be larger than the expected contribution by the Milky Way (MW). Figure 5.1 shows that this criterion distinguishes FRBs from other radio sources, even if borderline cases do exist. DM is fundamental to obtain an estimation of the amount of plasma crossed by the electromagnetic wave during is path to the observer and so acquire a rough knowledge of the source distance. Considering the electron number density of the crossed plasma n_e, the path length l and the distance to the FRB d, the dispersion measure is defined as:

$$\mathrm{DM} = \int_0^d n_e(l)\, dl. \tag{5.1}$$

In pulsar astronomy, this quantity is typically quoted in units of cm^{-3} pc. The distribution

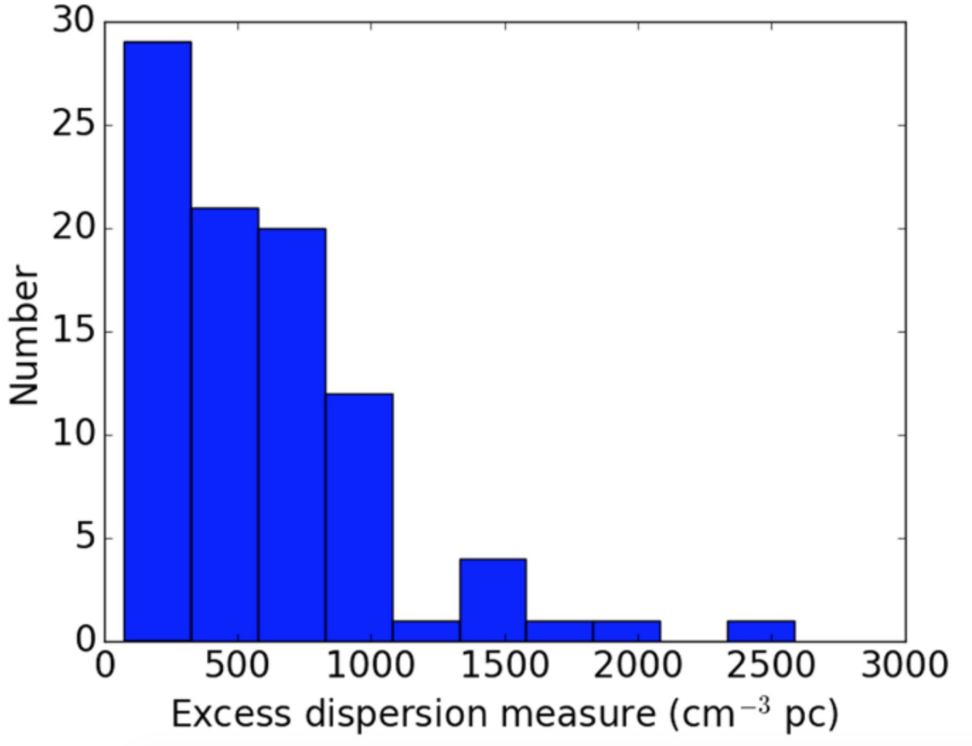

Figure 5.2: FRB excess dispersion measure (DM_E). Figure from Petroff et al. (2019).

of FRB DMs is displayed in 5.2. The amount of dispersion can be directly calculated from the time delay (Δt) between the arrival of the lowest (ν_{lo}) and highest frequency (ν_{hi}) signal:

$$\Delta t = \frac{e^2}{2\pi m_e c}(\nu_{lo}^{-2} - \nu_{hi}^{-2})\ \mathrm{DM} \tag{5.2}$$

being m_e the mass of the electron, c the speed of light. The chromatic effect is clearly visible in the main panel of Figure 5.3, where we report the case of the very bright Lorimer burst. The inset shows the same signal after the correction (de-dispersion) for this effect.

Equation (5.2) represents a zeroth order approximation and more accurate estimation for the frequency-dependent part of the arrival times can be written as:

$$\tau(\nu) = 4.15\ \mathrm{ms}\left(\frac{\mathrm{DM}}{\nu^2}\right) \pm 28.6\ \mathrm{ps}\left(\frac{\mathrm{RM}}{\nu^3}\right) \pm 0.251\ \mathrm{ps}\left(\frac{\mathrm{EM}}{\nu^4}\right) \tag{5.3}$$

in units of ms, being ν in gigahertz and RM and EM the Faraday rotation measure and the emission measure respectively. The latter, similarly to DM, is depends on the amount of plasma crossed by electromagnetic wavelength:

$$\mathrm{EM} = \int_0^d n_e(l)^2\ dl\ , \tag{5.4}$$

while RM is related to physical quantities by

$$\mathrm{RM} = -0.81 \int_0^d B(l)_{\|} n_e(l)\ dl \tag{5.5}$$

in units of rad m^{-2}, being $B(l)_{\|}$ the component of the magnetic field parallel to the line of sight. This quantity is directly connected to the polarization position angle Θ in case of linear polarization:

$$\Theta = \mathrm{RM}\ \lambda^2. \tag{5.6}$$

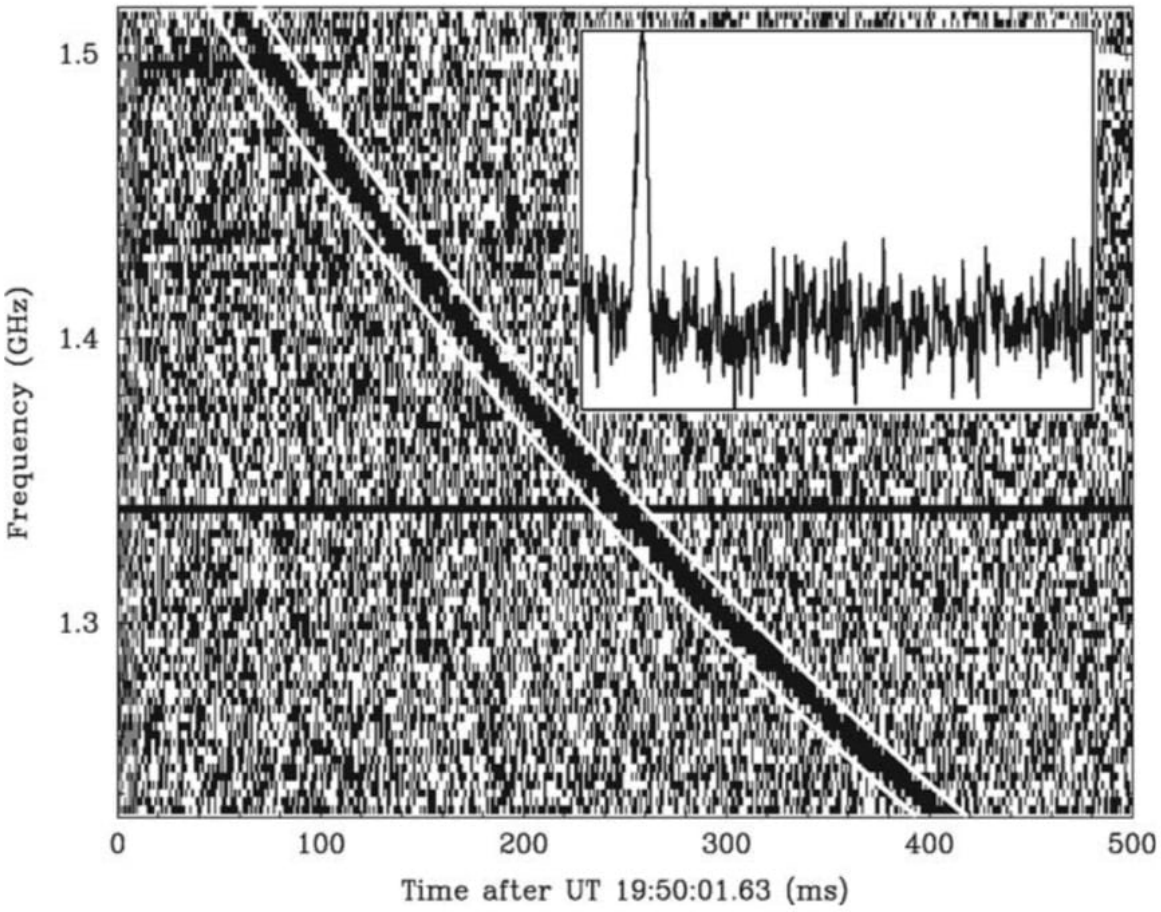

Figure 5.3: Dynamic spectrum of FRB010724 (aka the Lorimer Burst Lorimer et al. 2007) as detected at the Parkes telescope. In the main panel the chromatic dispersion is clearly visible in the difference among signal arrival times at different frequencies, while in inset the de-dispersed signal is shown. Figure from Lorimer et al. (2007).

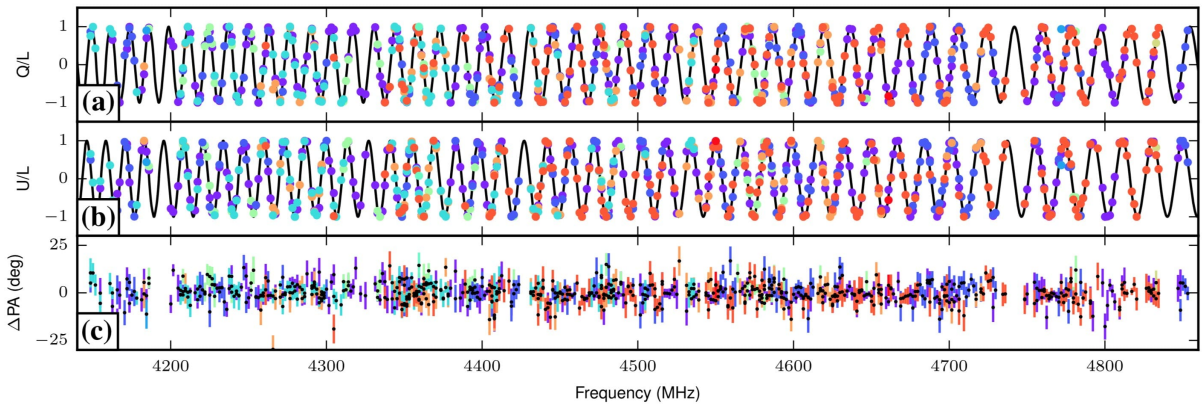

Figure 5.4: The effect of Faraday rotation on the repeating burst FRB 121102. Panels (a) and (b) show the frequency-dependent values of the normalized Stokes parameters, indicating the frequency dependence of the polarization position angle. The black line represents the best-fit Faraday rotation model, while the different colors distinguish different bursts detected from the same source during the same observing session. Panel (c) reports the residuals with respect to the best-fit model. Image from Michilli et al. (2018).

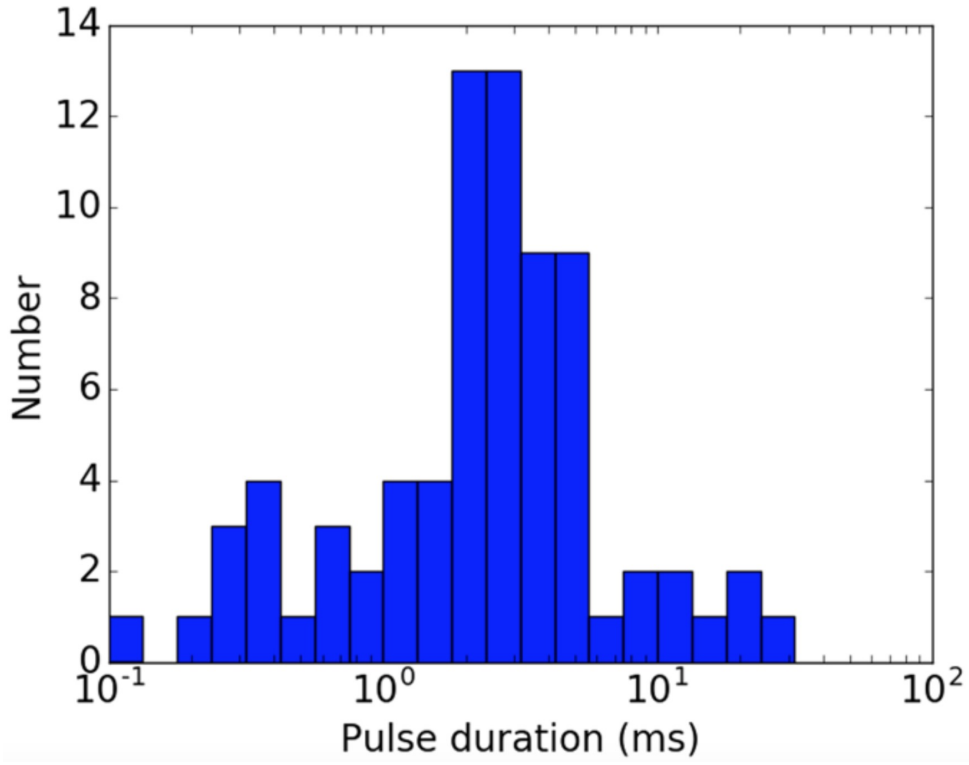

Figure 5.5: Pulse duration distribution for FRBs. Figure from Petroff et al. (2019).

This provides a direct connection between the measured polarization angle and the magnetization of the plasma crossed by the electromagnetic wave. Figure 5.4 shows the frequency-dependent variation of the Stokes parameters due to Faraday rotation for FRB 121102, the FRB with the so far highest measured linear polarization degree and RM (100% and $\approx 10^5$ rad m^{-2} respectively, Michilli et al. 2018). In those cases in which both DM and RM are known and assuming they are associated with the same plasma region, equation (5.5) can be rearranged to obtain an estimation of the average line-of-sight magnetic field:

$$< \mathrm{B}_{\parallel} >= \frac{\mathrm{RM}}{0.81\ \mathrm{DM}}. \tag{5.7}$$

However, the Faraday rotation observed in FRBs is expected to be mainly due to the circumburst plasma, so the observed value should be corrected considering their cosmological origin:

$$\mathrm{RM_{LOCAL}} = \mathrm{RM_{OBS}}(1+z)^2 \tag{5.8}$$

Pulse width

The pulse time width of FRBs is a combination of multiple factors and can be general expressed as:

$$\mathrm{W} = \sqrt{W_{int}^2 + t_{samp}^2 + \Delta t_{DM}^2 + \Delta t_{DMerr}^2 + \tau_s^2} \tag{5.9}$$

being t_{samp} is the data sampling interval, Δt_{DM} is the delay due to the dispersion across the analyzed energy channel, Δt_{DM} is the contribution due to the uncertainty on the value of the true dispersion measure, while τ_s is the delay due to the different propagation paths followed by the different different photons composing the signal. Figure 5.5 shows the distribution of pulse widths, that span the range from 10^{-1} up to 3×10^1 ms, with a pronounced peak around $\approx$ a few

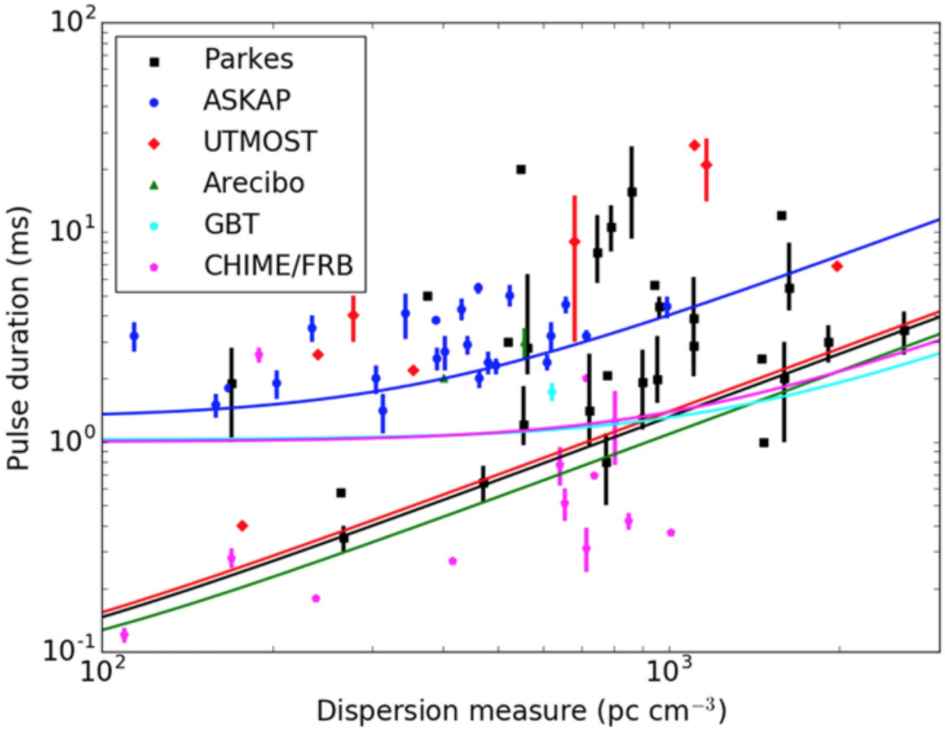

Figure 5.6: Pulse duration (W) vs dispersion measure (DM). Solid lines represent the temporal broadening due to the combined effect of DM smearing and the instrument sampling time. Image from Petroff et al. (2019).

milliseconds. However, these values should be handled with care. Figure 5.6 shows FRBs in the W vs DM plane, where the solid lines represent the effect of the instrumental pulse broadening for every facility, combined with survey sampling time as a function of DM: in the cases for which the points closely follow the solid line the intrinsic pulse duration could be much lower and the broadening is mainly due to instrumental effects.

Polarization

Stokes parameters and so polarization have been measured only in a handful of cases, showing different characteristics from one burst to another. A number of bursts shows a high degree of linear polarization (> 30%), with particularly high degree for FRB 121102 (100%, Michilli

FRB	Linear %	Circular %	RM rad m^{-2}	DM pc cm^{-3}	Reference
110523	44 ± 3	23 ± 30	−186 ± 14	623	Masui et al. 2015
121102	100	0	$\sim 1.0 \times 10^5$	560	Michilli et al. 2018
140514	0 ± 10	21 ± 7	-	563	Petroff et al. 2015
150215	43 ± 5	3 ± 1	1.5 ± 10.5	1106	Petroff et al. 2017
150418	8.5 ± 1.5	0 ± 4.5	36 ± 52	776	Keane et al. 2016
151230	35 ± 13	6 ± 11	0	960	Caleb et al. 2018
150807	80 ± 1	-	12 ± 0.7	267	Ravi et al. 2016
160102	84 ± 15	30 ± 11	−221 ± 6	2596	Caleb et al. 2018
180301	∼ 30	∼ 70	−3100	520	Price et al. 2018

Table 5.1: FRB Polarization

et al. 2018), FRB 160102 and FRB 150807 (> 80% in both cases, Caleb et al. 2018; Ravi et al. 2016). FRB 140514 represents an exception, showing no significative linear polarization (∼ 0%, Petroff et al. 2015). High circular polarization degree was measured only for FRB 180301 (∼ 70%, Price et al. 2018), while is compatible with zero in more cases, like FRB 110523, FRB 121102, FRB 150418, FRB 151230. A resume of these (and other) measures is reported in Table 5.2.

5.3 Distance estimation

As of October 2019, a direct distance measurement is available only for three cases: the repeating burst FRB 121102 and the two non-repeating bursts FRB 180924 and FRB 190523, for which the host galaxies were identified thanks to interferometric techniques. In the case of the repeating burst, Tendulkar et al. (2017) used the arcsec localization provided by Bannister et al. (2017) to identify a dwarf, star-forming galaxy at $z \approx 0.19$, while in the other two cases Bannister et al. (2019) and Ravi et al. (2019) identified the two hosts as massive, red galaxies at $z \approx 0.32$ and $z \approx 0.66$ respectively. In all the other cases, the rough, arcmin localization usually provided by radio telescopes (most of all single-dish telescope, see next paragraphs) is not enough to identify a host galaxies at cosmological distance (Vedantham et al. 2016; Eftekhari et al. 2018), so indirect distance constraints have to be used.

As anticipated, the dispersion measure provides an identification of the amount of plasma present between the source and the observer. In FRB astronomy the dispersion measure excess ($\mathrm{DM_E}$) is usually defined as the excess with respect to the contribution by the Milky Way:

$$\mathrm{DM_E} = \mathrm{DM} - \mathrm{DM_{MW}} = \mathrm{DM_{IGM}} + \left(\frac{\mathrm{DM_{HOST}} + \mathrm{DM_{LOCAL}}}{1 + \mathrm{z}}\right) \tag{5.10}$$

where $\mathrm{DM_{IGM}}$ is the DM contribution due to the intergalactic medium (IGM), $\mathrm{DM_{HOST}}$ is the host galaxy contribution and $\mathrm{DM_{LOCAL}}$ is the circumburst contribution. Equation 5.10 suggests that $\mathrm{DM_E}$ is an upper limit for $\mathrm{DM_{IGM}}$, the quantity we are most interested in for a distance estimation. Obviously, every distance estimation made using this equation is strongly affected by our (current) ignorance about the FRB source and so about the environment where it resides so, without further information about the host galaxy and the circumburst environment, we can only separate the Galactic and the extragalactic contribution. What is more, $\mathrm{DM_{MW}}$ is uncertain at least at the tens of percent levels in the majority of cases (Petroff et al. 2019). However, literature provides distance estimation made under simplified assumptions. For example, Deng & Zhang (2014) provided a $\mathrm{DM_{IGM}}$/redshift relation assuming a uniform distribution of ionized baryons between the source and the observer:

$$\langle \mathrm{DM_{IGM}} \rangle = K_{\mathrm{IGM}} \int_0^z \frac{(1+z)x(z)\,\mathrm{d}z}{\sqrt{\Omega_{\mathrm{m}}(1+z)^3 + \Omega_\Lambda}} \tag{5.11}$$

where K_{IGM} is a normalization constant that assumes standard Planck cosmological parameters (see also Yang & Zhang 2016), $x(z)$ is the baryons ionizing fraction, Ω_{m} is the energy density of matter and Ω_Λ is the energy density of dark energy. For the local universe this relation is roughly equivalent to $\mathrm{DM_{IGM}} \simeq z \times 1000\ \mathrm{cm^{-3}\ pc}$ (even if other authors prefer $z \times 855\ \mathrm{cm^{-3}\ pc}$) and so the very commonly-used relation can be extracted:

$$z \sim \frac{\mathrm{DM}}{1000\ \mathrm{cm^{-3}\ pc}}. \tag{5.12}$$

Using this kind of relations, a plot like that in Figure 5.7 can be built: the flux density E_ν is plotted against the dispersion measure, which is directly related to the redshift, reported in the

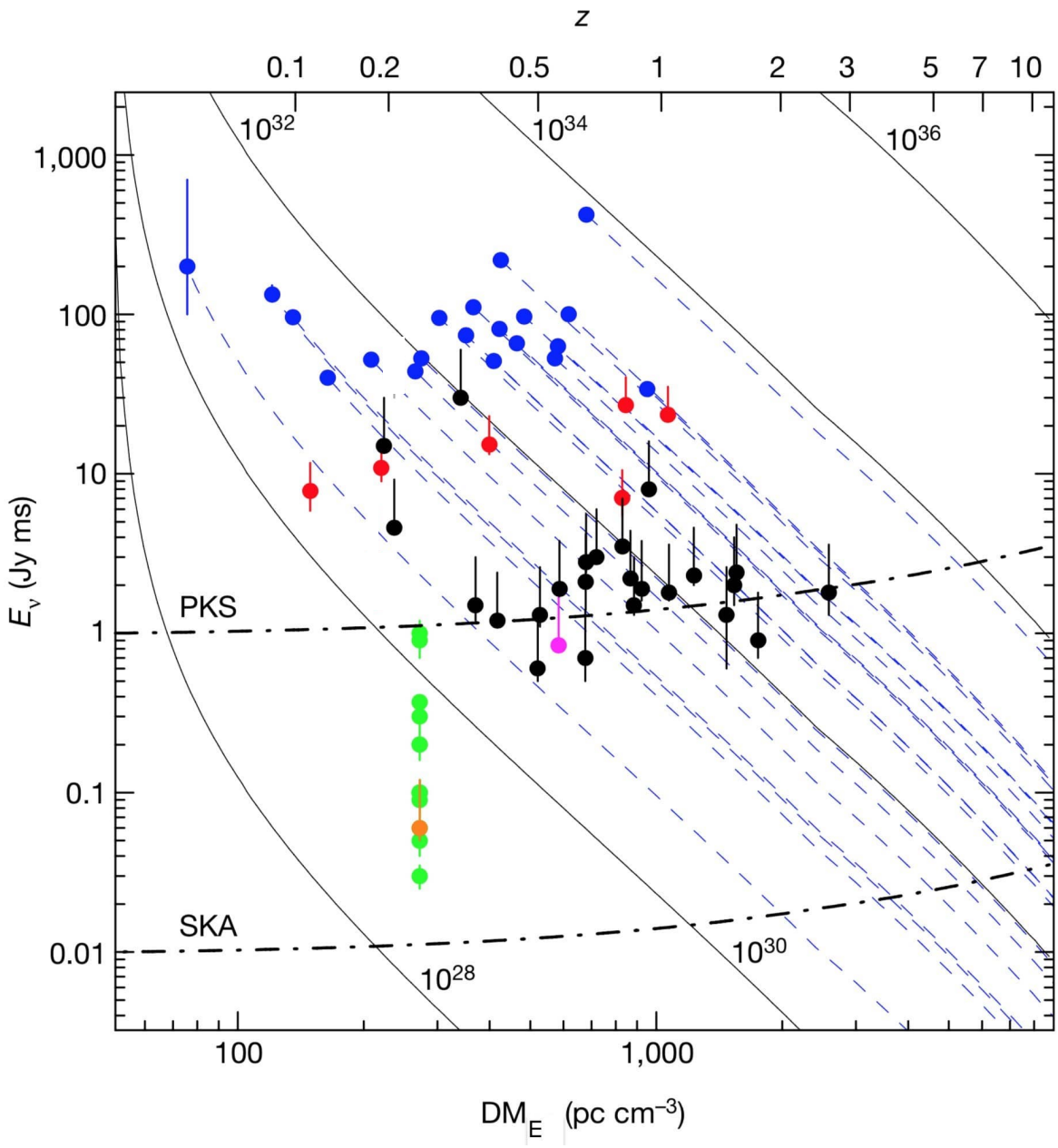

Figure 5.7: Energy density E_ν in Jy ms versus the excess dispersion measure DM_E and redshift (z). The colors distinguish FRB detected with different facilities: ASKAP (blue), Parkes (black), UTMOST (red), Green Bank Telescope (magenta) and Arecibo (Orange), while in green are reported multiple bursts of FRB 121102. Redshift is calculated considering a host contribution of $50(1 + z)^{-1}$ pc cm^{-3}. The blue-dashed curves show the fluences expected for the ASKAP-detected bursts if they were detected at larger distances. The black curves show contours of constant spectral-energy density, in units of erg Hz^{-1}. The dash-dotted curves are lines of constant fluence. Figure adapted from Shannon et al. (2018).

second, upper x-axis and calculated assuming $\mathrm{DM_{HOST}} = 50(1+z)^{-1}\mathrm{pc\ cm^{-3}}$. The plot also shows that FRBs not only span more than 3 order of magnitude in energy density, but have also been detected from $z \sim 0.08$ (corresponding to a luminosity distance $\mathrm{D_L} \approx 300$ Mpc), up to $z \approx 3$ (corresponding to $\mathrm{D_L} \approx 26$ Gpc).

5.4 Radio telescopes

The FRB search is currently performed using both single-dish facilities and interferometric methods. In the first case, since the sensitivity of a radio telescope is roughly proportional to the size of the antenna, large-diameter instruments are usually implied, e.g. Parkes (64 m), Lovell (76 m), Effelsberg (100 m), the Green Bank Telescope (110 m), Arecibo (305 m), FAST (500 m). The high sensitivity makes single-dish instruments perfect to study in detail already-localized bursts, during follow-up campaigns: an example is the series of bursts associated to the repeating FRB 121102 detected and studied using Arecibo and the Green Bank Telescope (Spitler et al. 2016; Scholz et al. 2016). At the same time, the large focus cabins allows the installation of a number of different receivers, and so broadband and polarization analysis can be carried on. The main drawback of the single-dish approach is the very poor new-discoveries localization, with a typical accuracy of a few arcmin, insufficient for the identification of the host galaxy at cosmological distance.

On the other side, interferometric facilities are typically composed by many, small-size antennas distributed on a large area. Examples are the Australian Square Kilometer Pathfinder (ASKAP, Johnston et al. 2008), the Canadian Hydrogen Intensity Mapping Experiment (CHIME, Bandura et al. 2014), the Upgraded Molonglo Synthesis Telescope (UTMOST, Green & Flynn 2015) and the Low-Frequency Array (LOFAR, van Haarlem et al. 2013). Their use is relatively new in the field of FRB astronomy and the major advantage is that signals from the single telescopes are combined to obtain a spatial resolution similar to that of a single-dish telescope with a diameter equal to the baseline of the network. What is more, these networks can be arranged to obtain a very large field of view (dozens of degrees, tipically), which are ideal to discover FRBs, as testified by the results obtained by ASKAP (Shannon et al. 2018). The main drawback is the reduced bandwidth, due to the small number of detectors that can be mounted at the focus of these telescopes.

The pros and cons of these two designs suggest that, even if we are now entering the era of interferometric search of new FRBs, the most convenient approach is probably a combination of both techniques, where the single-dish facilities perform broad-band follow-up campaigns on new transients discovered using interferometry.

5.5 Emission and spectrum

Even if there is still no consensus around the FRB sources, their millisecond duration suggests they are produced in compact region: variability studies (see e.g. Michilli et al. 2018) detected burst substructures as short as $\sim 30\ \mu$s (Farah et al. 2018 detected also a 7.5 μs sub-pulse in FRB 170827) that, ignoring beaming effects, imply emission sites $\lesssim 10$ km. Further information comes from the radiation brightness temperature T_b, which is the effective temperature of a blackbody in the Rayleigh-Jeans regime and that is commonly used in astrophysics to distinguish coherent and incoherent emission. It can be defined as:

$$T_b = \frac{I_\nu\, \lambda^2}{2k} \tag{5.13}$$

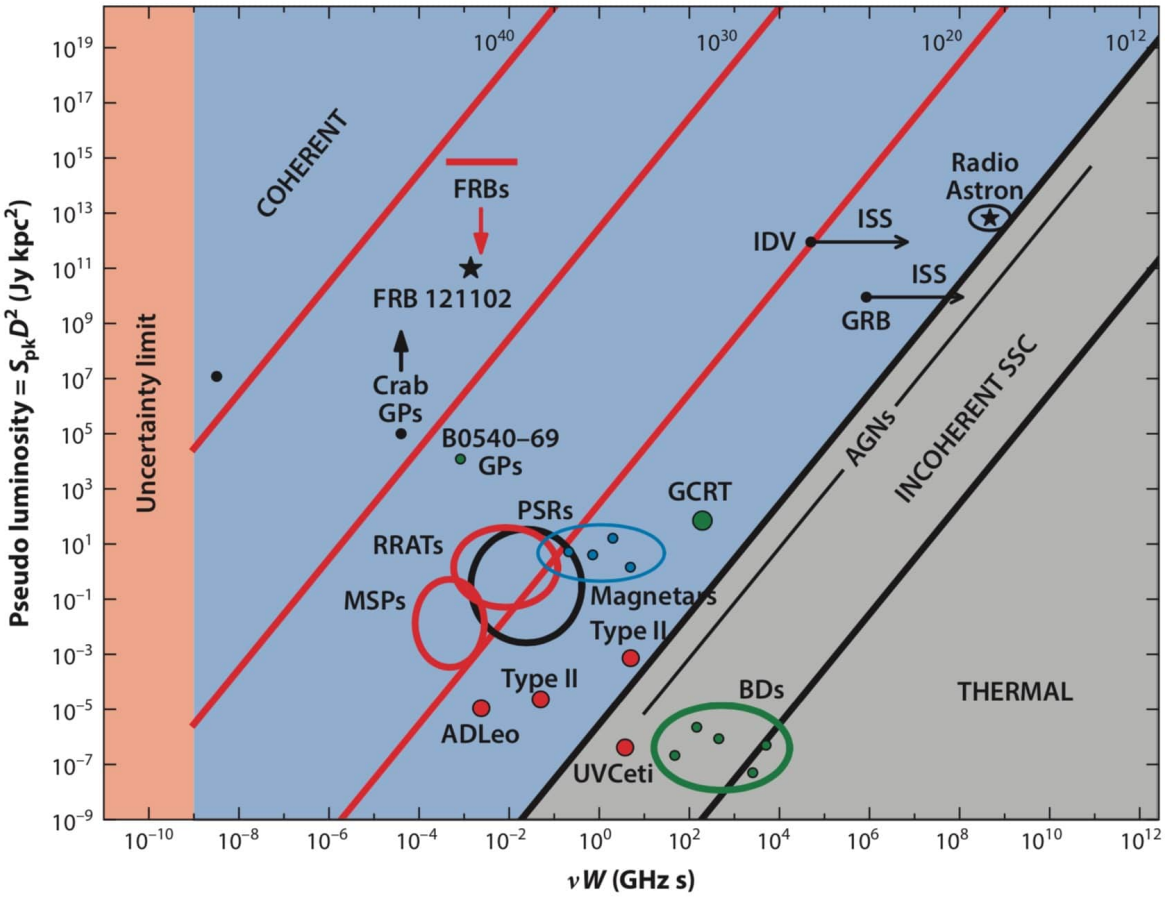

Figure 5.8: Time-luminosity phase space for radio transients showing the product of peak flux S_{pk} and squared distance versus the product of frequency and pulse width W. The "uncertainty" limit on the left indicates that $\nu W \lesssim 1$ as follows from the uncertainty principle. The separation line between the "coherent" and the "incoherent" region is represented by the emission from active galactic nuclei (AGNs), as explained in the text. The following astrophysical classes are shown: rotating radio transient (RRAT), brown dwarf (BD), Galactic center radio transient (GCRT), giant pulse (GP), intraday variable (IDV), interstellar scintillation (ISS), millisecond pulsar (MP), pulsar radio source (PRS). Image from Cordes & Chatterjee (2019).

being I_ν the specific intensity, k the Boltzmann's constant and λ the wavelength. For a transient burst of duration W, peak flux density S_{pk} and subtending the angle Ω_s, the specific intensity is $I_\nu \sim S_{pk}/\Omega_s$. Considering a source of size $\sim cW$ at distance d, the subtended angle can be written as $\Omega_s \sim (cW/d)^2$. From these considerations, the brightness temperature of a FRB can be written as:

$$T_b \sim \frac{S_{pk}\, d^2}{2k(\nu W)^2}. \tag{5.14}$$

In the case of thermal sources (like e.g. stars), T_b is equal to the physical temperature, being an upper limit in the other cases. Figure 5.8 shows the location of various astrophysical transient in the $S_{pk}D^2$ vs νW plane, where lines of constant brightness temperatures can be drawn: the lower-right corner represent the phase space in which incoherent sources reside, while coherent sources are in the remaining part of the plane, the dividing line being represented by active galactic nuclei (AGN), whose incoherent emission is limited by inverse Compton scattering to $T_b \approx 10^{12}$ K. However, FRBs reside deepely in the the "coherent region" of this plane, far from the AGN threshold line.

Coherent radiation mechanisms involve the emission from a large number of particles (N) with a definite and distinct phase relationship, that enhances the emitted power P ($P \propto N^2$) with respect to incoherent emission mechanisms (where usually $P \propto N$). This radiation can be produced by a number of different emission mechanisms, like e.g. masers, Dicke's superradiance. For a more complete list of theoretical models that appeared so far in the literature, see the review by(Platts et al. 2019).

The main difficulty in the study of FRB spectra is the relatively narrow band in which they are observed, since no emission has been detected outside the 400 MHz − 8 GHz range. Given this poor knowledge, the flux density is usually modelled with a simple powerlaw:

$$S \propto \nu^\alpha \ . \tag{5.15}$$

The first attempts to constrain the spectral index α exploited the non detection at very low frequency: Karastergiou et al. (2015) inferred $\alpha \gtrsim +0.1$ from LOFAR FRB non-detection down to 145 MHz, while Chawla et al. (2017) used the Green Bank Telescope non-detection down to 350 MHz to infer $\alpha > -0.9$. However, the strongest constraint came only recently with the work by Macquart et al. (2019), that found $\alpha = -1.6^{+0.3}_{-0.2}$ studying ASKAP FRBs. Interestingly, this result is quite close to the spectral index observed in pulsars $\alpha \sim -1.4$ (Bates et al. 2013). These very different results suggest the presence of a turnover under $\sim$ 1 GHz or a spectrum different from a powerlaw, being modified by emission envelopes (Hessels et al. 2018; Gourdji et al. 2019) or scattering (CHIME/FRB Collaboration et al. 2019b).

5.6 Repeating bursts

Up to August 2019, only two bursts were found to repeat, namely FRB 121102 and FRB 180814.J0422+73, even if only the former was studied in great detail, given the very high number of observed repetitions. FRB 121102 was discovered on November 2, 2012 in Arecibo data (Spitler et al. 2014), even if its repeating nature came out only years later during routine follow-up observations (Spitler et al. 2016). This triggered dedicated studies and a variable radio source coincident with the position of the burst was identified (Chatterjee et al. 2017), while the repeating bursts were exploited to obtain a very accurate sky localisation ($\approx$ 12 mas) using interferometric techniques (Marcote et al. 2017). Bursts from this source have been detected with waiting times as short as a few ten seconds (Scholz et al. 2016; Gajjar et al. 2018) (even if shorter values cannot be excluded (Zhang 2018)), with a highly non-Poissonian repeating

FRB	N_{bursts}	DM	DM_E[a]	Avg. Width[b]	Avg. Fluence[c]
		pc cm^{-3}	pc cm^{-3}	ms	Jy ms
180814.J0422+73	5	189	87	18.7	24.7
180916.J0158+65	10	349.2	200	2.6	5.4
181030.J1054+73	2	103.5	40	1.0	5.9
181128.J0456+63	2	450.5	110	4.0	3.5
181119.J12+65	3	364.05	34	3.5	1.8
190116.J1249+27	2	441	20	2.8	1.8
181017.J1705+68	2	1281.6	43	16.8	8.5
190209.J0937+77	2	425.0	46	6.6	1.3
190222.J2052+69	2	460.6	87	2.7	5.5

Table 5.2: CHIME-discovered repeating bursts properties (CHIME/FRB Collaboration et al. 2019a,c).

[a] : calculated using the NE2001 model (Cordes & Lazio 2002).

[b] : Average width.

[c] : Average fluence.

rate (Oppermann et al. 2018). Moreover, they seem very sporadic, with periods of very high activity interspersed by low-activity intervals (Chatterjee et al. 2017; Gajjar et al. 2018). When compared to other FRBs, 121102 shows a very high rotation measure ($\approx 10^5$rad m^{-2}) and the highest degree of linear polarization ($\approx 100\%$, see Table 5.2).

In both cases the pulse widths vary on a large range, from $\sim 30\ \mu s$ up to ~ 10 ms for FRB 1211102 and from ~ 2 ms up to ~ 60 ms in the case of FRB 180814.J0422+73.

Recently, CHIME/FRB Collaboration et al. (2019c) reported the discovery of eight new repeating bursts, whose main features are reported in Table 5.2. All these novel repeating bursts (FRB 180814.J0422+73 and the eight new ones) have similar DM value as the non-repeating bursts observed with the same instrument. On the other hand, they do show evidence of larger widths, that may suggest a different emission mechanism between the two FRB sub-classes. Furthermore, the repeating bursts are also quite different from one another, showing complex morphologies and sub-bursts in the vast majority -but not all- cases. Two of the new bursts (namely FRB 180916.J0158+65 and FRB 181030.J1054+73) show very low DMs, so that a Galactic origin cannot be excluded. In any case, their short distance and precise localization make them ideal targets for future follow-up campaigns.

The possibility that repeating and non-repeating FRBs are due to to different mechanisms or kinds of progenitors is still unclear.

5.7 Rates

Given the unknown distance, the rate of observable FRBs is usually expressed in terms of observable events over a certain flux density over the whole sky. These estimations are roughly consistent with an all-sky rate of detectable events $R_{\rm FRB,sky} \gtrsim 10^3$sky^{-1} day^{-1} over a fluence density $F \gtrsim 1$ Jy ms. In Table 5.7 we report a synthesis of the various $R_{\rm FRB}$ that can be found in the Literature basing on different surveys and methodologies. The dependence of these rates

Rate sky^{-1} day^{-1}	Confidence Interval %	F_{lim} Jy ms	Reference
$\sim$ 225	-	6.7	Lorimer et al. (2007)
5000-16000	68	3.0	Thornton et al. (2013)
1300-9600	99	4.4	Rane et al. (2016)
4000-12000	95	1.5	Champion et al. (2016)
1100-7000	99	3.8	Crawford et al. (2016)
272-924	95	6.0	Lawrence et al. (2017)
800-3200	90	2.0	Bhandari et al. (2018)
29-45	68	37	Shannon et al. (2018)

Table 5.3: Summary of all-sky FRB rates found in literature.

Transient	Volumetric rate $\times F_{\mathrm{FRB,vol}}$	Reference
CCSN	$\sim 10^{1} - 10^{2}$	Dahlen et al. (2004)
Ibc-SN	~ 10	Guetta & Della Valle (2007); Dahlen et al. (2012)
SLSN ($z = 1$)	$\sim 10^{-2} - 10^{-1}$	Quimby et al. (2013); Prajs et al. (2017)
GRB	$\sim 10^{-1}$	Frail et al. (2001)
BNS	$\sim 10^{-1} - 10$	Abbott et al. (2017c)
SN Ia ($z < 0.3$)	~ 1	Cappellaro et al. (2015)

Table 5.4: Volumetric rates of various astrophysical transients with respect to the $F_{\mathrm{FRB,vol}}$ (see text for details). Abbreviations: SN, Supernova; CCSN, core-collapse SN; SLSN, superluminous SN; GRB, beaming-corrected gamma-ray burst; BNS, Binary NS merger.

on the fluence limit if usually modelled as a simple powerlaw:

$$R(> F_{\rm min}) \propto F_{min}^{\gamma} \tag{5.16}$$

with $\gamma = -1.5$ in Euclidean geometry and considering standard candles. A range of different estimations can be found in literature: Macquart & Ekers (2018) and Lawrence et al. (2017) estimate respectively $\gamma = -2.6^{+0.7}_{-1.3}$ and $\gamma = 0.91^{+0.34}_{-0.34}$ analysing a sample of Parkes FRBs, while James (2019) found $\gamma = -1.1^{+0.2}_{-0.2}$ for the fainter, more distant Parkes population and $\gamma = -2.2^{+0.5}_{-0.5}$ for the brighter and closer ASKAP population, suggesting a break leading to the hypothesis that the progenitor population has his maximum in the $1 < z < 3$ range. This wide difference testifies the importance of non-trivial selection effects introduced by different radio telescopes, that undermine the results of analysis performed on samples of FRBs collected with different instruments.

However, assuming that FRB sources are distributed cosmologically out to $z \sim 1$, $R_{\rm FRB,sky}$ implies a volumetric rate $R_{\rm FRB,vol} \sim 2 \times 10^3$ Gpc^{-3} yr^{-1}. This value can be compared with the volumetric rates of other astrophysical transients, in order to obtain further hints on the nature of the FRB source. The results of this comparison are reported in Table 5.4.

5.8 Proposed progenitors

The very few constraints on FRB emission led to the blossoming of a wide number of proposed models for their emission mechanisms and progenitors, even larger than the number of detected events. A taste of the situation can be given by the work of Platts et al. (2019)[1], whose effort resulted in a complete collection of all the proposed models. These, in the majority of cases, involve NSs, since the large rotational energy, and the very strong magnetic fields they can have, together with the complex environment in which they reside, seem to match the requirement of a compact, bright source of coherent radiation. However, a lot of models implying different sources have been also proposed and a complete description is beyond the aim of this section. Instead, following the treatment of Petroff et al. (2019), we report here a brief overview on the main families of proposed progenitors, with a few representative cases for each class by the way of example.

5.8.1 Neutron stars

Many theories suggest that FRBs originate from NSs, which can be isolated, interacting (in pairs or with other objects) or colliding.

In the first group there are theories suggesting that FRBs are due to some rotationally-powered pulsars as part of their normal activity, like super-giant pulses (Connor et al. 2016), or from their open magnetic field lines at the poles (Lyutikov et al. 2016), or from normal pulsars having an unstable rotational axis (Katz 2017). Alternatively, FRBs could be magnetar hyperflares (Popov & Postnov 2010), or starquakes on the surface (Wang et al. 2018) or maser emission from the ionized medium surrounding these compact objects (Metzger et al. 2019). Other models involve a cataclysmic event, like the collapse of a supramassive NS in a blackhole (BH) (Falcke & Rezzolla 2014; Zhang 2014). However, models involving flares or mergers should also face the fact that no counterparts in X and γ-rays have been so far detected (with the only possible exception of the yet debated case of FRB 131104 DeLaunay et al. 2016) and so some mechanism for the suppression of the flux outside the radio bands should be invoked.

[1] Also condensed in the table at https://frbtheorycat.org/index.php/Main_Page

The second group of theories calls for the interaction of NSs with a set of different objects, like supernova explosions (Egorov & Postnov 2009), fast moving plasma (Zhang 2017a) or supermassive BHs (Zhang 2017b). In other cases, the emission would come from the NS accretion of dark matter (Van Waerbeke & Zhitnitsky 2019), ionized plasma (Istomin 2018), material from a white dwarf (WDs) (Gu et al. 2016) or rocky objects (D'Ai et al. 2016; Geng & Huang 2015; Mottez & Zarka 2014).

Finally, other theories suggest that FRBs might be the result of a BNS merger (Lyutikov 2013; Totani 2013; Wang et al. 2016; Dokuchaev & Eroshenko 2017) or of the collision of NS with another compact object, like a WD (Liu 2018) or an axion star (Iwazaki 2015).

5.8.2 Black holes progenitors

Fewer theories invoke BHs as FRB progenitors, with different proposed mechanisms. Maybe the first example to be proposed in this sense is the model by Rees (1977), that predicted millisecond-long radio pulses as a result of the evaporation of BHs. In other cases, radio bursts are expected from the interaction between the (supermassive or stellar-mass) BH and its surrounding environment (Vieyro et al. 2017; Gupta & Saini 2018; Yi et al. 2019). Other scenarios involve mergers of two of these objects (Liu et al. 2016; Zhang et al. 2016), of a BH and a NS (Mingarelli et al. 2015; Abramowicz et al. 2018), or a BH and a WD (Li et al. 2018). These models exclude electromagnetic emission other than the FRB itself without making ad-hoc assumptions, since merging episodes involving BHs are usually electromagnetically weak.

5.8.3 Other progenitors

WDs have been proposed as sources of FRBs only in a few cases, since matching the required energy budget is challenging without the interaction with more compact objects. Both Gu et al. (2016) and Moriya (2016) suggest that a radio burst could result from the accretion of material on the WD surface, while Kashiyama et al. (2013) propose a mechanism involving the merging of two of these objects.

Other authors propose peculiar mechanisms, like a primordial BH turning into a white hole (Barrau et al. 2014) or the activity of Galactic flare stars (Loeb et al. 2014). The latter attributes all the DM excess to the circumburst medium and it is now considered outdated.

Finally, some models invoke exotic states of matter, like for example superconducting cosmic strings (Vachaspati 2008; Ye et al. 2017; Cao & Yu 2018) or strange stars (Falcke & Rezzolla 2014; Shand et al. 2016; Zhang et al. 2018).

Chapter 6

A cumulative search for hard X/γ–Ray emission associated with fast radio bursts in *Fermi*/GBM data

Authors: R. Martone[1 2], C. Guidorzi[1], R. Margutti[3], L. Nicastro[4], L. Amati[4], F. Frontera[1 4], M. Marongiu[1 2], M. Orlandini[4], E. Virgilli[1]

Article by Martone et al., A&A 631, A62 (2019)
reproduced with permission ©ESO
DOI:10.1051/0004-6361/201936284

Summary

Despite deep, broadband investigation, FRBs have been uniquely detected at radio frequencies. The only possible exception in this sense is represented by FRB 131104, for which a γ–ray transient positionally and temporally consistent was claimed (DeLaunay et al. 2016). The transient had a duration of $\sim$ 400 s and a 15–150 keV fluence $S_\gamma \sim 4\times10^{-6}$ erg cm^{-2}. However, the claim raised some scepticism, since it was later suggested as due to a nearby AGN. Furthermore, Cunningham et al. (2019) performed a search for high-energy FRB counterparts of in *Fermi*/GBM data, finding no evidence for such a fluent counterpart for any burst.

Our work is aimed at testing the systematic presence of associated high-energy transients throughout a sample of the FRB population. In contrast to other previous works, we focused on cumulative lightcurves in order to emphasise possible common features reaching a better statistical sensitivity, with no assumption on the specific signal shape. We used an approach similar to that used in machine learning methodologies to accurately model the highly-variable *Fermi*/GBM instrumental background on a time interval comparable to the duration of the proposed γ–ray counterpart of FRB 131104.

We were able to constrain the fluence of the possible γ–ray signal in the 8–1000 keV band down to 6.4×10^{-7} (7.1×10^{-8}) erg cm^{-2} for a 200-s (1-s) integration time. These two fluence lim-

[1]Department of Physics and Earth Science, University of Ferrara, via Saragat 1, I–44122, Ferrara, Italy
[2]ICRANet, Piazzale della Repubblica 10, I–65122, Pescara, Italy
[3]Center for Interdisciplinary Exploration and Research in Astrophysics and Department of Physics and Astronomy, Northwestern University, 2145 Sheridan Road, Evanston, IL 60208-3112, USA
[4]INAF–Osservatorio di Astrofisica e Scienza dello Spazio di Bologna, Via Piero Gobetti 93/3, I-40129 Bologna, Italy

its exclude $\sim 94\%$ of *Fermi*/GBM detected long gamma–ray bursts and $\sim 96\%$ of *Fermi*/GBM detected short gamma–ray bursts. Furthermore, we found the radio-to-gamma fluence ratio to be $\eta > 10^8$ Jy ms erg^{-1} cm^2. This constrain points to a different emission mechanism from that powering magnetar giant flares. Finally, we exclude a γ–ray counterpart as fluent as the one possibly associated with FRB 131104 to be a common feature of FRBs.

A copy of the full text (editorial version) of this paper is reported in Appendix of the thesis.

Conclusions

This thesis describes the different aspects of my work within the field of time domain astronomy.

The first part addresses some of the issues that are still open after more than 50 years since the birth of GRB science. Some insight on the engine powering GRBs can be obtained through the $E_{p,i} - E_{iso}$ correlation (a.k.a. Amati relation). At the beginning of my work, I investigated the nature of a few apparent outliers of this relation. For two of them (980425 and 031203), which were sub-energetic, I investigated the possibility that a substantial fraction of energy was released in the X-ray band, and consequently missed by the instruments that detected them (BATSE and *INTEGRAL*/IBIS). Following the same line of reasoning, I studied the emission from similar sub-energetic events (060218, 100316D, and 161219B) that were also observed in the soft X-ray band and that did match the Amati relation. In particular, I simulated where these bursts would lie in the $E_{p,i} - E_{iso}$ plane, had they been observed by BATSE and INTEGRAL. As a result, I found that these GRBs would have been tagged as outliers. This demonstrates the importance of this bias effect and corroborates the validity of the $E_{p,i} - E_{iso}$ correlation. Furthermore, the work shows that the location of GRB 980425 in the $E_{p,i} - E_{iso}$ plane can be explained in terms of an observational bias without calling for "ah hoc" physical models for the GRBs involving off-axis emission (e.g. Ramirez-Ruiz et al. 2005).

I further explored another aspect of GRB prompt emission carrying out a systematic broad-band, temporally-resolved spectral analysis for a number of very fluent GRBs. The aim was to test three out of the most widely discussed models: the empirical Band function, and more physically grounded models like the synchrotron, and the Comptonisation model "grbcomp". Time-slicing was obtained using the unbiased Bayesian Block algorithm. The procedure I have come up with enabled a fine tracking of the temporal evolution and comparison of the different model parameters throughout the prompt phase. Notably, in a non-negligible fraction of time-resolved spectra, no model provided an acceptable description. Whenever this was the case, the time profiles of the same GRB observed at different energy channels looked markedly more different from each other than for the less problematic GRBs.

I concluded the GRB part with the description of the robotic pipeline designed by myself for the rapid, fully robotic optical follow-up of GRB afterglows with the LCO network. The code exploits the flexibility and reliability of scientific Python libraries to listen to socket-distributed notices and to submit observation requests directly to the LCO network servers. It turned out able to follow a GRB up, for the first time with a network like LCO, autonomously, proving the effectiveness of this kind of design. Furthermore, for the first time in astronomy, the system features an instant messaging system that ensures a fast, reliable, and versatile interaction with the users for free. Currently, it is adopted by different international groups interested in the rapid follow-up of different kinds of transients. Given the exponential growth of transients expected in the coming years, these solutions maximise the science return.

In the final part I described my work on the novel and exciting topic of FRBs. Discovered by chance only a decade ago at radio wavelength, they soon attracted a great surge of interest in the entire international community. To date, the efforts to understand their origin have been hampered by the poor localisation in the radio and the yet total absence of solid counterparts at

other wavelengths. Together with my collaborators, I carried out a cumulative analysis to search for the possible presence of high energy signals temporally and positionally coincident with a list of known FRBs. To this aim, I preliminarily set and calibrated a procedure to account for the complex *Fermi*/GBM background variability. As a result, I could set very strong upper limits on the possible high-energy emission associated with FRBs. As a result, I excluded both an emission mechanism similar to the one powering magnetar giant flares, and the contemporaneous emission of typical short and long GRBs. When new generation radiotelescopes will boost the number of observed FRBs, thanks to its cumulative nature our approach can be used to set gradually more constraining limits to the possible presence of high-energy emission associated to this class of elusive transients.

Bibliography

Abbott, B. P., Abbott, R., Abbott, T. D., et al. 2016a, Physical Review Letters, 116, 061102

Abbott, B. P., Abbott, R., Abbott, T. D., et al. 2016b, Physical Review Letters, 116, 241103

Abbott, B. P., Abbott, R., Abbott, T. D., et al. 2017a, Astrophysical Journal, Letters, 848, L13

Abbott, B. P., Abbott, R., Abbott, T. D., et al. 2017b, Physical Review Letters, 119, 161101

Abbott, B. P., Abbott, R., Abbott, T. D., et al. 2017c, Astrophysical Journal, Letters, 848, L12

Abramowicz, M. A., Bejger, M., & Wielgus, M. 2018, Astrophysical Journal, 868, 17

Ackermann, M., Asano, K., Atwood, W. B., et al. 2010, Astrophysical Journal, 716, 1178

Aglietta, M., Badino, G., Bologna, G., et al. 1987, Helvetica Physica Acta, 60, 619

Akerlof, C., Balsano, R., Barthelmy, S., et al. 1999, Nature, 398, 400

Alexeyev, E. N., Alekseev, E. N., Alexeyeva, L. N., et al. 1987, in The Standard Model. The Supernova 1987A, 739–744

Amati, L. 2006, MNRAS, 372, 233

Amati, L., Frontera, F., Tavani, M., et al. 2002, A&A, 390, 81

Atwood, W. B., Abdo, A. A., Ackermann, M., et al. 2009, Astrophysical Journal, 697, 1071

Axelsson, M., Baldini, L., Barbiellini, G., et al. 2012, Astrophysical Journal, Letters, 757, L31

Band, D., Matteson, J., Ford, L., et al. 1993, ApJ, 413, 281

Bandura, K., Addison, G. E., Amiri, M., et al. 2014, in Society of Photo-Optical Instrumentation Engineers (SPIE) Conference Series, Vol. 9145, Proceedings of the SPIE, 914522

Bannister, K. W., Deller, A. T., Phillips, C., et al. 2019, Science, 365, 565

Bannister, K. W., Shannon, R. M., Macquart, J. P., et al. 2017, Astrophysical Journal, Letters, 841, L12

Barrau, A., Rovelli, C., & Vidotto, F. 2014, Physical Review D, 90, 127503

Barthelmy, S. D., Barbier, L. M., Cummings, J. R., et al. 2005, Space Sci. Rev., 120, 143

Bates, S. D., Lorimer, D. R., & Verbiest, J. P. W. 2013, Monthly Notices of the Royal Astronomical Society, 431, 1352

Beloborodov, A. M. & Mészáros, P. 2017, Space Science Reviews, 207, 87

Berger, E. 2009, Astrophysical Journal, 690, 231

Bhandari, S., Keane, E. F., Barr, E. D., et al. 2018, Monthly Notices of the Royal Astronomical Society, 475, 1427

Bhat, P., Meegan, C. A., von Kienlin, A., et al. 2016, ApJS, 223, 28

Bionta, R. M., Blewitt, G., Bratton, C. B., et al. 1987, Physical Review Letters, 58, 1494

Blake, C. H., Bloom, J. S., Starr, D. L., et al. 2005, Nature, 435, 181

Bloom, J. S. 2011, What are Gamma-Ray Bursts? (Princeton and Oxford: Princeton University Press)

Bloom, J. S., Kulkarni, S. R., Djorgovski, S. G., et al. 1999, Nature, 401, 453

Boella, G., Butler, R. C., Perola, G. C., et al. 1997, Astronomy and Astrophysics Supplement, 122, 299

Burgess, J. M. 2014, MNRAS, 445, 2589

Burke-Spolaor, S. & Bannister, K. W. 2014, Astrophysical Journal, 792, 19

Burrows, D. N., Hill, J. E., Nousek, J. A., et al. 2005, Space Sci. Rev., 120, 165

Caleb, M., Flynn, C., Bailes, M., et al. 2016, Monthly Notices of the Royal Astronomical Society, 458, 708

Caleb, M., Keane, E. F., van Straten, W., et al. 2018, Monthly Notices of the Royal Astronomical Society, 478, 2046

Campana, S., Mangano, V., Blustin, A. J., et al. 2006, Nature, 442, 1008

Cao, X.-F. & Yu, Y.-W. 2018, Physical Review D, 97, 023022

Cappellaro, E., Botticella, M. T., Pignata, G., et al. 2015, Astronomy and Astrophysics, 584, A62

Champion, D. J., Petroff, E., Kramer, M., et al. 2016, Monthly Notices of the Royal Astronomical Society, 460, L30

Chatterjee, S., Law, C. J., Wharton, R. S., et al. 2017, Nature, 541, 58

Chawla, P., Kaspi, V. M., Josephy, A., et al. 2017, Astrophysical Journal, 844, 140

CHIME/FRB Collaboration, Amiri, M., Bandura, K., et al. 2019a, Nature, 566, 235

CHIME/FRB Collaboration, Amiri, M., Bandura, K., et al. 2019b, Nature, 566, 230

CHIME/FRB Collaboration, Andersen, B. C., Bandura, K., et al. 2019c, Astrophysical Journal, Letters, 885, L24

Colgate, S. A. 1974, Astrophysical Journal, 187, 333

Connor, L., Sievers, J., & Pen, U.-L. 2016, Monthly Notices of the Royal Astronomical Society, 458, L19

Cordes, J. M. & Chatterjee, S. 2019, Annual Review Astronomy and Astrophysics, 57, 417

Cordes, J. M. & Lazio, T. J. W. 2002, arXiv e-prints, arXiv:0207156

Costa, E. & Frontera, F. 2003, in American Institute of Physics Conference Series, Vol. 662, Gamma-Ray Burst and Afterglow Astronomy 2001: A Workshop Celebrating the First Year of the HETE Mission, ed. G. R. Ricker & R. K. Vanderspek, 123–129

Costa, E., Frontera, F., Heise, J., et al. 1997, Nature, 387, 783

Crawford, F., Rane, A., Tran, L., et al. 2016, Monthly Notices of the Royal Astronomical Society, 460, 3370

Cucchiara, A., Levan, A. J., Fox, D. B., et al. 2011, ApJ, 736, 7

Cunningham, V., Cenko, S. B., Burns, E., et al. 2019, Astrophysical Journal, 879, 40

Dahlen, T., Strolger, L.-G., Riess, A. G., et al. 2012, Astrophysical Journal, 757, 70

Dahlen, T., Strolger, L.-G., Riess, A. G., et al. 2004, Astrophysical Journal, 613, 189

D'Ai, A., Kennea, J. A., Krimm, H. A., et al. 2016, GRB Coordinates Network, 20296, 1

Dai, Z., Daigne, F., & Mészáros, P. 2017, Space Science Reviews, 212, 409

Daigne, F., Bošnjak, Ž., & Dubus, G. 2011, Astronomy and Astrophysics, 526, A110

Daigne, F. & Mochkovitch, R. 1998, MNRAS, 296, 275

DeLaunay, J. J., Fox, D. B., Murase, K., et al. 2016, Astrophysical Journal, Letters, 832, L1

Della Valle, M., Chincarini, G., Panagia, N., et al. 2006a, Nature, 444, 1050

Della Valle, M., Malesani, D., Bloom, J. S., et al. 2006b, Astrophysical Journal, Letters, 642, L103

Deng, W. & Zhang, B. 2014, Astrophysical Journal, Letters, 783, L35

Dokuchaev, V. I. & Eroshenko, Y. N. 2017, arXiv e-prints, arXiv:1701.02492

Eftekhari, T., Berger, E., Williams, P. K. G., & Blanchard, P. K. 2018, Astrophysical Journal, 860, 73

Egorov, A. E. & Postnov, K. A. 2009, Astronomy Letters, 35, 241

Falcke, H. & Rezzolla, L. 2014, Astronomy and Astrophysics, 562, A137

Farah, W., Flynn, C., Bailes, M., et al. 2018, Monthly Notices of the Royal Astronomical Society, 478, 1209

Feroci, M., Stella, L., van der Klis, M., et al. 2012, Experimental Astronomy, 34, 415

Fong, W., Berger, E., & Fox, D. B. 2010, Astrophysical Journal, 708, 9

Foster, G., Karastergiou, A., Geyer, M., et al. 2018, Monthly Notices of the Royal Astronomical Society, 481, 2612

Frail, D. A., Kulkarni, S. R., Sari, R., et al. 2001, Astrophysical Journal, Letters, 562, L55

Frontera, F., Amati, L., Costa, E., et al. 2000, ApJS, 127, 59

Frontera, F., Amati, L., Farinelli, R., et al. 2013, ApJ, 779, 175

Fryer, C. L., Rueda, J. A., & Ruffini, R. 2014, Astrophysical Journal, Letters, 793, L36

Fynbo, J. P. U., Watson, D., Thöne, C. C., et al. 2006, Nature, 444, 1047

Gajjar, V., Siemion, A. P. V., Price, D. C., et al. 2018, Astrophysical Journal, 863, 2

Gal-Yam, A., Ofek, E. O., Poznanski, D., et al. 2006, Astrophysical Journal, 639, 331

Galama, T. J., Vreeswijk, P. M., van Paradijs, J., et al. 1998, Nature, 395, 670

Gehrels, N., Chincarini, G., Giommi, P., et al. 2004, ApJ, 611, 1005

Gehrels, N., Norris, J. P., Barthelmy, S. D., et al. 2006, Nature, 444, 1044

Gendre, B., Stratta, G., Atteia, J. L., et al. 2013, ApJ, 766, 30

Geng, J. J. & Huang, Y. F. 2015, Astrophysical Journal, 809, 24

Ghirlanda, G., Ghisellini, G., & Lazzati, D. 2004, ApJ, 616, 331

Ghisellini, G., Ghirlanda, G., Nava, L., & Celotti, A. 2010, Monthly Notices of the Royal Astronomical Society, 403, 926

Gourdji, K., Michilli, D., Spitler, L. G., et al. 2019, Astrophysical Journal, 877, L19

Granot, J., Piran, T., & Sari, R. 2000, in American Institute of Physics Conference Series, Vol. 526, Gamma-ray Bursts, 5th Huntsville Symposium, ed. R. M. Kippen, R. S. Mallozzi, & G. J. Fishman, 489–493

Granot, J. & Sari, R. 2002, Astrophysical Journal, 568, 820

Green, A. J. & Flynn, C. 2015, in IAU General Assembly, Vol. 29, 2256233

Gu, W.-M., Dong, Y.-Z., Liu, T., Ma, R., & Wang, J. 2016, Astrophysical Journal, Letters, 823, L28

Guetta, D. & Della Valle, M. 2007, Astrophysical Journal, Letters, 657, L73

Guidorzi, C., Dichiara, S., & Amati, L. 2016, A&A, 589, A98

Guidorzi, C., Kobayashi, S., Perley, D. A., et al. 2011, MNRAS, 417, 2124

Guiriec, S., Connaughton, V., Briggs, M. S., et al. 2011, ApJ, 727, L33

Guiriec, S., Daigne, F., Hascoët, R., et al. 2013, Astrophysical Journal, 770, 32

Gupta, P. D. & Saini, N. 2018, Journal of Astrophysics and Astronomy, 39, 14

Hessels, J. W. T., Spitler, L. G., Seymour, A. D., et al. 2018, arXiv:1811.10748 [[arXiv]1811.10748]

Hirata, K., Kajita, T., Koshiba, M., et al. 1987, Physical Review Letters, 58, 1490

Istomin, Y. N. 2018, Monthly Notices of the Royal Astronomical Society, 478, 4348

Iwazaki, A. 2015, arXiv e-prints, arXiv:1512.06245

Izzo, L., Rueda, J. A., & Ruffini, R. 2012, Astronomy and Astrophysics, 548, L5

James, C. W. 2019, Monthly Notices of the Royal Astronomical Society, 486, 5934

Johnston, S., Taylor, R., Bailes, M., et al. 2008, Experimental Astronomy, 22, 151

Kaneko, Y., Preece, R. D., Briggs, M. S., et al. 2006, ApJS, 166, 298

Karastergiou, A., Chennamangalam, J., Armour, W., et al. 2015, Monthly Notices of the Royal Astronomical Society, 452, 1254

Kashiyama, K., Ioka, K., & Mészáros, P. 2013, Astrophysical Journal, Letters, 776, L39

Katz, J. I. 2017, Monthly Notices of the Royal Astronomical Society, 467, L96

Keane, E. F., Johnston, S., Bhandari, S., et al. 2016, Nature, 530, 453

Keane, E. F., Kramer, M., Lyne, A. G., Stappers, B. W., & McLaughlin, M. A. 2011, Monthly Notices of the Royal Astronomical Society, 415, 3065

Keith, M. J., Jameson, A., van Straten, W., et al. 2010, Monthly Notices of the Royal Astronomical Society, 409, 619

Klebesadel, R. W., Strong, I. B., & Olson, R. A. 1973, Astrophysical Journal, Letters, 182, L85

Klotz, A., Gendre, B., Stratta, G., et al. 2008, Astronomy and Astrophysics, 483, 847

Kovacevic, M., Izzo, L., Wang, Y., et al. 2014, Astronomy and Astrophysics, 569, A108

Kulkarni, S. R., Frail, D. A., Wieringa, M. H., et al. 1998, Nature, 395, 663

Kumar, P. & Zhang, B. 2015, Phys. Rep., 561, 1

Lawrence, E., Vander Wiel, S., Law, C., Burke Spolaor, S., & Bower, G. C. 2017, Astronomical Journal, 154, 117

Leibler, C. N. & Berger, E. 2010, Astrophysical Journal, 725, 1202

Li, L.-B., Huang, Y.-F., Geng, J.-J., & Li, B. 2018, Research in Astronomy and Astrophysics, 18, 061

Lien, A., Sakamoto, T., Barthelmy, S. D., et al. 2016, ApJ, 829, 7

Liu, T., Romero, G. E., Liu, M.-L., & Li, A. 2016, Astrophysical Journal, 826, 82

Liu, X. 2018, Astrophysics and Space Science, 363, 242

Lloyd, N. M. & Petrosian, V. 2000, Astrophysical Journal, 543, 722

Loeb, A., Shvartzvald, Y., & Maoz, D. 2014, Monthly Notices of the Royal Astronomical Society, 439, L46

Lorimer, D. R., Bailes, M., McLaughlin, M. A., Narkevic, D. J., & Crawford, F. 2007, Science, 318, 777

Lü, H.-J., Zhang, B., Liang, E.-W., Zhang, B.-B., & Sakamoto, T. 2014, MNRAS, 442, 1922

Lyutikov, M. 2013, Astrophysical Journal, 768, 63

Lyutikov, M., Burzawa, L., & Popov, S. B. 2016, Monthly Notices of the Royal Astronomical Society, 462, 941

Macquart, J.-P. & Ekers, R. D. 2018, Monthly Notices of the Royal Astronomical Society, 474, 1900

Macquart, J.-P., Shannon, R. M., Bannister, K. W., et al. 2019, Astrophysical Journal, Letters, 872, L19

Marcote, B., Paragi, Z., Hessels, J. W. T., et al. 2017, Astrophysical Journal, Letters, 834, L8

Margutti, R., Moretti, A., Pasotti, F., et al. 2008, Astronomy and Astrophysics, 480, 677

Margutti, R., Zaninoni, E., Bernardini, M. G., et al. 2013, MNRAS, 428, 729

Masui, K., Lin, H.-H., Sievers, J., et al. 2015, Nature, 528, 523

McLaughlin, M. A., Lyne, A. G., Lorimer, D. R., et al. 2006, Nature, 439, 817

Meegan, C., Lichti, G., Bhat, P. N., et al. 2009, ApJ, 702, 791

Melandri, A., Mundell, C. G., Kobayashi, S., et al. 2008, ApJ, 686, 1209

Meszaros, P., Rees, M. J., & Papathanassiou, H. 1994, Astrophysical Journal, 432, 181

Metzger, B. D., Margalit, B., & Sironi, L. 2019, Monthly Notices of the Royal Astronomical Society, 485, 4091

Metzger, M. R., Djorgovski, S. G., Kulkarni, S. R., et al. 1997, Nature, 387, 878

Michilli, D., Seymour, A., Hessels, J. W. T., et al. 2018, Nature, 553, 182

Mingarelli, C. M. F., Levin, J., & Lazio, T. J. W. 2015, Astrophysical Journal, Letters, 814, L20

Moretti, A., Margutti, R., Pasotti, F., et al. 2008, Astronomy and Astrophysics, 478, 409

Moriya, T. J. 2016, Astrophysical Journal, Letters, 830, L38

Mottez, F. & Zarka, P. 2014, Astronomy and Astrophysics, 569, A86

Nappo, F., Pescalli, A., Oganesyan, G., et al. 2017, Astronomy and Astrophysics, 598, A23

Norris, J. P., Gehrels, N., & Scargle, J. D. 2010, Astrophysical Journal, 717, 411

Ofek, E. O., Cenko, S. B., Gal-Yam, A., et al. 2007, Astrophysical Journal, 662, 1129

Oganesyan, G., Nava, L., Ghirlanda, G., & Celotti, A. 2017, ApJ, 846, 137

Oganesyan, G., Nava, L., Ghirlanda, G., & Celotti, A. 2018, Astronomy and Astrophysics, 616, A138

Oppermann, N., Yu, H.-R., & Pen, U.-L. 2018, Monthly Notices of the Royal Astronomical Society, 475, 5109

Page, K. L., Starling, R. L. C., Fitzpatrick, G., et al. 2011, MNRAS, 416, 2078

Palmer, D. M., Barthelmy, S. D., Cummings, J. R., et al. 2017, GRB Coordinates Network, 20999, 1

Pe'er, A. 2015, Advances in Astronomy, 2015, 22

Petroff, E., Bailes, M., Barr, E. D., et al. 2015, Monthly Notices of the Royal Astronomical Society, 447, 246

Petroff, E., Burke-Spolaor, S., Keane, E. F., et al. 2017, Monthly Notices of the Royal Astronomical Society, 469, 4465

Petroff, E., Hessels, J. W. T., & Lorimer, D. R. 2019, The Astronomy and Astrophysics Review, 27, 4

Pian, E., Tomasella, L., Cappellaro, E., et al. 2017, Monthly Notices of the Royal Astronomical Society, 466, 1848

Platts, E., Weltman, A., Walters, A., et al. 2019, Physical Review Report, 821, 1

Popov, S. B. & Postnov, K. A. 2010, in Evolution of Cosmic Objects through their Physical Activity, ed. H. A. Harutyunian, A. M. Mickaelian, & Y. Terzian, 129–132

Prajs, S., Sullivan, M., Smith, M., et al. 2017, Monthly Notices of the Royal Astronomical Society, 464, 3568

Preece, R. D., Briggs, M. S., Mallozzi, R. S., et al. 1998, Astrophysical Journal, Letters, 506, L23

Price, D. C., Gajjar, V., Dhar, A., et al. 2018, The Astronomer's Telegram, 11376, 1

Quimby, R. M., Yuan, F., Akerlof, C., & Wheeler, J. C. 2013, Monthly Notices of the Royal Astronomical Society, 431, 912

Ramirez-Ruiz, E., Granot, J., Kouveliotou, C., et al. 2005, Astrophysical Journal, Letters, 625, L91

Rane, A., Lorimer, D. R., Bates, S. D., et al. 2016, Monthly Notices of the Royal Astronomical Society, 455, 2207

Ravi, V., Catha, M., D'Addario, L., et al. 2019, Nature, 572, 352

Ravi, V., Shannon, R. M., Bailes, M., et al. 2016, Science, 354, 1249

Ravi, V., Shannon, R. M., & Jameson, A. 2015, Astrophysical Journal, Letters, 799, L5

Rees, M. J. 1977, Nature, 266, 333

Reichart, D. E. 1997, Astrophysical Journal, Letters, 485, L57

Ripa, J. & Meszaros, A. 2015, arXiv e-prints, arXiv:1507.05761

Rizzuto, D., Guidorzi, C., Romano, P., et al. 2007, MNRAS, 379, 619

Roming, P. W. A., Kennedy, T. E., Mason, K. O., et al. 2005, Space Sci. Rev., 120, 95

Ruffini, R., Bernardini, M. G., Bianco, C. L., et al. 2008, in The Eleventh Marcel Grossmann Meeting On Recent Developments in Theoretical and Experimental General Relativity, Gravitation and Relativistic Field Theories, 368–505

Ruffini, R., Bianco, C. L., Fraschetti, F., Xue, S.-S., & Chardonnet, P. 2001, Astrophysical Journal, Letters, 555, L117

Rykoff, E. S., Smith, D. A., Price, P. A., et al. 2004, Astrophysical Journal, 601, 1013

Salvaterra, R., Della Valle, M., Campana, S., et al. 2009, Nature, 461, 1258

Sari, R., Piran, T., & Narayan, R. 1998, ApJ, 497, L17

Scargle, J. D., Norris, J. P., Jackson, B., & Chiang, J. 2013, ApJ, 764, 167

Scholz, P., Spitler, L. G., Hessels, J. W. T., et al. 2016, Astrophysical Journal, 833, 177

Shand, Z., Ouyed, A., Koning, N., & Ouyed, R. 2016, Research in Astronomy and Astrophysics, 16, 80

Shannon, R. M., Macquart, J. P., Bannister, K. W., et al. 2018, Nature, 562, 386

Smartt, S. J., Chen, T. W., Jerkstrand, A., et al. 2017, Nature, 551, 75

Spitler, L. G., Cordes, J. M., Hessels, J. W. T., et al. 2014, Astrophysical Journal, 790, 101

Spitler, L. G., Scholz, P., Hessels, J. W. T., et al. 2016, Nature, 531, 202

Stamatikos, M., Barthelmy, S. D., Cummings, J. R., et al. 2016, GRB Coordinates Network, 20188, 1

Strong, I. B. 1975, in Astrophysics and Space Science Library, Vol. 48, Neutron Stars, Black Holes and Binary X-ray Sources, ed. H. Gursky & R. Ruffini, 47–58

Tendulkar, S. P., Bassa, C. G., Cordes, J. M., et al. 2017, Astrophysical Journal, Letters, 834, L7

Thornton, D., Stappers, B., Bailes, M., et al. 2013, Science, 341, 53

Titarchuk, L., Farinelli, R., Frontera, F., & Amati, L. 2012, ApJ, 752, 116

Totani, T. 2013, Publications of the Astronomical Society of Japan, 65, L12

Vachaspati, T. 2008, Physical Review Letters, 101, 141301

van Haarlem, M. P., Wise, M. W., Gunst, A. W., et al. 2013, Astronomy and Astrophysics, 556, A2

van Paradijs, J., Groot, P. J., Galama, T., et al. 1997, Nature, 386, 686

Van Waerbeke, L. & Zhitnitsky, A. 2019, Physical Review D, 99, 043535

Vanderplas, J., Connolly, A., Ivezić, Ž., & Gray, A. 2012, in Conference on Intelligent Data Understanding (CIDU), 47 –54

Vedantham, H. K., Ravi, V., Hallinan, G., & Shannon, R. M. 2016, Astrophysical Journal, 830, 75

Vieyro, F. L., Romero, G. E., Bosch-Ramon, V., Marcote, B., & del Valle, M. V. 2017, Astronomy and Astrophysics, 602, A64

Virgili, F. J., Liang, E.-W., & Zhang, B. 2009, Monthly Notices of the Royal Astronomical Society, 392, 91

Wang, L.-J., Han, Y.-H., Xu, D., et al. 2016, Astrophysical Journal, 831, 41

Wang, X.-G., Zhang, B., Liang, E.-W., et al. 2018, Astrophysical Journal, 859, 160

Yang, B., Jin, Z.-P., Li, X., et al. 2015, NatCo, 6

Yang, Y.-P. & Zhang, B. 2016, Astrophysical Journal, Letters, 830, L31

Ye, J., Wang, K., & Cai, Y.-F. 2017, European Physical Journal C, 77, 720

Yi, S.-X., Cheng, K. S., & Luo, R. 2019, Monthly Notices of the Royal Astronomical Society, 483, 4197

Yonetoku, D., Murakami, T., Nakamura, T., et al. 2004, ApJ, 609, 935

Zhang, B. 2011, Comptes Rendus Physique, 12, 206

Zhang, B. 2014, Astrophysical Journal, Letters, 780, L21

Zhang, B. 2017a, Astrophysical Journal, Letters, 836, L32

Zhang, B. 2018, Astrophysical Journal, Letters, 854, L21

Zhang, B.-B., Zhang, B., & Castro-Tirado, A. J. 2016, ApJ, 820, L32

Zhang, F. 2017b, Astronomy and Astrophysics, 598, A88

Zhang, Y., Geng, J.-J., & Huang, Y.-F. 2018, Astrophysical Journal, 858, 88

Appendix

In this section, we report the published papers, in order of appearance in the thesis.

A&A 608, A52 (2017)
DOI: 10.1051/0004-6361/201730704

Astronomy & Astrophysics

False outliers of the $E_{p,i} - E_{iso}$ correlation?

R. Martone[1,2], L. Izzo[3], M. Della Valle[4,5], L. Amati[6], G. Longo[2], and D. Götz[7]

[1] Dipartimento di Fisica e Scienze della Terra, Universitá di Ferrara, via Saragat 1, 44122 Ferrara, Italy
e-mail: mrtrnt@unife.it
[2] Universitá di Napoli "Federico II", Dipartimento di Fisica "Ettore Pancini", C. U. Monte S. Angelo, 80126 Napoli, Italy
[3] Instituto de Astrofisica de Andalucia (IAA-CSIC), Glorieta de la Astronomia s/n, 18008 Granada, Spain
[4] INAF–Osservatorio Astronomico di Napoli, Salita Moiariello, 16, 80131 Napoli, Italy
[5] International Center for Relativistic Astrophysics, Piazza della Repubblica 10, 65122 Pescara, Italy
[6] INAF–IASF Bologna, via P. Gobetti, 101, 40129 Bologna, Italy
[7] AIM–CEA/DRF/Irfu/Service d'Astrophysique, Orme des Merisiers, 91191 Gif-sur-Yvette, France

Received 27 February 2017 / Accepted 9 August 2017

ABSTRACT

Context. In the context of an in-depth understanding of GRBs and their possible use in cosmology, some important correlations between the parameters that describe their emission have been discovered, among which the "$E_{p,i} - E_{iso}$" correlation is the most studied. Because of this, it is fundamental to shed light on the peculiar behaviour of a few events, namely GRB 980425 and GRB 031203, that appear to be important outliers of the $E_{p,i} - E_{iso}$ correlation.
Aims. In this paper we investigate if the locations of GRB 980425 and GRB 031203, the two (apparent) outliers of the correlation, may be due to an observational bias caused by the lacking detection of the soft X-ray emissions associated with these GRBs, from respectively the Burst And Transient Source Experiment (BATSE) detector on-board the Compton Gamma-Ray Observer and INTEGRAL, that were operating at the epoch at which the observations were carried out. We analyse the observed emission of other similar sub-energetic bursts (GRBs 060218, 100316D and 161219B) observed by *Swift* and whose integrated emissions match the $E_{p,i} - E_{iso}$ relation. We simulate their integrated and time-resolved emissions as would have been observed by the same detectors that observed GRB 980425 and GRB 031203, aimed at reconstructing the light curve and spectra of these bursts.
Methods. We estimate the $E_{p,i}$ and the E_{iso} parameters from the time-resolved and total integrated simulated spectra of GRBs 060218, 100316D and 161219B as observed by *Beppo*SAX, BATSE, INTEGRAL, and the Wide Field Monitor (WFM) proposed for the Large Observatory For X-ray Timing (LOFT) and enhanced X-ray Timing and Polarimetry (eXTP) missions.
Results. If observed by old generation instruments, GRBs 060218, 100316D, and 161219B would appear as outliers of the $E_{p,i}$–E_{iso} relation, while if observed with *Swift* or the WFM GRB 060218 would perfectly match the correlation. We also note that the instrument BAT alone (15−150 keV) did measure GRB 060218 as an outlier.
Conclusions. We suggest that if GRB 980425 and GRB 031203 would have been observed by *Swift* and by eXTP, they might have matched the $E_{p,i}$–E_{iso} relation. This provides strong support to the idea that instrumental biases can cause some events in the lower left corner of the $E_{p,i} - E_{iso}$ plane to appear as outliers of the so-called Amati relation.

Key words. gamma-ray burst: general – gamma-ray burst: individual: GRB 060218 – methods: data analysis

1. Introduction

Observations of long-duration gamma-ray bursts (GRBs) in the past decades have shown the many empirical relations that link some of the fundamental parameters of GRBs such, as the isotropic energy E_{iso} that is emitted in gamma rays, and the peak energy of the prompt emission spectrum $E_{p,i}$, the peak luminosity L_p of the prompt emission (Amati et al. 2002; Ghirlanda et al. 2004; Yonetoku et al. 2004; Liang & Zhang 2005; Dainotti et al. 2008; Bernardini et al. 2012; Margutti et al. 2013; Izzo et al. 2015).

We focus on the most popular of them, the $E_{p,i} - E_{iso}$ correlation, which is also known as the Amati relation (Amati et al. 2002; Amati 2006). This relation stated that the total gamma-ray isotropic energy (E_{iso}) emitted in long GRBs correlates with the rest-frame value of the energy spectrum at which their gamma-ray emission peak ($E_{p,i}$). We here estimate the isotropic output using the quantity $E_{\gamma,iso}$, which represents the total energetic output in the rest-frame range 1−10 000 keV.

To date more than 200 GRBs match the $E_{p,i}$–E_{iso} relation; however, after 20 yr, it is still debated that the closest GRBs ever discovered, GRB 980425 at $z = 0.0085$ ($d = 40$ Mpc), appears to be a remarkable outlier of the Amati relation (Ghisellini et al. 2006; Amati 2006). This situation is still more disturbing after noting that GRB 980425 was found to be the first GRB associated with a supernova (SN), the SN 1998bw (Galama et al. 1998), and therefore it is recognized as the prototype of the GRB-SN connection (Woosley & Bloom 2006; Della Valle 2011). The existence of outliers of the Amati relation should also be clarified in view of both understanding the emission processes at play in the GRB phenomenon and the frequent use of GRBs in cosmological studies (Amati et al. 2008; Amati & Della Valle 2013; Izzo et al. 2015). We suggest that the location of GRB 980425 in the $E_{p,i} - E_{iso}$ plane is very likely due to an observational bias caused by the sensitivity range 25−2000 keV of the Burst And Transient Source Experiment (BATSE) detector on board the Compton Gamma-Ray Observer (CGRO; Meegan et al. 1992). Similar arguments apply to the case of an other sub-energetic and nearby ($z = 0.105$) event: GRB 031203 (Mazzali et al. 2006; Watson et al. 2006).

To reach our goal, we show that nearby and sub-energetic bursts with an associated SN, GRB 060218 (Campana et al. 2006), GRB 100316D (Starling et al. 2011) and GRB 161219B (Cano et al. 2017) observed by the *Swift* Burst Alert Telescope

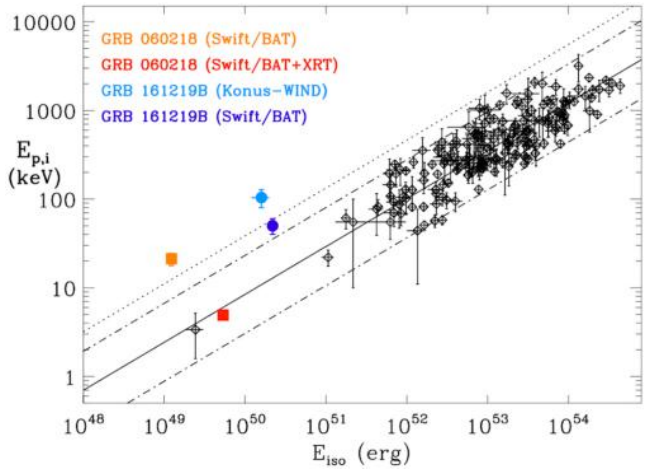

Fig. 1. Location in the $E_{\rm p,i} - E_{\rm iso}$ plane of GRB 161219B as observed by *Swift*-BAT and Konus-WIND and of GRB 060218 as observed by *Swift*-BAT and by *Swift*-BAT+XRT. *Swift*-BAT is more sensitive than Konus-WIND, thus allowing a more precise estimate of the $E_{\rm p,i}$ and $E_{\rm iso}$ parameters for GRB 161219B and finding it more consistent with the Amati relation. In the outstanding case of GRB 060218, the emission in the soft X-ray band, which can only be detected by using *Swift*-XRT, makes this event, which otherwise would have been classified as an outlier, fully consistent with the $E_{\rm p,i} - E_{\rm iso}$ correlation. In the plot, the dot-dashed (dotted) lines refer to the 2 (3) sigma error around the best-fit line.

(BAT; Barthelmy et al. 2005) in the energy range 15−150 keV and the X-Ray Telescope (XRT; Burrows et al. 2005) in the energy range 0.3−10 keV, consistent with the $E_{\rm p,i} - E_{\rm iso}$ relation, would appear as outliers of the Amati relation if they had been observed with BATSE.

These GRBs are perfect for our purposes because, unlike other similar low-energetic events, they have a continuous coverage in time of their prompt emission by *Swift*-BAT, and in the case of GRB 060218 and GRB 100316D, also by XRT. The importance of the different instrument characteristics in determining the position of an event in the $E_{\rm p,i} - E_{\rm iso}$ plane can be appreciated considering Fig. 1, where we highlight the positions of GRB 060218 and GRB 161219B according to different detectors: it is clearly visible that when using measurements by instruments with better sensitivity and lower energy threshold these events become more consistent with the correlation. GRB 060218 is the emblem of this kind of behaviour, perfectly matching the best-fit of the $E_{\rm p,i} - E_{\rm iso}$ correlation when seen by *Swift*-XRT+BAT, and appearing as an outlier when observed with *Swift*-BAT alone, as we show in this work.

This work is organized as follows: in Sect. 2 we present the spectral properties of GRBs 060218, 100316D and 161219B and we introduce the method at the base of this paper. In Sect. 3 we describe the spectral analysis of these three GRBs, and in Sect. 4 we present the simulations of these GRBs as if they were observed by BATSE and other detectors. In the last section we report our conclusions.

2. *Swift* data analysis

In the following part of this article, we mainly focus on the case of GRB 060218, which presents one of the best datasets of the observed GRBs. Additional material regarding GRB 100316D and GRB 161219B, such as figures and tables, can be found in the appendix.

2.1. GRB 060218

GRB 060218 was discovered by *Swift* (Campana et al. 2006) and was found to be associated with SN 2006aj (Pian et al. 2006) at the redshift of $z = 0.0331$. Soft X-ray observations pointed out the presence of a thermal component, which originated in the breakout of a shock propagating into the wind surrounding the progenitor star (Campana et al. 2006; Waxman et al. 2007). The main feature that distinguish this GRB from more energetic GRBs is the long duration (∼3000 s) of the prompt emission observed down to X-rays, which is clearly different from the canonical emission observed in almost all GRBs (Nousek et al. 2006). Thanks to this very long duration (and its proximity) it was possible to detect most of the prompt emission with both BAT (15−150 keV) and XRT (0.2−10 keV). The integrated BAT+XRT spectrum is characterized by an intrinsic peak energy of $E_{\rm p,i} = 4.9$ keV and a total integrated isotropic energy of $E_{\rm iso} = 6.2 \times 10^{49}$ erg. With these values, GRB 060218 matches the Amati relation (see Fig. 6).

Owing to its low luminosity, low redshift, and the associated Sn, GRB 060218 has been considered a "twin" of GRB 980425 and GRB 031203 (Ghisellini et al. 2006), but it shows a different time duration and high-energy emission. It is consequently very interesting to derive the spectrum of GRB 060218 and its location in the $E_{\rm p,i} - E_{\rm iso}$ plane as it would have been observed by the same instruments as observed GRB 980425 (*Beppo*SAX, Frontera et al. 2000; BATSE, Meegan et al. 1992) and GRB 031203 (INTEGRAL, Mereghetti et al. 2003). We also consider the case for eXTP (Amati et al. 2013; Zhang et al. 2016), a planned mission dedicated to observing the X-ray transient sky in the soft X-ray energies.

We have reproduced the *Swift* data analysis as reported in Campana et al. (2006) using the same time intervals, and the results are reported in Fig. 2. The XRT spectral data were obtained for the corresponding BAT time intervals following the canonical procedure for GRB data reduction, starting with the `xrtpipeline` package, which runs all the tasks for XRT data processing in sequence. Since the X-ray emission from GRB 060218 was very bright, we applied the pile-up correction for the Window Timing mode, as the source presented count rates higher than 100 counts s^{-1} for a large part of its emission. We therefore selected a box with an annulus centred on the brightest pixel, as has been well described in Romano et al. (2006). After the pile-up correction, we obtained background files with XSELECT and generated the corresponding ancillary response function file with the `xrtmkarf` package. Finally, we grouped the data in order to have at least ten counts in each spectral bin; for this, we used the `grppha` package.

Since the complete dataset is composed of four spectra for which there are no XRT data, we divided the sample into two sub-datasets: 1) the first 4 BAT spectra lasting a total of $t_{\rm D1} = 340$ s, and 2) the following 12 BAT and XRT spectra, lasting a total of $t_{\rm D2} = 2387$ s and which cover the range 0.3–150 keV, with a data gap between 10–15 keV. The spectral data analysis was performed using the XSPEC fitting package (Arnaud 1996), assuming solar abundances as given in Wilms et al. (2000) and a cosmological model with $\Omega_\Lambda = 0.73$, $H_0 = 70\,{\rm km\,s^{-1}\,Mpc^{-1}}$ and $q_0 = -0.5$. For the BAT + XRT dataset, we found that the best fit in all single spectra is given by an absorbed black-body plus a power law with an exponential cut-off, in agreement with the results of Campana et al. (2006). The results of the time-resolved spectral analysis of the two datasets are shown in Tables 1 and 2, while in Fig. 2 we report as an example the best-fit for the *Swift*-BAT+XRT spectrum 5 using a function composed of an

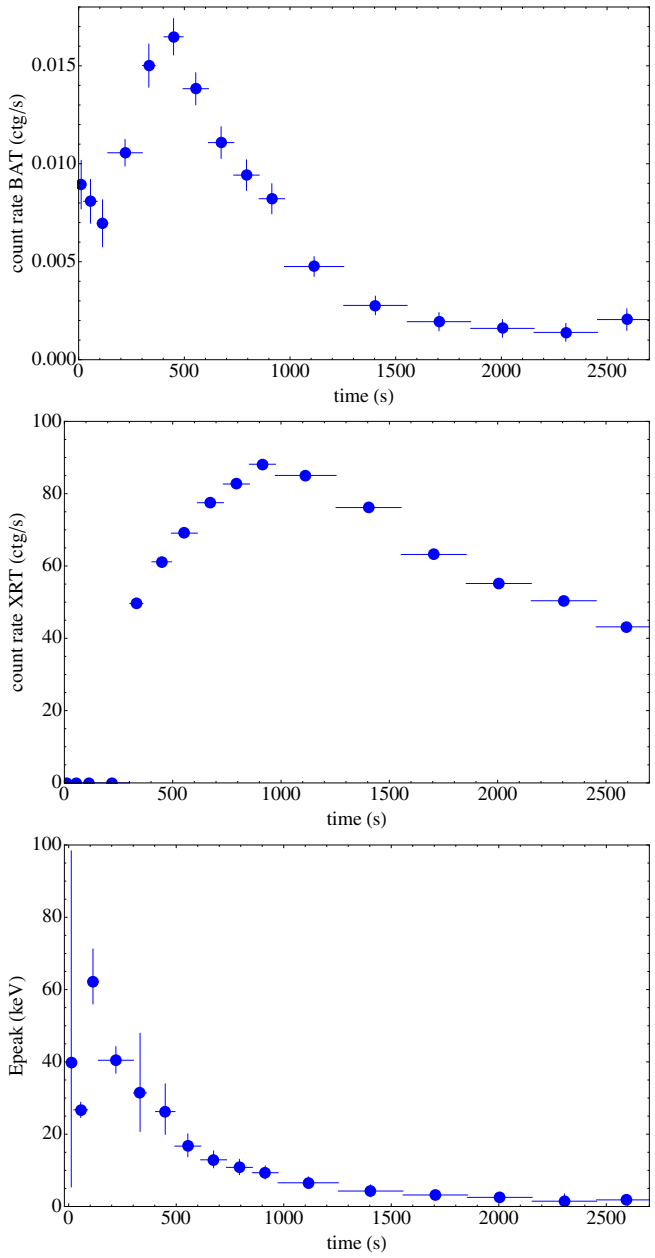

Fig. 2. Net count rate as detected by *Swift*-BAT (15–150 keV; *upper panel*) and by *Swift*-XRT (0.3–10 keV; *middle panel*) after pileup correction. *Lower panel*: variation of the intrinsic peak energy of GRB 060218 as detected by *Swift*.

absorbed black-body plus a power law with an exponential energy cut-off.

The last step consists of computing the integrated spectrum of GRB 060218. We obtained integrated spectra for both datasets using the `mathpha` task, which is provided within the `heasoft` package for data analysis[1]. We then fitted the integrated spectra considering a cut-off power law for the first dataset and an absorbed cut-off power law (Band 2003) plus a black body for the second dataset, obtaining results that are very similar to those presented in Campana et al. (2006). We fixed the galactic column density to the value $N(H_{\rm gal}) = 1.42 \times 10^{21}$ cm^{-2} (see Dickey & Lockman 1990), while for the extragalactic column density, we chose the median of the densities obtained in the

[1] http://heasarc.gsfc.nasa.gov/lheasoft

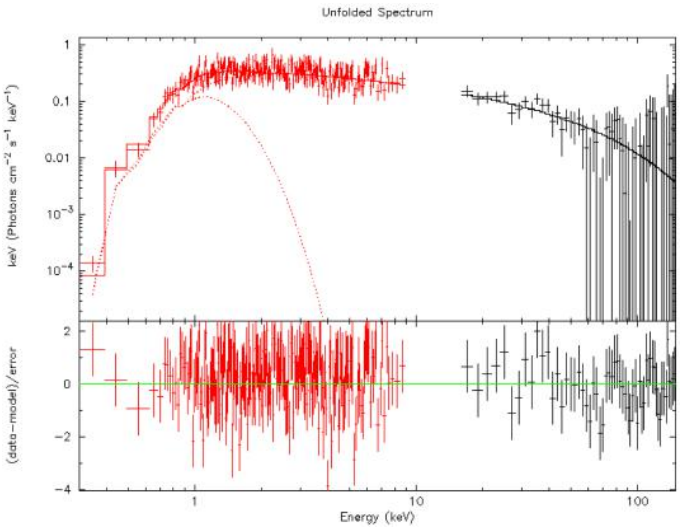

Fig. 3. Best-fit of the *Swift*-BAT+XRT spectrum number 5 (see Table 2) obtained with an absorbed blackbody and a power-law with an exponential energy cutoff function.

different spectra into which our dataset is divided: $N(H_{\rm intr}) = 3.58 \times 10^{21}$ cm^{-2}. The results of the fits are shown in Table 2. From these results, we have computed the values for the intrinsic peak energy $E_{\rm p,i}$ and isotropic energy emitted in the time intervals corresponding to the two datasets, and the evolution of $E_{\rm p}$ is shown in Fig. 2. Finally, we compute the total integrated $E_{\rm p,i}$ and $E_{\rm iso}$ values for *Swift*, by considering a Band function alone and we obtain $E_{\rm p,i,D2} = 4.92 \pm 0.57$ keV and $E_{\rm iso,D2} = (3.10 \pm 0.10) \times 10^{49}$ erg.

2.2. GRB 100316D

GRB 100316D was also discovered by *Swift* (Stamatikos et al. 2010) in the environment of an extended galaxy at the redshift $z = 0.059$ (Vergani et al. 2010). The initial BAT and XRT light curves were very similar to the observed emission of GRB 060218 (Sakamoto et al. 2010) and a thermal component was also observed in X-rays (Starling et al. 2012), although its presence has not been confirmed (Margutti et al. 2013). An SN associated with the burst was also discovered a few days after the GRB discovery when its luminosity was still increasing (Chornock et al. 2010; Bufano et al. 2012). The similarity between the temporal and spectral properties of GRB 100316D with those of GRB 060218, makes GRB 100316D an additional test bed for our purposes. Its T_{90} spectrum, however, is best fitted in the 15−150 keV energy range by a simple power-law function with photon index $\gamma = -2.56 \pm 0.18$. We then derive that this GRB is extremely soft, with a peak energy below the lower energy threshold of *Swift*-BAT ($E_{\rm p,i} \leq 15$ keV). In analogy with GRB 060218, we considered the luminous X-ray tail for the computation of the $E_{\rm p,i}$ and $E_{\rm iso}$ parameters. However, XRT started to observe GRB 100316D only 144 s after the *Swift*-BAT trigger, and 297 s after the first emission observed by BAT, see Fig. A.2.

In order to build an integrated spectrum including both BAT and XRT data, we simulated the XRT emission in the time interval (T_0 − 153, T_0+144) s, using the `fakeit` package available in the HEAsoft software packages, and considering the best fit found for the BAT spectrum. After obtaining an XRT spectrum for the first *Swift* orbit using the same procedure as described in the previous section, we computed a total integrated

Table 1. *Swift*-BAT (15−150 keV) spectral fits data results of the first dataset of GRB 060218, that includes the first four BAT spectra (Δt_{D1} = 340 s).

#	Δt (s)	γ	E_{cutoff} (keV)	Norm Photons keV^{-1} cm^{-2} s^{-1}	Flux (10^{-9} erg/cm^2/s)	χ^2/d.o.f.
1	64	$2.07^{+0.44}_{-0.38}$	–	$6.6^{+2.6}_{-2.2} \times 10^{-3}$	5.0	63.2/56
2	64	$2.61^{+0.43}_{-0.37}$	–	$9.6^{+2.9}_{-2.5} \times 10^{-3}$	4.3	59.6/56
3	49	$2.55^{+0.66}_{-0.51}$	–	$7.2^{+3.1}_{-2.5} \times 10^{-3}$	3.4	43.0/56
4	163	$0.91^{+0.85}_{-1.07}$	$35.9^{+3.2}_{-3.0}$	$9.9^{+0.95}_{-0.95} \times 10^{-2}$	5.1	26.2/55

Table 2. *Swift*-BAT+XRT (0.3−150 keV) spectral fit data results of the second dataset of GRB 060218, which includes the last 12 spectra (Δt_{D2} = 2387 s).

#	Δt (s)	γ	E_{cutoff} (keV)	Norm CPO Photons keV^{-1} cm^{-2} s^{-1}	kT (keV)	Norm BB 10^{37} erg s^{-1}	Flux BAT (10^{-9}) (erg/cm^2/s)	Flux XRT (10^{-9}) (erg/cm^2/s)	χ^2/d.o.f.
5	60	$1.36^{+0.11}_{-0.12}$	47^{+23}_{-13}	$0.51^{+0.07}_{-0.07}$	$0.197^{+0.033}_{-0.030}$	$1.23^{+0.30}_{-0.33}$	7.0	3.7	277.8/281
6	90	$1.361^{+0.067}_{-0.078}$	$39.7^{+10.8}_{-8.2}$	$0.68^{+0.05}_{-0.06}$	$0.171^{+0.023}_{-0.017}$	$1.19^{+0.34}_{-0.33}$	7.7	4.7	391.9/412
7	120	$1.290^{+0.065}_{-0.070}$	$22.8^{+4.1}_{-3.3}$	$0.80^{+0.05}_{-0.05}$	$0.151^{+0.018}_{-0.016}$	$1.67^{+0.47}_{-0.38}$	5.5	5.5	398.3/505
8	120	$1.159^{+0.084}_{-0.090}$	$14.9^{+2.4}_{-2.0}$	$0.80^{+0.06}_{-0.07}$	$0.177^{+0.017}_{-0.016}$	$2.05^{+0.35}_{-0.32}$	4.1	6.1	491.6/527
9	120	$1.244^{+0.082}_{-0.088}$	$13.9^{+2.4}_{-2.0}$	$0.96^{+0.07}_{-0.07}$	$0.169^{+0.017}_{-0.016}$	$2.12^{+0.40}_{-0.36}$	3.3	6.2	553.9/539
10	120	$1.225^{+0.082}_{-0.089}$	$11.7^{+2.0}_{-1.7}$	$1.06^{+0.07}_{-0.07}$	$0.162^{+0.015}_{-0.014}$	$2.47^{+0.41}_{-0.41}$	2.7	6.6	461.5/542
11	280	$1.296^{+0.065}_{-0.072}$	$9.0^{+1.3}_{-1.2}$	$1.19^{+0.05}_{-0.05}$	$0.150^{+0.008}_{-0.008}$	$2.98^{+0.37}_{-0.34}$	1.3	6.0	717.9/670
12	300	$1.15^{+0.18}_{-0.23}$	$4.9^{+1.7}_{-1.2}$	$1.15^{+0.05}_{-0.06}$	$0.153^{+0.007}_{-0.007}$	$3.67^{+0.39}_{-0.38}$	2.6	4.7	727.2/631
13	300	$0.80^{+0.21}_{-0.22}$	$2.57^{+0.50}_{-0.37}$	$1.09^{+0.06}_{-0.06}$	$0.152^{+0.006}_{-0.006}$	$4.58^{+0.36}_{-0.35}$	0.023	3.4	570.0/566
14	300	$1.33^{+0.22}_{-0.23}$	$3.67^{+1.21}_{-0.75}$	$1.02^{+0.06}_{-0.06}$	$0.145^{+0.005}_{-0.005}$	$5.20^{+0.43}_{-0.43}$	0.038	2.7	583.9/528
15	300	$1.74^{+0.27}_{-0.27}$	$5.5^{+4.6}_{-1.7}$	$0.95^{+0.06}_{-0.06}$	$0.147^{+0.005}_{-0.005}$	$5.58^{+0.48}_{-0.51}$	0.060	2.3	475.1/488
16	277	$1.49^{+0.31}_{-0.32}$	$3.45^{+1.79}_{-0.90}$	$0.80^{+0.06}_{-0.06}$	$0.144^{+0.004}_{-0.004}$	$5.97^{+0.46}_{-0.48}$	0.014	1.9	519.1/430

spectrum for both detectors by using the `mathpha` package, which is also available in the HEAsoft suite. The fit of this latter spectrum, with a total exposure time of 891 s, is best fit with an absorbed power-law with an exponential cut-off at $E_{cut} = 18.7^{+1.1}_{-1.0}$ keV and a photon index of $\gamma = -1.26^{+0.02}_{-0.02}$, see also Fig. A.1. With these values, we estimate an intrinsic peak energy of $E_{p,i} = 14.69^{+0.94}_{-0.89}$ keV and an isotropic energy of $E_{iso} = 4.841^{+0.026}_{-0.025} \times 10^{49}$ erg, which implies that GRB 100316D satisfies the Amati relation although its location is borderline (see Fig. 7). Finally, we built three distinct time-resolved spectra that we used for the simulation with other detectors. The details of these three time-resolved spectra are shown in Table A.1.

2.3. GRB 161219B

GRB 161219B has been discovered by *Swift*-BAT (D'Ai et al. 2016) and by Konus WIND (Frederiks et al. 2016). Its redshift has been identified two days later (Tanvir et al. 2016) to be $z = 0.1475$, while the emerging SN was observed 7.24 days after the initial trigger (de Ugarte Postigo et al. 2016). The T_{90} duration observed by *Swift*-BAT is 6.9 s, but a more detailed analysis of BAT data revealed an extended emission, lasting ∼20 s, anticipating the burst (Palmer et al. 2016), as well as a tail lasting up to 40 s from the GRB trigger, see Fig. A.3. *Swift* XRT started to observe this GRB only 108 s after the BAT trigger (D'Ai et al. 2016), therefore we do not have a continuity in the observations between BAT and XRT for this GRB.

The T_{90} spectrum of this GRB, as observed by *Swift*-BAT, is best fitted by a power-law function with an exponential cut-off at $E_0 = 92.3^{+68.2}_{-29.0}$ keV and a photon index of $\gamma = -1.40^{+0.23}_{-0.24}$ (Cano et al. 2017). The corresponding intrinsic peak energy is $E_{p,i} = 62.3^{47.0}_{-19.9}$ keV and the isotropic energy $E_{iso} = 8.50^{+8.46}_{-3.75} \times 10^{49}$ erg, in the 1−10 000 keV energy range. With these values, the location of GRB 161219B is within three sigma of the Amati relation, while when we consider the data provided by the Konus-WIND mission (Frederiks et al. 2016), this burst would not satisfy the correlation at all, see Fig. 1.

In order to obtain more reliable values of the average $E_{p,i}$ and E_{iso} of the whole event, we repeated the analysis by also including the first soft/weak pulse and the soft tail described previously and shown in Fig. A.3. The BAT data were downloaded, screened, and analysed by following the standard procedures[2] and using the usual HEASOFT packages. The total spectrum is best fitted by a Band function (Band et al. 1993) with the following parameters: $\alpha = -1.14^{+0.16}_{-0.13}$, $\beta = -2.37^{+0.52}_{-1.59}$, and

[2] The *Swift*-BAT data analysis is described at https://swift.gsfc.nasa.gov/analysis/

$E_{p,i} = 55.5^{+14.9}_{-8.9}$ keV. The total integrated isotropic energy in the 1−10 000 keV energy range is $E_{iso} = 1.83 \times 10^{51}$ erg, which places this GRB well inside the limits of the Amati relation. Finally, we obtained and analysed four time-resolved spectra from the total emission of GRB 161219B, to be used in the simulations with other detectors. Figure A.3 clearly shows that we have extracted two single spectra from the GRB main pulse and an additional two spectra for the precursor and the soft tail. The best-fit results of the *Swift*-BAT data for each single spectrum are shown in Table A.2.

3. Simulated observations with other detectors

After deriving the spectral emission of the GRBs 060218, 100316D and 161219B as observed by *Swift*, we simulated observing them with old instruments dedicated to GRB observations, such as *Beppo*SAX, BATSE, INTEGRAL, and with a planned instrument that is very sensitive to soft X-ray frequencies, that is, the Wide Field Monitor (WFM).

The energy range of *Beppo*SAX (see Frontera et al. 2000) was very wide: from 2 keV to about 700 keV. This broad range was obtained thanks to two distinct detectors: the Wide Field Camera (WFC; Jager et al. 1997) which operated between 2 and 30 keV and the Gamma Ray Burst Monitor (GRBM; Frontera et al. 1997), whose energy range was 40−700 keV. We here only considered the GRBM detector because it was the GRB alert detector on board *Beppo*SAX. The BATSE Large Area Detector (LAD) was an experiment on board the Compton Gamma-Ray Observer (CGRO), and it consisted of eight detector module of NaI(TI), covering a wide energy range from 20 keV to 2 MeV. An interesting feature of the BATSE-LAD was that the location of these eight detectors allowed to cover a very wide fraction of the sky, $\Omega = 4\pi$. The INTErnational Gamma-Ray Astrophysics Laboratory (INTEGRAL) is a facility designed to investigate high-energy objects, carrying detectors for the X-ray and gamma-ray part of the spectrum, with an energy of between 15 keV and 10 MeV (Mereghetti et al. 2003). eXTP (Zhang et al. 2016) is a proposed mission for timing analysis of the X-ray transient sky and is expected to also mount a wide field monitor instrument that is able to detect GRBs in the energy range 2−70 keV (Feroci et al. 2012).

The time-resolved spectral best fits obtained in Sect. 2 (see also Tables 1, 2, A.1, and A.2) represent our input spectral models in the simulated observations. We used the standard `fakeit` procedure within the XSPEC package to simulate the observed spectra for all instruments, which requires correct background and a spectral response matrix for all detectors, plus an additional ancillary response file for the WFM and INTEGRAL cases. We obtained the response matrices, background, and ancillary files for each detector from the specific web sites[3] or from the literature (Kaneko et al. 2006; Guidorzi et al. 2011).

Before spectral fitting, we grouped any spectra to have a number of ten counts per bin, using the `grppha` tool of the `heasoft` package. Then, we used XSPEC to find the best model of each single time-resolved simulated spectrum, as if the GRB was really observed by the considered detector.

However, in order to obtain the total integrated spectrum and given the different sensitivities of the four detectors, we needed

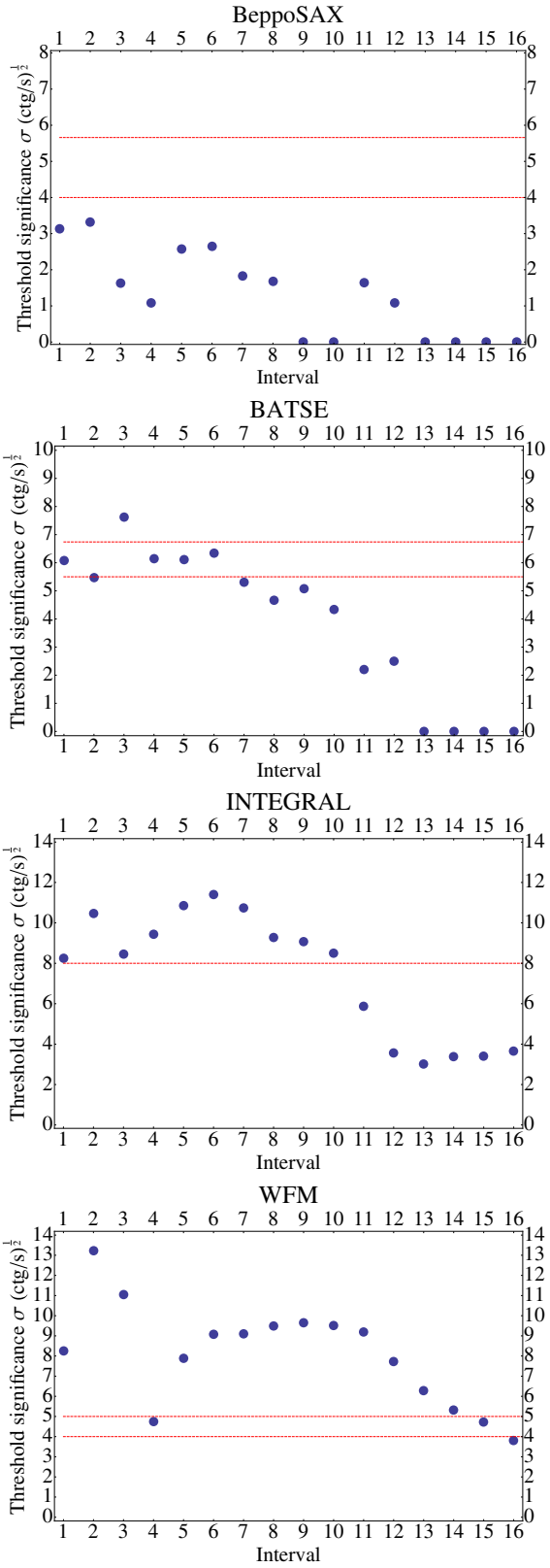

Fig. 4. Threshold significance σ as a function of the interval for *Beppo*SAX, BATSE, INTEGRAL, and WFM. The red, horizontal lines represent the σ_0 threshold as calculated from 1 (see also Band et al. 1993). In the case of *Beppo*Sax, BATSE, and WFM, we report two horizontal lines because the value of the threshold σ_0 depends on the angle between the direction perpendicular to the plane of the detector and the direction of the source. We use the lower value throughout the whole analysis.

[3] http://www.isdc.unige.ch/extp/public-response-files.html
http://saxgrbm.iasfbo.inaf.it/
http://heasarc.gsfc.nasa.gov/W3Browse/cgro/batsegrbsp.html

Table 3. Time-integrated spectral fit results for the observed *Swift* data and for the simulated spectra of GRB 060218.

# (keV)	Δt (s)	α (γ)	$E_{\rm p,i}$ (keV)	Norm # keV^{-1} cm^{-2} s^{-1}	χ^2/d.o.f.	$E_{\rm iso}$ (10^{49} erg)
Swift (BAT+XRT) (0.3–150)	2383	$-1.178^{+0.061}_{-0.062}$	$4.62^{+0.60}_{-0.54}$	$0.935^{+0.017}_{-0.017}$	1083.0/871	$5.35^{+0.53}_{-0.53}$
Swift (BAT) (15–150)	2727	$-0.72^{+0.19}_{-0.12}$	$21.3^{+3.1}_{-3.5}$	$4.8^{+2.1}_{-2.1} \times 10^{-3}$	1.4/57	$1.23^{+0.12}_{-0.11}$
INTEGRAL (15–200)	971	$-1.81^{+0.036}_{-0.032}$	$8.4^{+2.3}_{-2.0}$	$1.91^{+0.20}_{-0.20}$	0.25/34	$3.420^{+0.023}_{-0.020}$
BATSE (25–1900)	490	$-1.213^{+0.091}_{-0.067}$	$33.3^{+8.3}_{-7.6}$	$0.032^{+0.095}_{-0.095}$	109.1/112	$1.268^{+0.027}_{-0.024}$
eXTP-WFM (2–50)	2450	$-1.831^{+0.012}_{-0.012}$	$4.19^{+0.46}_{-0.42}$	$1.28^{+0.024}_{-0.024}$	346.8/476	$4.861^{+0.015}_{-0.014}$

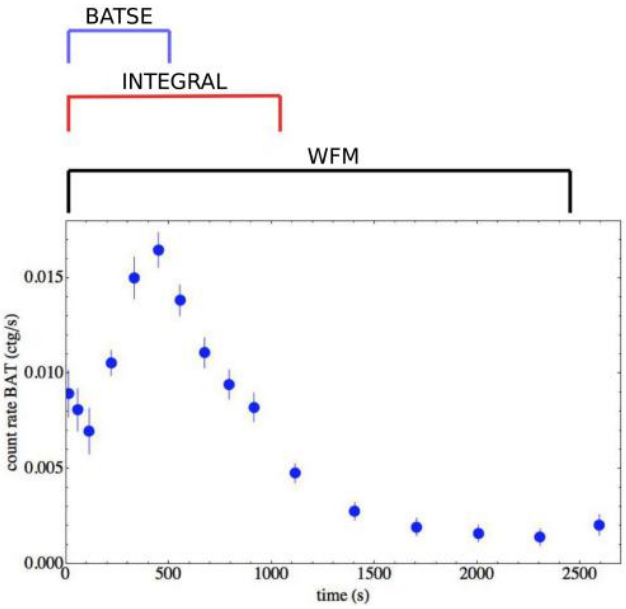

Fig. 5. Light curve of GRB 060218 as observed by *Swift*-BAT compared with the effective emission observed by *Beppo*SAX, BATSE, and WFM.

to consider the effective duration of each GRB emission as observed by each single detector. For this reason we computed the threshold significance σ for any single simulated time-resolved spectrum and for each detector in order to determine the real duration of the GRB. Following Band (2003), the threshold significance is given by

$$\sigma_0 = \frac{A_{\rm eff} f_{\rm det} f_{\rm mask} \Delta t \int_{E_1}^{E_2} \epsilon(E) N(E) {\rm d}E}{\sqrt{A_{\rm eff} f_{\rm det} \Delta t \int_{E_1}^{E_2} B(E) {\rm d}E}}, \quad (1)$$

where $A_{\rm eff}$ is the effective area of the detector, $f_{\rm det}$ is the fraction of the detector plane that is active, $f_{\rm mask}$ is the fraction of the coded mask that is open, Δt is the exposure of the photon spectrum $N(E)$, $\epsilon(E)$ is the efficiency of the detector, and $B(E)$ is the background. E_1 and E_2 correspond to the minimum and maximum energy threshold for any detector considered in this analysis.

As final results, we obtained different time intervals for each detector in which the burst would trigger it, and the intervals also provide a signal with a sufficient number of counts to be analysed with XSPEC, see Fig. 4 for the case of GRB 060218: while *Beppo*SAX would not have been triggered at all, WFM would have missed only the last 277 s, and BATSE and INTEGRAL would have seen the first 490 s and 971 s, respectively.

Table 4. Redshift, $E_{\rm peak}$, and $E_{\rm iso}$ values obtained from *Swift* observations.

Event	Redshift (z)	$E_{\rm iso}$ (10^{52} erg)	$E_{\rm peak}$ (keV)
GRB 060908	1.88	$7.2^{+1.9}_{-1.9}$	553^{+260}_{-260}
GRB 060927	5.46	$12.0^{+2.8}_{-2.8}$	275^{+75}_{-75}
GRB 140206A	2.74	$36.806^{+0.058}_{-0.058}$	$364.4^{+4.7}_{-4.6}$
GRB 141220A	1.34	$1.6136^{+0.0098}_{-0.0095}$	265^{+12}_{-11}
GRB 151029A	2.74	$8.013^{+0.069}_{-0.068}$	$117.6^{+4.1}_{-4.1}$
GRB 160227A	2.38	$5.924^{+0.039}_{-0.038}$	248^{+15}_{-14}
GRB 161117A	1.55	$14.858^{+0.018}_{-0.018}$	$145.2^{+1.2}_{-1.2}$
GRB 170113A	1.97	$0.7299^{+0.0053}_{-0.0052}$	$200.9^{+9.1}_{-8.8}$

We then computed the time-integrated spectra for each detector by summing with `mathpha` the spectra with a positive detection and then obtained the best fit for each of them, which were a cut-off power law in every case.

After we calculated the $E_{\rm peak}$ from the simulated spectra, we estimated the relative $E_{\rm iso}$ by first calculating the corresponding bolometric fluence $S_{\rm bolo}$ using the relation (see Schaefer 2007):

$$S_{\rm bolo} = S_{\rm obs} \frac{\int_{\frac{1}{1+z}}^{\frac{10^4}{1+z}} E\phi {\rm d}E}{\int_{E_{\rm min}}^{E_{\rm max}} E\phi {\rm d}E}, \quad (2)$$

where Φ is the differential photon spectrum (dN/dE) and $S_{\rm obs}$ is the observed fluence calculated from the spectrum, z is the redshift and $E_{\rm min}$ and $E_{\rm max}$ are the extremes of the detector bandpass. For GRB 060218, we report the result of our calculation in Fig. 6 and Table 3: while the location estimated with WFM matches the Amati relation, the locations obtained with BATSE and INTEGRAL do not match it. In the same figure we also report the location of GRB 060218 as observed by *Swift*-BAT+XRT (060218 *Swift*). On the basis of all these results, we conclude that these different locations in the $E_{\rm p,i} - E_{\rm iso}$ plane of GRB 060218 as observed by BATSE and INTEGRAL are due to their lack of a highly sensitive soft X-ray detector capabilities.

Similar conclusions are drawn for the cases of GRB 100316D and GRB 161219B. These events show an extended soft emission similar to that of GRB 060218, although GRB 161219B shows a higher energy output, enabling us to explore a different region of the $E_{\rm peak}/E_{\rm iso}$ plane in search of a bias effect. The results of our spectral analysis are reported in Tables A.1 and A.2, while the positions on the $E_{\rm peak}/E_{\rm iso}$ plane of these two events according to the different detectors we considered are reported in Fig. 7. GRB 161219B is an outlier of the Amati relation

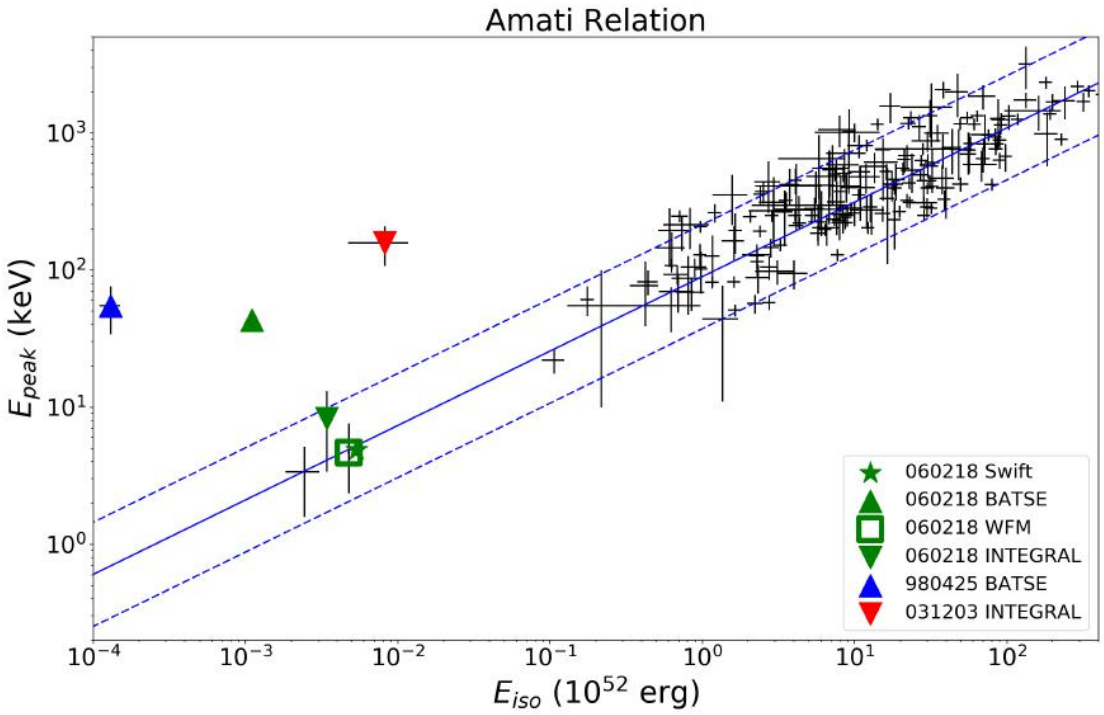

Fig. 6. $E_{p,i}$ – E_{iso} plane (Amati relation). We report in green the position of GRB 060218: according to *Swift* (BAT+XRT) (star), as it would have been observed by BATSE (triangle), INTEGRAL (reverse triangle) and WFM (square). We also show the location in the $E_{p,i}$ – E_{iso} plane of the two outliers GRB 980425 (blue triangle) and GRB 031203 (red reverse triangle).

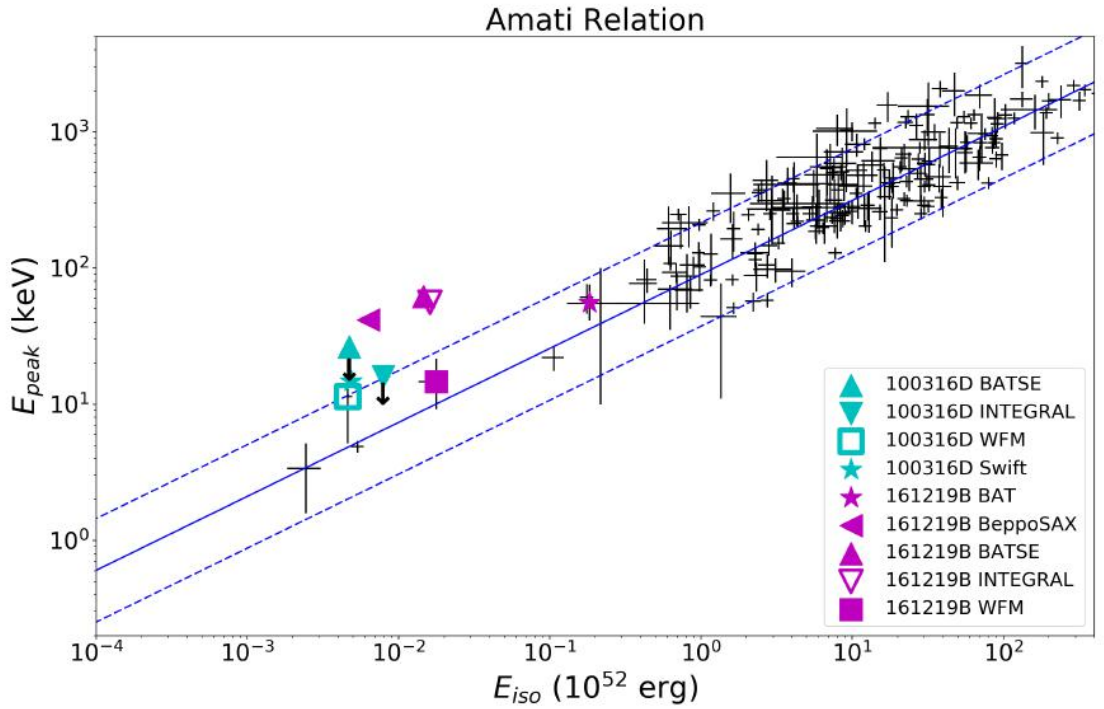

Fig. 7. $E_{p,i}$ – E_{iso} plane (Amati relation). We report in cyan the position of GRB 100316D: according to *Swift* (BAT+XRT) (star), as it would have been observed by BATSE (triangle – upper limit), INTEGRAL (reverse triangle – upper limit) and WFM (square). We also show the location of GRB 161219B: according to *Swift* (BAT) (star), *Beppo*SAX (left triangle), BATSE (triangle), INTEGRAL (reverse triangle), and WFM (square – upper limit).

for all the detectors considered in this work, with the exception of the eXTP-WFM, while only BATSE would have measured GRB 100316D to lie outside the Amati relation (but with an unconstrained lower limit for the $E_{p,i}$ value).

As a countercheck to our result, we applied our approach to a set of eight cosmological bursts ($z > 0.1$), reported in Table 3, whose $E_{p,i}$ and E_{iso} have been measured by *Swift*-BAT and perfectly match the Amati relation (see Fig. 8). We

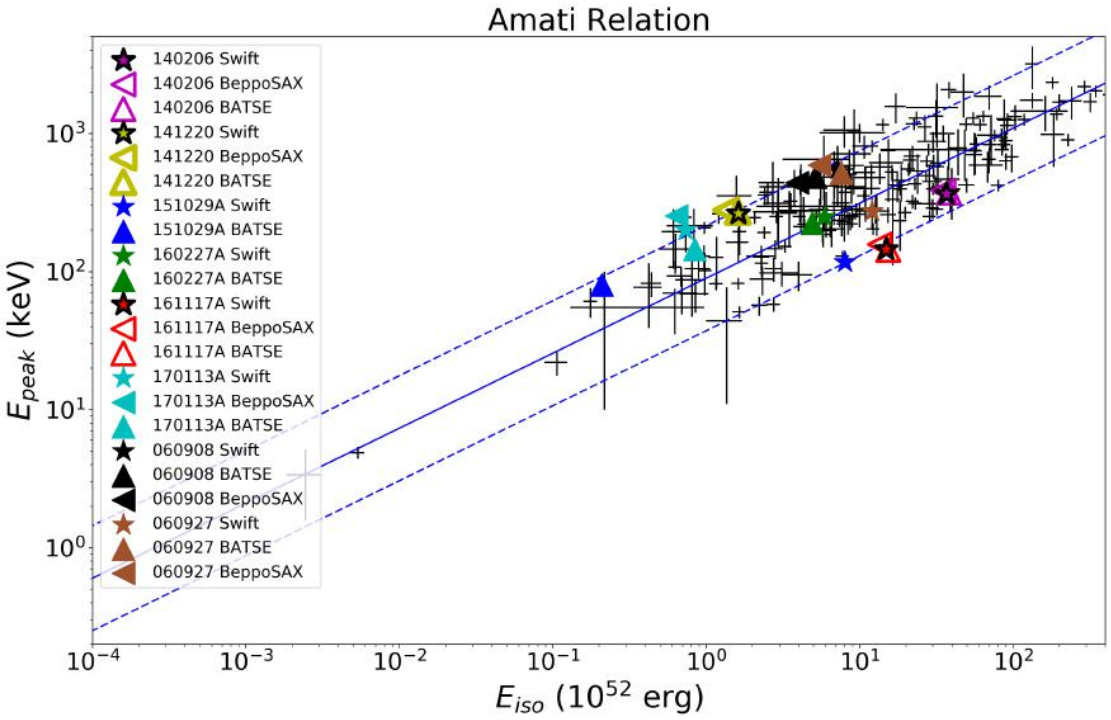

Fig. 8. Positions in the $E_{p,i}$ – E_{iso} plane of the eight cosmological GRBs, described in the text, characterized by a higher energy and a higher redshift than GRB 060218, GRB 161219B, and GRB 100316D. We note that the emission of these events as observed by BATSE and *Beppo*-SAX still satisfies the $E_{p,i}$ – E_{iso} correlation.

Table 5. Time-integrated spectral fit results for the observed *Swift* data and for the simulated spectra of GRB 100316D.

# (keV)	Δt (s)	α (γ)	$E_{p,i}$ (keV)	Norm # keV^{-1} cm^{-2} s^{-1}	χ^2/d.o.f.	E_{iso} (10^{49} erg)
Swift (BAT+XRT) (0.3–150)	890	$-1.256^{+0.018}_{-0.018}$	$14.69^{+0.94}_{-0.89}$	$0.4446^{+0.0053}_{-0.0053}$	568.7/971	$4.841^{+0.026}_{-0.025}$
INTEGRAL (15–200)	497	$-2.38^{+0.26}_{-0.23}$	15.9	$4.9^{+6.1}_{-2.6}$	1.8/35	$7.91^{+0.92}_{-0.51}$
BATSE (25–1900)	200	$-2.358^{+0.059}_{-0.047}$	26.5	$6.9^{+1.5}_{-1.5}$	102/113	$4.722^{+0.104}_{-0.097}$
eXTP-WFM (2–50)	891	$-1.62^{+0.14}_{-0.14}$	$11.4^{+17.7}_{-6.2}$	$0.710^{+0.084}_{-0.041}$	415/476	$4.61^{+0.33}_{-0.14}$

Table 6. Time-integrated spectral fit results for the observed *Swift* data and for the simulated spectra of GRB 161219B.

# (keV)	Δt (s)	α (γ)	$E_{p,i}$ (keV)	Norm # keV^{-1} cm^{-2} s^{-1}	χ^2/d.o.f.	E_{iso} (10^{49} erg)
Swift (BAT) (15–150)	62	$-1.435^{+0.050}_{-0.042}$	$56^{+20}_{-14.0}$	$20.1^{+3.4}_{-3.4}$	1.2/55	$183^{+5.1}_{-4.2}$
*Beppo*SAX (40–700)	8	$-1.46^{+0.60}_{-0.72}$	$41.5^{+1.9}_{-1.9}$	$13.44^{+0.76}_{-0.76}$	339/223	$6.328^{+0.039}_{-0.038}$
INTEGRAL (15–200)	62	$-1.5304^{+0.0059}_{-0.0058}$	$56.0^{+3.4}_{-3.2}$	$2.1506^{+0.0059}_{-0.0058}$	5.9/34	$16.127^{+0.060}_{-0.057}$
BATSE (25–1900)	62	$-1.336^{+0.013}_{-0.012}$	$61.8^{+3.8}_{-3.6}$	$1.202^{+0.063}_{-0.063}$	38.15/112	$1.465^{+0.100}_{-0.097}$
eXTP-WFM (2–50)	62	$-1.7297^{+0.0053}_{-0.0051}$	$14.7^{+3.6}_{-4.2}$	$1.173^{+0.023}_{-0.023}$	475/478	$17.72^{+0.36}_{-4.15}$

performed time-integrated simulations for the BATSE-LAD and *Beppo*SAX-GRBM instruments using the observed dataset from *Swift*. The simulated points in the E_p – E_{iso} plane are reported in Fig. 8. According to our analysis, we do not see a strong effect/bias for these events in these cases. All these GRBs are consistent with the $E_{p,i}$ – E_{iso} correlation, even if they would have been observed by BATSE-LAD and *Beppo*SAX-GRBM. This result implies that this effect is strong only for sub-energetic events and with a soft X-ray prolonged emission.

We note that during the complete duration of the prompt emission, the value of the peak energy is almost in the energy interval 2–70 keV (see Fig. 2), which is the nominal energy range of the Wide Field Monitor proposed for the LOFT (Feroci et al. 2012) and eXTP (Zhang et al. 2016) mission concepts. Its sensitivity, with respect to other current and past GRB detectors, is almost one order of magnitude higher[4], suggesting that events similar to GRB 060218 could also be detected at larger distances

[4] http://sci.esa.int/loft/53447-loft-yellow-book/

($z \approx 0.1-0.2$). It is therefore interesting to estimate the cosmological region of the Universe in which we can detect low-luminosity GRBs-SNe with WFM and, eventually, provide an estimate of the rate of such events. We therefore estimated the maximum distance at which GRB 060218-like bursts would still trigger the eXTP-WFM. A positive trigger of eXTP-WFM depends on the assumed threshold significance, defined in Eq. (1), but we also need to correct the observed spectrum there because the assumed distance of the GRB is different. We specifically modified:

- the exposure time Δt_z, which varies as $\Delta t_{\rm rest}(1+z)$, where $\Delta t_{\rm rest}$ corresponds to the observed time interval in the rest frame: $\Delta t_{\rm rest} = \Delta t_{\rm obs}/1.0331$;
- the cut-off energy $E_{\rm cutoff}$, which is parameterized as the peak energy E_p, and which varies as $E_{\rm cutoff,z} = E_{\rm cutoff,obs}\frac{1.0331}{1+z}$;
- the normalization of the spectral model, which varies following the functional form:

$$K_z = K_{\rm obs}\left(\frac{1+z}{1.0331}\right)^2\left(\frac{d_l(0.0331)}{d_l(z)}\right)^2. \quad (3)$$

We note that the subscripts *obs* correspond to the quantities observed by *Swift* and the subscript z to the quantities that would be observed if GRB 060218 were to remain at redshift z. With these corrections, we computed the threshold significance σ for the time-resolved spectrum 6 in Fig. 5, which is the spectrum with the highest expected σ and does not belong to the initial hard emission of GRB 060218, translated into different redshifts. Assuming a value of $\sigma = 4$ for the eXTP-WFM, which is the expected final value for the mission, we obtain that an event similar to GRB 060218 would trigger the WFM up to a redshift $z = 0.1$, see also Fig. A.4.

We also determined at which redshift GRB 060218 would have been observed by *Swift*-BAT, and we obtained a redshift of $z = 0.05$ as the detection limit for GRB 060218 with *Swift*-BAT. The cosmological comoving element volume at redshift z is given by

$$V(z) = \frac{4\pi}{3}d_{\rm c}(z)^3, \quad (4)$$

where $d_{\rm c} = d_l/(1+z)$ is the cosmological comoving distance. At these distances ($z = 0.1$), the comoving element volume is 30 times larger than the volume at $z = 0.0331$ and 8 times larger than the volume at $z = 0.05$.

4. Conclusions

The main results of our analysis can be summarized as follows:

i) If GRB 060218, 161219B, and 100316D were observed with detectors not sensitive at low energies (~0.3 keV) such as INTEGRAL and/or BATSE, they would be outliers of the Amati relation (see Amati & Dichiara 2013, for a quantitative analysis of the instrumental bias). On the other hand, GRB 060218 and GRB 100316D perfectly match the $E_{\rm p,i} - E_{\rm iso}$ relation after being observed with *Swift* (down to 0.3 keV). On the basis of this result, we suggest that GRB 980425 and GRB 031203 are not "true" outliers of the Amati relation, and their location in the $E_{\rm p,i} - E_{\rm iso}$ plane is the result of an observational bias, and is not related to a combination of the geometry of GRB explosions with the line of sight of the observer (e.g. GRB viewed off-axis Yamazaki et al. 2004; Ramirez-Ruiz et al. 2005; Eichler & Levinson 2004).

ii) This conclusion is strengthened by the fact that *Swift*-BAT (15−150 keV) did measure GRB 060218 as an outlier and *XMM-Newton* observed an X-ray echo that suggests the presence of an extended soft emission associated with GRB 031203 (Watson et al. 2006).

iii) In the case of GRB 100316D, we note that the WFM observes it at the border of the 1σ boundary of the Amati relation. We therefore derive that it is not sufficient to observe below the limit of the soft X-rays energy range (~0.3 keV), but it is necessary to use a detector with high sensitivities at these energies, such as *Swift*-XRT, in order to obtain as much information as possible about the total energy emitted by these low-luminosity GRBs.

iv) To give more weight to our conclusions, we applied the same approach to a sample of "high-luminosity" GRBs whose $E_{\rm p,i}$ and $E_{\rm iso}$ parameters, reported in Table 3, have been measured by *Swift*-BAT. All these GRBs are more energetic and located at higher redshift than GRB 060218, GRB 100316D and GRB 161219B, and they are therefore not expected to show a soft X-ray tail. In these cases the GRBs always match the $E_{\rm p,i} - E_{\rm iso}$ relation regardless of whether it is observed by *Swift*, BATSE, or *Beppo*SAX (see Fig. 8).

v) After simulating WFM observations, we showed that GRB 060218 could have been observed up to $z = 0.1$ which is about three times farther than it was observed with *Swift*-BAT (Guetta & Della Valle 2007). As a consequence, we are likely lacking a significant fraction of low-luminosity and sub-energetic GRBs, whose high-energy emission remains undetected due to the poor sensitivity and limits of current operating detectors.

Acknowledgements. This research has made use of data, software and web tools obtained from the High Energy Astrophysics Science Archive Research Center (HEASARC), a service of the Astrophysics Science Division at NASA/GSFC and of the Smithsonian Astrophysical Observatory's High Energy Astrophysics Division. This work made use of data supplied by the UK *Swift* Science Data Centre at the University of Leicester. We thank the anonymous referee for his useful comments and suggestions that improved our paper. We thank Sergio Campana for providing us the *Swift*-BAT spectral dataset of GRB 060218. Special thanks go to Prof. Mauro Orlandini, who contributed to the statistical analysis contained in the work and Cristiano Guidorzi for his useful suggestions. LI7 acknowledges support from the Spanish research project AYA 2014-58381-P. D.G. acknowledges the financial support of the UnivEarthS Labex program at Sorbonne Paris Cité (ANR-10-LABX-0023 and ANR-11-IDEX-0005-02).

References

Amati, L. 2006, MNRAS, 372, 233
Amati, L., & Della Valle, M. 2013, Int. J. Mod. Phys. D, 22, 1330028
Amati, L., & Dichiara, S. 2013, Acta Polytechnica, 53, 686
Amati, L., Frontera, F., Tavani, M., et al. 2002, A&A, 390, 81
Amati, L., Guidorzi, C., Frontera, F., et al. 2008, MNRAS, 391, 577
Amati, L., Del Monte, E., D'Elia, V., et al. 2013, Nucl. Phys. B Proc. Suppl., 239, 109
Arnaud, K. A. 1996, in Astronomical Data Analysis Software and Systems V, eds. G. H. Jacoby, & J. Barnes, ASP Conf. Ser., 101, 17
Band, D. L. 2003, ApJ, 588, 945
Band, D., Matteson, J., Ford, L., et al. 1993, ApJ, 413, 281
Barthelmy, S. D., Barbier, L. M., Cummings, J. R., et al. 2005, Space Sci. Rev., 120, 143
Bernardini, M. G., Margutti, R., Zaninoni, E., & Chincarini, G. 2012, MNRAS, 425, 1199
Bufano, F., Pian, E., Sollerman, J., et al. 2012, ApJ, 753, 67
Burrows, D., Hill, J., Nousek, J., et al. 2005, Space Sci. Rev., 120, 165
Campana, S., Mangano, V., Blustin, A. J., et al. 2006, Nature, 442, 1008
Cano, Z., Izzo, L., de Ugarte Postigo, A., et al. 2017, A&A, 605, A107
Chornock, R., Berger, E., Levesque, E. M., et al. 2010, ArXiv e-prints [arXiv:1004.2262]
D'Ai, A., Kennea, J. A., Krimm, H. A., et al. 2016, GRB Coordinates Network, 20296, 1

Dainotti, M. G., Cardone, V. F., & Capozziello, S. 2008, MNRAS, 391, L79
de Ugarte Postigo, A., Cano, Z., Izzo, L., et al. 2016, GRB Coordinates Network, 20342, 1
Della Valle, M. 2011, Int. J. Mod. Phys. D, 20, 1745
Dickey, J. M., & Lockman, F. J. 1990, ARA&A, 28, 215
Eichler, D., & Levinson, A. 2004, ApJ, 614, L13
Feroci, M., Stella, L., van der Klis, M., et al. 2012, Exp. Astron., 34, 415
Frederiks, D., Golenetskii, S., Aptekar, R., et al. 2016, GRB Coordinates Network, 20323, 1
Frontera, F., Costa, E., dal Fiume, D., et al. 1997, A&AS, 122, 357
Frontera, F., Amati, L., Costa, E., et al. 2000, ApJS, 127, 59
Galama, T. J., Vreeswijk, P. M., van Paradijs, J., et al. 1998, Nature, 395, 670
Ghirlanda, G., Ghisellini, G., & Lazzati, D. 2004, ApJ, 616, 331
Ghisellini, G., Ghirlanda, G., Mereghetti, S., et al. 2006, MNRAS, 372, 1699
Guetta, D., & Della Valle, M. 2007, ApJ, 657, L73
Guidorzi, C., Lacapra, M., Frontera, F., et al. 2011, A&A, 526, A49
Izzo, L., Muccino, M., Zaninoni, E., Amati, L., & Della Valle, M. 2015, A&A, 582, A115
Jager, R., Mels, W. A., Brinkman, A. C., et al. 1997, A&AS, 125, 557
Kaneko, Y., Preece, R. D., Briggs, M. S., et al. 2006, ApJS, 166, 298
Liang, E., & Zhang, B. 2005, ApJ, 633, 611
Margutti, R., Soderberg, A. M., Wieringa, M. H., et al. 2013, ApJ, 778, 18
Mazzali, P. A., Deng, J., Nomoto, K., et al. 2006, Nature, 442, 1018
Meegan, C. A., Fishman, G. J., Wilson, R. B., et al. 1992, Nature, 355, 143
Mereghetti, S., Götz, D., Borkowski, J., Walter, R., & Pedersen, H. 2003, A&A, 411, L291
Nousek, J. A., Kouveliotou, C., Grupe, D., et al. 2006, ApJ, 642, 389
Palmer, D. M., Barthelmy, S. D., Cummings, J. R., et al. 2016, GRB Coordinates Network, 20308, 1
Pian, E., Mazzali, P. A., Masetti, N., et al. 2006, Nature, 442, 1011
Ramirez-Ruiz, E., Granot, J., Kouveliotou, C., et al. 2005, ApJ, 625, L91
Romano, P., Campana, S., Chincarini, G., et al. 2006, A&A, 456, 917
Sakamoto, T., Barthelmy, S. D., Baumgartner, W. H., et al. 2010, GRB Coordinates Network, 10511, 1
Schaefer, B. E. 2007, ApJ, 660, 16
Stamatikos, M., Sakamoto, T., Starling, R. L. C., et al. 2010, GCN Report, 278, 1
Starling, R. L. C., Wiersema, K., Levan, A. J., et al. 2011, MNRAS, 411, 2792
Starling, R. L. C., Page, K. L., Pe'Er, A., Beardmore, A. P., & Osborne, J. P. 2012, MNRAS, 427, 2950
Tanvir, N. R., Kruehler, T., Wiersema, K., et al. 2016, GRB Coordinates Network, 20321, 1
Vergani, S. D., D'Avanzo, P., Malesani, D., et al. 2010, GRB Coordinates Network, 10495, 1
Watson, D., Vaughan, S. A., Willingale, R., et al. 2006, ApJ, 636, 967
Waxman, E., Mészáros, P., & Campana, S. 2007, ApJ, 667, 351
Wilms, J., Allen, A., & McCray, R. 2000, ApJ, 542, 914
Woosley, S. E., & Bloom, J. S. 2006, ARA&A, 44, 507
Yamazaki, R., Yonetoku, D., & Nakamura, T. 2004, in Gamma-Ray Bursts: 30 yr of Discovery, eds. E. Fenimore, & M. Galassi, AIP Conf. Ser., 727, 416
Yonetoku, D., Murakami, T., Nakamura, T., et al. 2004, ApJ, 609, 935
Zhang, S. N., Feroci, M., Santangelo, A., et al. 2016, in Proc. SPIE, 9905, 99051Q

Appendix A: Tables and figures

In this section we report the light curves and the statistical results of the spectral analysis performed on GRB 100316D and GRB 161219B. We use these two events as a further verification of our thesis on the behaviour of the statistical bias we described in the conclusions of our work.

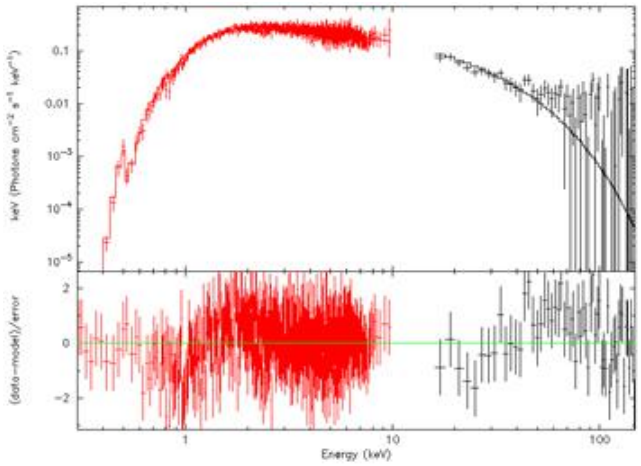

Fig. A.1. Best fit of the *Swift*-BAT+XRT integrated spectrum of GRB 100316D with an absorbed power-law function with an exponential cut-off.

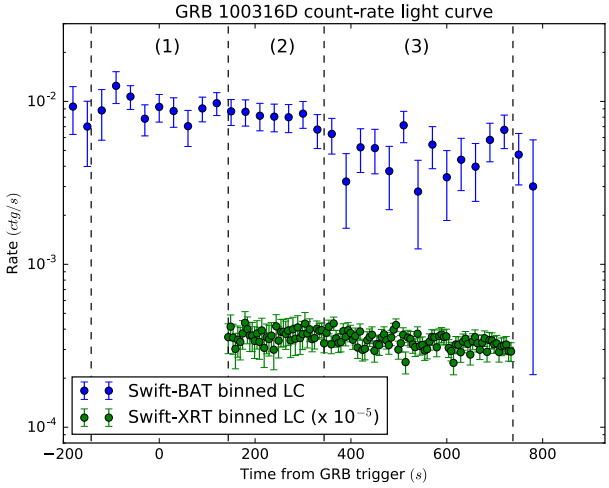

Fig. A.2. *Swift*-BAT (blue circles) and XRT (green circles) count-rate light curve of GRB 100316D. Both curves are binned while the XRT curve is also rescaled by 10^{-5}. The dashed black lines mark the time intervals of the time-resolved spectra considered in our analysis (see also Table A.1).

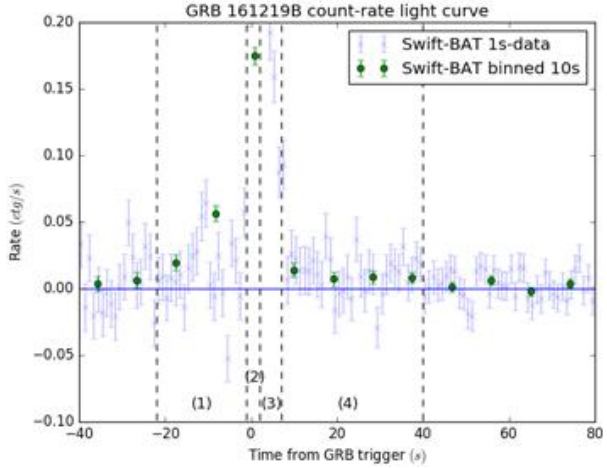

Fig. A.3. *Swift*-BAT count-rate light curve of GRB 100316D binned at 1 s (blue data) and at 10 s (green circles). The dashed black lines mark the time intervals of the time-resolved spectra considered in our analysis (see also Table A.2).

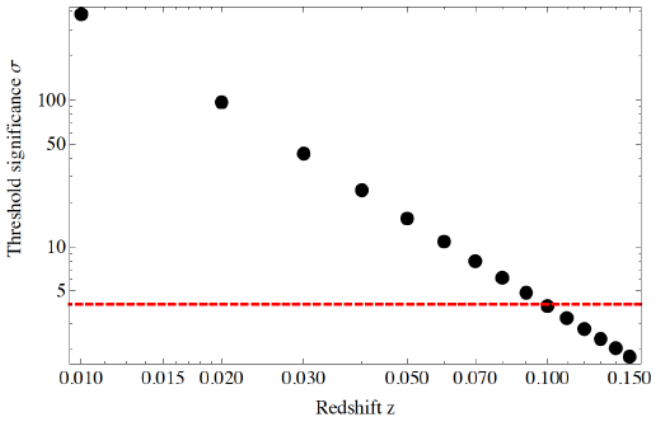

Fig. A.4. eXTP threshold significance for the brightest time-resolved spectrum of GRB 060218 (spectrum 6) as a function of the redshift. The eXTP detector would trigger on GRB 060218 up to redshift $z = 0.01$.

Table A.1. *Swift*-BAT+XRT (0.3−150 keV) spectral fit data results of the GRB 100316D dataset.

#	Δt (s)	γ	$E_{\rm cutoff}$ (keV)	Norm CPO Photons keV^{-1} cm^{-2} s^{-1}	Flux BAT (10^{-9}) (erg/cm^2/s)	Flux XRT (10^{-9}) (erg/cm^2/s)	χ^2/d.o.f.
1	297	$1.75^{+0.84}_{-0.68}$	$45.3^{+48.5}_{-21.2}$	$1.31^{+2.77}_{-1.30}$	4.13	–	63.7/55
2	200	$1.32^{+0.03}_{-0.03}$	$35.7^{+5.18}_{-4.35}$	$0.28^{+0.01}_{-0.01}$	3.97	2.23	856.2/814
3	394	$1.29^{+0.03}_{-0.03}$	$20.7^{+2.59}_{-2.28}$	$0.28^{+0.01}_{-0.01}$	2.07	2.04	880.6/895

Notes. For the first spectrum, we used BAT data alone.

Table A.2. *Swift*-BAT (15−150 keV) spectral fit data results of the GRB 161219B dataset.

#	Δt (s)	γ	$E_{\rm cutoff}$ (keV)	Norm CPO Photons keV^{-1} cm^{-2} s^{-1}	Flux BAT (10^{-9}) (erg/cm^2/s)	χ^2/d.o.f. (10^{-9})
1	21	$2.20^{+1.55}_{-0.85}$	–	$3.0^{+8.3}_{-2.9}$	5.1	51.6/56
2	3	$1.51^{+0.28}_{-0.31}$	$112.8^{+212.5}_{-47.9}$	$11.5^{+13.5}_{-6.6}$	170.8	79.8/77
3	4	$1.21^{+0.29}_{-0.32}$	$68.0^{+51.1}_{-22.2}$	$4.7^{+5.8}_{-2.7}$	156.7	84.9/77
4	33	$2.05^{+0.35}_{-0.32}$	–	$2.8^{+6.3}_{-2.7}$	8.4	55.2/78

Appendix B: Simulated light curves

In this section we report the simulated light curves for the three instruments we analysed and that could have led to a positive detection of an emission like that of GRB 060218. These instruments could have detected only a fraction of the total emission. The x axis covers the total time extension of the dataset we analysed.

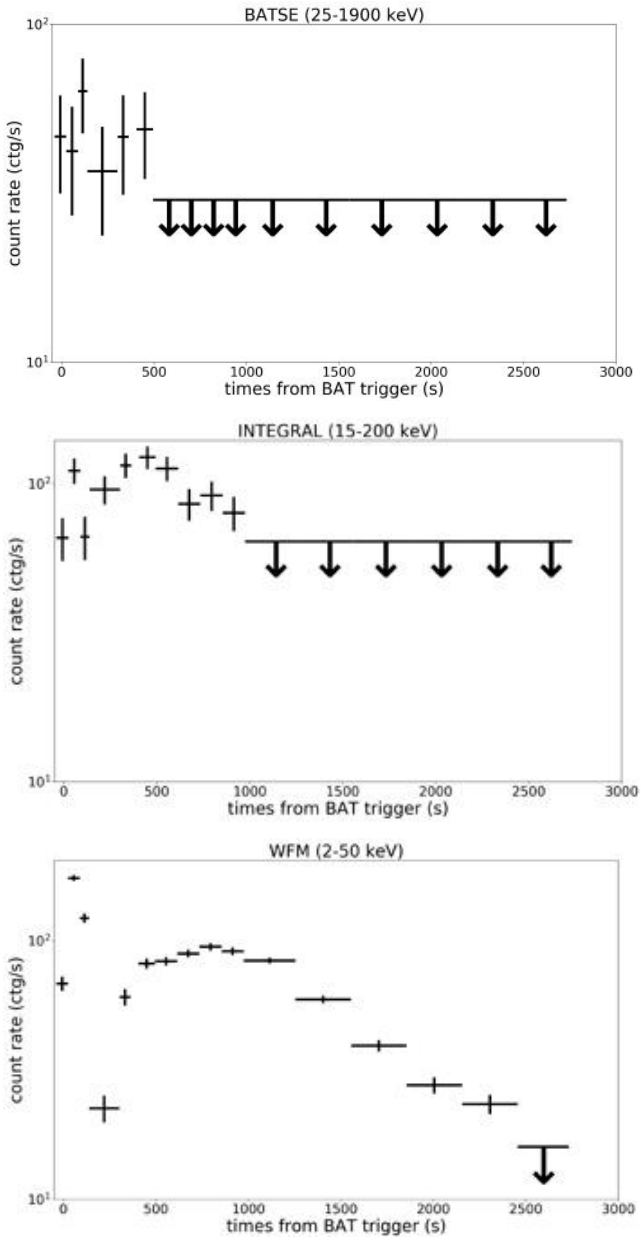

Fig. B.1. Light curve of GRB 060218 as seen by BATSE, INTEGRAL and the WFM-eXTP according to our simulations. The last intervals of our analysis would have been below the detection threshold of the instrument, and therefore no counts are expected.

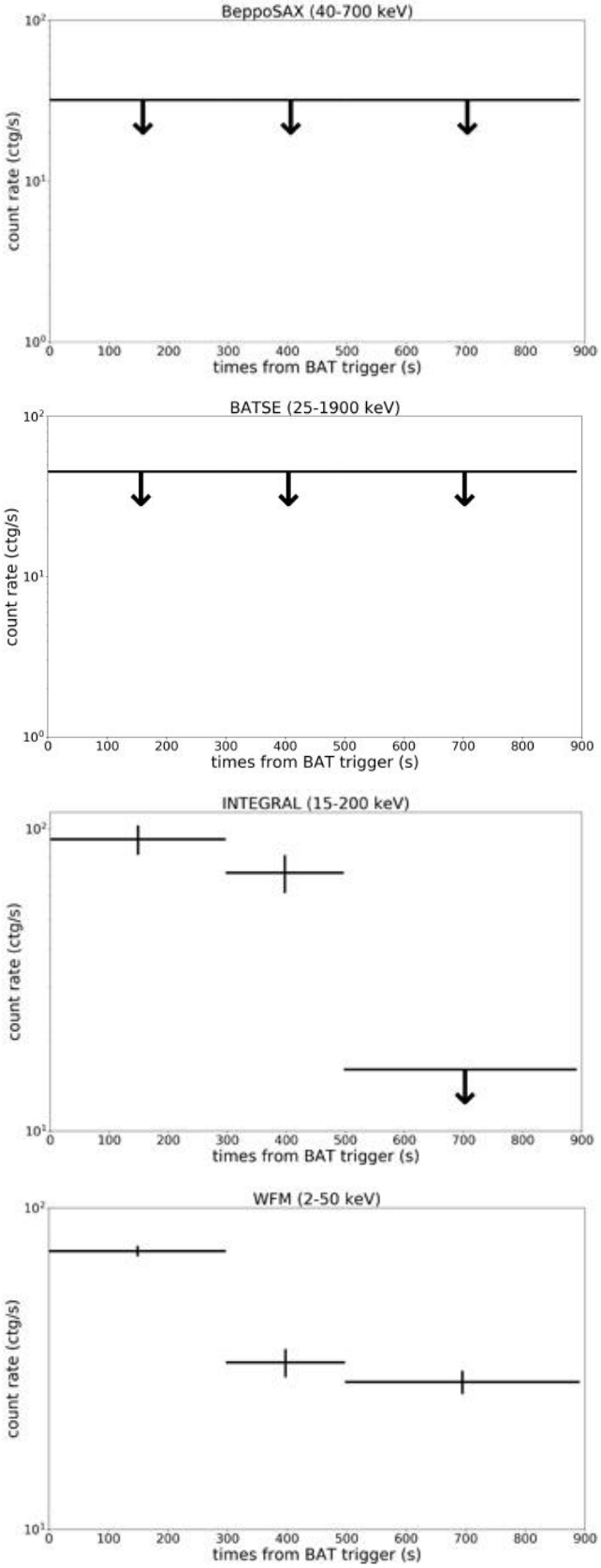

Fig. B.2. Light curve of GRB 100316D as seen by *Beppo*-SAX, BATSE, INTEGRAL, and the WFM-eXT according to our simulations.

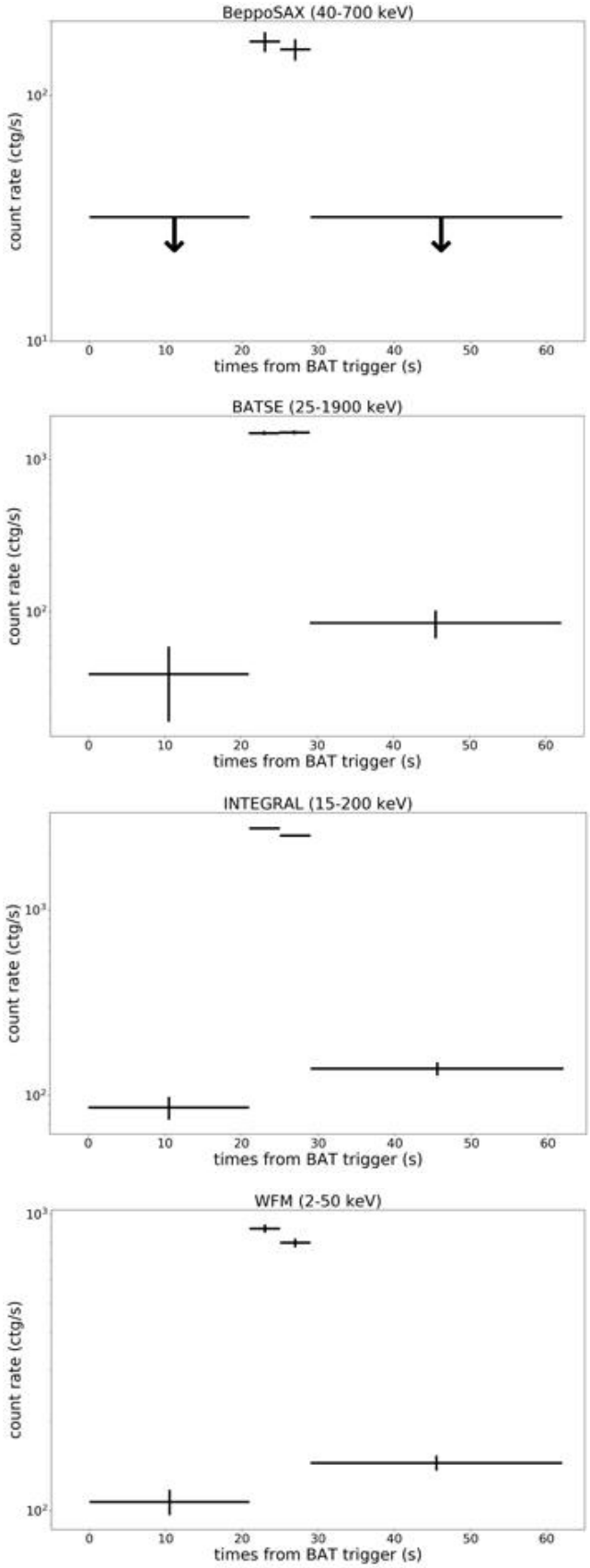

Fig. B.3. Light curve of GRB 161219B as seen by *Beppo*-SAX, BATSE, INTEGRAL, and the WFM-eXTP, according to our simulations.

Experimental Astronomy (2019) 48:25–48
https://doi.org/10.1007/s10686-019-09634-y

ORIGINAL ARTICLE

A robotic pipeline for fast GRB followup with the Las Cumbrés observatory network

R. Martone[1,2] · C. Guidorzi[1] · C. G. Mundell[3] · S. Kobayashi[4] · A. Cucchiara[5] · A. Gomboc[6] · N. Jordana[3] · T. Laskar[3] · M. Marongiu[1,2] · D. C. Morris[5] · R. J. Smith[4] · I. A. Steele[4]

Received: 4 March 2019 / Accepted: 12 June 2019 / Published online: 11 July 2019

Abstract

In the era of multi-messenger astronomy the exploration of the early emission from transients is key for understanding the encoded physics. At the same time, current generation networks of fully-robotic telescopes provide new opportunities in terms of fast followup and sky coverage. This work describes our pipeline designed for robotic optical followup of gamma-ray bursts with the Las Cumbrés Observatory network. We designed a Python code to promptly submit observation requests to the Las Cumbrés Observatory network within 3 minutes of the receipt of the socket notice. Via Telegram the pipeline keeps the users informed, allowing them to take control upon request. Our group was able to track the early phases of the evolution of the optical output from gamma-ray bursts with a fully-robotic procedure and here we report the case of GRB180720B as an example. The developed pipeline represents a key ingredient for any reliable and rapid (minutes timescale) robotic telescope system. While successfully utilized and adapted for LCO, it can also be adapted to any other robotic facilities.

Keywords GRB · LCO · Telegram

✉ R. Martone
mrtrnt@unife.it

1 Department of Physics and Earth Science, University of Ferrara, via Saragat 1, I–44122, Ferrara, Italy

2 ICRANet, Piazzale della Repubblica 10, I–65122, Pescara, Italy

3 Department of Physics, University of Bath, Claverton Down, Bath, BA2 7AY, UK

4 Astrophysics Research Institute, Liverpool John Moores University, Liverpool, L3 5RF, UK

5 University of the Virgin Islands, #2 John Brewers Bay, 00802 St Thomas, VI, USA

6 Centre for Astrophysics and Cosmology, University of Nova Gorica, Vipavska 11c, Ajdovščina 5270, Slovenia

1 Introduction

Gamma-ray bursts (GRBs) are detected as short-lived, intense flashes of high-energy γ-rays [1] so-called prompt emission, produced by the core-collapse of a massive star (see [2] for a review) or the merger of two neutron stars [3, 4] or a neutron star and stellar-mass black hole [5–7]. Propagation of the expanding fireball into the circumburst medium produces long-lived radiation - the afterglow - that is detectable across the electromagnetic spectrum; detection of the first optical afterglow [8] confirmed the cosmological origin of GRBs and highlighted the need for accurate prompt localisations and increasingly rapid followup observations. The first prompt optical emission was detected by [9] in 1999, who discovered the possibility to study just the outburst to undestand its processes. The launch of NASA's Neil Gehrels *Swift* in 2004 [10] opened a new era of rapid-response multimessenger astronomy, providing unprecedented real-time discoveries of GRBs with arcmin localisations of prompt γ-ray emission. It's became clear to develope the global network of fully robotic telescopes, to have 24h of night time in both hemispheras (ROTSE [11], MASTER [12], TAROT [13], BOOTES [14]). In parallel, the development of the world's largest fully autonomous robotic optical telescopes such as the 2-m Liverpool Telescope [15] and the identical 2-m Faulkes Telescopes [16, 17] that can respond to GRB discoveries within minutes of the alert notification provided new insights into the nature of the early afterglow [18–22], the physics of reverse shocks [23–27]; and the importance of ordered magnetic fields in the relativistic ejecta [28–31]. The rapid evolution of the blast-wave emission and the complexity of early time light curves within the first few minutes to hours of the GRB drove the development of autonomous software systems for immediate response to the GRB trigger combined with rapid, automatic identification, classification and selection of subsequent followup observations [32, 33].

The development of Las Cumbrés Observatory that now includes the two 2-m Faulkes Telescopes in a network with nine 1-m and nine 0.4-m telescopes has opened new opportunities for global monitoring of time-variable and transient phenomena at optical and infrared wavelengths. Here we present a new GRB pipeline that builds on our experience of developing autonomous systems for immediate GRB followup [32]. The goal of this pipeline is to optimise receipt of and response to transient

Table 1 LCO telescopes and their localization

Emisphere	Name	Location	Code
North	McDonald Observatory	Texas-USA	ELP
	Haleakala Observatory	Hawaii-USA	OGG
	Wise Observatory	Israel	TLV
	Teide Observatory	Canary Islands-Spain	TFN
South	Cerro Tololo Inter-American Observatory	Chile	LSC
	Siding Spring Observatory	Australia	COJ
	South African Astronomical Observatory	South Africa	CPT

triggers – particularly GRBs – for which the location and time of discovery is completely unpredictable and for which a rapid response is vital to maximise the chance of capturing the physics encoded in the prompt optical and early afterglow radiation. This is to ultimately determine the nature of the progenitors, energetics and explosion physics. Whilst optimised for GRB followup, the pipeline is of general use for other kinds of multi-messenger trigger e.g. gravitational wave, neutrino, high-energy cosmic rays, supernovae (SNe) and could be extended to other telescope networks.

2 The Las Cumbrés observatory

2.1 The network

The Las Cumbrés Observatory Global Telescope Network[1] [34] is a network designed for time domain astronomy at optical and near-IR wavelengths. It consists of a series of telescopes located at different sites in both the northern and southern hemispheres and whose schedules are managed by a common scheduler. The presence of this central "brain" makes the network able to work as a single facility, with the obvious advantages of many observing points.

The network is owned and operated by the Las Cumbrés Observatory Global Telescope (LCOGT), a young organisation whose main goals are providing professional scientists affordable and reliable instruments to get professional-class data, and non-professional users an easy and user-friendly way to feed their interest with professional instruments in a supervised environment.

The LCOGT organisation pursues this mission using a set of small to medium-aperture instruments spread among four continents: the three classes of 0.4, 1, and 2 meters are available at the present moment. The basic developing strategy requires the presence of all this three main classes of telescopes in each site: the idea is to have medium-class instruments to study faint objects and something able to lighten their load when their larger aperture is not needed: a 0.4-meters telescope is perfect to handle this task. The available sites, their location and international identification code can be found in Table 1, while additional information about on-site instrumentation can be found in [34]. Current-state information can be found at the LCO web site.

2.2 Instruments

The LCO network gives easy access to professional-class instruments for both imaging and spectroscopy on all the cited classes of telescopes, depending on the sites. Our past and present proposals (see Table 2) are focused on imaging with only 1 and 2 meters telescopes, so we briefly describe these classes together with the imaging instruments mounted on them.

[1] https://lco.global

Table 2 Table of past and present proposals by our group awarded with time on LCO network

Name	Title	PI	Start	End
CON2014A-001	”Fast Transients in the Era of Rapid Followup”	C. Mundell	01-01-14	31-12-14
ARI2015A-001	”Studies of Gamma-ray Bursts and the associated Supernovae”	S. Kobayashi	01-01-15	31-12-15
ARI2016A-004	”Studies of Gamma-ray Bursts and the associated Supernovae”	S. Kobayashi	01-01-16	31-12-16
ARI2017AB-005	”Followup observations of GRBs”	S. Kobayashi	01-01-17	31-12-17
ARI2018A-002	”Followup observations of GRBs”	S. Kobayashi	01-12-17	30-06-18
ARI2018B-001	”Followup observations of GRBs”	S. Kobayashi	01-06-18	30-11-18

Table 3 Telescopes main specs

Aperture m	f/#	Mount	Slew rate degrees s^{-1}	Location
1	f/10	Alt/Az	2	[COJ, OGG]
2	f/8	Equatorial	6	[COJ, CPT, LSC, ELP]

The 2-m telescopes are present in:

– COJ - 1 unit[2]
– OGG - 1 unit[3]

These are two Faulkes Telescopes featuring a Ritchev-Chrétien Cassegrain f/10 optics and an Alt-Az configuration. These telescopes are capable to perform rapid repointing with a turnaround of 45 seconds on average, thanks to a maximum slewing speed of 2 degrees/s. These details are summarised in Table 3. The imaging instrument available on this class is the "Spectral"[4] and the FLOYD spectrograph.[5]

The 1-m telescopes are available in:

– COJ - 2 units
– CPT - 2 units
– LSC - 3 units
– ELP - 2 units

These telescopes feature a Ritchev-Chrétien Cassegrain f/8 optics and an Alt-Az configuration. This class is capable to perform a very rapid repointing with a turnaround of less than 30 seconds, thanks to a slewing speed of 6 deg/s. These details are summarised in Table 3. This class features the "Sinistro" imaging instrument[6] and a the NRES spectrograph (Table 4).[7]

All the observation sites are equipped with a local weather station, providing information on humidity levels, weather conditions, wind speed, temperature, sky transparency, and other relevant quantities. This information, together with the operational statuses of the instruments, are used by the automatic system that controls the aperture of the dome and that communicates with the scheduler. The same info is available to users and can be queried both via the web interface[8] or through the central database via API scripts (Section 3.2).

[2]Faulkes Telescope South (FTS)
[3]Faulkes Telescope North (FTN)
[4]https://lco.global/observatory/instruments/spectral/
[5]https://lco.global/observatory/instruments/floyds/
[6]https://lco.global/observatory/instruments/sinistro/
[7]https://lco.global/observatory/instruments/nres/
[8]https://weather.lco.global/#/bpl (weather) https://lco.global/observatory/status/ (instruments status)

Table 4 Instruments main specs

Name	Detector format (μm)	Readout (s)	Filters	Mounted on (class) (m)	FOV (')	Pixel size (")
Sinistro	4096x4097x15	4	UBVRI, u' g' r' i' z' sYw	1	26.5	0.389
Spectral	4096x4097x15	14	UBVRI, u' g' r' i' z' sYw, H_{alpha}, H_{beta}, OIII, D51, UV, v	2	10.5	0.304

2.3 Observation requests handling and management

A global network like the LCOGT requires a very high level of automation, so all the steps from the handling of observation requests to observations are managed from the central headquarter located near Santa Barbara, California and automatically executed by the on-site node. LCOGT network entered in an agreement with the NOAO and other partners offering observing time as part of their general call for proposals.

Observations requests can be submitted both via the web interface[9] or through API scripts.[10] A request consists of a certain number of exposures, for which the required instrumental configuration (e.g., aperture, filters, exposure times) must be specified. Further constraints (e.g., seeing, transparency, moon distance) can be also set. The system provides also the possibility to push for high priority request, through a protocol called "Target of Opportunity" (ToO): this is designed for observations of transients and relatively short-lived phenomena. This kind of requests is granted a priority route to go quickly through all the different steps up to the final node. The ToO requests can override previous, lower-priority observations, that will be resumed at its end.

Once the request is complete and submitted, the scheduler funnels it through a specific node on the basis of the user requests and of the information from the node itself, such as visibility of the target, telescopes availability, weather conditions, and other relevant quantities.

When individual exposures are completed, the relative temporary-reduced, quick-look files are produced and made available on the proposal web page along with the original raw files. The former ones are produced from the latter ones using a fast, light version of the data pipeline described in [34], while the finally reduced products are usually released several hours later using the complete, slower version of the same pipeline. All these products can be downloaded both via the web interface or through API scripts.[11]

2.4 Our GRB-driven proposals

The GRB pipeline described in this paper has been developed under proposal ARI2018B–001 (PI: S. Kobayashi), whose aim is monitoring of GRB/SNe optical light curves (Section 1). The main goal is the prompt followup of GRB discovered by space-based observatories like the Neil Gehrels *Swift* Observatory or *INTEGRAL* [35]. The development phase has exploited the great experience our group has gained since our first observations with the LCO network in 2014: a brief history of our proposals on the LCO network is reported in Table 2. The proposal on which we developed our code, ARI2018B–001, has been granted the following observation time:

– 3 hours at standard priority on 2-m class units;

[9] https://observe.lco.global/create/

[10] https://developers.lco.global/?python#introduction

[11] https://developers.lco.global/#get-related-frames

– 6.5 hours at high priority (ToO) on 2-m class units;
– 7 hours at high priority (ToO) on 1-m class units.

The observing period began June 1, 2018, and lasted for six months.

3 GRB pipeline description

3.1 GCN analysis

The GRB pipeline[12] is designed to optimally exploit the potential of the LCO network, in particular: (i) its worldwide distribution of observing facilities, that allows a good sky coverage in both hemispheres; (ii) prompt response to ToO requests. It continuously listens to the Gamma-ray burst Circular Network (GCN [36]) Notices[13] and, in case of a promptly observable target, reacts by promptly submitting a customised observation sequence. A rapid and effective management of this phase is essential to track the early-time light curve of the possible optical afterglow: in this respect, reducing at minimum the human-in-the loop involvement is critical to avoid possible mistakes and rapidly perform the most appropriate observing sequence.

The first task is the continuous monitoring of the trigger notices from both *Swift* and *INTEGRAL* missions. Every such notice is a message distributed via socket and e–mail that provides basic information about a trigger from one of satellites connected to the Inter–Planetary Network (IPN),[14] such as the time of the event, the detector, the kind of trigger and other secondary parameters. In case of an event that the on-board system recognises to be a GRB, an estimation of the position is provided too, together with the related uncertainty.

We conveniently make use of the socket-distributed version of the GCN notices, that consists of a text message formatted in the JavaScript Object Notation (JSON),[15] a light format that is both human and machine readable.

To ensure the maximum portability and a smooth interaction with the LCO network, the whole pipeline presented in this paper is written in Python 3.6. The code has been tested both under MacOs 10.12 and on Fedora 21.

The handling of incoming, socket-distributed notices is performed using the `gcn` Python library.[16] The basic structure of this part of the code is composed by a client that continuously waits for notices distributed via the VOEvent Transport Protocol.[17] When a VOEvent is received, the socket notice is passed on to a handler, that extracts the required information. Among the setting options, the user can easily select the type of events that will set the handler on.

[12] https://github.com/kobe90/LCO_pipeline
[13] The system of Notices and Circulars is described at https://gcn.gsfc.nasa.gov
[14] https://heasarc.gsfc.nasa.gov/w3browse/all/ipngrb.html
[15] https://www.json.org
[16] https://github.com/lpsinger/pygcn
[17] http://www.ivoa.net/documents/Notes/VOEventTransport/

The GCN-Notice system can generate different kinds of VOEvent, that are reported at a web page[18] and that correspond to different actions and alerts. As of September 2018, the GRB pipeline is designed to handle *Swift* and *INTEGRAL* Burst Notices, so we used the so-called "BAT Position Notice"[19] (for *Swift*) and "REFINED Notice" (for *INTEGRAL*).[20]

Once an event of the selected type is received, the handler can extract information using the `xml` syntax. We extract the following basic pieces of information:

- Name of the trigger (which uniquely identifies it);
- Position: right ascension (RA) and declination (DEC);
- Position error radius;
- galactic latitude.

The VOEvent is further checked to see whether it matches our interests by looking at the boolean values of the following variables:

- not-a-GRB variable: if `False` the event is probably a real GRB;
- catalog variables: if at least one is `True`, the emission that triggered the instrument was probably from a known source, i.e. uninteresting for a GRB programme;
- test variable: if set to `True` the VOEvent was the result of a test and not a real event.

The extracted position is then double checked against our local catalogue of known variable X-ray sources that can occasionally mimic the occurrence of a GRB.

Notices from *INTEGRAL* are slightly different, in that they lack the catalogue variable, only the information contained in the first (not-a-GRB) and third (test variable) labels is processed. Also in this case the position of the burst candidate is crosschecked against our local catalogue.

The same information is also used to build two visibility plots (one per hemisphere) for the LCO sites accessible to our proposal. An example of this kind of products can be found in Fig. 1. Sun distance, Moon distance and phase, together with the Galactic visual extinction, are also calculated. The last is estimated using the SFD radio maps [37], that can be easily queried using the `SFDmap` library.[21] Only candidates for which the expected visual extinction is $A_V < 5$ mag are considered. Note that the described visibility plots are built using only the trigger and the observatory locations, regardless of the actual availability and status of each telescope.

3.2 Visibility of the target

As briefly outlined in Section 2.2, the availability of a certain telescope can be queried via a boolean output (answering the question "Can the telescope work now?") and

[18] https://gcn.gsfc.nasa.gov/filtering.html.
[19] https://gcn.gsfc.nasa.gov/swift.html
[20] https://gcn.gsfc.nasa.gov/integral.html
[21] https://github.com/kbarbary/sfdmap

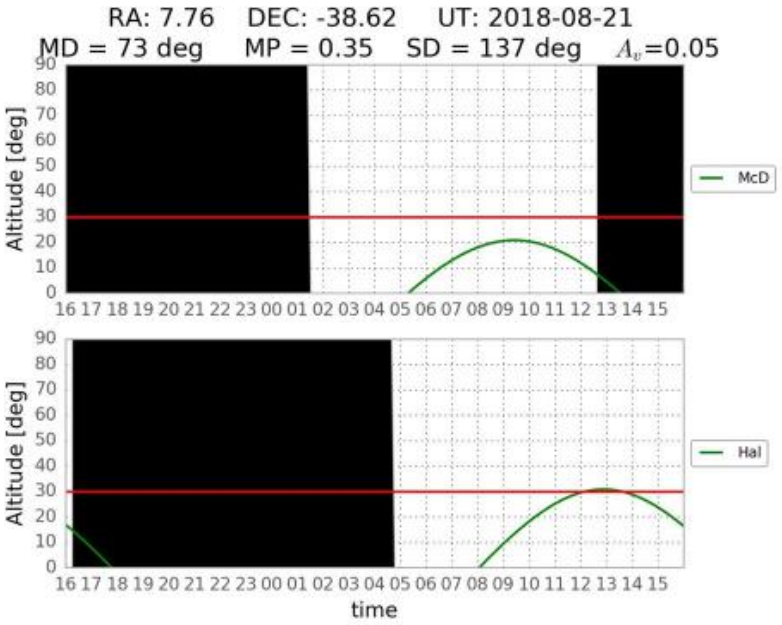

(a) visibility-north

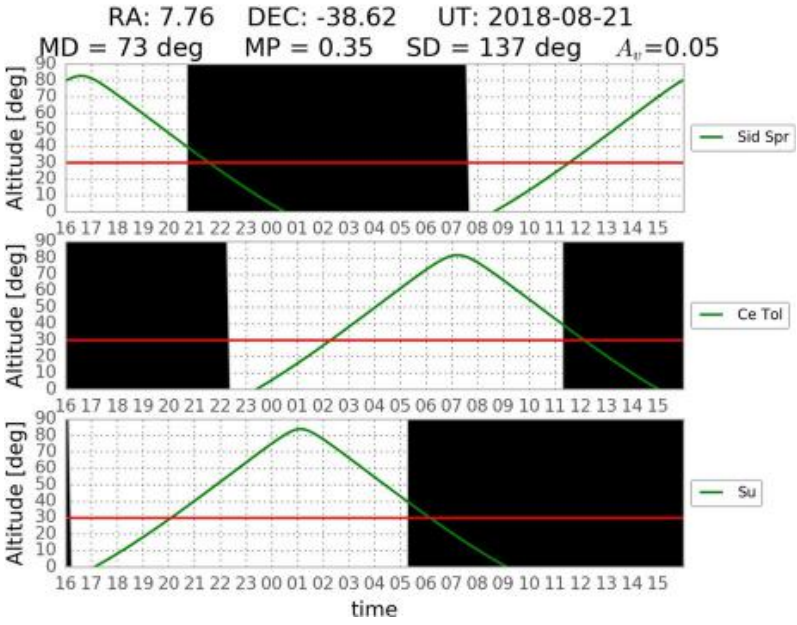

(b) visibility-south

Fig. 1 Visibility plot (altitude vs Universal Time (UT)) for the northern (**a**) and southern (**b**) hemisphere sites of the LCO network we access to. The black regions indicate the daytime, while the red, horizontal line indicates the minimum altitude at which the telescopes can observe. On the right-hand side the observatory shortened names are indicated, while on the top further burst information is summarised: equatorial coordinates (J2000), UT, MD (Moon Distance), MP (Moon Phase), SD (Sun Distance), A_v (Galactic visual extinction)

with a certain number of input arguments that can be grouped into two main categories: instrumental status and weather conditions. These pieces of information have to be combined with that contained in the visibility plots to know the effective visibility of the event from each instrument. A certain target is qualified as observable by a certain telescope if:

1. its altitude is $\geq 30°$;

2. the Sun is $> 12°$ below horizon (Nautical Dawn/Sunset);
3. the Moon distance is $\geq 30°$;
4. good local weather conditions;
5. the telescope status is operational.

Requirements 1-3 can be answered from the burst and telescope positions, while 4 and 5 can be easily checked querying the LCO network. We used some templates[22] to build and test a function that checks data collected by on-site weather sensors. The environmental conditions are considered good, whenever all the following requirements are fulfilled:

– air temperature > -20 °C;
– air humidity < 90 %;
– wind speed < 15 km/h;
– sky brightness < 18 mag/arcsec^2.

Finally, the operational status of each telescope is checked through a function that returns the list of available units[23]).

The list of instruments that can effectively observe the target is then stored for the submission phase and is also provided to users in a compact format, as described in the following.

3.3 Distribution to the users

A user is anyone that receives the GRB pipeline notices through one of the distribution channels (described in the following), and that is enabled to interact and take control of the followup activities.

As far as the choice for the optimal strategy is concerned, human action is preferable. Upon receiving essential, readable-on-the-fly information, any user aiming at taking control, has to explicitly reply to the GRB pipeline. In this case, the pipeline sends a confirmation of the user choice (both to him and other users) and then comes back to the listening mode.

The promptly distributed information includes:

– visibility plots;
– list of instruments able to promptly observe the event and their location;
– amount of residual observing time of our proposal.

While the first two items are already described above in Section 3.2, the last one is obtained querying the LCO proposal repository.[24] The observing time is classified into categories based on the instrument class (1m or 2m in the case of our proposal) and on the observing priority: for obvious reasons the GRB pipeline only sends ToO requests.

[22] https://developers.lco.global/?python#retrieve-weather.
[23] Examples are available at https://developers.lco.global/?python#telescope-states.
[24] Some templates are available: https://developers.lco.global/?python#proposals.

Communications with users is possible through two channels: (i) via ordinary emails; (ii) via Telegram,[25] a multi-platform open-API messaging system with bidirectional communication enabled. While the interaction with mail servers can be done routinely in Python using a wide collection of specific libraries, we opted for using the `Python-telegram-bot` library[26] to manage Telegram messages both ways. The Telegram channel makes use of a bot that acts as an ordinary, human user, distributing messages. A person that is interested in our Telegram notice just needs to create a Telegram account and contact our bot: this way they will be added to our list of interacting users. Unlike the Telegram notice, the email is a sort of reminder and lacks the possibility of interacting with the pipeline: the idea is that very rapid, interacting Telegram notices are dedicated to a smaller group of core users strongly involved and more interested in taking control whenever this is considered as a preferable option.

An example of Telegram interaction is provided in Fig. 2. After the "Are you awake?" question the programme waits for an answer from any of the users for one minute; if no one replies, it autonomously submits the observation request (Section 3.4 for further details). Differently, the user that responds is notified to be in charge (while other users are notified that someone else is in charge). Consequently, the pipeline stops taking care of the present trigger and gets back to the GCN Notice listening mode. There are also cases in which no one of the LCO instruments is able to observe the target: in this case users are informed and the programme resumes the socket listening activities (Fig. 3).

3.4 Submission

The Neil Gehrels *Swift* Observatory working strategy relies on the complex and very efficient interplay between its three on-board instruments: the Burst Alert Telescope (BAT), the X-ray Telescope (XRT) and the UV/Optical Telescope (UVOT). When a signal is detected and identified by the large-field instrument (BAT), the satellite rapidly slews to point XRT and UVOT that observe at lower energies. The distributed *Swift* GCN Notices reflect this strategy. The first Notice is produced after the BAT trigger and contains the first rough estimation of the position (usually with an error radius of a few arcminutes), then, in the absence of observing constraints, XRT and UVOT are automatically pointed towards the source and more accurate information about position (with an error radius usually within a few arcsecs), flux and magnitude (for UVOT) is produced and distributed whenever credible candidates are found within the BAT error circle. The time lag between the BAT detection and XRT and UVOT pointing is quite variable, depending on a number of observational and technical constraints (see Section 4.1 for further details). A good strategy for a fast optical followup should exploit UVOT Notices too, since the detection (or lack thereof) of an UVOT counterpart is a further piece of information that can be used to refine the data acquisition (see below).

[25] https://telegram.org

[26] https://github.com/python-telegram-bot/python-telegram-bot

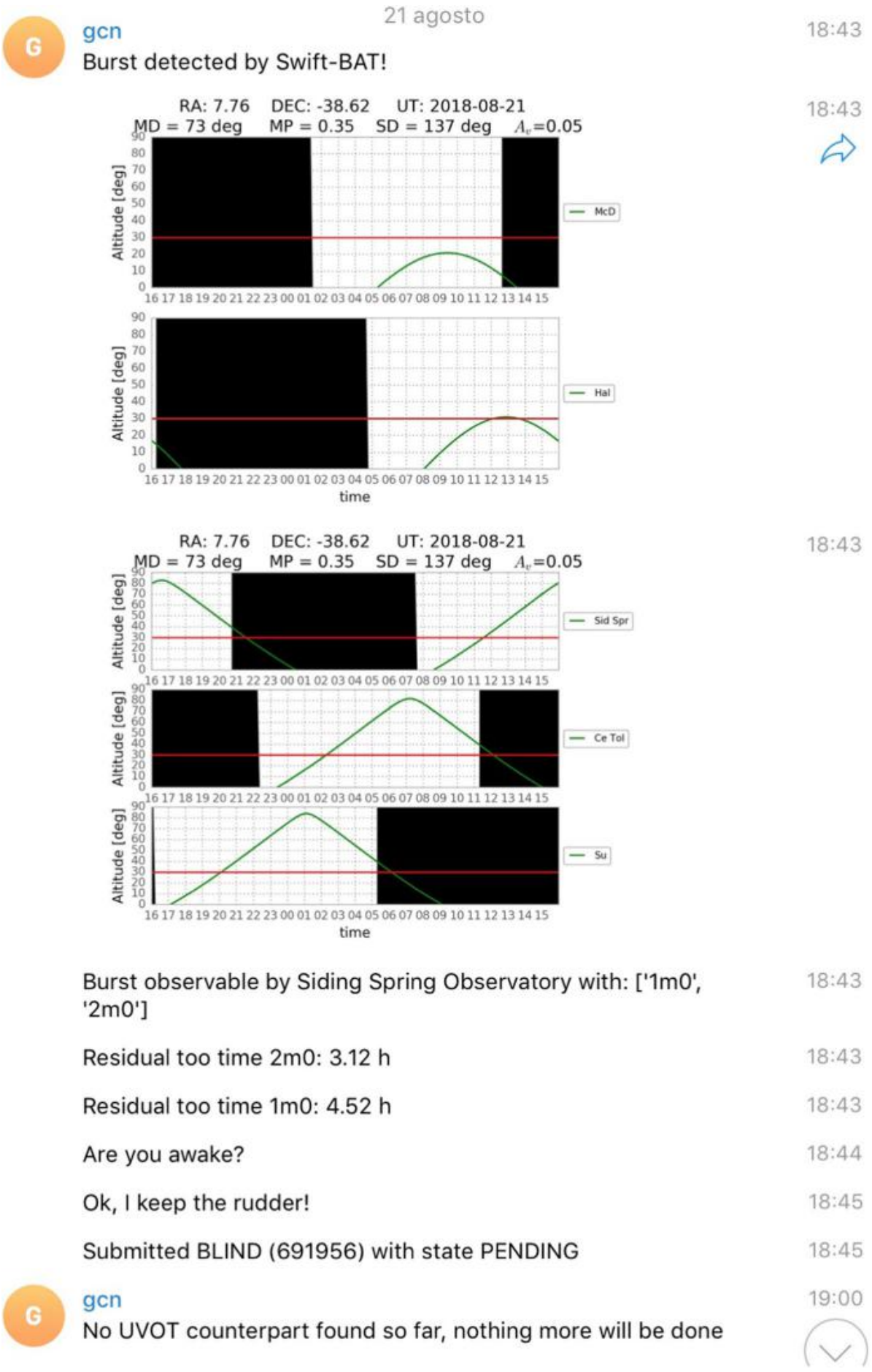

Fig. 2 Example of a notice distributed via Telegram. In this case the users remain quiet, thus letting the pipeline move on to the submission phase

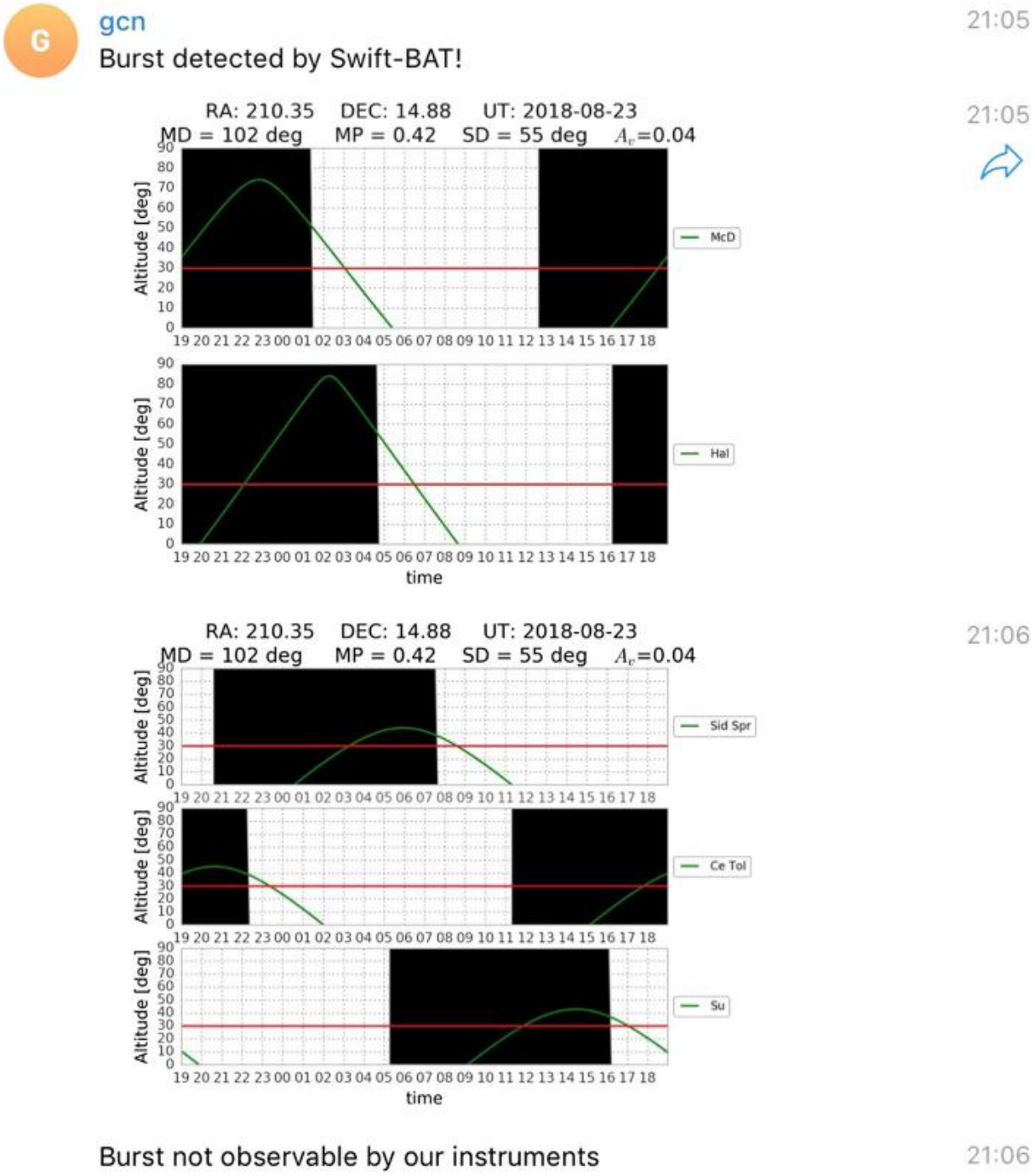

Fig. 3 Example of a notice distributed via Telegram in case of non-observable target

The basic principle of our strategy for *Swift* is the prompt submission of a fast, preliminary observation request once the first burst notice from BAT has come along. Then, the GRB pipeline may send a second one, better tailored to the UVOT counterpart brightness, in the case of an optical detection by UVOT. Following this guideline, after the first submission, the pipeline waits for 15 minutes for a UVOT notice: in case of no optical detection, no additional requests are sent to the LCO network and the already-sent preliminary request becomes definitive. Differently, the GRB

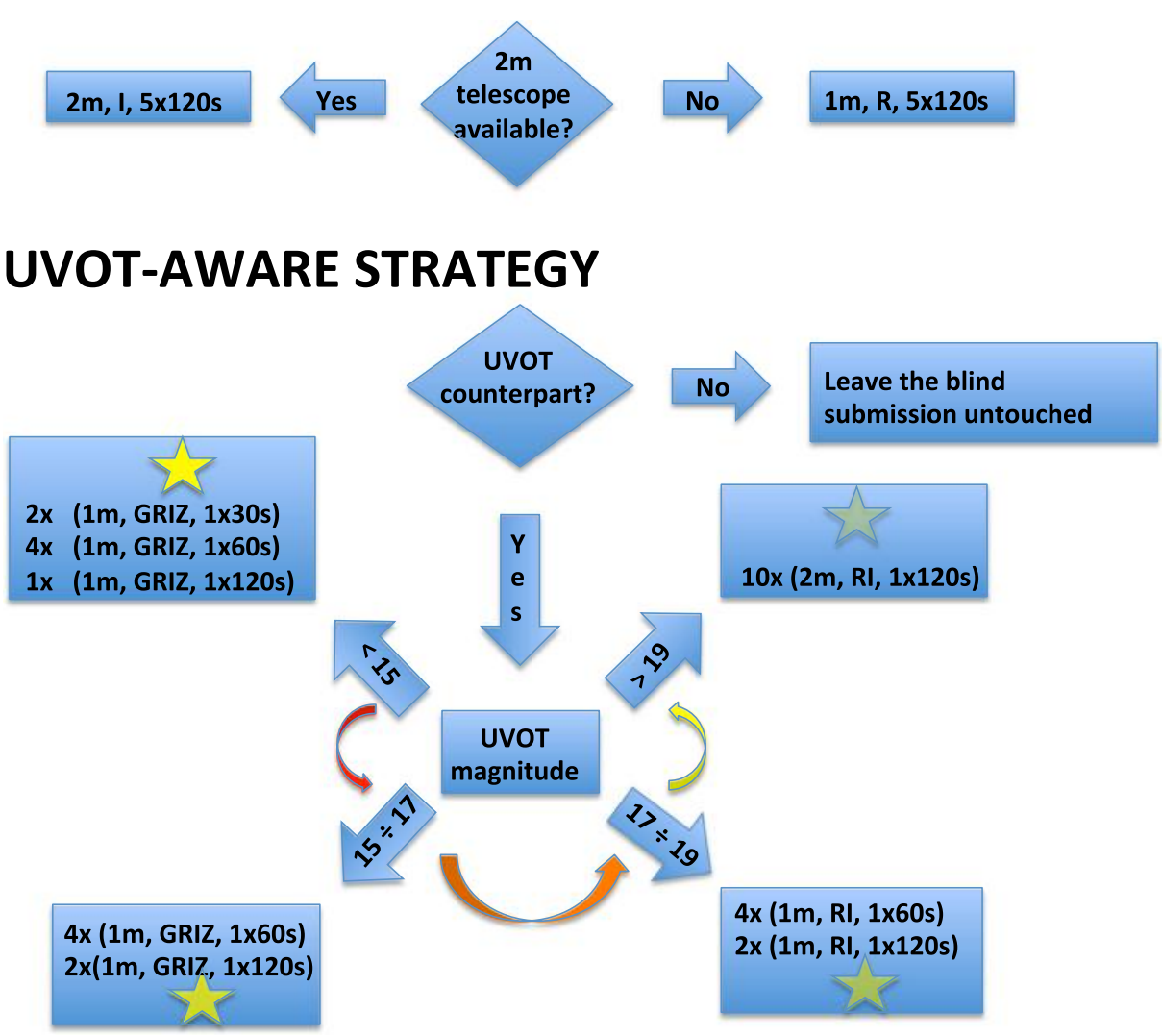

Fig. 4 Sketch of the observation strategy, before and after UVOT information reception. "Blind" observation request describes the observing strategy when no information from UVOT is available (yet) and is based on the BAT estimated position. The only two-option choice is driven by the availability of 2m-class telescopes. The blind request is always submitted when the bursts is observable by at least one of the instruments we use. The blind step is the only one in the case of *INTEGRAL* burst Notices. UVOT-aware observation request: observing strategy upon receiving a Notice of a UVOT detection within 15 minutes of the reception of a *Swift*-BAT Notice. If no UVOT counterpart detection has been detected, nothing more is done for that trigger; otherwise, the choice is driven by the estimated UVOT magnitude in the w filter, as reported in the corresponding GCN Notice

pipeline extracts from the UVOT Notice the refined position and the estimated optical magnitude in the White[27] filter. A flow chart describing the different branches of possibilities is shown in Fig. 4.

The strategy based on *INTEGRAL* Notices is simpler, given that the "REFINED" Notice is not followed by anything and there are no prompt re-pointings of different

[27] http://www.swift.ac.uk/analysis/uvot/filters.php

energy instruments. This is the reason why the strategy in this case is the same as the "Blind" one for *Swift* and no further steps are required.

The submission of an observation request, like almost all the other operations on the LCO network, can be done both via web interface[28] and API script.[29]

4 Statistical analysis

4.1 Prompt UVOT information

The existence of a time delay between the BAT trigger and the detection of a UVOT counterpart is something unavoidable, due to the *Swift* working strategy and affected by wide number of factors, such as the slewing time of the facility, and other observation constraints. This justifies the need for a waiting time between the "Blind strategy" and the "UVOT-aware" steps of our strategy (Fig. 4). Since a rapid and proper response to trigger notices is the first aim of the GRB pipeline, an optimal choice of this waiting time is fundamental: one has to find a trade-off between the need to wait for the UVOT information and the need to proceed quickly. To find the optimal duration of the waiting time, we derived the distribution of the delay times between the BAT position notice and the UVOT notice. We used the information available at the *Swift* web page.[30] We included all *Swift* GRBs with a UVOT detection, that represent $\approx 25\%$ of the total. We discarded all the bursts with a time delay $T_{\mathrm{UVOT}} - T_{\mathrm{BAT}} > 100$ min that were due to delayed followups, most of which were probably due to observing constraints. The remaining dataset consists of 376 events and its $T_{\mathrm{UVOT}} - T_{\mathrm{BAT}}$ distribution and some related quantities are displayed in Fig. 5. The distribution is asymmetric, with a long tail extending to large time delays all the way up to the 100-minute threshold. Nonetheless, the vast majority of times clusters around a few minutes, as shown by the median ($\sim$ 1.7 min) and interquartile span ($\sim$ 1.1 min). When no threshold on the BAT-UVOT delay is set, 93% of GRBs with a UVOT counterpart have a delay shorter than 15 min. This makes us confident that the GRB pipeline can exploit UVOT information in more than 90% cases. A clearer picture can be obtained looking at Fig. 6, where we reported all the GRBs from start of *Swift* up to now in the V-mag/T-T_{BAT} plane. Most detections occur in the first 200 s after the BAT trigger. The brightest events are mostly seen around $\sim$ 100 s and not earlier. This time roughly corresponds to the time of the peak of the distribution of optical afterglows. This is probably the result of a mere observation bias, since rare events are more likely to be found around the most sampled times.

4.2 LCO response to ToO requests

To get a complete picture of the time delay from the reception of a GCN up to the frame acquisition, we analyse the time required by LCO to start acquiring data once

[28] https://observe.lco.global/create/

[29] https://developers.lco.global/?python#observations

[30] https://swift.gsfc.nasa.gov/archive/grb_table/

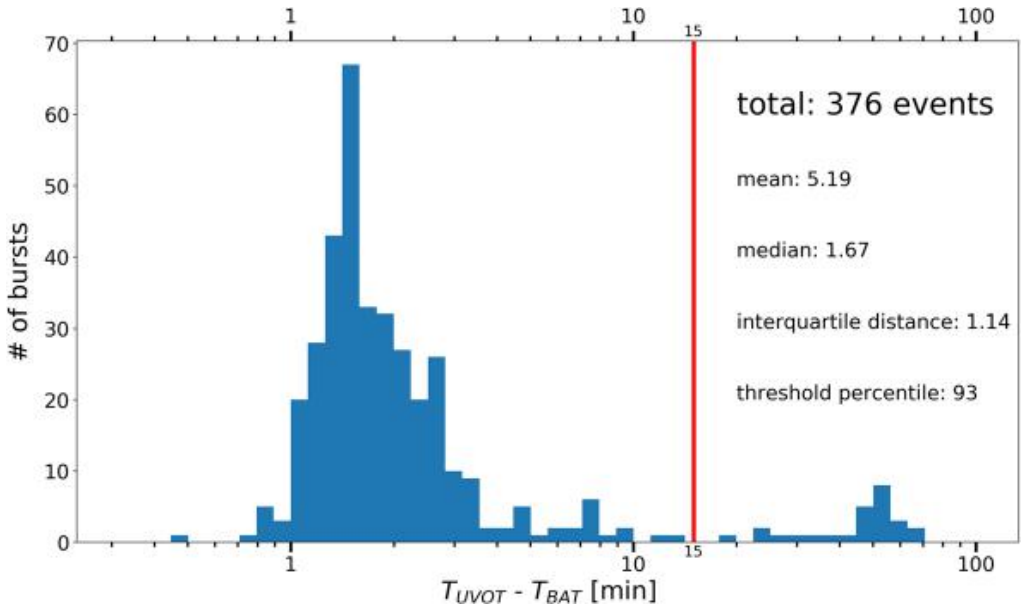

Fig. 5 Distribution of the time delay between the arrival of the *Swift*-UVOT Notice trigger and the *Swift*-BAT Notice trigger built on a dataset of 376 events. In $\sim$ 90% of cases, this delay is $<$ 15 minutes. The distribution has been obtaining considering only events with $T_{UVOT} - T_{BAT} < 100$ min, since larger deltas are usually connected with pathological cases

an observation request is received. This delay depends mainly on the pressure of users on the network, meaning a large number of observation requests for the scheduler to manage. This number varies randomly and so does the time delay, too. We built our time delay distributions considering observation requests from all our approved proposals on LCO (Section 2), covering the entire time span (Figs. 7 and 8 and 9). The

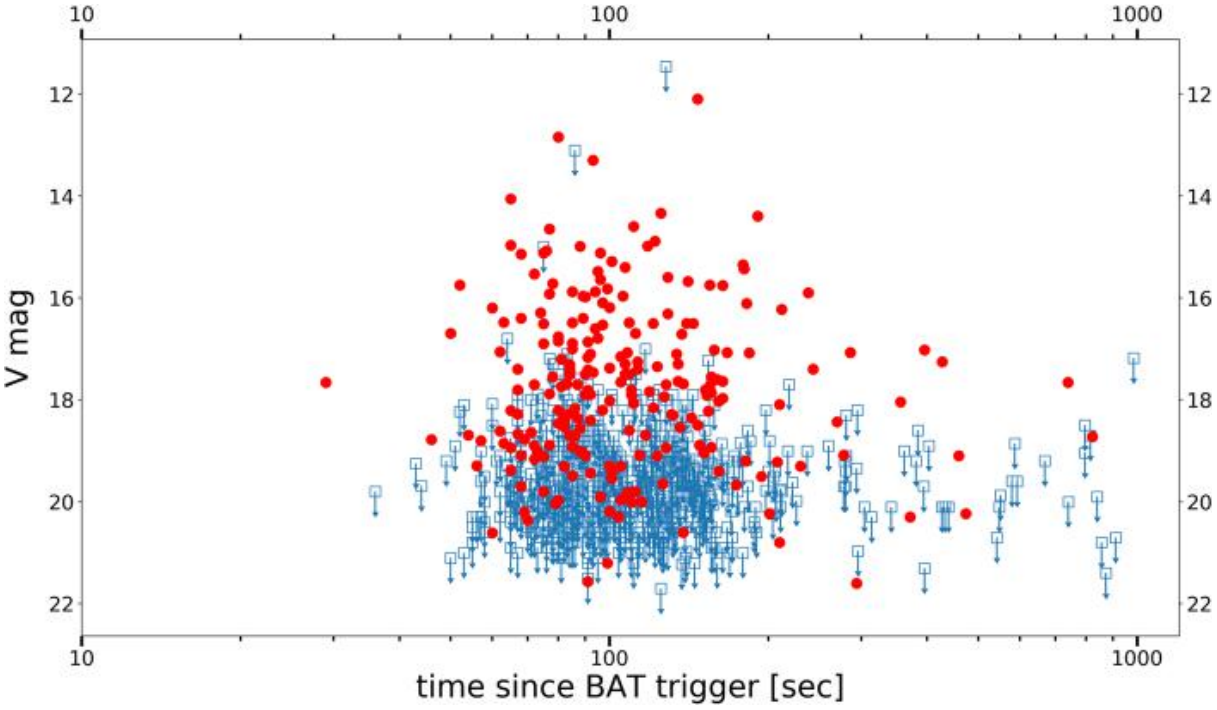

Fig. 6 Scatter plot of GRBs promptly observed by *Swift*-UVOT, showing V-mag vs. $T - T_{BAT}$. Red dots and blue squares show detections and upper limits, respectively. Unusually long delays ($T - T_{BAT} >$ 1000 s) have been omitted

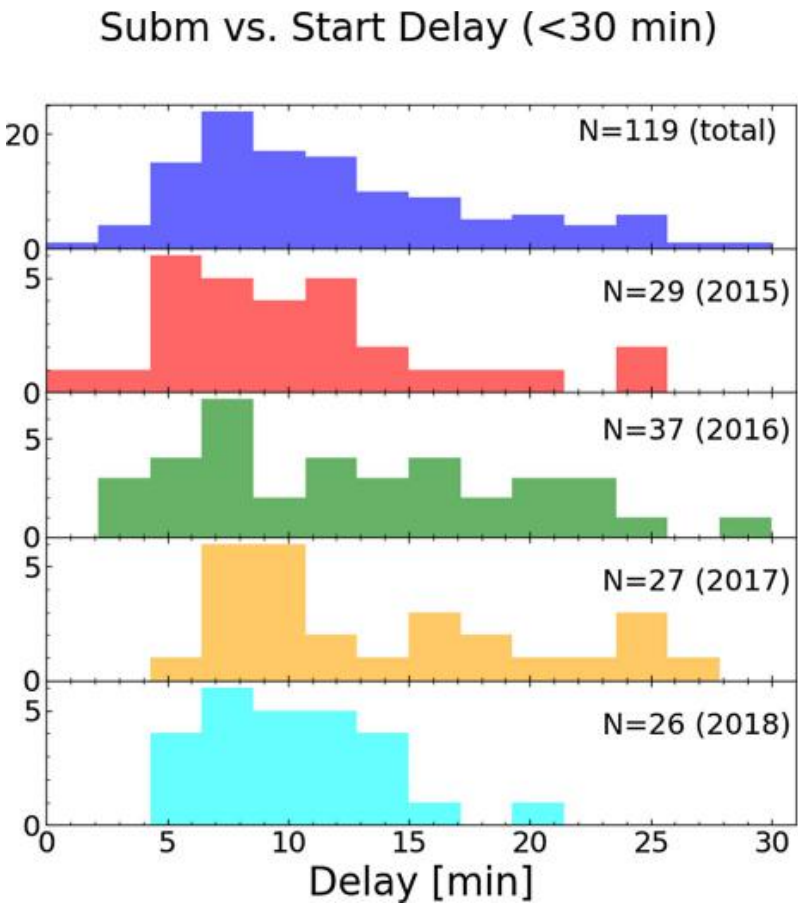

Fig. 7 Time delay between ToO request submission and observation start for our proposals on the LCO network from January 2015 up to now

reason why the distribution has sligthly changed over the years is that the scheduler algorithms have continuously been adjusted in response to the various changes that occurred in the meanwhile.

5 Example of a successful case

On July 20, 2018, at 14:21:44 UT *Swift*-BAT triggered GRB 180720B (α, δ)= (0.530°, −2.933°; J2000) and a GCN Notice [38] was promptly distributed via both email and socket. We received the socket message at 14:22:44 UT and the pipeline began operations[31] to convey burst information, wait for human intervention and then submit a "blind" observation request. We were informed by the pipeline at 14:22:45 UT and the very first observation request was automatically submitted at 14:24:07

[31] Please note that we used a slightly different procedure in this case, being in a first testing phase. The main differences where:

– we used a 7-minutes waiting time for the UVOT counterpart;
– we submitted a slightly different "blind" observation request, composed by 5 exposure of 120s in the i' filter.

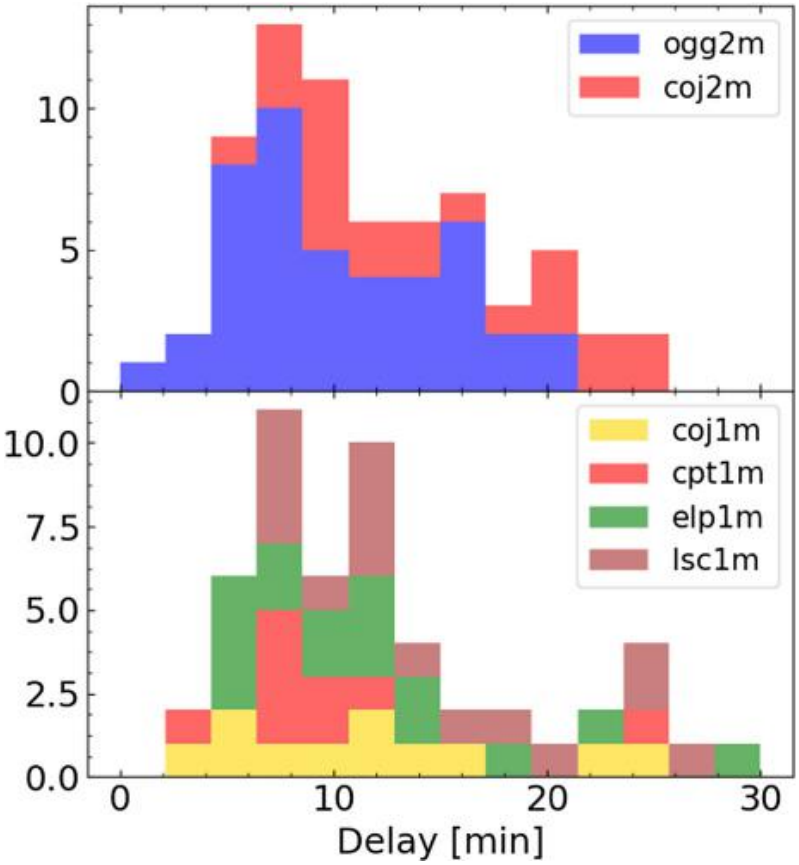

Fig. 8 Time delay between ToO request submission and observation start for our proposals on the LCO network from January 2015 up to now, for each individual telescope (color-coded): 2-m units (*top*), and 1-m units (*bottom*). A KS test comparing the distributions of ogg2m (Hawaii) vs. that of coj2m (Siding Springs) yields a 4.4% probability of being drawn from the same population, with ogg2m seemingly faster than coj2m on average

UT, after 1 minute of waiting for the human intervention. It is worth noting that the email Notice was received at 14:24, at the moment of our first submission. The 2-m unit at Siding Spring Observatory started observing at 14:33:34 UT (710 s from the BAT trigger) and completed the sequence at 14:46:43 (1499 s from the BAT trigger)

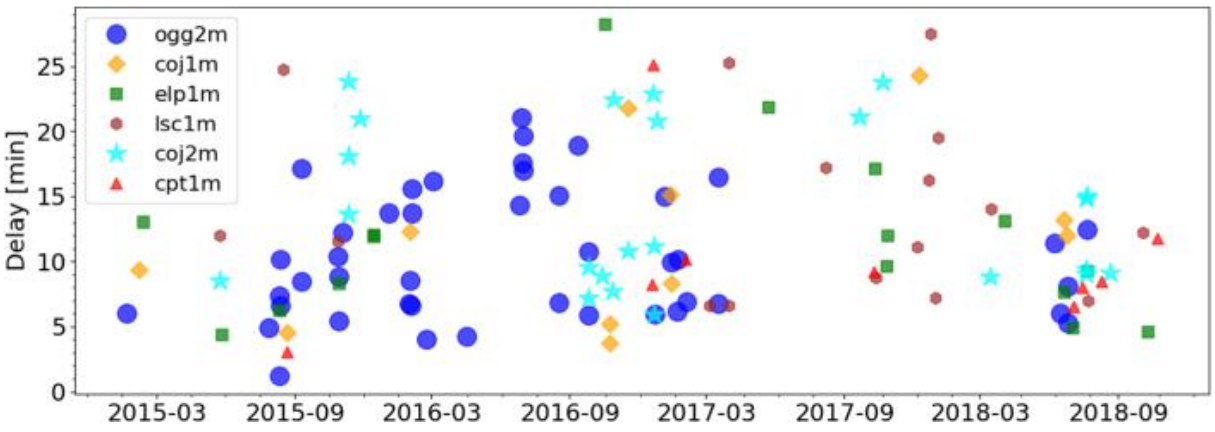

Fig. 9 Delay [minutes] between ToO submission time and effective start time as a function of epoch for our proposals on the LCO network, starting from January 2015 up to now. Markers uniquely indicate observatories and observing units accessible to our programme.

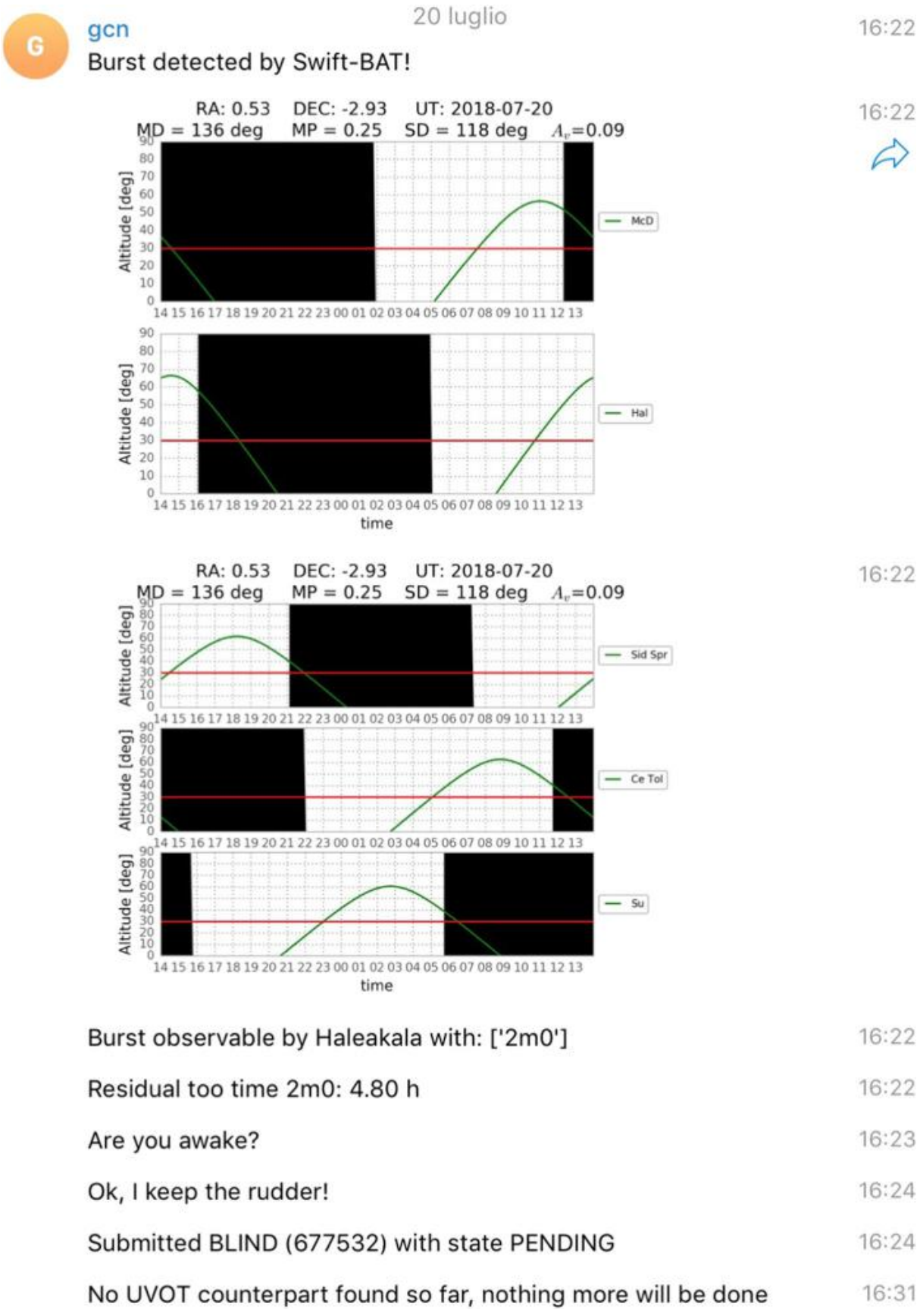

Fig. 10 Screenshot of the Telegram output for GRB 180720B. Note that times are in the CET frame, so GMT+2 at the moment of the burst. The pipeline indicated the burst as promptly visible from Haleakala, but a few minutes later the burst became observable from Siding Spring, that finally performed the observation as established by the scheduler

UT[32] Data became available a few minutes after the end of the observation sequence and so we were able to promptly analyse the frame less than 30 minutes after the burst and to identify the optical afterglow. Our discovery was issued to the community about an hour after the explosion [39]. Figure 10 reports a screenshot for the Telegram set of notification for this burst we distributed to our users.

6 Conclusions

This work describes the automatic pipeline that we developed and used for fast followup of optical GRB counterparts with the LCO network. Designed to respond to triggers by *Swift* and *INTEGRAL* with the maximum rapidity allowed by LCO, proved to be successful in ensuring the monitoring of the first minutes of the flux evolution of the GRB optical counterpart. It is developed under Python environment, to ensure the highest cross-platform compatibility and to exploit the large amount of astronomy-oriented packages and utilities available.

The ability of fast reading the notices benefits from receiving alerts via socket, while communicating the content to the users is handled via the Telegram platform. The advantages of this combination are the rapidity, reliability, and the absence of any cost notification delivering.

The submission step takes advantage of the peculiarities of the LCO network, whose many eyes (spread all over the globe) are managed by a single, central scheduler in a full-robotic design. The scheduler is directly triggered by the pipeline observation requests, which for *Swift* bursts are tailored on the available UVOT information.

We described the example of GRB 180720B, for which the pipeline enabled us to track the optical evolution of the burst a few minutes after the notice arrival. Specifically, observations were submitted 143 s and began 710 s after the BAT trigger [39].

Based on our experience in the Target-of-Opportunity observations with LCO network, we have carried out a statistical study of the response times of the whole system. The results are critical to understand the potential and current limitations of the network being used for any fast followup programme. Furthermore, they represent a starting point and a useful reference for future improvements and upgrades of the network. The ultimate goal of the pipeline is to optimise receipt and response to any programmes on the prompt followup of transient triggers, for which the study of the early phases is key to capture the encoded physics. While conceived for GRB followup, its portability and versatility make it a valuable reference for other fast transient programmes in the era of transient sky. The same configuration can be further exploited using notices from *Fermi* [40] to trigger large-field-of-view ($> 1^\circ \times 1^\circ$) telescopes. The opportunities of following up rapid transients are due to

[32]The pipeline flagged the burst as promptly visible from Haleakala, but a few minutes later the burst became observable from Siding Spring, too. According to internal rules, the scheduler finally decided to convey our observation request towards Siding Spring, that finally performed the observation.

dramatically increase in the next years, also thanks to the upcoming Large Synoptic Survey Telescope [41].

Acknowledgements We thank Leo Singer for his help and support in the developing of the code. Support for this work was provided by Università di Ferrara through grant FIR 2018 "A Broad-band study of Cosmic Gamma-Ray Burst Prompt and Afterglow Emission" (PI Guidorzi).

References

1. Klebesadel, R.W., Strong, I.B., Olson, R.A.: Astrophys. J. Lett. **182**, L85 (1973). https://doi.org/10.1086/181225
2. Woosley, S.E.: Models for gamma-ray burst progenitors and central engines (gamma-ray bursts). Cambridge Astrophys. Series **51**, 191 (2012)
3. Lipunov, V.M., Postnov, K.A., Prokhorov, M.E., Panchenko, I.E., Jorgensen, H.E.: Astrophys. J. **454**, 593 (1995). https://doi.org/10.1086/176512
4. Abbott, B.P., Abbott, R., Abbott, T.D., Acernese, F., Ackley, K., Adams, C., Adams, T., Addesso, P., Adhikari, R.X., Adya, V.B., et al: Astrophys. J. Lett. **848**, L12 (2017). https://doi.org/10.3847/2041-8213/aa91c9
5. Eichler, D., Livio, M., Piran, T., Schramm, D.N.: Nature **340**, 126 (1989). https://doi.org/10.1038/340126a0
6. Paczynski, B.: Acta Astronomica **41**, 257 (1991)
7. Narayan, R., Paczynski, B., Piran, T.: ApJ **395**, L83 (1992). https://doi.org/10.1086/186493
8. van Paradijs, J., Groot, P.J., Galama, T., Kouveliotou, C., Strom, R.G., Telting, J., Rutten, R.G.M., Fishman, G.J., Meegan, C.A., Pettini, M., Tanvir, N., Bloom, J., Pedersen, H., Nørdgaard-Nielsen, H.U., Linden-Vørnle, M., Melnick, J., Van der Steene, G., Bremer, M., Naber, R., Heise, J., in't Zand, J., Costa, E., Feroci, M., Piro, L., Frontera, F., Zavattini, G., Nicastro, L., Palazzi, E., Bennett, K., Hanlon, L., Parmar, A.: Nature **386**, 686 (1997). https://doi.org/10.1038/386686a0
9. Akerlof, C., Balsano, R., Barthelmy, S., Bloch, J., Butterworth, P., Casperson, D., Cline, T., Fletcher, S., Frontera, F., Gisler, G., Heise, J., Hills, J., Kehoe, R., Lee, B., Marshall, S., McKay, T., Miller, R., Piro, L., Priedhorsky, W., Szymanski, J., Wren, J.: Nature **398**(6726), 400 (1999). https://doi.org/10.1038/18837
10. Gehrels, N., Chincarini, G., Giommi, P., Mason, K.O., Nousek, J.A., Wells, A.A., White, N.E., Barthelmy, S.D., Burrows, D.N., Cominsky, L.R., Hurley, K.C., Marshall, F.E., Mészáros, P., Roming, P.W.A., Angelini, L., Barbier, L.M., Belloni, T., Campana, S., Caraveo, P.A., Chester, M.M., Citterio, O., Cline, T.L., Cropper, M.S., Cummings, J.R., Dean, A.J., Feigelson, E.D., Fenimore, E.E., Frail, D.A., Fruchter, A.S., Garmire, G.P., Gendreau, K., Ghisellini, G., Greiner, J., Hill, J.E., Hunsberger, S.D., Krimm, H.A., Kulkarni, S.R., Kumar, P., Lebrun, F., Lloyd-Ronning, N.M., Markwardt, C.B., Mattson, B.J., Mushotzky, R.F., Norris, J.P., Osborne, J., Paczynski, B., Palmer, D.M., Park, H.S., Parsons, A.M., Paul, J., Rees, M.J., Reynolds, C.S., Rhoads, J.E., Sasseen, T.P., Schaefer, B.E., Short, A.T., Smale, A.P., Smith, I.A., Stella, L., Tagliaferri, G., Takahashi, T., Tashiro, M., Townsley, L.K., Tueller, J., Turner, M.J.L., Vietri, M., Voges, W., Ward, M.J., Willingale, R., Zerbi, F.M., Zhang, W.W.: ApJ **611**, 1005 (2004). https://doi.org/10.1086/422091
11. Akerlof, C.W., Kehoe, R.L., McKay, T.A., Rykoff, E.S., Smith, D.A., Casperson, D.E., McGowan, K.E., Vestrand, W.T., Wozniak, P.R., Wren, J.A., Ashley, M.C.B., Phillips, M.A., Marshall, S.L., Epps, H.W., Schier, J.A.: Publ. ASP **115**(803), 132 (2003). https://doi.org/10.1086/345490
12. Lipunov, V., Kornilov, V., Gorbovskoy, E., Shatskij, N., Kuvshinov, D., Tyurina, N., Belinski, A., Krylov, A., Balanutsa, P., Chazov, V., Kuznetsov, A., Kortunov, P., Sankovich, A., Tlatov, A., Parkhomenko, A., Krushinsky, V., Zalozhnyh, I., Popov, A., Kopytova, T., Ivanov, K., Yazev, S., Yurkov, V.: Adv. Astron. **2010**, 349171 (2010). https://doi.org/10.1155/2010/349171
13. Boër, M., Bringer, M., Klotz, A., Moly, A.M., Toublanc, D., Calvet, G., Eysseric, J., Leroy, A., Meissonnier, M., Malina, R., Sanchez, P., Pollas, C., Pedersen, H.: Astron. Astrophys. Suppl. **138**, 579 (1999). https://doi.org/10.1051/aas:1999356

14. Castro-Tirado, A.J., Soldán, J., Bernas, M., Páta, P., Rezek, T., Hudec, R., Mateo Sanguino, T.J., de La Morena, B., Berná, J.A., Rodríguez, J., Peña, A., Gorosabel, J., Más-Hesse, J.M., Giménez, A.: Astron. Astrophys. Suppl. **138**, 583 (1999). https://doi.org/10.1051/aas:1999362
15. Steele, I.A., Smith, R.J., Rees, P.C., Baker, I.P., Bates, S.D., Bode, M.F., Bowman, M.K., Carter, D., Etherton, J., Ford, M.J., Fraser, S.N., Gomboc, A., Lett, R.D.J., Mansfield, A.G., Marchant, J.M., Medrano-Cerda, G.A., Mottram, C.J., Raback, D., Scott, A.B., Tomlinson, M.D., Zamanov, R. In: Oschmann, J.M. Jr.. (ed.) Ground-based Telescopes, Proceedings of the SPIE, vol. 5489, pp. 679–692 (2004). https://doi.org/10.1117/12.551456
16. Tsapras, Y., Street, R., Horne, K., Snodgrass, C., Dominik, M., Allan, A., Steele, I., Bramich, D.M., Saunders, E.S., Rattenbury, N., Mottram, C., Fraser, S., Clay, N., Burgdorf, M., Bode, M., Lister, T.A., Hawkins, E., Beaulieu, J.P., Fouqué, P., Albrow, M., Menzies, J., Cassan, A., Dominis-Prester, D.: Astronomische Nachrichten **330**, 4 (2009). https://doi.org/10.1002/asna.200811130
17. Lewis, F., Street, R., Roche, P., Stroud, V., Russell, D.M.: Adv. Astron. **2010**, 873059 (2010). https://doi.org/10.1155/2010/873059
18. Monfardini, A., Kobayashi, S., Guidorzi, C., Carter, D., Mundell, C.G., Bersier, D.F., Gomboc, A., Melandri, A., Mottram, C.J., Smith, R.J., Steele, I.A.: Astrophys. J. **648**, 1125 (2006). https://doi.org/10.1086/506170
19. Mundell, C.G., Melandri, A., Guidorzi, C., Kobayashi, S., Steele, I.A., Malesani, D., Amati, L., D'Avanzo, P., Bersier, D.F., Gomboc, A., Rol, E., Bode, M.F., Carter, D., Mottram, C.J., Monfardini, A., Smith, R.J., Malhotra, S., Wang, J., Bannister, N., O'Brien, P.T., Tanvir, N.R.: ApJ **660**, 489 (2007). https://doi.org/10.1086/512605
20. Melandri, A., Mundell, C.G., Kobayashi, S., Guidorzi, C., Gomboc, A., Steele, I.A., Smith, R.J., Bersier, D., Mottram, C.J., Carter, D., Bode, M.F., O'Brien, P.T., Tanvir, N.R., Rol, E., Chapman, R.: ApJ **686**, 1209 (2008). https://doi.org/10.1086/591243
21. Virgili, F.J., Mundell, C.G., Pal'shin, V., Guidorzi, C., Margutti, R., Melandri, A., Harrison, R., Kobayashi, S., Chornock, R., Henden, A., Updike, A.C., Cenko, S.B., Tanvir, N.R., Steele, I.A., Cucchiara, A., Gomboc, A., Levan, A., Cano, Z., Mottram, C.J., Clay, N.R., Bersier, D., Kopač, D., Japelj, J., Filippenko, A.V., Li, W., Svinkin, D., Golenetskii, S., Hartmann, D.H., Milne, P.A., Williams, G., O'Brien, P.T., Fox, D.B., Berger, E.: ApJ **778**, 54 (2013). https://doi.org/10.1088/0004-637X/778/1/54
22. Kopač, D., Mundell, C.G., Japelj, J., Arnold, D.M., Steele, I.A., Guidorzi, C., Dichiara, S., Kobayashi, S., Gomboc, A., Harrison, R.M., Lamb, G.P., Melandri, A., Smith, R.J., Virgili, F.J., Castro-Tirado, A.J., Gorosabel, J., Järvinen, A., Sánchez-Ramírez, R., Oates, S.R., Jelínek, M.: ApJ **813**, 1 (2015). https://doi.org/10.1088/0004-637X/813/1/1
23. Gomboc, A., Kobayashi, S., Guidorzi, C., Melandri, A., Mangano, V., Sbarufatti, B., Mundell, C.G., Schady, P., Smith, R.J., Updike, A.C., Kann, D.A., Misra, K., Rol, E., Pozanenko, A., Castro-Tirado, A.J., Anupama, G.C., Bersier, D., Bode, M.F., Carter, D., Curran, P., Fruchter, A., Graham, J., Hartmann, D.H., Ibrahimov, M., Levan, A., Monfardini, A., Mottram, C.J., O'Brien, P.T., Prema, P., Sahu, D.K., Steele, I.A., Tanvir, N.R., Wiersema, K.: ApJ **687**, 443 (2008). https://doi.org/10.1086/592062
24. Gomboc, A., Kobayashi, S., Mundell, C.G., Guidorzi, C., Melandri, A., Steele, I.A., Smith, R.J., Bersier, D., Carter, D., Bode, M.F. In: Meegan, C., Kouveliotou, C., Gehrels, N. (eds.) American Institute of Physics Conference Series, American Institute of Physics Conference Series, vol. 1133, pp. 145–150 (2009). https://doi.org/10.1063/1.3155867
25. Japelj, J., Kopač, D., Kobayashi, S., Harrison, R., Guidorzi, C., Virgili, F.J., Mundell, C.G., Melandri, A., Gomboc, A.: ApJ **785**, 84 (2014). https://doi.org/10.1088/0004-637X/785/2/84
26. Laskar, T., Alexander, K.D., Berger, E., Fong, W.f., Margutti, R., Shivvers, I., Wlliams, P.K.G., Kopač, D., Kobayashi, S., Mundell, C., Gomboc, A., Zheng, W., Menten, K.M., Graham, M.L., Filippenko, A.V.: Astrophys. J. **833**, 88 (2016). https://doi.org/10.3847/1538-4357/833/1/88
27. Laskar, T., Alexander, K.D., Berger, E., Guidorzi, C., Margutti, R., Fong, W.f., Kilpatrick, C.D., Milne, P., Drout, M.R., Mundell, C.G., Kobayashi, S., Lunnan, R., Barniol Duran, R., Menten, K.M., Ioka, K., W.lliams, P.K.G.: Astrophys. J. **862**, 94 (2018). https://doi.org/10.3847/1538-4357/aacbcc
28. Mundell, C.G., Steele, I.A., Smith, R.J., Kobayashi, S., Melandri, A., Guidorzi, C., Gomboc, A., Mottram, C.J., Clarke, D., Monfardini, A., Carter, D., Bersier, D.: Science **315**, 1822 (2007). https://doi.org/10.1126/science.1138484
29. Steele, I.A., Mundell, C.G., Smith, R.J., Kobayashi, S., Guidorzi, C.: Nature **462**, 767 (2009). https://doi.org/10.1038/nature08590

30. Mundell, C.G., Kopac, D., Arnold, D.M., Steele, I.A., Gomboc, A., Kobayashi, S., Harrison, R.M., Smith, R.J., Guidorzi, C., Virgili, F.J., Melandri, A., Japelj, J.: Nature **504**, 119 (2013). https://doi.org/10.1038/nature12814
31. Troja, E., Lipunov, V.M., Mundell, C.G., Butler, N.R., Watson, A.M., Kobayashi, S., Cenko, S.B., Marshall, F.E., Ricci, R., Fruchter, A., Wieringa, M.H., Gorbovskoy, E.S., Kornilov, V., Kutyrev, A., Lee, W.H., Toy, V., Tyurina, N.V., Budnev, N.M., Buckley, D.A.H., González, J., Gress, O., Horesh, A., Panasyuk, M.I., Prochaska, J.X., Ramirez-Ruiz, E., Rebolo Lopez, R., Richer, M.G., Roman-Zuniga, C., Serra-Ricart, M., Yurkov, V., Gehrels, N.: Nature **547**, 425 (2017). https://doi.org/10.1038/nature23289
32. Guidorzi, C., Monfardini, A., Gomboc, A., Mottram, C.J., Mundell, C.G., Steele, I.A., Carter, D., Bode, M.F., Smith, R.J., Fraser, S.N., Burgdorf, M.J., Newsam, A.M.: PASP **118**, 288 (2006). https://doi.org/10.1086/499289
33. Mundell, C.G., Guidorzi, C., Steele, I.A.: Adv. Astron. **2010**, 718468 (2010). https://doi.org/10.1155/2010/718468
34. Brown, T.M., Baliber, N., Bianco, F.B., Bowman, M., Burleson, B., Conway, P., Crellin, M., Depagne, É., De Vera, J., Dilday, B., Dragomir, D., Dubberley, M., Eastman, J.D., Elphick, M., Falarski, M., Foale, S., Ford, M., Fulton, B.J., Garza, J., Gomez, E.L., Graham, M., Greene, R., Haldeman, B., Hawkins, E., Haworth, B., Haynes, R., Hidas, M., Hjelstrom, A.E., Howell, D.A., Hygelund, J., Lister, T.A., Lobdill, R., Martinez, J., Mullins, D.S., Norbury, M., Parrent, J., Paulson, R., Petry, D.L., Pickles, A., Posner, V., Rosing, W.E., Ross, R., Sand, D.J., Saunders, E.S., Shobbrook, J., Shporer, A., Street, R.A., Thomas, D., Tsapras, Y., Tufts, J.R., Valenti, S., Vander Horst, K., Walker, Z., White, G., Willis, M.: Publ. ASP **125**, 1031 (2013). https://doi.org/10.1086/673168
35. Lavigne, J.M., Jean, P., Kandel, B., Borrel, V., Roques, J.P., Lichti, G., Schönfelder, V., Diehl, R., Georgii, R., Kirchner, T., Durouchoux, P., Cordier, B., Diallo, N., Sanchez, F., Payne, B., Leleux, P., Caraveo, P., Teegarden, B., Matteson, J., Slassi-Sennou, S., Skinner, G., Connell, P.: Nucl. Phys. B Proc. Suppl. **60**, 69 (1998). https://doi.org/10.1016/S0920-5632(97)00502-1
36. Barthelmy, S.D., Butterworth, P., Cline, T.L., Gehrels, N., Fishman, G.J., Kouveliotou, C., Meegan, C.A.: Astrophys. Space Sci. **231**(1–2), 235 (1995). https://doi.org/10.1007/BF00658623
37. Schlegel, D.J., Finkbeiner, D.P., Davis, M.: ApJ **500**, 525 (1998). https://doi.org/10.1086/305772
38. Siegel, M., Burrows, D., Deich, A., Gropp, J., Kennea, J., LaPorte, S.e.: GRB coordinates network. Circular Service, 22973 (2018)
39. Martone, R., Guidorzi, C., Kobayashi, S., Mundell, C., Gomboc, A., Steele, I., Cucchiara, A., Morris, D.: GRB coordinates network. Circular Service, 22976 (2018)
40. Meegan, C., Lichti, G., Bhat, P.N., Bissaldi, E., Briggs, M.S., Connaughton, V., Diehl, R., Fishman, G., Greiner, J., Hoover, A.S., van der Horst, A.J., von Kienlin, A., Kippen, R.M., Kouveliotou, C., McBreen, S., Paciesas, W.S., Preece, R., Steinle, H., Wallace, M.S., Wilson, R.B., Wilson-Hodge, C.: ApJ **702**, 791 (2009). https://doi.org/10.1088/0004-637X/702/1/791
41. LSST Science Collaboration, Abell, P.A., Allison, J., Anderson, S.F., Andrew, J.R., Angel, J.R.P., Armus, L., Arnett, D., Asztalos, S.J., Axelrod, T.S., et al. arXiv e-prints (2009)

A&A 631, A62 (2019)
https://doi.org/10.1051/0004-6361/201936284

Astronomy & Astrophysics

A cumulative search for hard X/γ-ray emission associated with fast radio bursts in *Fermi*/GBM data

R. Martone[1,2], C. Guidorzi[1], R. Margutti[3], L. Nicastro[4], L. Amati[4], F. Frontera[1,4], M. Marongiu[1,2], M. Orlandini[4], and E. Virgilli[1]

[1] Dipartimento di Fisica e Scienze della Terra, Università di Ferrara, Via Saragat 1, 44122 Ferrara, Italy
e-mail: mrtrnt@unife.it
[2] ICRANet, Piazza della Repubblica 10, 65122 Pescara, Italy
[3] Center for Interdisciplinary Exploration and Research in Astrophysics and Department of Physics and Astronomy, Northwestern University, 2145 Sheridan Road, Evanston, IL 60208-3112, USA
[4] INAF–Osservatorio di Astrofisica e Scienza dello Spazio di Bologna, Via Piero Gobetti 93/3, 40129 Bologna, Italy

Received 10 July 2019 / Accepted 11 September 2019

ABSTRACT

Context. Fast radio bursts (FRBs) are millisecond-long bursts uniquely detected at radio frequencies. FRB 131104 is the only case for which a γ-ray transient positionally and temporally consistent was claimed. This high-energy transient had a duration of $\sim$ 400 s and a 15–150 keV fluence $S_\gamma \sim 4 \times 10^{-6}$ erg cm^{-2}. However, the association with the FRB is still debated.
Aims. We aim at testing the systematic presence of an associated transient high-energy counterpart throughout a sample of the FRB population.
Methods. We used an approach like that used in machine learning methodologies to accurately model the highly-variable *Fermi*/GBM instrumental background on a time interval comparable to the duration of the proposed γ-ray counterpart of FRB 131104. A possible γ-ray signal is then constrained considering sample average lightcurves.
Results. We constrain the fluence of the possible γ-ray signal in the 8–1000 keV band down to 6.4×10^{-7} (7.1×10^{-8}) erg cm^{-2} for a 200-s (1-s) integration time. Furthermore, we found the radio-to-gamma fluence ratio to be $\eta > 10^8$ Jy ms erg^{-1} cm^2.
Conclusions. Our fluence limits exclude $\sim$94% of *Fermi*/GBM detected long gamma-ray bursts and $\sim$96% of *Fermi*/GBM detected short gamma-ray bursts. In addition, our limits on the radio-to-gamma fluence ratio point to a different emission mechanism from that of magnetar giant flares. Finally, we exclude a γ-ray counterpart as fluent as the one possibly associated with FRB 131104 to be a common feature of FRBs.

Key words. gamma rays: general – gamma-ray burst: general – radio continuum: general

1. Introduction

Fast radio bursts (FRBs) are millisecond-long radio pulses detected around ~1 GHz. They were serendipitously discovered at the Parkes Radio Telescope (Lorimer et al. 2007; Thornton et al. 2013) and are now routinely detected by a number of different facilities (see Petroff et al. 2019, for a review). These observations are collected in the FRB catalogue (frbcat[1]; Petroff et al. 2016), that contains ~90 FRBs (as of August 2019): this number is currently dramatically increasing thanks to recent wide-field facilities, with about half sample detected in the latest couple of years.

FRBs come without a direct distance indicator, so this information has to be inferred indirectly from the dispersion measure (DM), that tracks the amount of free electrons along the line of sight. The distance information encoded in the DM contains a degeneracy between the contribution of the intergalactic medium (IGM) and that due to the host galaxy and to the local environment surrounding the FRB source. Measured DMs are larger than the Galactic contribution (DM_{MW}) for all the FRBs of the sample, so the extra-galactic origin is widely accepted. However, the estimates on redshift z have large uncertainties, with the bulk of the population inferred to be at $0.1 \lesssim z \lesssim 1$. As of August 2019, according to the publicly available information, a direct distance measurement is available only for the repeating burst FRB 121102 and for the two non-repeating bursts FRB 180924 and FRB 190523. In the former case, interferometric techniques led to the identification of the host, that turned out to be a dwarf galaxy at $z \simeq 0.193$ (Chatterjee et al. 2017; Tendulkar et al. 2017); in the other two cases the hosts were found to be two luminous, early-type galaxies at respectively $z \simeq 0.32$ and $z \simeq 0.66$ (Bannister et al. 2019; Ravi et al. 2019).

Additionally, the relatively coarse radio localisation of FRBs of $\sim$ few arcmin severely limits the possibility of multi-wave follow-up, and, as a result, prevents solid inferences on the underlying emission mechanism. Consequently, the number of proposed models dramatically increased in the last years (see Platts et al. 2019, for a review). The ms duration directly implies a small size $R \lesssim 10^6$ cm of the radiating region, so FRB sources should be compact objects radiating through a coherent emission process. Given their large rotational energies and magnetic fields (up to 10^{15} G), and the turbulent environment in which they reside, newborn rapidly rotating neutron stars (NS) or magnetars are considered among the most promising FRB progenitor candidates, even if models involving other compact objects, such as black holes (BHs) and white dwarfs (DWs) are not ruled out (see Petroff et al. 2019; Katz 2018, for reviews).

[1] http://www.frbcat.org

The search for signals at non-radio wavelengths ended up with no identified counterpart, with the only exception being the detection (3.2σ confidence) of a 400-s long γ-ray transient possibly associated to FRB 131104 reported by DeLaunay et al. (2016; hereafter D16) using data of the Burst Alert Telescope (BAT; Barthelmy et al. 2005) aboard the *Neil Gehrels Swift* Observatory (Gehrels et al. 2004). This result raised some scepticism (Shannon & Ravi 2017). Recently, Cunningham et al. (2019) performed a systematic search for FRB counterparts in the *Fermi*/Gamma-ray Burst Monitor (GBM; Meegan et al. 2009), *Fermi*/Large Area Telescope (LAT; Atwood et al. 2009), and in the *Swift*/BAT data at the times of the FRBs. Concerning *Fermi*/GBM data, the authors focused on the background modelling and subtraction of the individual lightcurves, investigating the presence of a significant excess. They found no evidence for it.

Motivated by these developments, we present here the first cumulative homogeneous search for long-duration γ-ray emission possibly coincident with FRBs. In particular, we performed a cumulative analysis examining the entire FRB catalogue and exploiting the dozens of FRBs for which contemporaneous *Fermi*/GBM data are available.

We organised our paper as follows: in Sect. 2 we describe the dataset selection and reduction, together with the procedure we used; in Sect. 3 we outline the results, reporting a special case that required specific analysis; in Sect. 4 we discuss our findings compared with D16's results. Finally, in Sect. 5 we summarise our work and discuss possible future developments.

2. Data analysis

2.1. Sample selection

We used *Fermi*/GBM-NaI data exploiting its extended bandpass (8–1000 keV) and large field-of-view (2/3 of the whole sky, thanks to its open-sky design), which are both crucial when a cumulative analysis of a (potentially) broad-band signal from poorly localised sources is performed. We compiled our initial list from the FRB catalogue (as of February 4, 2019) discarding all the events that were Earth-blocked within the *Fermi*/GBM field-of-view. In addition, we decided to preliminarily exclude the only two repeating sources, FRB 121102 and FRB 180814.J0422+73, which in principle could belong to a different class and for which systematic researches of *Fermi*/GBM counterparts ended with no candidates (e.g. Palaniswamy et al. 2018; Scholz et al. 2016, 2017). Our first sample consists of 38 FRBs. We list in Table 1, among other quantities, time, position, and radio fluence of the FRBs of this initial sample.

2.2. Data reduction

We calculated the position of each FRB with respect to the GBM payload orientation to identify the best exposed NaI detectors at the FRB time. For every FRB, we considered the lightcurves of the three most illuminated detectors and summed them. In particular, we used the *Fermi* `ctime` files, with a resolution of 0.256 s in 8 energy bins. `ctime` files were preferred over `tte` files because we needed both to explore different time intervals around the FRB times (see below), and to explore times at which no events triggered the GBM (and so no `tte` files were produced). We retrieved the `ctime` and `position history` daily files from the GBM Continuous Data FTP archive[2].

[2] https://fermi.gsfc.nasa.gov/ssc/data/access/

2.3. Procedure

Our search was aimed at identifying long-lived, high-energy signals temporally and spatially coincident with radio detection and common over the FRB population. This was performed searching for significant signals over the background level in the cumulative GBM lightcurves. This means that, unlike other complementary works (e.g. Cunningham et al. 2019), we do not focus on individual FRBs, but rather on the population as a whole, making no assumptions on the spectral shape. The search for weak, long-lasting signals in the lightcurves requires accurate knowledge of the background. In the case of GBM, the orbit inclination of ∼26° with respect to the Earth equator makes the background significantly more variable than for an equatorial orbit. In addition, in the softest energy channels it is necessary to take into account the occultation steps caused by known bright X-ray sources, like the Crab Nebula and Scorpius X-1. We addressed this issue through an approach like that used in machine learning methodologies, aimed at modelling and characterising the background along the orbit. In particular, the approach was designed to define the following aspects:

A.1 the size of the time window around the FRB time where we search for the signal;
A.2 the size of the two time windows (before and the after the FRB time) to be used to fit the background;
A.3 the algorithm to produce the final background-subtracted, averaged lightcurves.

The implementation in a software tool (e.g. using a neural network model) is foreseen but its description goes beyond the goals of this paper. The following steps summarise the adopted procedure:

1. we simulated a sample of non Earth-occulted randomly selected sky positions at random times to act as a training set to define a background-fitting procedure;
2. we built a second different simulated sample to act as a validation set to test the reliability of our procedure;
3. we finally applied the background modelling procedure to the FRB dataset.

The sizes of the training and validation sets were the same as that of the FRB one. We used the same data reduction procedure described in Sect. 2.2, focusing on the sum of the lightcurves of the three best exposed detectors for each sample element. Hereafter, we set the origin of the time axes at the FRB epoch. The strategy consisted in selecting a time window around $t = 0$ (central interval) and then using two intervals (before and after the origin) to fit and interpolate the background (background intervals). We then fitted the background using polynomials, progressively increasing their degree (up to 5) until the p-values for both the χ^2 and the run tests were within the 0.05–0.95 range. We set the sizes of the background and of the central interval following the analysis of the training sample. The final choice was the result of a trade-off between the need of exploring a long interval around $t = 0$ and that of accurately interpolating the background within the central interval. To define A.1 and A.2, we considered two different schemes:

– a total time window of 800 s extending from −400 to 400 s, with a central interval [−50, 150 s] and the background interval spanning [−400, −50 s] and [150, 400 s]; hereafter, this will be referred to as "short window" (SW);

– a total time window of 1100 s extending from −400 to 700 s, with a central interval [−50, 350 s] and the background interval spanning [−400, −50 s] and [350, 700 s]; hereafter, this will be referred to as "long window" (LW).

Events which passed the tests on the background intervals with both schemes were tagged as good events. In case of bad fit

Table 1. *Fermi*/GBM visible (i.e. not Earth-blocked) FRBs.

FRB	Time (UTC)	α_{J2000} (°)	δ_{J2000} (°)	θ [a] (°)	ϕ [b] (°)	l_{el} [c] (°)	F_R [d]	GBM NaI [e] units	Taken [f]	Comments [g]
090625	21:53:51.4	46.95	−29.93	41	98	45	0.07	9,0,1	N	VUO
110214	07:14:10.4	20.32	−49.79	103	57	54	1.74	2,5,1	Y	SXF, HBO
110523	15:06:19.7	326.3	0.16	103	257	27	0.02	8,4,7	N	VUO
110626	21:33:17.5	315.93	−44.74	79	219	66	0.02	8,7,11	Y	–
110703	18:59:40.6	352.71	−2.87	65	263	70	0.07	8,7,3	Y	–
121002	13:09:18.4	273.7	−85.2	46	213	22	0.08	7,6,8	N	Missing data
130628	03:58:00.2	135.76	3.44	60	356	76	0.04	5,3,1	Y	SXF, HBO
130729	09:01:51.2	205.34	−6.0	82	82	14	0.12	2,10,1	Y	VUO, HBO
131104	18:04:11.2	101.04	−51.28	117	275	45	0.08	4,8,3	N	VUO
150215	20:41:41.7	274.36	−4.9	61	54	94	0.07	1,2,0	Y	VUO, HBO
150418	04:29:06.7	109.15	−19.01	14	232	72	0.06	6,7,0	Y	–
150610	05:26:59.4	161.11	−40.09	132	147	3	0.05	10,11,9	N	Missing data
150807	17:53:55.8	340.63	−55.08	64	207	1	1.52	7,11,8	Y	–
151206	06:17:52.8	290.35	−4.13	80	36	83	0.03	2,5,1	Y	VUO, HBO
160317	09:00:36.5	118.45	−29.61	59	250	66	0.10	7,8,6	Y	–
160608	03:53:01.1	114.17	−40.8	39	268	29	–	6,7,3	N	VUO
170416	23:11:12.8	333.25	−55.03	21	43	83	3.26	0,1,6	Y	–
170428	18:02:34.7	326.75	−41.85	71	103	15	1.14	10,9,2	Y	–
170707	06:17:34.4	44.75	−57.27	102	351	59	1.74	5,4,3	Y	VUO, HBO
170712	13:22:17.4	339.0	−60.95	140	344	20	1.78	5,4,2	N	Missing data
170827	16:20:18.0	12.33	−65.55	54	85	10	0.08	1,9,0	Y	–
171020	10:27:58.6	333.75	−19.67	106	120	47	12.60	10,9,2	Y	VUO, HBO
171116	14:59:33.3	52.75	−17.23	56	171	53	2.11	9,11,7	N	VUO
171213	14:22:40.5	54.75	−10.93	88	157	20	4.47	11,10,9	Y	VUO, HBO
180110	07:34:35.0	328.25	−35.45	83	34	49	13.80	2,5,1	Y	VUO, HBO
180128.2	04:53:26.8	335.5	−60.25	60	311	29	2.22	3,4,5	N	Missing data
180212	23:45:04.4	215.25	−3.58	70	106	27	3.22	10,9,2	N	Missing Data
180324	09:31:46.7	94.0	−34.78	53	91	85	2.38	9,1,0	N	Missing Data
180525	15:19:06.5	220.0	−2.2	67	161	84	10.10	9,11,10	N	VUO
180725.J0613+67	17:59:32.8	93.25	67.07	59	24	4	0.48	1,5,0	Y	Focused analysis
180727.J1311+26	00:52:04.5	197.75	26.43	72	290	54	0.56	4,3,8	Y	OS by Sco X-1
180729.J1316+55	00:48:19.2	199.0	55.53	81	297	79	1.36	4,3,8	Y	–
180729.J0558+56	17:28:18.3	89.5	56.5	130	43	22	0.36	2,5,10	Y	–
180730.J0353+87	03:37:25.9	58.25	87.2	117	305	46	2.00	4,5,8	Y	–
180801.J2130+72	08:47:14.8	322.5	72.72	150	147	11	1.12	10,11,2	N	Missing data
180812.J0112+80	11:45:32.9	18.0	80.78	13	131	50	0.72	0,6,9	Y	–
180814.J1554+74	14:20:14.4	238.5	74.02	41	62	24	1.00	1,0,9	Y	–
180817.J1533+42	01:49:20.2	233.25	42.2	115	285	48	1.04	4,8,3	N	VUO

Notes. [a]Azimuth with respect to the payload. [b]Zenith with respect to the payload. [c]Elevation upon the Earth limb. [d]Radio fluence in units of 10^{-16} erg cm^{-2}, obtained multiplying the radio fluence density by the band width reported in the `frbcat`. [e]List of the best exposed detectors. [f]Whether or not a given FRB was used to build the cumulative lightcurve. [g]HBO: hard band Only; SXF: solar X-ray flare; OS: occultation step; VUO: variability of unknown origin; missing data: *Fermi*/GBM data unavailable.

possibly caused by occultation steps of bright X/γ-ray sources, we added a step component to our polynomial fitting function. The result was then tested using the same approach and thresholds already described in the case of a simple polynomial fit. Figure 1 shows the case of FRB 180727.J1311+26 which is affected by an occultation step of Sco X-1. Several events had to be discarded due to data gaps. In some cases the fit quality did not improve due to unidentified source(s) of variability, which was expected given the number of variable Galactic X-ray sources that contribute to the diffuse background around the lower boundary of the GBM passband. Driven by the need to reduce the amount of background contamination sacrificing the smallest possible amount of data, we carried out the same analysis in parallel on a restricted band, ignoring the first two channels of the `ctime` file, corresponding to selecting $E \gtrsim 27$ keV. Hereafter, this will be referred to as the "hard band". As expected, the number of poor fits dropped substantially. Overall, given the two background fitting schemes (LW and SW) and the two energy ranges (8–1000 keV and 27–1000 keV), we extracted a maximum of four lightcurves for each element of the training and validation sets. The corresponding individual lightcurves (four lightcurves per FRB) were then averaged over the sample to obtain four average time series.

Concerning A.3, we considered two different schemes:

– we averaged the individual background-subtracted lightcurves (hereafter, subtract-and-average strategy);

– we performed the background fitting and subtraction on the averaged (non-background subtracted) lightcurves (hereafter, average-and-subtract strategy).

We finally evaluated the robustness of the background interpolation procedure by calculating, for each average lightcurve, the significance of the total background-subtracted counts in

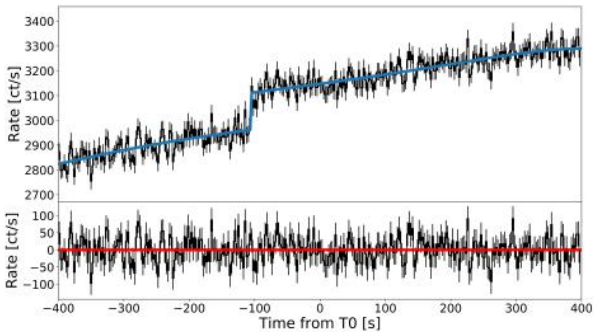

Fig. 1. Example of step function fitting applied to a case of Sco X-1 occulation step that occurred ~100 s before FRB 180727.J1311+26. *Top panel*: 8–1000 keV lightcurve along with the modelled background (solid line). *Bottom panel*: residuals of the background modelling.

the central interval. This was done through a polynomial fit of the average lightcurves in the background interval using the same strategy adopted for the individual cases (χ^2 + run tests and 0.05–0.95 thresholds) and finally interpolating in the central interval. Our main results are summarised as follows:

– LWs are too long to ensure a reliable interpolation of the background, since we obtained 5-σ excesses in the central intervals. This holds true for both the total and the hard band.

– SWs allow for a good interpolation of the background, since we obtained no significant excesses (>3σ) on the central interval in either the training or validation samples for both energy ranges.

– The subtract-and-average strategy leads to a 5-σ excesses in the central interval, so it does not ensure a reliable interpolation of the background.

– The average-and-subtract strategy leads to no significant excesses (>3σ) on the central interval, so it does ensure a reliable interpolation of the background.

Therefore, we hereafter consider only the SW procedure for the analysis of the FRB sample, using the average-and-subtract strategy.

2.4. An intriguing case: FRB 180725.J0613+67

The case of FRB 180725.J0613+67 required a dedicated analysis, since it went off during the rise of an occultation step of the Crab nebula.

To properly model the step in a data-independent way, we followed this strategy: first, we extracted the lightcurves of the orbits preceding and following the one of the FRB; second, we aligned the two lightcurves making the two Crab occultation steps coincide temporally; third, we averaged the two lightcurves; fourth we used a polynomial+step to fit the mean lightcurve using the step amplitude as a free parameter; fifth, we fitted the FRB 180725.J0613+67 lightcurve with the same function forcing the step amplitude to be equal to that obtained from the mean of the adjacent orbits. The result is shown in Fig. 4. This event was included in our final sample as it passed our filtering procedure.

3. Results

Following the procedure of Sect. 2.3, the FRB sample shrank to 15 and 22 elements for the total and the hard energy band, respectively. The fit of the average lightcurves led to no >3σ excess in the central interval for both energy ranges. We also produced a second set of mean lightcurves, considering a weighted average, being the weights the radio fluences reported in Table 1. The rationale behind this choice is the assumption of a common spectral ratio between radio and hard X/γ-ray frequencies for all FRBs, although we acknowledge it might be a simplistic assumption given the spectral variability in the radio band observed in multiple bursts from the repeating FRB 121102 (Spitler et al. 2016; Gajjar et al. 2018; Hessels et al. 2019). The results of the radio fluence calculation are reported in the F_R column of Table 1: we report an empty entry for FRB 160608 because there was no fluence information from the catalogue. When we calculated the weighted average lightcurves, we assigned to this event a putative fluence corresponding to the average value of the available sample. No significant excess was found in fluence-weighted case either. The four lightcurves so obtained are displayed in Fig. 2 (total band) and Fig. 3 (hard band).

We calculated the corresponding 5σ upper limits on the total fluence in the whole energy *Fermi*/GBM band-pass 8–1000 keV (and 27–1000 keV sub-band) and in five different time ranges (Table 2). Following D16, we assumed both a power-law (with $\Gamma = 1.16$) and a bremsstrahlung spectrum (with $T = 75$ keV), while we calculated the radio-to-γ-ray fluence ratio $\eta = F_{\rm radio}/F_\gamma$ assuming the average radio fluence for the bursts reported in `frbcat`. The most conservative fluence upper limits for the power-law model for 200 s (1 s) integration time imply $\eta > 10^{8.0}$ ($10^{8.9}$) Jy ms erg^{-1} cm^2, considering the average radio fluence density of our sample (~58 Jy ms). The same calculation for the bremsstrahlung model yields $\eta > 10^{8.3}$ ($10^{9.2}$) Jy ms erg^{-1} cm^2 for 200 s (1 s) integration time.

The final sample contains 6 events detected by the Australian SKA Pathfinder (ASKAP; Johnston et al. 2008). These events are worth an additional, specific analysis, given their likely closer average distance compared to that of the remaining sample (Shannon et al. 2018), which translates into stronger constraints on the intrinsic energy with respect to the rest of the known FRB population. The upper limits for this subset are reported in Table 3. Only in two cases (170416, 170428) we could study the background in the full band.

4. Discussion

This work was motivated by the controversial association proposed by D16 between FRB 131104 and a γ-ray signal positionally and temporally coincident with the radio burst. The detection was marginal (3.2σ confidence) and the analysis revealed a prolonged emission ($T_{90} = 377 \pm 24$ s), with a γ-ray fluence $F_{\gamma,\rm D16} = 4 \times 10^{-6}$ erg cm^{-2} in the 15–150 keV band.

Our approach was specifically conceived to investigate the presence of a comparably long emission in the *Fermi*/GBM data. Given the highly-variable background of this instrument on long timescales, the entire ~400 s-long window turned out to be too difficult to model, so we analysed a 200 s-long window around the time of the FRB. For a proper comparison, the FRB 131104 γ-ray fluence should be rescaled on the 200 s window. Given the uncertain emission history, we assumed a constant luminosity over the entire ~400-s window, finding $F_{\gamma,\rm D16,resc} \approx 2 \times 10^{-6}$ erg cm^{-2} in the 15–150 keV band for the 200-s window. Our upper limits on the same integration time were ≈ a few $\times 10^{-7}$ erg cm^{-2} in all cases in the 8–1000 keV band. In particular, the most conservative upper limits were obtained assuming a power-law spectrum: the value of 6.4×10^{-7} erg cm^{-2} over 200-s integration time is a factor ~4 lower than $F_{\gamma,\rm D16,resc}$. These limits are even stronger when a thermal bremsstrahlung spectrum is

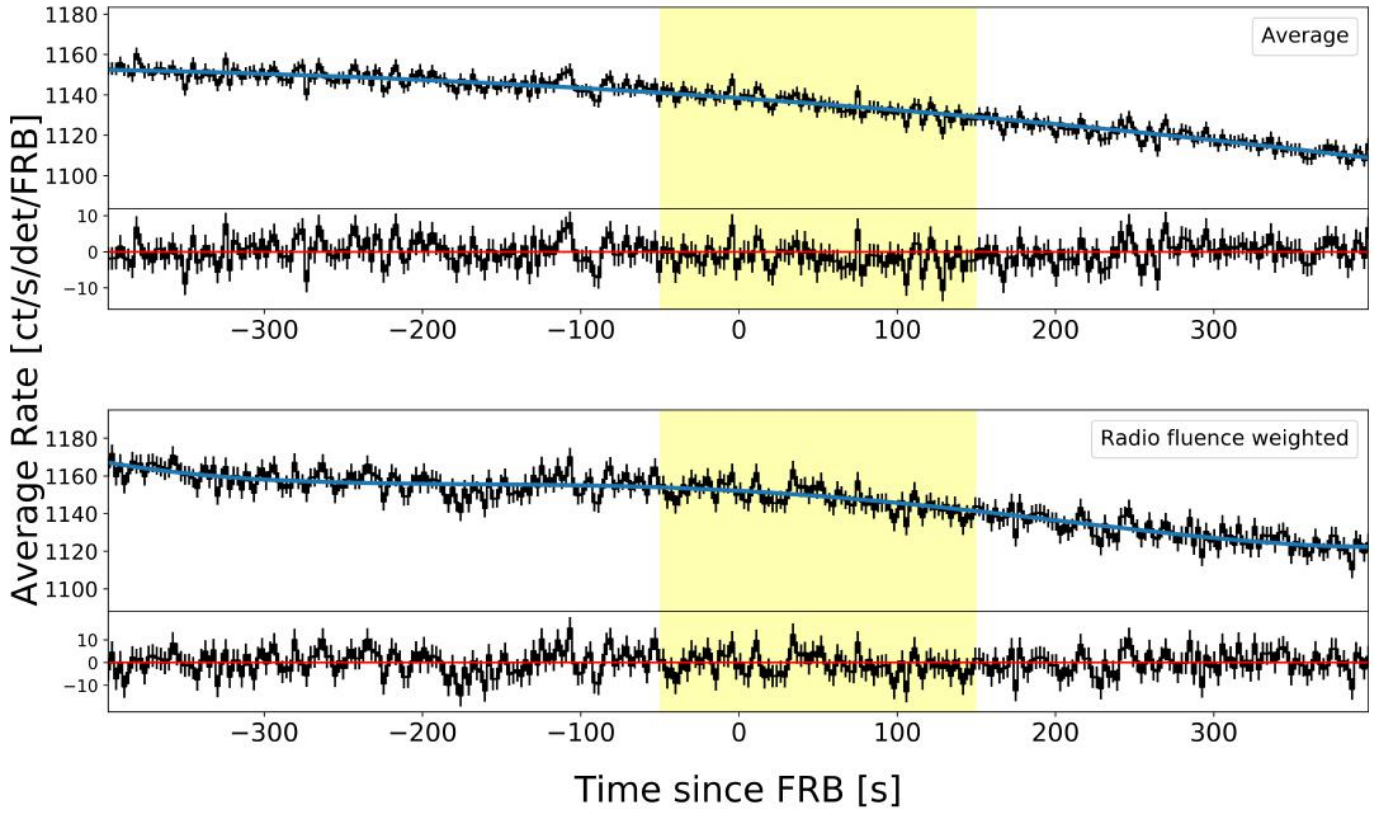

Fig. 2. Cumulative lightcurves, background fitting and residuals in the 8–1000 keV energy band. In the *upper panel* we report the result in the case of the arithmetic average of individual lightcurves, while in the *lower panel* the individual lightcurves are weighted with the radio fluence of the corresponding FRB. The polynomial degrees are respectively 2 and 4.

assumed, the most conservative value being 2.8×10^{-7} erg cm^{-2}, almost one order of magnitude lower than $F_{\gamma,\mathrm{D16,resc}}$. Thus we can exclude that a signal with the same γ-ray fluence as that found by D16 is a common feature among FRBs.

Concerning the connection with other astrophysical transients, we tested two kinds of scenarios:

1. extragalactic magnetar giant flares;
2. gamma-ray bursts (GRBs).

Magnetar giant flares are energetic (3×10^{44}–2×10^{46} erg) and short-lived (100 ms) events that peak in the hard X-ray band and can be observed up to 30 Mpc (e.g. Mazets et al. 1979; Feroci et al. 2001; Palmer et al. 2005; Hurley et al. 2005; Svinkin et al. 2015). For galactic magnetars, a dimmer tail (a factor $\sim 10^{-3}$ the peak value) extending up to hundreds of seconds has also been observed. Tendulkar et al. (2016; hereafter T16) explored the possible connection between these giant-flares and FRBs estimating the radio-to-gamma fluence ratio η for both classes of sources. Using the radio fluence upper limits for the Galactic source SGR 1806−20, they found $\eta_{\mathrm{SGR}} \lesssim 10^{7}$ Jy ms erg^{-1} cm^{2} and, using γ-ray fluence upper limits for 15 FRBs, $\eta_{\mathrm{FRB}} \gtrsim 10^{7-9}$ Jy ms erg^{-1} cm^{2}. Giving the incompatibility of the two, T16 concluded that the two kinds of events cannot be associated. In this regard, we used our 1-s fluence upper limits to further constrain η_{FRB}. Our most conservative result $\eta_{\mathrm{FRB}} > 10^{8.9}$ Jy ms erg^{-1} cm^{2} (obtained for the power-law spectral shape) is incompatible with $\eta_{\mathrm{SGR}} \lesssim 10^{7}$ Jy ms erg^{-1} cm^{2} found for SGR 1806−20, suggesting FRBs are not produced by the same mechanism(s) powering giant flares from extragalactic magnetars.

The possible FRB–GRB connection can be explored using our fluence upper limits on both the prolonged (200 s) and short (1 s) timescales. Figure 5 shows the fluence distribution of the GBM catalog of LGRBs (Bhat et al. 2016), compared with our most conservative limit on the prolonged emission (200-s upper limit): we exclude ∼94% of the Long GRBs (LGRBs, $T_{90} > 2$ s) and all the very long GRBs ($T_{90} > 100$ s). Finally, we compared our 1-s limits with the fluence distribution of *Fermi*/GBM Short GRBs (SGRBs, $T_{90} < 2$ s). Figure 6 shows that ∼96% of SGRBs are incompatible with our most conservative upper limit. To conclude, we reject the possibility that the simultaneous presence of a LGRB or a SGRB is a common feature among FRBs, even if a connection in terms of a common progenitor is not excluded (Margalit et al. 2019).

5. Conclusions

FRB 131104 is the first FRB for which a positional and temporal-coincident γ-ray signal possibly associated has been observed. This association has been questioned on several grounds and remains controversial. We investigated if the presence of a γ-ray signal is a common feature among FRBs observable by *Fermi*/GBM. Given the wide sky coverage (all the not-Earth-occulted sky, i.e. ∼1/3 of the whole sky) and the extended band-pass (8–1000 keV), *Fermi*/GBM continuous data offer the possibility for a stringent test.

Compared to previous analogous works, our approach was innovative for two reasons. First, we investigated a long (200 s) time interval around the radio signal. This turned out to be challenging, given the highly-variable *Fermi*/GBM background due to its ∼26°-inclined orbit. This forced us to develop a background modelling strategy based on an approach like that used in machine learning methodologies. This allowed for the inves-

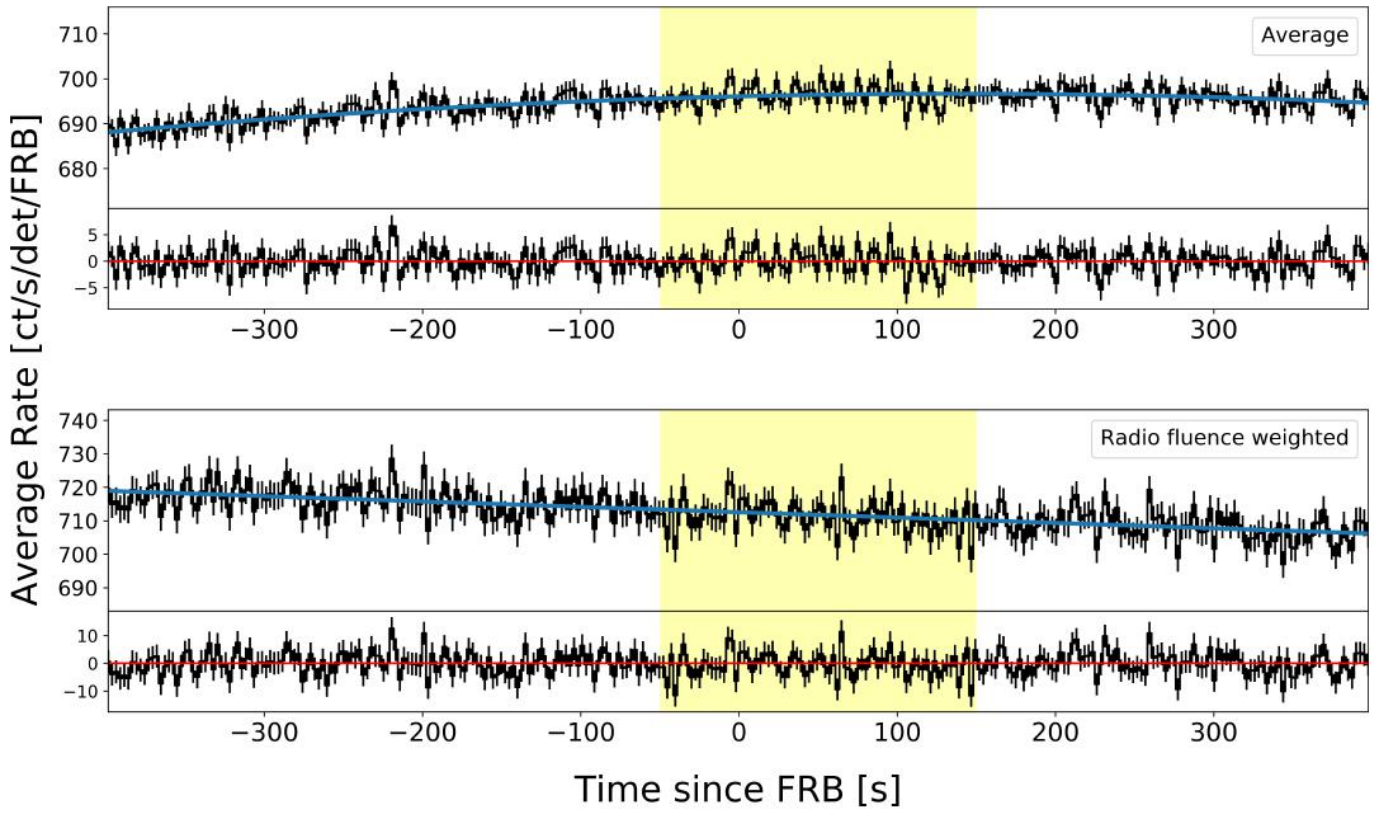

Fig. 3. Cumulative lightcurves, background fitting and residuals in the 27–1000 keV energy band. In the *upper panel* we report the result in the case of the arithmetic average of individual lightcurves, while in the *lower panel* the individual lightcurves are weighted with the radio fluence of the corresponding FRB. The polynomial degrees are respectively 2 and 1.

Table 2. 5-σ upper-limits on fluence for the power-law and thermal bremsstrahlung spectral shapes.

Mode [a]	Passband [b]	Window [s]	PL [c] [e]	TB [d] [e]
AA	TB	[−50,150]	4.0	1.0
AA	HB	[−50,150]	3.2	1.4
WA	TB	[−50,150]	6.1	1.6
WA	HB	[−50,150]	6.4	2.8
AA	TB	[0,150]	3.4	0.89
AA	HB	[0,150]	2.9	1.2
WA	TB	[0,150]	5.4	1.4
WA	HB	[0,150]	5.5	2.4
AA	TB	[0,100]	2.8	0.74
AA	HB	[0,100]	2.3	1.0
WA	TB	[0,100]	4.4	1.2
WA	HB	[0,100]	4.5	1.9
AA	TB	[0,50]	2.0	0.52
AA	HB	[0,50]	1.6	0.69
WA	TB	[0,50]	3.1	0.82
WA	HB	[0,50]	3.2	1.4
AA	SB	[0,1]	0.43	0.11
AA	HB	[0,1]	0.36	0.15
WA	SB	[0,1]	0.71	0.19
WA	HB	[0,1]	0.71	0.31

Notes. [a]AA: arithmetic average; WA: weighted average. [b]TB: total band (8–1000 keV); HB: hard band (27–1000 keV). [c]Power-law spectra, assuming $\Gamma = 1.16$. [d]Thermal bremsstrahlung spectra, assuming $T = 75$ keV. [e]In units of 10^{-7} erg cm^{-2}.

Table 3. 5-σ upper-limits on fluence for the power-law and thermal bremsstrahlung spectral shapes for the ASKAP bursts.

Mode [a]	Passband [b]	Window [s]	PL [c] [e]	TB [d] [e]
AA	TB	[−50,150]	11	2.9
AA	HB	[−50,150]	6.3	2.7
WA	TB	[−50,150]	12	3.2
WA	HB	[−50,150]	8.0	3.4
WA	TB	[0,150]	9.4	2.5
WA	HB	[0,150]	5.5	2.4
WA	TB	[0,150]	11	2.8
WA	HB	[0,150]	7.0	3.0
AA	TB	[0,100]	7.7	2.0
AA	HB	[0,100]	4.5	1.9
WA	TB	[0,100]	8.7	2.3
WA	HB	[0,100]	5.7	2.4
AA	TB	[0,50]	5.5	1.5
AA	HB	[0,50]	3.2	1.4
WA	TB	[0,50]	6.1	1.6
WA	HB	[0,50]	4.1	1.8
AA	TB	[0,1]	1.3	0.33
AA	HB	[0,1]	0.71	0.31
WA	TB	[0,1]	1.4	0.37
WA	HB	[0,1]	0.89	0.38

Notes. [a]AA: arithmetic average; WA: weighted average. [b]TB: total band (8–1000 keV); HB: hard band (27–1000 keV). [c]Power-law spectra, assuming $\Gamma = 1.16$. [d]Thermal bremsstrahlung spectra, assuming $T = 75$ keV. [e]In units of 10^{-7} erg cm^{-2}.

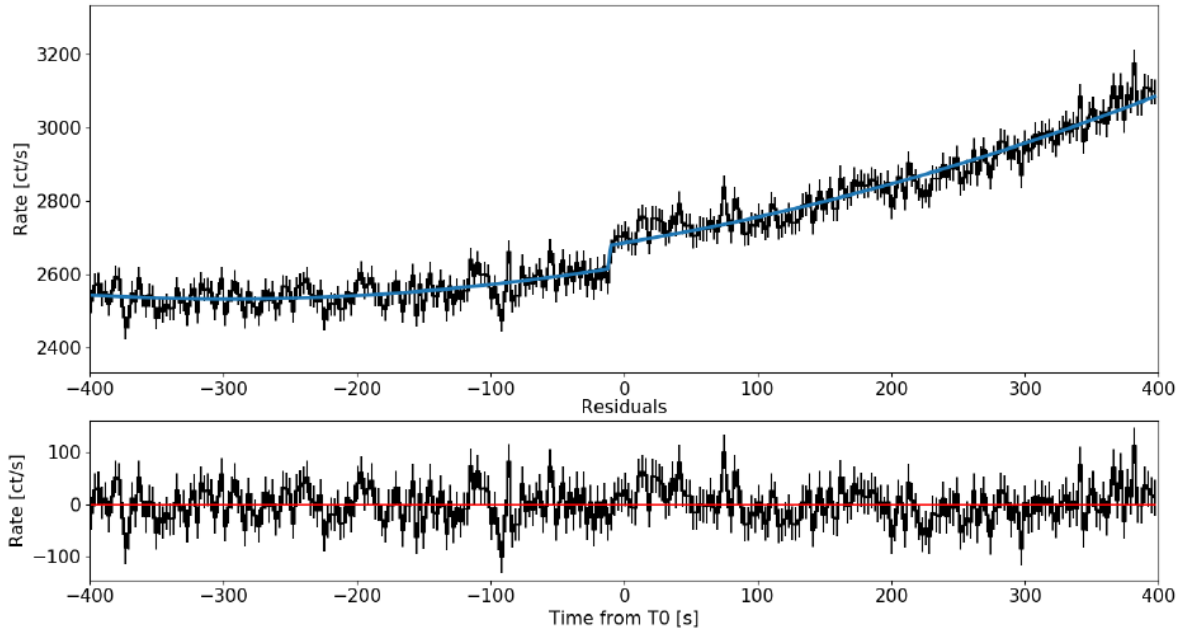

Fig. 4. *Top panel*: 8–1000 keV lightcurve for FRB 180725.J0613+67 along with the modelled background (solid line). The step-like increase around the time of the FRB is due to an occultation step of Crab and was modelled using the adjacent orbits. *Bottom panel*: residuals of the background modelling.

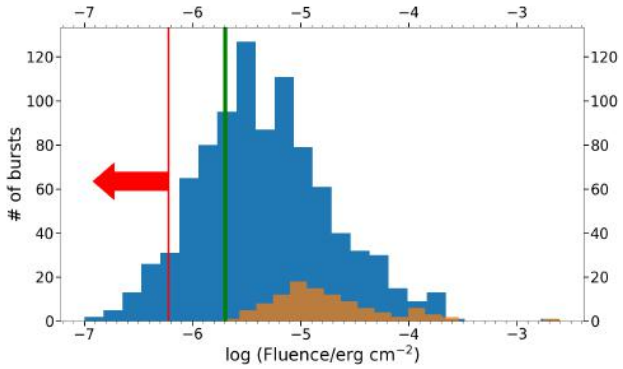

Fig. 5. 200-s fluence limit (red line) in the 8–1000 keV band compared with the distribution of LGRBs (2 s $< T_{90} <$ 100 s, blue) and very long GRBs ($T_{90} >$ 100 s, brown) detected by *Fermi*/GBM. The green line represents the quantity $F_{\gamma,\mathrm{D16,resc}}$ (see text).

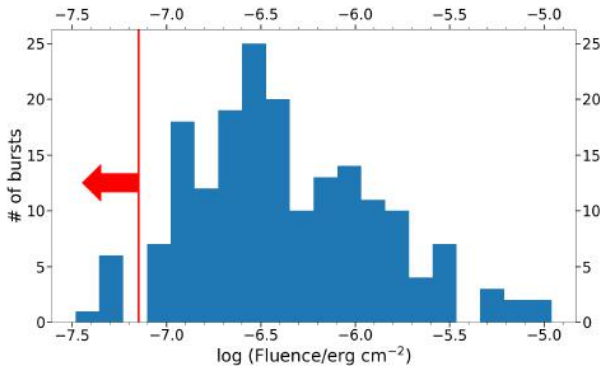

Fig. 6. 1-s fluence limit in the 8–1000 keV band compared with the fluence distribution of SGRBs $T_{90} \leq 2$ s detected by *Fermi*/GBM.

tigation of a previously unexplored extended interval that is crucial to search for faint and comparably long emission. Second, we carried out a sample study, building and studying cumulative lightcurves, thus improving the sensitivity under the assumption of a common behaviour.

We investigated the γ-ray lightcurves over four long integration times (200, 150, 100, and 50 s), finding no signal down to $\sim 10^{-7}$ erg cm^{-1} (5-σ limit): this excludes an emission like that reported by D16 to be a common feature among FRBs. Furthermore, we analysed the presence of a short-lived (1 s) signal, obtaining a 5-σ upper limit of $\sim 10^{-8}$ erg cm $^{-2}$.

Our cumulative approach is complementary to that adopted in other similar works, which searched for high-energy counterparts in individual FRBs.

Concerning the possible FRB–LGRB connection, our most conservative limit excludes the systematic presence of the 94% of *Fermi*/GBM-detected LGRBs (2 s $< T_{90} <$ 100 s) and the systematic presence of the entire very long GRBs ($T_{90} >$ 100 s) population. On the other hand, the possible simultaneous emission from a SGRB is constrained using our upper-limits on the shortest integration time. Our 1-s upper limit excludes the 96% of *Fermi*/GBM-detected SGRBs ($T_{90} <$ 2 s) to be a common FRB-associated feature. Moreover, our limits on the radio-to-gamma fluence ratio η ($\eta_{\mathrm{FRB}} > 10^{8.9}$ Jy ms erg^{-1} cm^2 for 1 s integration time) suggest a different emission process powering FRBs and giant flares from extragalactic magnetars, thus corroborating previous results obtained on smaller samples.

Our analysis benefits from the collective properties of the publicly available FRB catalogue, so it can be further extended to future richer samples and powered by the implementation of our algorithm in a software tool (e.g. training a neural network). Given that the number of FRB discoveries is dramatically rising thanks to the new and forthcoming radio facilities, a (conservative) rate of $\sim$1000 year^{-1} has been suggested (Petroff et al. 2019; Lorimer 2018). Given that we could use $\sim$1/3 of the catalogued FRBs, the limits we posed in this paper could be further lowered by a factor $\sim$7 in a matter of just a few years.

References

Atwood, W. B., Abdo, A. A., Ackermann, M., et al. 2009, ApJ, 697, 1071
Bannister, K. W., Deller, A. T., Phillips, C., et al. 2019, Science, 365, 565
Barthelmy, S. D., Barbier, L. M., Cummings, J. R., et al. 2005, Space Sci. Rev., 120, 143
Bhat, P., Meegan, C. A., von Kienlin, A., et al. 2016, ApJS, 223, 28
Chatterjee, S., Law, C. J., Wharton, R. S., et al. 2017, Nature, 541, 58
Cunningham, V., Cenko, S. B., Burns, E., et al. 2019, ApJ, 879, 40
DeLaunay, J. J., Fox, D. B., Murase, K., et al. 2016, ApJ, 832, L1
Feroci, M., Hurley, K., Duncan, R. C., & Thompson, C. 2001, ApJ, 549, 1021
Gajjar, V., Siemion, A. P. V., Price, D. C., et al. 2018, ApJ, 863, 2
Gehrels, N., Chincarini, G., Giommi, P., et al. 2004, ApJ, 611, 1005
Hessels, J. W. T., Spitler, L. G., Seymour, A. D., et al. 2019, ApJ, 876, L23
Hurley, K., Boggs, S. E., Smith, D. M., et al. 2005, Nature, 434, 1098
Johnston, S., Taylor, R., Bailes, M., et al. 2008, Exp. Astron., 22, 151
Katz, J. I. 2018, Progress in Particle and Nuclear Physics, 103, 1
Lorimer, D. R. 2018, Nat. Astron., 2, 860
Lorimer, D. R., Bailes, M., McLaughlin, M. A., Narkevic, D. J., & Crawford, F. 2007, Science, 318, 777
Margalit, B., Berger, E., & Metzger, B. D. 2019, ApJ, submitted [arXiv:1907.00016]
Mazets, E. P., Golentskii, S. V., Ilinskii, V. N., Aptekar, R. L., & Guryan, I. A. 1979, Nature, 282, 587
Meegan, C., Lichti, G., Bhat, P. N., et al. 2009, ApJ, 702, 791
Palaniswamy, D., Li, Y., & Zhang, B. 2018, ApJ, 854, L12
Palmer, D. M., Barthelmy, S., Gehrels, N., et al. 2005, Nature, 434, 1107
Petroff, E., Barr, E. D., Jameson, A., et al. 2016, PASA, 33, e045
Petroff, E., Hessels, J. W. T., & Lorimer, D. R. 2019, A&ARv, 27, 4
Platts, E., Weltman, A., Walters, A., et al. 2019, Phys. Rep., 821, 1
Ravi, V., Catha, M., D'Addario, L., et al. 2019, Nature, 572, 352
Scholz, P., Spitler, L. G., Hessels, J. W. T., et al. 2016, ApJ, 833, 177
Scholz, P., Bogdanov, S., Hessels, J. W. T., et al. 2017, ApJ, 846, 80
Shannon, R. M., & Ravi, V. 2017, ApJ, 837, L22
Shannon, R. M., Macquart, J. P., Bannister, K. W., et al. 2018, Nature, 562, 386
Spitler, L. G., Scholz, P., Hessels, J. W. T., et al. 2016, Nature, 531, 202
Svinkin, D. S., Hurley, K., Aptekar, R. L., Golenetskii, S. V., & Frederiks, D. D. 2015, MNRAS, 447, 1028
Tendulkar, S. P., Kaspi, V. M., & Patel, C. 2016, ApJ, 827, 59
Tendulkar, S. P., Bassa, C. G., Cordes, J. M., et al. 2017, ApJ, 834, L7
Thornton, D., Stappers, B., Bailes, M., et al. 2013, Science, 341, 53